Mechanical behavior of nanoporous gold functionalized with surface oxide and organic films

Vom Promotionsausschuss der
Technischen Universität Hamburg

zur Erlangung des akademischen Grades

Doktor-Ingenieurin (Dr.-Ing.)

genehmigte Dissertation (Monografie)

von

Olga Matts

aus

Tjumen, Russland

2025

Erstgutachter: Prof. Dr.-Ing. Jörg Weissmüller

Zweitgutachter: Prof. Dr. rer. nat. Patrick Huber

Vorsitzender: Prof. Dr.-Ing. Shan Shi

Tag der mündlichen Prüfung: October 28, 2025

Acknowledgments

During my doctoral journey, I have been fortunate to receive support and assistance from numerous individuals. I would like to take this opportunity to express my deepest gratitude and heartfelt appreciation for the invaluable guidance and encouragement that I have received along the way.

I would like to begin by expressing my heartfelt gratitude to my supervisors, Dr. Nadiia Mameka and Prof. Dr. Jörg Weissmüller. Their mentorship has been pivotal in my research, and I am profoundly grateful for the opportunity to work on such an intriguing and rewarding topic. Their unwavering support, combined with the freedom to explore and innovate over the past three years, has greatly enhanced my academic experience. I also appreciate the opportunities they provided for me to present and discuss my findings at various conferences, which have enriched my understanding and engagement in the field. I want to give special thanks to Dr. Nadiia Mameka, whose influence extends beyond academia. Her valuable insights and compassionate guidance have shaped me into a better researcher and individual. I feel fortunate to have had the privilege of learning from her.

I am deeply thankful to my second Ph.D. reviewer Prof. Dr. Patrick Huber for his thoughtful comments, encouragement, and expertise, which greatly contributed to improving the quality of my Ph.D. research.

I would also like to express my gratitude to Dr. Jürgen Markmann for his invaluable assistance with experimental setups and for his expert guidance in navigating laboratory challenges. His insights during our weekly group meetings and productive discussions have been instrumental in shaping my research.

I am deeply grateful to my colleagues at Helmholtz-Zentrum Hereon: Prof. Dr. Shan Shi, Seoyun Sohn, Dr. Stefan Berger, Dr. Hansol Jeon, Wei-Che Chang, Lina Sun, Dr. Henry Ovri, Dr. Yong Li, and Lena Dyckoff as well as our research team at Hamburg University of Technology (TUHH). The collaborative spirit and camaraderie we shared not only made our time in the lab enjoyable but also fostered an enriching environment for learning and growth.

Additionally, I would like to thank my peers from the Shenyang National Laboratory for Materials Science, particularly during the Sino-German Center Mobility Workshop on "Coupling between Nanocrystal Deformation and Surface Chemistry", as well as my short research visit to Shenyang, China. I am grateful to Prof. Hai-Jun Jin, Dr. Lingzhi Liu, Fan Peng, Li Wang, and Xingyuan Liu for their support and inclusion in such an international endeavor.

I would also like to acknowledge Dr. Tobias Krekeler, Dr. Gunnar Schaan, and Dr. Martin Ritter for their assistance with the electron microscopy unit at TUHH. Their expertise and guidance greatly enriched my research process.

My sincere thanks go to the administrative staff at Helmholtz-Zentrum Hereon, including Stephanie Kropf-Eilers, Sabine Schrader, and Uwe Benn, as well as to Haide Alfort-Springer and Robert Günter from TUHH. Your efficiency and support have been invaluable in ensuring a seamless research experience.

I would like to thank the German Research Foundation for funding this work via SFB 986 "Taylor-Made Multiscale Materials Systems - M3", sub-project B10. Your support has made this research possible.

Lastly, I want to extend my gratitude to my family and friends for their unwavering support during this challenging yet rewarding endeavor. Their encouragement has been my anchor, reminding me of the importance of perseverance and passion in achieving my goals. I am excited to carry these lessons into the next chapter of my life.

Abstract

This thesis investigates functional mechanical properties of smart stimuli-sensitive hybrids based on nanoporous gold and organic layers. As a metal skeleton, unimodal and hierarchical nanoporous nested networks fabricated via an electrochemical dealloying were employed. Three electrochemistry-inspired approaches are integrated to surface modification of nanoporous gold – reversible capacitive assembly of ionic charges in the electric double layer, electrosorption of oxygen-species, and chemisorption of electroactive ferrocene-terminated alkanethiol self-assembled monolayers. To probe functionalities such as actuation and tunable stiffness, *in situ* experiments are carried out in electrochemical environment.

In situ dilatometry is employed to investigate the impact of the electrochemically-controlled interface on the actuation behavior of the hybrids. The findings demonstrate remarkable differences in the strain responses of the materials with respect to the pore morphology and surface state. The contribution of the surface stress to the reproducible macroscopic actuation is experimentally confirmed for all hybrids under study. The negative values of the electrocapillary coupling parameters are determined pointing to the compressive surface stress in the metal surface upon the capacitive charging and electrosorption of oxygen-species.

In nanoporous gold modified with the ferrocene-bearing self-assembled molecules, the actuation strain non-linearly scales with the ferrocene surface fraction testifying to the impact of the redox-events in the monolayer on the macroscopic actuation of the nanoporous network. The estimation of the mean actuation coefficient in the hybrids with the electroactive self-assembled monolayers pointed out to an enhanced strain response compared to those induced by conductive polymers.

Along with actuation, the thesis explores the size-dependence of the effective elastic modulus of the hybrids via *in situ* dynamic mechanical analysis. Experimental observations in this study at a structural size below 100 nm support a hypothesis that the effective elastic behavior is dominated by the surface excess elasticity at this scale when specific adsorption is involved. Subsequently, the electro-elastic coupling parameters have been estimated for bulk nanoporous networks.

Overall, this thesis discusses the electro-chemo-mechanical coupling in the nanoporous hybrids. It demonstrates that hierarchical nanoporous gold serves as a robust platform for enhancing the functional properties of nanoporous materials. Incorporating organic films allows nanoporous gold to convert chemical processes into mechanical motion, paving the way for further research and practical applications of nanoscale materials with tunable properties.

Contents

List of Figures

List of Tables

List of Symbols

Symbol	Notation	Unit
L and $\tilde{L}$	ligament size and ligament spacing	nm
f	surface stress	N m^{-1}
γ	surface tension	N m^{-1}
ς	electrocapillary coupling parameter	V
λ	electro-elastic coupling parameter	V
I	electric current	A
E_{SHE}	electric potential given vs. standard hydrogen electrode	V
E_{pa}, E_{pc}, ΔE_{peak}	electric potential at anodic peak, cathodic peak, and peak shift	V
φ_x	solid/volume fraction of x = Au, PPy, etc.	-
m	sample mass	mg
V	sample volume	mm^3
A and A_{ECSA}	geometric and electrochemically active surface areas	cm^2
α_{m}	mass-specific surface area	m^2 g^{-1}
Q	net charge	C
q	charge density: Q/A (planar), Q/A_{ECSA} (nanoporous)	C m^2
$\delta l/l$	relative macroscopic length change (strain)	-
Δk	cantilever's curvature change	km^{-1}
Θ_{OH}, Θ_{Fc}	surface coverage of OH-species and ferrocene-terminated molecules	ML
Γ_{Fc}	superficial density of ferrocene-terminated molecules	mol cm^{-2}
$\Gamma_{\mathrm{Fc}}^{\mathrm{theor}}$	theoretical value of Γ_{Fc} of 4.5×10^{-10}	mol cm^{-2}
$\Phi_{\mathrm{Fc^+}}$	ferrocene fractional surface coverage	-
$t_{1/2}$	half-time indicates responsiveness of a material	s
ε	prestrain of a material induced by compression machine	-
τ	apparent excess thickness	pm
$\mathbb{C}$	surface excess elastic constant	N m^{-1}
K and B	bulk modulus and biaxial modulus of bulk	GPa
Y (Y^{eff})	Young's modulus (effective for nanoporous material)	MPa
Y' and Y''	storage and loss moduli	MPa
$\delta Y'/Y_0'$	relative stiffness change	%
σ	stress	MPa
σ_{M}	matched load	MPa
W_{V}	volumetric work density	J m^{-3}
W_{M}	mass-specific strain energy density	J kg^{-1}

List of Abbreviations

np-Au	nanoporous gold
hnp-Au	hierarchical nanoporous gold
SAM	self-assembled monolayer
Fc-SAM	ferrocene-terminated self-assembled monolayer (molecule)
FcC_6	6-(Ferrocenyl)hexanethiol SAM ($C_{16}H_{22}FeS$)
FcC_{11}	11-(Ferrocenyl)undecanethiol SAM ($C_{21}H_{32}FeS$)
OH/O	electrosorbed oxygen-species
RTO	Au-O replacement turnover process
ECSA	electrochemically active surface area
EDL	electric double layer
SHE	standard hydrogen electrode
SEM	scanning electron microscopy
TEM	transmission electron microscopy
CV	cyclic voltammetry
CA	chronoamperometry
DMA	dynamic mechanical analysis
WE	working electrode
CE	counter electrode
RE	reference electrode
UPW	ultrapure water
PPy	polypyrrole

Chapter 1

Introduction

1.1 Dealloyed nanoporous materials with interface-controlled behavior

Dealloying refers to a selective dissolution of less noble (sacrificial) elements from an alloy, resulting in a porous structure predominantly composed of the more noble alloy constituent [1–3]. Nanoporous metals produced via dealloying occupy a distinct position within the length-scale spectrum of porous materials [4, 5]. These metals can encompass a diverse range of elements, from lithium [6] to gold [7], and can be found in various forms, including thin films [8, 9], bulk samples [10, 11], and structures that range from monoporosity [12–14] to hierarchical porosity [15, 16].

Nanoporous metals have garnered significant interest due to their remarkable properties, such as high specific surface area, low density, and fast mass transport [17–19]. Incorporating a nanoporous network within an aqueous electrolyte allows for modulation of the superficial charges at the metal-electrolyte interface [10] (Chapter 2). Aqueous electrochemical interfaces play a pivotal role in various promising applications [20]. The distinct mechanical, physical, chemical, and magnetic properties of nanoporous metals make them suitable for a wide array of applications in fields such as catalysis [21, 22], actuators [23, 24], sensors [25], optics [26], plasmonics [27, 28], and energy conversion/storage [29, 30].

This thesis primarily focuses on one notable example – nanoporous gold (np-Au) – characterized by a bicontinuous network of nanometer-sized metallic struts (ligaments) and interconnected pores [9] (Figure 1.1). The ability to control pore and ligament dimensions, precisely tailor composition, modify surface properties, and eliminate support effects makes this material particularly ideal as a model system for investigating nanoscale size and interface effects [31].

The surface area, surface roughness, and surface curvature of np-Au can be readily adjusted by means of chemical or/and thermal annealing [5, 32], as well as by introducing a multiscale porosity [16, 33]. Recently, Shi *et. al.* [15] advanced a dealloying-coarsening-dealloying methodology based on the approach of [33] to fabricate the crack-free mm-sized samples. The authors [15] reported enhanced mechanical properties of hierarchical np-Au (hnp-Au) when evaluated under uniaxial compression in air atmosphere. This finding sets the stage for the current investigations into the comparison of the functional properties of np-Au and hnp-Au in electrolyte environment. The impact

of the surface and the size on the properties of np-Au will be elaborated in the following sections of this thesis.

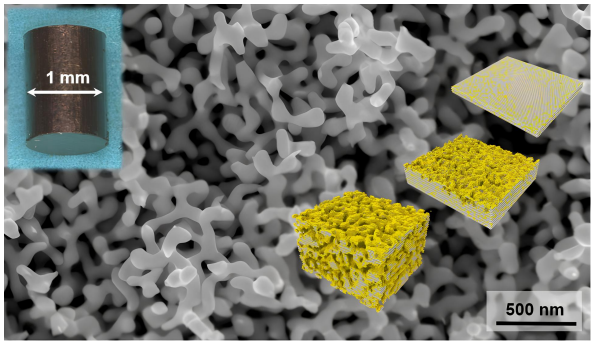

Figure 1.1: Nanoporous gold. An optical image of a real np sample (left top corner), Kinetic Monte Carlo simulation of the microstructure evolution during dealloying of np-Au (right) adapted from [34], the microstructure (background).

1.2 Surface functionalization of np-Au and its impact on mechanical behavior

In the realm of high surface area materials, significant attention is focused on surface characterization and modification, largely due to the unique energetic properties of surface atoms. Each atom in a bulk material possesses a specific energy level, while surface atoms exhibit higher energy due to reduced coordination with neighboring atoms and the presence of dangling bonds. This elevated energy is termed as surface excess free energy. To minimize the energy, surface atoms contract resulting in surface and bulk stresses in solids [35].

The microscopic origin of surface stress is illustrated in Figure 1.2. The act of creating a surface – such as through the truncation of a bulk crystal – generates dangling interatomic bonds. These dangling bonds tend to relax, leading to the formation of enhanced bonding within the surface plane. Consequently, surface atoms generally exhibit a tendency for closer interatomic spacing compared to their bulk counterparts. This phenomenon aligns with the empirical observation that atomic bonds are typically shortened when a coordination number (or bond order) is reduced [36].

The constraints imposed by the crystal lattice on the surface atoms prevent them from approaching one another. As a result, the enhancement of in-plane bonding induces stress within the bulk crystal. The stress induced by surface atoms can be conceptualized as a capillary force, which is quantitatively described by the surface stress. The inclination towards strengthened bonding at clean metallic surfaces is evidenced by the prevalent observation of positive surface stress in metals, which exerts a compressive force on the underlying lattice in a tangential direction. However, it is also thermodynamically feasible to observe negative surface stress values, which tend to expand the underlying lattice [35]. Such negative surface stress has been documented in the context of metal alloy surfaces [37]. Using a combined experimental and theoretical approach, Lemier and Weissmüller [37] reported that hydrogen enrichment at the grain

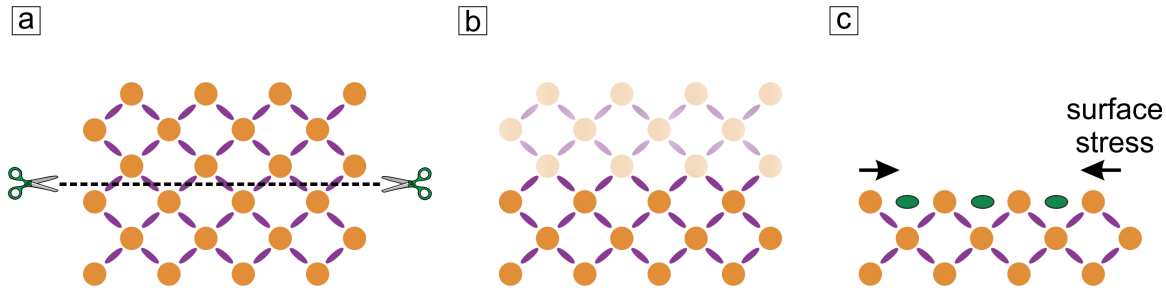

Figure 1.2: Microscopic origin of surface stress. (a) Cross-section through a bulk crystal with atoms (orange circles) and interatomic bonds (violet ovals). Truncating the crystal as indicated (dashed line) creates a surface. The unrelaxed, as-truncated surface with dangling bonds (b) that relax to form new bonds (green ovals) in the surface plane (c), strengthening the in-plane bonding. As a consequence, the surface atoms favor a closer interatomic spacing than the bulk resulting in a stress on the bulk crystal. Redrawn from [35].

boundaries in nanocrystalline palladium causes tensile stress in the core, resulting in compressive surface stress.

Local surface stress components can be varied by tailoring the surface parameters of np materials or inserting a physical interphase/coating system, serving as a key technique to enhance the performance and longevity of materials [38]. To gain new functionalities of np-Au, various core-shell nanoporous composites have been created using electrochemical and surface functionalization methods, including electroplating, atomic layer deposition (ALD), chemical vapor deposition, etc. These composites include systems such as np-Au/Ag [39], np-Au/CuO [40], np-Au/self-assembled monolayers (SAM) [41–44], np-Au/Pt [45, 46], np-Au/TiO_2 [47, 48], np-Au/Al_2O_3 [49], np-Au/MnO_2 [50], np-Au/ZnO [51], np-Au/Sn [52], np-Au/RuO_2 [53], Au/MoS_2 [54], np-Au/electrosorbed oxygen-species [55, 56], np-Au/polypyrrole (PPy) [57, 58], and np-Au/polyaniline [59]. Among other properties, surface contribution to the mechanical actuation, elastic, and plastic behavior of np-Au was investigated in the listed above references and is selectively summarized in Figure 1.3.

Biener *et al.* [49] revealed that the ALD of nanometer-thick Al_2O_3 coating onto the surface of np-Au serves a dual purpose, first, mitigates the coarsening tendency of np-Au (stable up to 1000 °C) and, second, enhances its stiffness and hardness as the thickness of the deposited coating increases (Figure 1.3a). The mechanical characteristics of the resulting core-shell structures are influenced by both the Young's modulus and the volumetric fractions of the core and shell components. The authors noted that the alumina coating appears to elevate the critical stress level beyond the already high threshold (≈ 1 GPa) necessary for plastic deformation in "bare" Au ligaments [49].

SAM provides exceptional opportunities to enhance fundamental understanding of interfacial phenomena on (mechanical) properties of nanoporous metals. The impact of 6-mercapto-1-hexanol SAM on the mechanical properties of np-Au was investigated in a study by Miyazawa *et al.* [44]. As illustrated in Figure 1.3b, the load-displacement curves demonstrate that the hardness of the SAM-modified np-Au is lower than that of the unmodified samples. The authors employed the first-principles shear test simulations to explain the findings. According to them, the reduced hardness of the SAM-modified np-Au results from the facilitation of dislocation endpoint movement at

the surface, which is influenced by the chemical interactions associated with the Au-S bonding.

Later, Mameka *et al.* [41] exploited electroinactive alkanethiol SAMs with various chain lengths and terminal groups for the surface functionalization of bulk np-Au (Figure 1.3c). The mechanical behavior was studied via *in situ* uniaxial compression. The authors revealed that the thiol adsorption on np-Au caused the increased flow stress up to 50 %. The strengthening phenomenon was attributed to the adsorption locking of dislocation endpoints at the surface mediated by the fairly strong Au-S interaction, in contrast to [44]. In other words, the adsorbed species tend to pin the dislocation, enhancing the flow stress. However, there is still a room to discuss on the effect of the SAM on the mechanics of np metals. Earlier work of Norman and Badia [60] on the effect of more complex organic adsorbates such as the electroactive SAM on the planar Au showed that the oxidation of the monolayer induces a surface stress variation. This motivated the current research of this thesis on the impact of the electroactive SAM [61] on the mechanics of a np metal.

Interface-controlled mechanical properties of np-Au were studied in electrolyte as shown in Figures 1.3d-f. The actuation behavior of np-Au coated with electroactive PPy was explored by Roschning and Weissmüller [57]. The authors observed enhanced actuation, ε, amplitudes of np-Au modified with different fractions of PPy, φ_{PPy}, upon cycling in aqueous electrolyte of perchlorate acid, as well as PPy-strengthened np-Au under compression in air (Figure 1.3d). They coupled the actuation response with the surface stress variations upon the redox reaction of PPy via the electrocapillary coupling parameter, ς [62]. The coefficient is a tool to quantify the surface stress variations as a function of the transferred charge density. There is a number of data on the actuation properties of np metals [23, 24, 63–65], however, a limited data available on the impact of the complex organic adsorbates on the actoric functionalities and coupling in np metals [57, 58, 66].

Another mechanical study on np-Au was carried out by Mameka *et al.* [56] using *in situ* dynamic mechanical analyzer. They reported the first experimental observation on the variation in the effective macroscopic stiffness of bulk np-Au when the surface state is modulated by the potential control in electrolyte (Figure 1.3e). The effective stiffness changes of up to 8 % were attributed to the reversible OH-electrosorption. To explain the findings, the authors employed the continuum theory of the surface excess elasticity [67] where the surface is considered as a separate layer of a given thickness with an elastic modulus different from its bulk. This approach evaluates the impact of the surface state changes on the surface free energy, the relative change in area by elastic strain, and the superficial charge density. The magnitude and even sign of the surface excess elastic constants were reported for "clean" and oxygen-species electrosorbed np-Au surfaces. The results differ from the ones obtained via atomistic calculations [68]. The charge dependence of the surface excess elastic constant is quantified by the electro-elastic coupling parameter, λ. Further studies on the surface excess elasticity of metals are crucial for predicting and manipulating changes in material stiffness.

Electrically-tuned strength and flow stress of np-Au was discovered by Jin and Weissmüller [55] in response to external electric signals. Figure 1.3f illustrates the increased plastic flow stress due to the anodic oxide formation (red line) versus np-Au with a clean surface (gray line). According to the results, the authors highlight that

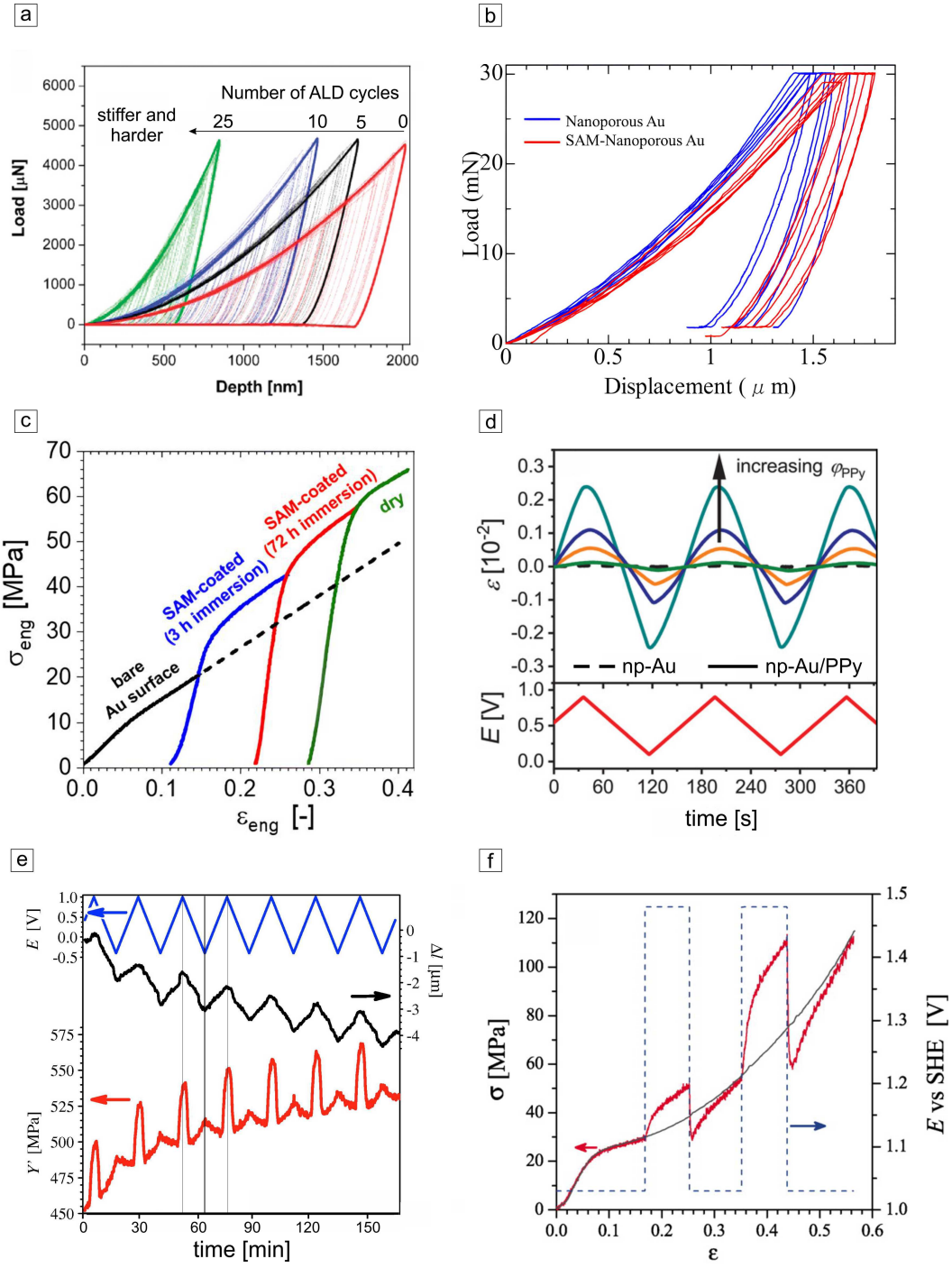

Figure 1.3: Mechanical properties of surface-modified np-Au studied in air (a)-(c) and electrolyte (d)-(f). (a) Nanoindentation load–displacement curves of np-Au samples coated with 0, 5, 10, and 25 ALD cycles of Al_2O_3 coating [49]. (b) The load-displacement curves prove that the hardness of the 6-mercapto-1-hexanol SAM-modified np-Au is lower than that of the non-modified samples [44]. (c) Comparison of the strengths, σ_{eng}, of "bare" np-Au and thiol SAM-modified np-Au during deformation, ε_{eng} [41]. (d) Enhanced actuation, ε, responses of np-Au coated with different fractions of PPy, φ_{PPy} [57]. (e) Electrical stiffness, Y', modulation and relative length change, Δl, of np-Au upon potential, E, control. The larger changes in Y' correspond to OH electrosorption/desorption regime [56]. (f) Tunable flow stress, σ, in np-Au under applied electric potential, E, in a range of the reversible anodic oxide formation [55]. Reprinted with permissions.

the surface stress does not play an important role in potential-dependent strengthening. They addressed several mechanisms governing the phenomenon, among which are changes in surface tension, adsorption locking, and surface excess elasticity.

There are few examples of the functional mechanical properties of np metals discovered so far. Further research is needed to achieve a more comprehensive understanding of the effective mechanical properties of nanomaterials, as well as the electro-chemo-mechanical coupling phenomena occurring at the interfaces.

1.3 Size-dependent mechanical properties of clean and adsorbate-covered nanoporous Au

As the dimensions of a material are reduced, resulting in a higher surface-to-volume ratio, the contributions of the surface to the overall macroscopic mechanical performance of the bulk material become increasingly pronounced [69]. This shift in mechanical behavior can be attributed to several factors, including the greater relative influence of surface defects, atomic arrangements, and potential surface-specific phenomena, such as adsorption effects or phase transitions, that are less significant in larger, bulk samples. The understanding of these surface effects is critical, particularly in the context of nanomaterials, where the mechanical properties cannot be directly extrapolated from bulk material behavior due to the increased impact of surface characteristics. This necessitates a comprehensive approach to characterize and predict the mechanical properties of materials at reduced scales, highlighting the interplay between surface and bulk phenomena.

Mechanical properties of an individual nanoobject reflect the interaction between free surface and the underlying crystal lattice [35]. Hence, np-Au can be represented as a network of interconnected nanowires (NW) of a certain diameter. The mechanical response of Au NWs was studied theoretically [70, 71] and experimentally [69, 72, 73]. The features of deformation mechanisms in Au NWs and np-Au were discussed in the experimental study by Dou and Derby [74]. The plasticity of Au NWs was found to be a size-dependent (Figure 1.4a), whereas the elasticity does not show a conclusive trend as a function of the specimen size (Figure 1.4b). A review by Park *et al.* [75] shows a combination of variability and overlap between the experimental measurements of the elastic properties of Au NWs and the stiffening or softening mechanisms identified through computational analysis. The discrepancy in the findings has been addressed to the main mechanism governing the softening and stiffening of a NW that is the loss of bonding neighbours or the electron redistribution at the surface, respectively [76].

1.3.1 Plasticity of np-Au

Nanoporous metals exhibit unique mechanical behaviors due to their finely textured microstructures and high surface area-to-volume ratio. Several dislocation movement mechanisms have been proposed for the deformation of np metals in the literature which are listed here along with brief explanations:

Dislocation starvation, storage, and interaction. In nanoporous metals, the high surface area can limit the availability of dislocations for slip, leading to dislo-

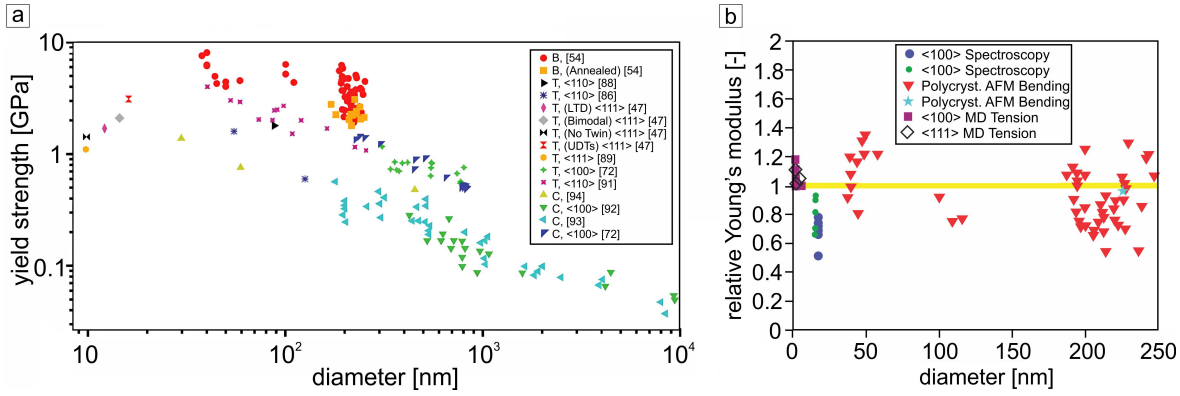

Figure 1.4: Summary of studies on the plasticity and elasticity of Au NWs. (a) Size-dependent response in the yield strength of Au NWs as a function of the NW diameter, based on the loading method of bending (B), tensile (T), and compression (C). Reprinted from [77]. (b) Normalized (versus bulk Au) experimental (atomic force microscopy, AFM) and computational (molecular dynamics, MD) results for the size-dependent Young's modulus of Au NWs. The yellow line indicates the reference of the bulk Au Young's modulus. Adapted from [75].

cation starvation as has been confirmed in gold nanopillars under compression [78, 79].

However, Jin *et al.* [80] argue that the dislocation starvation scenario cannot be transferred to np-Au, because the macroscopically coherent crystal lattice prevents the complete removal of lattice dislocations. Their electron backscatter diffraction (EBSD) data confirm that plastic deformation significantly enhances the defect density.

Later, Ngô *et al.* [81] by employing molecular dynamics simulation found out that the plastic deformation of np-Au under compressive load is accompanied by dislocation storage and dislocation interaction, along with a strong strain hardening, but not the dislocation-starvation scenario. The final dislocation density of several dislocations per ligament is extremely high, suggesting the drastic Taylor hardening.

A recent study on the deformation-induced accumulation of defects in np-Au leafs by Liu and Weissmüller [82] revealed the formation of twins on several sets of crystallographic planes. The interaction of the twins leads to the appearance of the Lomer-Cottrell locks [83]. This inhibits dislocation escaping from np-Au, thus avoiding the dislocation starvation scenario that is often considered in the "smaller is stronger" context of the small-scale plasticity. Instead, the authors addressed the strain hardening as it is apparently linked to the accumulation and interaction of twins.

Dislocation source truncation. Dislocations in metals often originate from sources such as Frank-Read sources, which consist of loops that can propagate under a shear stress [84]. In nanoporous structures, the confined geometry can truncate these dislocation sources by reducing their effective length. The result is the enhanced strength since fewer dislocations can be nucleated, reducing the overall dislocation density and hardening the material.

Grain boundary dislocation emission. In materials with fine microstructures, such as nanoporous metals, dislocations can be emitted from grain boundaries. The network of grains in nanoporous structures provides additional sites for dislocation generation. When shear stress is applied, grain boundaries play a critical role in activating dislocation sources, thus influencing the deformation behavior ([80, 85], and references

therein).

Dislocation junction formation. In the dense dislocation network that can develop during deformation, dislocations can interact to form junctions or nodes that can immobilize dislocation segments. These junctions are barriers to dislocation movement, contributing to strain hardening [86]. A TEM investigation confirmed the formation of dislocations and their subsequent glide towards ligament junctions [74]. The dynamics of junction formation and breaking under applied stress can significantly influence the mechanical response in np metals.

The size and distribution of pores within the metal can impact the mobility of dislocations [87]. Smaller pore sizes can create more significant obstacles for dislocation motion, leading to higher flow stresses. Conversely, larger pore sizes may facilitate dislocation movement but can lead to localization of plastic deformation, affecting overall ductility. These mechanisms collectively contribute to the unique mechanical properties of nanoporous metals, such as enhanced strength and tailored ductility, making them interesting for various applications in materials science and engineering.

Earlier works on the mechanical properties of np metals were discussed with respect to the scaling relations proposed by Gibson and Ashby [88] for metallic foams. The scaling law for the macroscopic yield strength, σ_{y}, links a relative density (ratio between the density of the porous and the massive material), φ, of np-Au to the local ligament strength, σ_{y}^{L}, via:

$$\sigma_{\mathrm{y}} = C_1 \sigma_{\mathrm{y}}^{L} \varphi^{3/2} \quad , \tag{1.1}$$

where $C_1 = 0.3$ indicates a geometry constant for np-Au at $\varphi \leq 0.3$. Note, ligaments tend to maintain their connectivity during (self-similar) coarsening at initial $\varphi \geq 0.3$, while networks with $\varphi \leq 0.3$ tend to disconnect [89], the phenomenon is known as loss of connectivity. The connectivity can be quantified via the *genus* - a number of cuts that can be made upon a closed surface without separating it into two disconnected bodies [90].

Experimental approaches [80, 91–99] and molecular dynamics simulations [81, 100] proved that np-Au exhibits a higher yield stress than predicted by the Gibson-Ashby model. The ligament size-dependent σ_{y} was addressed by Hodge *et al.* [92] on np-Au foams. The authors suggested that the strength is controlled not only by the relative foam density, but also by the structural size, and incorporated a Hall–Petch-type relation in the scaling equation of Gibson and Ashby [88].

A consistent data set on factors defining the mechanical behavior of bulk np-Au can be found in [99]. The authors confirmed the relevance of an apparent (effective) load-bearing solid fraction, φ^{eff}, of np-Au for the strength and Young's modulus. The effect of coarsening on the loss of the connectivity was discussed as well. When a solid fraction, φ, increases to above $\approx 1/3$, a transition from a homogeneous deformation to a localized densification takes place in np-Au under uniaxial compression [101].

A decisive contribution of the surface tension to the small-scale plasticity was presented by Lührs *et al.* [103]. The effective macroscopic plastic Poisson ratio, v_{p}, of np-Au provides a signature for a local tension–compression asymmetry of the nanoscale struts that form the network. The surface tension, γ, promotes compression while impeding tensile elongation. Because the transverse strain is partly carried by the elongation of ligaments oriented normal to the load axis, the surface-induced

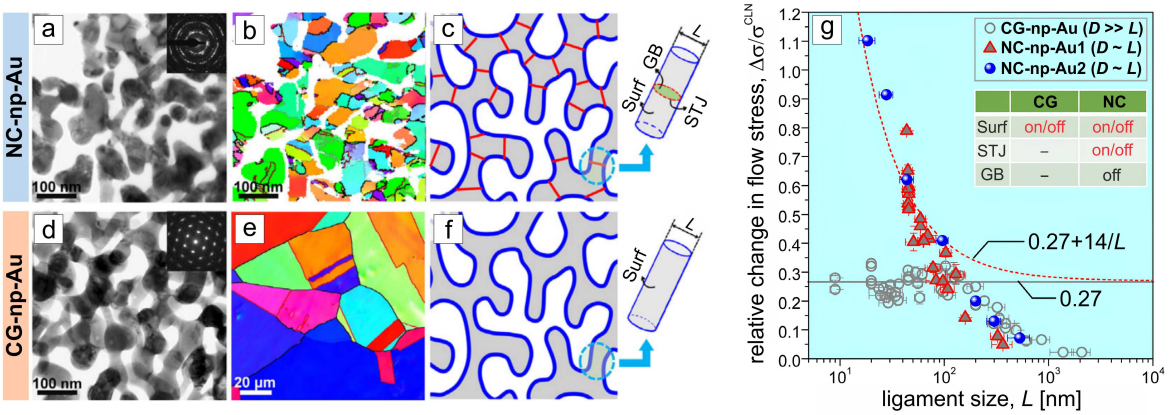

Figure 1.5: Np-Au with high-population STJs. TEM images and an inset selected area electron diffraction pattern (a) and (d), precession electron diffraction orientation maps (b) and (e), schematics of microstructures (c) and (f) of NC-np-Au (L = 43 nm) and CG-np-Au (L = 32 nm), respectively. GB, CG, and NC denote grain boundary, coarse-grained, and nanocrystalline, respectively. Results of the *in situ* compression of np-Au at a strain rate 10^{-4} s^{-1} in an electrochemical environment upon the OH-electrosorption (g). NC-np-Au1 dealloyed from Al_2Au, NC-np-Au2 obtained by compressing CG-np-Au to a strain of 55 %. Grain size given as D. Reprinted with a permission from [102].

tension–compression asymmetry acts to reduce v_p.

As it was already discussed in the previous section, the flow stress, σ, of np-Au can be controlled by the surface-modification, for example, via the anodic oxide formation [47]. This phenomenon was further elaborated by Mameka *et al.* [104], Wu *et al.* [105], and Zhang *et al.* [102]. The impact of capillarity for strength in np-Au was discussed by Mameka *et al.* [104]. They confirmed that the surface tension dominates over the surface stress upon the plastic deformation.

The studies [102, 105] report a size-dependent σ in np-Au. The change in σ due to the surface oxide is negligible when the ligament size, L, exceeds > 2 μm, increases with decreasing L for ≈ 200 nm $< L < 2$ μm, and then saturates at ≈ 27 % for $L < 200$ nm. These results indicate a transition from a bulk-like to a surface-mediated deformation behavior of nano-ligaments as L decreases from ≈ 2 μm to ≈ 200 nm. The observation at $L < 200$ nm support the notion that the deformation is dominated by the surface-dislocation-nucleation at this scale [105].

The effect of the surface triple junctions (STJs) on the mechanical response of np-Au was discussed in [102] (Figure 1.5). They decoupled the surface effect from the combined STJ and grain-boundary effects by comparing the mechanical responses of two types of np-Au: a nanocrystalline np-Au containing large quantities of surfaces, grain boundaries, and STJs, and a coarse-grained np-Au with large surface area but very few grain boundaries and STJs [102]. The strength of np-Au became sensitive to STJ modification when the structural size was less than ≈ 100 nm, indicating that STJs started to influence the ligament strength at sub-100 nm scale. The authors attributed the STJ effect to the emission of dislocations from STJs during plastic deformation. Hence, the structure and chemistry at STJs should be considered in understanding the mechanical response of sub-100 nm scale materials [102].

The literature indicates that in order to differentiate between surface contributions

and bulk-related effects in plasticity, one of the promising approaches is a research conducted in an electrolyte under controlled electric stimuli. In this thesis, an impact of electroactive ferrocene-terminated alkanethiol SAMs on the plasticity of np-Au within an electrolyte environment has been investigated.

1.3.2 Elasticity of np-Au

The elastic response of np-Au differs from solid Au due to size effects, where the high specific surface area supplies a large fraction of undercoordinated atoms that affect the bond strength. The understanding of the elasticity of a np metal begins with the studies on metallic NWs. Is smaller stiffer or more compliant? This question has been a controversial subject of scientific discussions for a long time. A theoretical prediction using the combine approach of the continuum mechanics and DFT on the elasticity of Au NWs by Elsner *et al.* [71] showed that the material becomes more compliant with the decrease of its diameter independently of the deformation mode. Their analytical continuum analysis of the effective stiffness of NWs under tensile, bending, and torsial loading revealed that surface excess elasticity becomes more significant at a NW diameter smaller than 10 nm.

Later, the effects of morphology and topology on the elastic response of np-Au were studied by Soyarslan *et al.* using the numerical simulations [106]. An outstanding size effect associated with surface elasticity showing a clear surface-area-to-volume ratio dependence controlled by the ligament diameter was found, especially pronounced beyond 10 nm of a ligament diameter.

So far, only one experimental result is available on the stiffness change of the "clean" (weak ion adsorption) np-Au surface [56]. The authors found that np-Au is proned to be stiffer with the accumulation of electrons (capacitive discharging) during cycling in aqueous electrolyte. The findings are explained by means of the theory of the surface excess elasticity.

The size-dependence of the stiffness variations of bulk mm-sized np-Au upon capacitive charging ("clean" surface, Section 4.3.1) or adsorbate-coverage (OH-electrosorption, Section 4.3.2; SAM, Section 4.3.6) is not available in the literature and have been investigated within the framework of this thesis.

The main factors influencing the elasticity of a np metal are a solid fraction and a network connectivity [15, 97, 98, 106, 107]. Predicting the elastic behavior theoretically has been attempted using the Gibson-Ashby scaling law which links the variations of the Young's modulus, Y, with the solid fraction, φ, as [88]:

$$Y = C_2 Y^L \varphi^2 \quad , \tag{1.2}$$

where $C_2 \approx 1$ is a geometry constant, and Y^L is the Young's modulus of the solid base material, for Au it takes value of $Y^L \approx 80$ GPa.

However, this model overestimates Y for $\varphi < 0.35$ due to the topological features of np metals. A modified version of the scaling relations was proposed by Roberts and Garboczi [108], where the authors introduced the percolation threshold for the solid fraction. Later, Soyarslan *et al.* have been corrected the equation proposed in [108] taking into account the limit of the full density, and demonstrated that their model is in the excellent agreement with literature data for the Young's modulus, when $\varphi < 0.5$.

The next important parameter is the network connectivity which has been suggested as a structural feature that accounts for the mechanical properties of np metals [97, 98]. Soyarslan *et al.* [106] discussed the role of the network connectivity as a potential source of anomalous compliance in np metals. The authors found out that the scaled genus density decreases with φ, in contrast to the Gibson-Ashby model. A genus-dependent scaling law for the elasticity of np-Au was discussed by Sohn *et al.* [109]. They reported the effective Young's modulus must be considered as the quadratic functions of a genus and a solid fraction. The evolution of the topology and φ during coarsening has a great impact on the mechanics of a np metal [97]. Numerical simulations settled the issue with the size-dependence of the elasticity of np-Au, but the experimental arguments are still under discussion.

1.4 Research objectives and outline of the thesis

As it was presented in the subsections above, nanoporous (np) metals due to their high surface-to-volume ratio offer exciting opportunities for exploring and unraveling the mechanical behavior of nanosystems. A remarkable step on the way to understand the small-scale mechanics was the implication of electrochemical environment into the experiments on np specimens affording an *in situ* variation of the surface state, providing unique access to the signatures of surface contributions to the elastic and plastic behavior. A number of properties such as actuation, tunable stiffness and strength were discovered in np metals. Following by an outstanding achievement – the fabrication of multiscale porosity in np networks that resulted in its enhanced mechanical response. Despite the fact that hybrids based on np-Au are well studied, there is still a room to investigate. First, there is no available experimental data on the functional properties of bulk hierarchical (h) np-Au. Second, the impact of the surface modifications of np-Au on its coupling parameters is of high importance and has not yet been discussed. Third, what are the limits of the surface effects for the functional response of np hybrids?

To tackle these open questions, the thesis explores approaches for the surface functionalization of bulk np-Au and hnp-Au by stimulation-sensitive organic layers in order to develop novel material concepts for multifunctional hard-soft hybrids as sensor and actuator materials. To achieve the aim, the surface modifications were carried out via (1) the anodic oxide and (2) the formation of the electroactive ferrocene-terminated alkanethiol self-assembled monolayers (Fc-SAM). The mechanical properties of the hybrids were studied *in situ* in electrolyte with respect to the surface state in three cases: clean (capacitively charged) np-Au, electrochemically oxidized np-Au, and the redox-active Fc-SAM/np-Au.

The following chapters outline the thesis:

Chapter 2 gives a short introduction to the theoretical background of surface stress and surface tension, following by the electrocapillary phenomena at the metal-electrolyte interface at clean and adsorbate-covered metal states. Furthermore, the surface processes upon the applied electric potential are considered. Next, the impact of the OH-electrosorption and self-assembled molecules on the Au surface is presented. The electron transfer in the electrolyte/ferrocene-terminated self-assembled monolayers/gold is discussed. The impact of non- and electroactive self-assembled monolayers

on the surface stress change is briefly introduced. In addition, the concepts of actuation and tunable elasticity in nanomaterials are presented.

In **Chapter 3** the synthesis route of nanoporous gold is given along with the formation of the surface oxide and organic films. The structure and characterization methods are listed. The *in situ* setups employed for the mechanical properties examination are described.

The results on the microstructural characterization, actuation, and the size-dependent mechanical behavior of np-Au upon the formation of the (1) surface oxide and (2) ferrocenylalkylthiolate self-assembled monolayers are presented in **Chapter 4**.

Chapter 5 discusses the origin of the electro-chemo-mechanical coupling in the surface-modified nanoporous hybrids taking into account the concepts of surface stress and surface excess elasticity. The electrocapillary and electro-elastic coupling parameters are also discussed.

Finally, **Chapter 6** summarizes the general results of the thesis. Following by the outlook on the potential research for further functionalization of nanoporous networks.

C

Chapter 2

Background

2.1 Surface stress and surface tension: Nomenclature and definition

The surface of a solid material is where distinct properties emerge, primarily due to the unique behavior of surface atoms. Unlike atoms in the bulk material, which are surrounded by neighboring atoms in a balanced arrangement, surface atoms have unsaturated bonds and possess different reactivity (Figure 1.2). This imbalance leads to alterations in their physical and chemical behavior. These changes are fundamental to the theory of solid mechanics, as they manifest in phenomena such as surface stress, which influences how materials respond to mechanical forces, and surface tension, which refers to the cohesive forces arising at the surface that impact interactions with fluids and other materials.

A confusion often arises over the use of the terms surface stress, surface tension, and surface free energy because, unlike in liquids, these terms for a solid are not necessarily equal. This distinction was first noted by Gibbs [110] and further discussed by Shuttleworth [111]. In the course of this work, surface tension is associated with the work required to create new surface area, whereas surface stress relates to the work needed to increase surface area through elastic deformation [112].

In a one-component system, surface tension, γ, is defined with respect to the work (excess free energy, $\mathrm{d}F$) required to create a new area of surface, $\mathrm{d}A$, at constant elastic strain (i.e. by increasing the number of atoms at the surface or interface), $\mathbf{E}^{\mathrm{S}}$, constant temperature, T, and chemical potential, μ_i:

$$\gamma = \left.\frac{\mathrm{d}F}{\mathrm{d}A}\right|_{\mathbf{E}^{\mathrm{S}},\mathrm{T},\mu_{\mathrm{i}}} \quad , \tag{2.1}$$

where $\mathbf{E}^{\mathrm{S}}$ is the tangential strain tensor at the surface. The surface tension, γ, necessarily is a positive scalar value due to the existence of a surface.

If an area of a solid surface, $\mathrm{d}A$, is changed by straining the body with respect to the strain, $\mathrm{d}\mathbf{E}^{\mathrm{S}}$, then the work is done by the surface stress, $\mathbf{s}$, which can be estimated in a laboratory frame by [111]:

$$\mathbf{s} = \gamma\mathrm{I} + \frac{\mathrm{d}\gamma}{\mathrm{d}\mathbf{E}^{\mathrm{S}}} \quad , \tag{2.2}$$

where $\mathbf{s}$ is a second rank tensor denoting the in-plane stress state by $\mathrm{d}F = A\mathbf{s}\mathrm{d}\mathbf{E}^{\mathrm{S}}$ (stretching the existing surface) [35], I is the second-order identity tensor.

According to Shuttleworth [111], the surface stress is not equal to the surface tension in solids. Cahn [112] proposed to simplify Eq. 2.2 introducing Lagrangian coordinates in a way:

$$\mathbf{s}^{\mathrm{L}} = \frac{\mathrm{d}\gamma^{\mathrm{L}}}{\mathrm{d}\mathbf{E}^{\mathrm{S}}} \quad , \tag{2.3}$$

where $\mathbf{s}^{\mathrm{L}}$ and $\mathrm{d}\gamma^{\mathrm{L}}$ are determined in an unstrained state ($\mathbf{E}^{\mathrm{S}} = 0$ at the reference state, A_{L}).

The surface stress, $\mathbf{s}$, is generally anisotropic. In clean metal surfaces, there is a common tendency for strengthened bonding, which is reflected by the overall trend of a positive surface stress in metals. This positive stress compresses the underlying lattice tangentially leading to the contraction in the surface plane. The reverse can be observed at negative surface stress values, which expand the underlying lattice, and are thermodynamically permissible [35, 113].

For crystallographically in-plane isotropic surfaces the stress state is also isotropic, hence, the surface stress, f, can be described entirely by a scalar and will be used in the body of this thesis as the trace of $\mathbf{s}$:

$$f = \frac{1}{2}\mathrm{tr}(\mathbf{s}) = \frac{\mathrm{d}\gamma}{\mathrm{d}\varepsilon_{\mathrm{elastic}}} \quad , \tag{2.4}$$

where $\varepsilon_{\mathrm{elastic}}$ is the scalar elastic strain, $\varepsilon_{\mathrm{elastic}} = \frac{1}{2}\mathrm{tr}(\mathbf{E}^{\mathrm{S}})$.

2.2 Electrocapillarity at the metal-electrolyte interface

2.2.1 Model of a metal-electrolyte interface

Consider a simple case of a planar interface between a metal and a dilute aqueous electrolyte solution in which no electrochemical reactions take place (only non-faradaic processes). When a solid interacts with an electrolyte solution, several processes occur that contribute to the surface charging. These processes may include adsorption of electrolyte's ions onto the solid's surface electrostatically (physical adsorption) or chemically (chemisorption), along with solvent adsorption and the polarization of the surface, which in metals results in either an excess or deficiency of electrons. Consequently, the concentration of ions in the vicinity of the charged surface changes – ions of opposite charge are attracted to the surface, while ions with the same charge as the surface are repelled. This leads to the formation of an electric double layer (EDL) at the solid-electrolyte interface [114].

There are several theoretical models that describe the EDL [115]. The primary distinction between the models lies in the progressive complexity of the representations of the structure of the counterion layer.

The initial concept of the EDL at the metal-electrolyte interface can be traced back to the 19$^{\mathrm{th}}$ century and credited to Helmholtz [116]. He described the EDL as

a flat capacitor, where one plate consists of a charged surface layer on the metal, and the other plate is formed by oppositely charged ions in the solution, drawn to the metal's surface through electrostatic forces (this is known as the theory of the condensed EDL). According to Helmholtz, the charges on both plates of this capacitor – one on the metal side and the other in the solution – should be equal and mutually compensate each other. A thickness of the EDL approximately coincides with the radius of the solvated ion, and the potential changes linearly with distance from the interface. However, the Helmholtz's theory faced difficulties in explaining experimental results. A disadvantage of Helmholtz's theory was that it could not explain the variation in the properties of the EDL with a change in the concentration and temperature of the electrolyte.

Later, Gouy [117] and Chapman [118] independently proposed the theory of a diffuse double layer using the Poisson–Boltzmann theory [119]. According to their theory, the inhomogeneous distributions of ionic species near an electrode surface occurs due to the two oppositely acting factors: the thermal motion of ions and the attractive-repulsive forces of the charged metal surface. The forces of electrostatic attraction prevent the ions that have passed from the metal into the solution from going into the liquid phase, while as a result of thermal motion, the ions tend to leave the near-electrode space. As a result, the EDL acquires a diffuse structure. The effective thickness of the double layer depends significantly on the concentration of the electrolyte solution, namely, it decreases with its increase. With an increase in temperature, the thickness of the EDL, on the contrary, increases, and the double layer itself becomes more diffuse. The potential in the double electric layer exponentially decreases with increasing distance from the metal surface [120].

Modern concepts of the EDL are founded on a theoretical model proposed by Stern in 1924 [121]. The author integrated the theories of Helmholtz and Gouy-Chapman, while also considering the non-electrostatic interactions between ions and metal surfaces. This incorporation allowed for a better understanding of phenomena related to the specific adsorption of ions. Subsequently, Stern's theory was refined by Graham [122] and Frumkin [123].

A scheme of the EDL is given in Figure 2.1. The thickness of the EDL at the metal side is less than 1 Å. While the corresponding layer from the electrolyte side is found to be as thick as 5-20 Å [124]. The thickness of the diffuse layer depends on the ion concentration in the electrolyte and is less than 100 Å for concentrations greater than 10^{-2} M [115].

The EDL consists of two layers - inner and outer. The first or inner, called the Stern layer, results from accumulating the counterions directly on the electrode surface. Then the diffusion layer extends outward from the Stern surface. The layer lies between the inner Helmholtz plane (IHP) with a potential ϕ_1 - the locus of electric centers of the specifically adsorbed anions along with the primary bound water molecules - and the outer Helmholtz plane (OHP) with a potential ϕ_2 - the locus of the centers of mobile, solvated ions. These ions interact with the metal surface only electrostatically and are so-called non-specifically adsorbed counterions.

The second (outer) layer is called the Gouy-Chapman (diffuse) layer. In contrast, solvated ions with respect to the Poisson-Boltzmann statistics exist within the Gouy-Chapman layer, extending until their concentration matches that of the bulk elec-

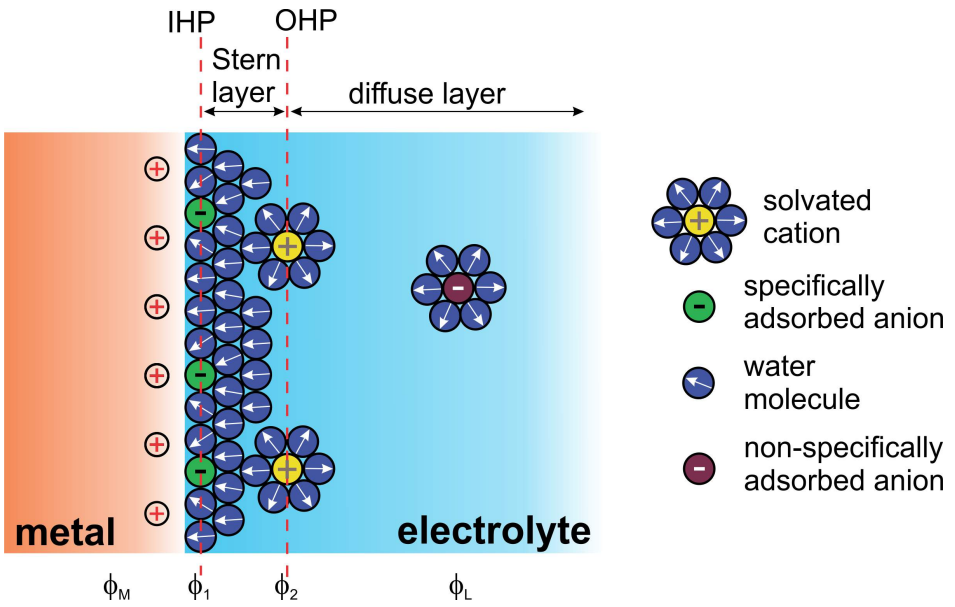

Figure 2.1: Schematic representation of the electric double layer with positive excess charge on a metal electrode. The region adjacent to the electrode surface consists of specifically adsorbed anions and is called the inner Helmholtz plane (IHP). The negative excess charge of the metal electrode is balanced by cations distributed in a diffuse layer, whereby the closest possible position of the electrical center of gravity to the electrode surface is called the outer Helmholtz plane (OHP). ϕ_M, ϕ_1, ϕ_2, and ϕ_L symbolize respectively the potential at the metal electrode, the inner and outer Helmholtz planes and in the interior of the electrolyte solution. Due to the high electrical conductivity of a metal, the ϕ_M is constant up to the surface.

trolyte solution. A thickness of this diffuse layer is primarily governed by the Poisson-Boltzmann theory, which describes the potential distribution in an electrolyte that interfaces with a charged surface. In the theoretical scenario of an infinitely large, flat surface, the potential distribution $\phi(x)$ can be determined in the direction perpendicular to the surface, denoted as x, via [38]:

$$\phi(x) = \phi_0 e^{-kx} \quad , \tag{2.5}$$

where ϕ_0 is the potential at the surface at $x = 0$ and the inverse Debye length, k, is determined as:

$$k = \lambda_D^{-1} = \sqrt{\frac{2c_0 z^2 e^2}{\epsilon_0 \epsilon k_B T}} \tag{2.6}$$

with the following meaning of the variables: λ_D - the Debye length, c_0 - the concentration of a monovalent ion of a singular type, z - the charge on each ion, e - the elementary charge, ϵ_0 and ϵ - the relative and vacuum permittivity, respectively, k_B - the Boltzmann constant, and T - the absolute temperature in K. When the concentration, c_0, is 0.1 M, it yields the Debye length, λ_D, of 0.96 nm. If the Debye length, λ_D, is larger than a pore radius (equal to a ligament size, L), the EDL will overlap in the pores, creating an electric field throughout the entire pore [125]. This means that charged particles that have the same charge as the electric field cannot move through the pore. To reduce the Debye length, higher concentrated electrolytes should be used. In this

case, the Gouy-Chapman diffuce layer effectively merges with the Helmholtz layer at the OHP.

The differential capacitance, C_{dl}, of the Gouy-Chapman layer can be expressed as the excess charge, q, per surface area on the metal surface, ϕ_0, as [38]:

$$C_{\mathrm{dl}} = \frac{\mathrm{d}q}{\mathrm{d}\phi_0} = \frac{\epsilon_0\epsilon}{\lambda_{\mathrm{D}}}\cosh\left(\frac{\mathrm{ze}\phi_0}{2k_{\mathrm{B}}T}\right) \quad . \tag{2.7}$$

At small potentials, the last term of Eq. 2.7 can be approximated by unity and yields:

$$C_{\mathrm{dl}} = \frac{\epsilon_0\epsilon}{\lambda_{\mathrm{D}}} \quad . \tag{2.8}$$

Hence, Eq. 2.8 resembles the capacitance of a planar electrode. The specific capacity, C_{dl}, of metallic electrodes is usually between 10 and 40 μF cm^{-2} [38].

2.2.2 Surface stress and surface tension at metal-electrolyte interface

Electrocapillarity refers to the change in capillary forces due to the application of an electric field [126]. Earlier studies on the surface stress of the metal-electrolyte interface were based on single, planar surfaces [62, 127–129]. The development of a new generation of actuator materials featuring highly curved surfaces and a large surface-to-volume ratio [10] posed a new challenge for the scientific community.

The surface stress, f, variations with respect to the transferred charge density (per area), q, can be characterized via the electrocapillary coupling coefficient, ς, as [35, 130]:

$$\varsigma = \left.\frac{\mathrm{d}f}{\mathrm{d}q}\right|_{\mathbf{E}^{\mathrm{S}},\mathrm{T},\mu_{\mathrm{i}}} \quad . \tag{2.9}$$

The surface stress of a solid is not even approximately equal to its surface tension, γ, and it exhibits a different (generally, stronger [35]) dependence on the potential, E. Furthermore, due to the stiffness of solids, the potential-dependent changes in the position or shape of solid surfaces are much smaller than those of liquid electrodes.

The relevant form of the Gibbs adsorption equation for polarizable solid electrode surfaces was reported in [35, 131]. Where the variation of surface tension, γ, induced by the changes in the applied electric potential, E, or the superficial charge density (per area), q, is expressed as:

$$\mathrm{d}\gamma = -s\mathrm{d}\,T - \Gamma_{\mathrm{i}}\mathrm{d}\mu_{\mathrm{i}} - q\mathrm{d}E + \mathbf{s}\mathrm{d}\mathbf{E}^{\mathrm{S}} \quad , \tag{2.10}$$

where s is the superficial excess entropy, T is the temperature, Γ_i is the superficial excess of i^{th} component at the surface, μ_i is the chemical potential, $\mathbf{s}$ is the surface stress tensor, and $\mathbf{E}^{\mathrm{S}}$ is the tangential strain tensor at the surface.

If the changes in the surface tension, $\mathrm{d}\gamma$, occurred with a change of the applied potential, $\mathrm{d}E$, but the other components of T, μ_i, and $\mathbf{E}^{\mathrm{S}}$ remained invariant, Eq. 2.10 yields the Lippmann's classical equation [126]:

$$-q = \left.\frac{\mathrm{d}\gamma}{\mathrm{d}E}\right|_{\mathbf{E}^{\mathrm{S}},\mathrm{T},\mu_{\mathrm{i}}} \quad . \tag{2.11}$$

Eq. 2.11 is a fundamental thermodynamic result for the electricified surfaces. It can be derived irrespective of the elastic properties of the underlying bulk material and applied to both solids and fluids [131, 132].

If the surface is charged by applying a potential, E, assuming that the double layer capacitance, $\mathrm{C_{dl}} = \mathrm{d}q/\mathrm{d}E$, is potential-independent, then surface tension, γ, can be integrated from Eq. 2.11 as [133]:

$$\Delta\gamma = \gamma - \gamma_0 = -\frac{1}{2}C_{\mathrm{dl}}(E - E_0)^2 = -\frac{1}{2}\frac{q^2}{C_{\mathrm{dl}}} \quad . \tag{2.12}$$

In this case, the electrocapillary curve exhibits a nearly parabolic shape with its maximum when $E = E_0$. At that point, the surface is uncharged. The "electrocapillary maximum" of γ occurs at the potential termed as the potential of zero charge (pzc) [35].

2.3 Electrochemical surface processes

Adsorbed atoms and molecules generally have a significant influence on the electronic structure of a surface. They rearrange the electronic charge within the chemical bond and may also add elementary dipoles if the adsorbed molecule has its own static dipole moment [134]. The amount of adsorbed species is given in terms of the coverage, Θ, which is the ratio of the number of adsorbed species to the number of surface atoms of the substrate [124]. Another way to quantitatify the coverage, Θ, is the ratio between the surface excess and the total surface excess of adsorbed species denoted as Γ and Γ_{max}, respectively, via $\Theta = \Gamma/\Gamma_{\mathrm{max}}$.

Relationships between the amount of adsorbate, Θ, on a solid surface and the concentration of that adsorbate, c_{A}, in the bulk fluid phase at thermodynamic equilibrium are described by adsorption isotherms. These relationships are fundamental in understanding how materials interact with adsorbates for catalysis, water treatment, and gas storage.

There are several models for the adsorption isotherms, but the most common one is the Langmuir isotherm. The Langmuir isotherm assumes that adsorption occurs at specific homogeneous sites within the adsorbent and that once a site is filled, no further adsorption can occur at that site. It also assumes that all sites have equal affinity for the adsorbate.

The Langmuir isotherm can be mathematically expressed as [35]:

$$\Theta = \left(1 + \exp\frac{\mu - \mu_0 - \Delta h^{\mathrm{ad}}}{RT}\right)^{-1} \quad , \tag{2.13}$$

where μ and μ_0 - the chemical potentials of the adsorbate at equilibrium and the standard state, respectively; Δh^{ad} - the molar enthalpy of adsorption.

Using simple model of electrosorption, the coupling parameter, ς, relevant for adsorption takes the form [135]:

$$\varsigma = -\frac{1}{zF}\frac{\mathrm{d}(\Delta h^{\mathrm{ad}})}{\mathrm{d}e}\bigg|_{\Gamma} \quad , \tag{2.14}$$

where Δh^{ad} - the enthalpy of adsorption, z - the ionic valency, e - the tangential (area) strain, F - the Faraday constant, and Γ - the specific excess of the adsorbate. When $\varsigma < 0$, a tensile strain promotes binding between the surface atoms and adsorbed-species more strongly. The details can be found in [35].

2.3.1 Surface relaxation and reconstruction

In this thesis, the reference material is gold which has its most stable face-centered cubic (fcc) structure. The three well-known low-index planes (111), (110), and (100) are derived from truncating a fcc lattice [38]. The surface atoms of these planes arrange themselves in distinct geometric patterns: the (111) plane exhibits a hexagonal arrangement, the (110) plane has a rectangular arrangement, and the (100) plane forms a square arrangement. Among these, the fcc (111) plane is the most densely packed, resulting in the lowest surface energy and the highest stability compared to the other planes [136]. An instability of the low index gold surfaces is well known led to reconstruction, faceting or relaxation, in order to minimize their surface energy [137].

Surface atoms often occupy positions that differ significantly from those predicted for a perfect termination of the bulk material. This discrepancy arises from unbalanced forces at the surface, which cause these atoms to be asymmetrically positioned relative to their counterparts in the bulk. If the in-plane spacing of the surface atoms remains unchanged, but the distance between the topmost atomic layers is altered, the phenomenon is called as a surface relaxation.

In metals, a distance between the first layer of atoms is reduced, due to a dipole layer at the surface, which is caused by the distortion of electron wavefunctions [38]. In contrast, when surface atoms are displaced laterally, it results in markedly different surface structures. This reorganization of surface atom positions leads to a reduction in surface energy and is referred to as surface reconstruction. The inhomogeneities of the surface stress is considered as a driving force for the surface reconstruction [138, 139]. A simple scheme of the surface reconstruction is given in Figure 2.2.

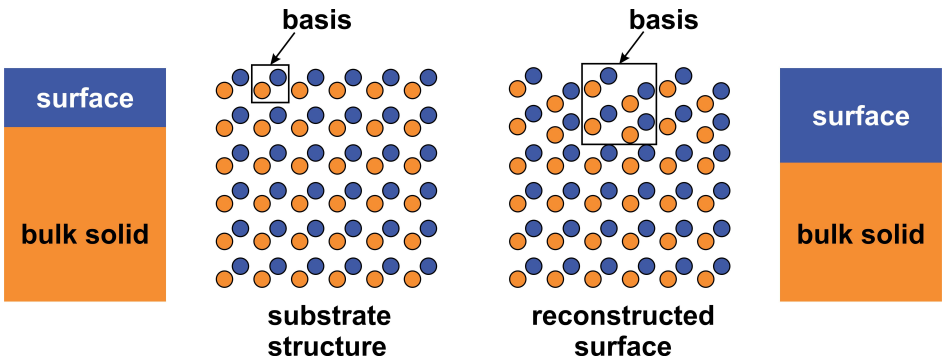

Figure 2.2: A schematic example of a change in the in-plane spacing of the surface atoms (surface reconstruction). The bulk and surface basis are indicated. Redrawn from [38].

By tuning the applied electrode potential (changing the electron density at the surface) or varying experimental conditions (for example, temperature), surface reconstruction can occur [140–142]. An anion adsorption significantly affects the structure of the Au (111) surface, affecting both activity and stability of atoms, and leading to changes in their arrangement [143]. When this rearrangement happens, about 4.5 % of the surface shifts upward, forming small islands. In a weakly adsorbing aqueous electrolyte of perchloric acid, the surface lifting occurs at the potential about 0.55 V (vs. standard calomel electrode) [124]. This alteration can influence how the electrode behaves in electrochemical processes. Near the point where the anion concentration starts to rise on the electrode, the surface reconstruction takes place [128, 142, 144].

2.3.2 Electrosorption of oxygen-species on gold

Electrosorption can be considered as a specialized form of adsorption which specifically involves an accumulation of charged species at an electrode surface under the influence of an electric field. This process is enhanced by the electrostatic interactions between charged particles in the solution and the charged surface of the electrode [145]. The DFT study confirms that the surface stress of metals varies during adsorption [146], along with the adsorption energies on metal surfaces during straining [147]. In this case, the electro-chemo-mechanical coupling is of importance [148].

In this section, the electrochemical adsorption of oxygen-species on gold will be discussed. A number of experimental [149–153] and theoretical [154–157] works was devoted to the topic of this section.

Np-Au is considered as a highly defect material due to increased number of dislocations, vacancies, steps, kinks, etc. It is accepted that O_2, CO, OH, and other species react preferentially at defect sites in the surface of the material [134]. Hence, a fundamental understanding of the adsorbate role on the functionality of np-Au is of great importance.

A typical CV response of a planar polycrystalline Au electrode upon the potential cycling in 0.1 M $HClO_4$ is shown in Figure 2.3a [158]. The anodic oxidation of gold involves a number of processes. The oxidation starts with the adsorption of water molecules followed by the reversible electrosorption of oxygen-species at $\approx$ 1.3 V (vs. SHE) [150]. The numbers on the plot in Figure 2.3a correspond to different switching potential at which the oxide formation on Au was studied [158]. The distinguished peaks are OC1, OC2, and OC3. The reduction peaks were integrated in order to evaluate the OH coverage, Θ_{OH}, on Au surfaces as summarized versus the applied potential, E_{SHE}, in Figure 2.3b. At low potentials, the peak OC1 occurs which can be attributed to the reversible reduction of OH. Higher applied potentials resulted in appearance of OC2 and OC3 peaks. The lower potentials of the peak OC2 can be attributed to a higher stability of the oxide. The more stable oxide OC2 shows a limiting behavior at the sub-monolayer level (AuO) whereas OC3 increases linearly with the potential (Au_2O_3) [159]. The peaks OC2 and OC3 were found at low electrolyte concentrations of weakly adsorbing ions, such as ClO_4^-. Here, it must be highlighted that the Au dissolution takes place in $HClO_4$ aqueous electrolyte with a rate 0.13 ng cm^{-2} [160].

According to Bruckenstein and Shay [149], the first monolayer of electrosorbed oxygen-species at a Au surface proceeds through a one electron transfer process that

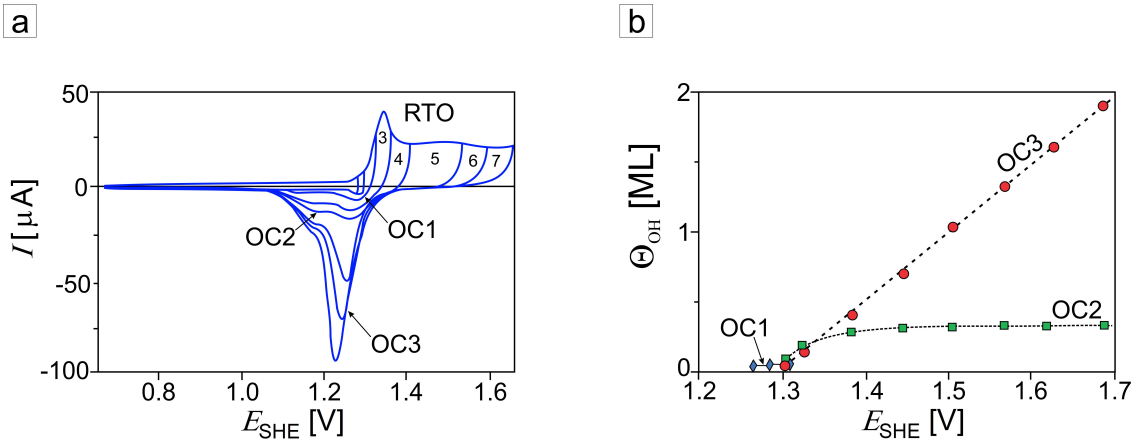

Figure 2.3: The potential-dependent formation of the oxide on a planar Au electrode: (a) a typical cyclic voltammetry behavior in 0.1 M $HClO_4$ at a scan rate 50 mV s^{-1}; (b) oxide coverage, Θ_{OH}, as a function of the applied electric potential, E_{SHE}. The oxide reduction peaks integrated to determine Θ_{OH} are indicated as OC1, OC2, and OC3. The replacement-turnover process is indicated as RTO. The numbers (3-7) correspond to the potential switches. Adapted from [161].

oxidizes water adsorbed on the Au to form an adsorbed OH-radical via:

$$Au - H_2O_{ads} \rightarrow Au - OH + H^+ + e^- \quad . \tag{2.15}$$

The metal-OH bond had been studied theoretically [154] and was found to be a strong bond primarily due to electrostatic forces. In this bond, electrons move from the metal to the OH group, allowing it to achieve a stable electronic state. When water molecules (or other solvents with negative groups) interact with the metal, they orient themselves so that their negative ends point toward the metal and their positive ends point away into the solution. This arrangement creates an additional electric double layer on the surface, leading to a negative surface potential. This potential contributes to the overall voltage difference between the metal and the solution [114]. The details on the Au hydroxides dipoles can be found in [155].

The next step in the mechanism of the oxide formation on Au takes place when a second electron transfers to form an oxide ion, forming a 2D gold oxide monolayer, the H–O bond is weakened [149]:

$$Au - OH + H_2O \rightarrow Au = O + H^+ + e^- \quad . \tag{2.16}$$

Along with the reaction (2.16), the replacement-turnover (RTO) is initiated due to interfacial place exchange between atoms of Au and O. This step is considerably slower than the first step (2.15). It proceeds as a final step in the oxide formation mechanism [149] via:

$$Au = O + H_2O \rightarrow O = Au - H_2O_{ads} \quad . \tag{2.17}$$

The RTO of Au and O leads to the further oxidation of the surface and the formation of 3D bulk oxide in the form of Au_2O_3 or hydrated Au_2O_3. The RTO begins at 1.45 V (vs. SHE) with respect to [159].

The adsorption of oxygen can significantly affect the morphology of the Au surface, either by favorably interacting with defects on the surface or by incorporating Au into the adsorbate layer, a process that is energetically favorable at higher coverages. The adsorbate-Au interactions get more covalent upon gold incorporation, which lowers the partial negative charge on the adsorbate, allowing for closer packing on the surface [162]. The Au-O bond was found to be 1.96-1.99 Å [163] or 2.10 Å [155]. Whereas the Au-Au bond ranges from about 2.88 to 3.00 Å [164] that is about 30 % longer than the Au-O bond [163]. This means that growing a layer on the crystal could put the adlayer under tension, leading to increased surface stress, and may even result in the breakage of the Au-Au bonds [163]. For anion adsorption, this suggests that $\mathrm{d}f/\mathrm{d}q = \varsigma > 0$, and in an excellent agreement with the experimental results [130].

A schematic representation of the three stage mechanism of the oxide formation on Au is given in Figure 2.4.

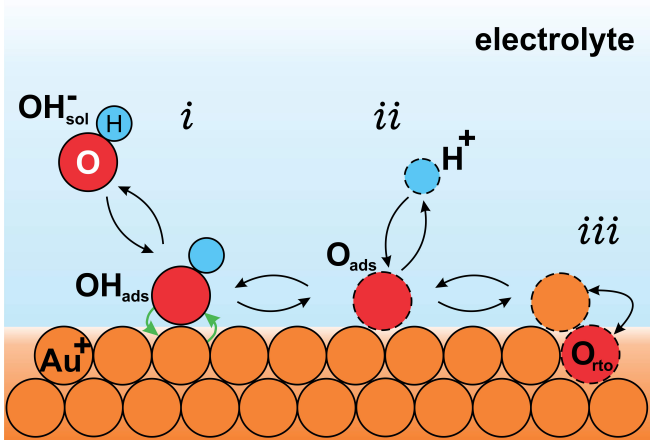

Figure 2.4: A schematic representation of the oxygen species electrosorption process: stage *i* corresponds to $OH^-_{sol} \rightleftharpoons OH_{ads} + e^-$; stage *ii* governs $OH_{ads} \rightleftharpoons O_{ads} + H^+ + e^-$; stage *iii* is $O_{ads} \rightleftharpoons O_{rto}$. Redrawn from [165].

2.3.3 Self-assembled monolayers on gold

One of the earliest contributions to the field of self-assembled monolayers (SAMs) emerged in 1946, when Bigelow and colleagues [166] unveiled their pioneering work on the creation of an oleophobic monomolecular layer. This was accomplished through the exquisite process of self-assembly of a surfactant onto a pristine metal surface. Later, in 1983, Nuzzo and Allara [167] demonstrated that bifunctional organic disulfide SAMs could be synthesized on gold substrates through adsorption from dilute solutions. This marked the initiation of an extensive and comprehensive research endeavor, where an in-depth investigations were undertaken to explore the alkanethiol SAM thoroughly. A number of research works on the investigation of these SAMs was published [61, 168–170].

As it was already mentioned in the Chapter 1, SAMs have found extensive applications in the modification of metal surface properties, influencing fields such as tribology [171], molecular and organic electronics [172], green energy [173], electronics [174, 175], and nanofabrication [169]. This versatility arises from the ability of

SAMs to effectively manipulate the physical, chemical, and electronic characteristics of metal and inorganic semiconductor surfaces [169]. A notable advantage of SAMs is their chemical tunability, which allows for atomic-scale adjustments to the electronic structure at molecule-electrode interfaces, ultimately impacting the performance of SAM-based devices [176, 177].

A SAM is an organized molecular assembly formed spontaneously on a surface. Based on a molecular composition, the SAM can be classified as alkanethiols, siloxanes, fatty acids and derivatives, or phosphines [61]. Due to high affinity of sulfur to gold, alkanethiol SAMs are widely studied. A typical structure of an alkanethiol SAM ($CH_3(CH_2)_nSH$) on a Au surface is given in Figure 2.5. The monolayer consists of three parts: a head (anchoring) group that binds to the surface and stabilizes surface atoms; a backbone moiety (hydrocarbon chain) acts as a physical barrier (1-3 nm thickness) and governs the van der Waals interactions; and a terminal (functional) group that determines the surface properties (interacts with the environment) [124]. The number of methylene repeat units in the alkyl chain characterizes the molecule as odd or even, and determines the tilt angle of the functional group [178]. For example, a ferrocene terminal group (Section 2.3.3.2) tilt angle with respect to the surface normal is 5 ± 1° higher in odd-SAM than in even-SAM for a number of the methylene units n = 9-15 [179].

A formation of the monolayer on a Au surface undergoes three main stages: physisorption, chemisorption, and ordering [180]. Due to high affinity of sulfur atoms to Au, an initial physisorption through van der Waals interactions occurs, and the alkanethiol molecule loses the mercaptan H atom, transforming itself in an alkanethiolate via [61]:

$$R - S - H + Au_n^0 \rightarrow R - S^- Au^+ \cdot Au_n^0 + \frac{1}{2}H_2 \quad . \tag{2.18}$$

This is followed by chemisorption of the molecules on the Au through the covalent linking with the S (a process that takes minutes), and finally a slow formation of ordered domains (a process takes several hours or even days). The packing and ordering of the monolayer are governed by the balance and interplay of various forces. The adsorbates adopt an arrangement minimizing the free energy of the layer and promoting the interactions between the neighboring molecules within the layer [124].

An increase in the SAM surface coverage results in the nucleation of standing-up domains that finally cover the entire Au (111) surface. The molecules on the substrate surface can be characterized by three distinguished angles: α - the molecular tilt, β - the angle of the hydrocarbon chain's plane rotation around the molecule's axis, and χ - the angle that indicates the direction of the tilt, based on the projection of the plane formed by the substrate normal and the hydrocarbon chain axis onto the substrate plane (Figure 2.5 [170] and references therein).

2.3.3.1 Arrangements of SAM on Au surface

If molecules adsorb to a crystalline surface, they often form a crystalline overlayer which is called a superlattice. This occurs if the adsorbates bind preferentially to specific sites [38]. Such arrangements of atoms were reported by Strong and Whitesides [168] while investigated the alkanethiol SAMs on Au surfaces using electron

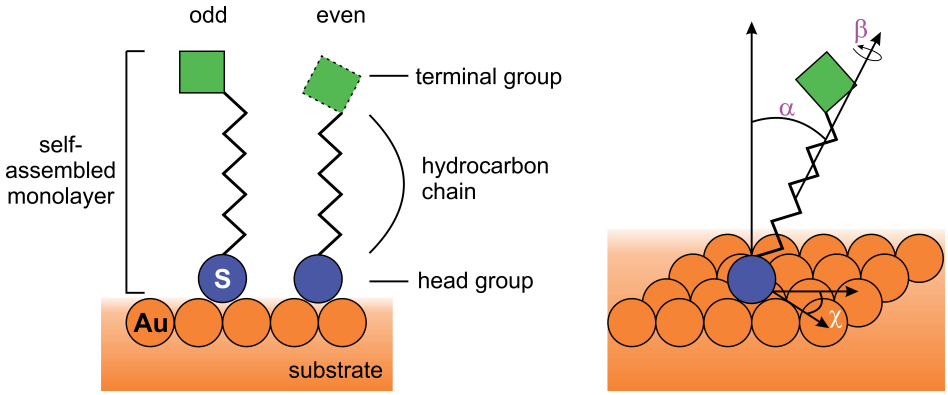

Figure 2.5: The schematic structure of an alkanethiol self-assembled monolayer on Au (111) surface. A standing up configuration (stable phase) of the molecule is illustrated where the angles are α = 30°, β = 55°, and χ = 14°. Adapted from [170].

diffraction. The authors reported a $(\sqrt{3}\times\sqrt{3})$R 30° (where R stands for rotated) structure of chemisorbed alkanethiols on Au(111) with an intermolecular spacing of 4.97 Å and calculated an area per molecule of 21.4 Å (Figure 2.6). The sulfur groups are positioned in the 3-fold hollow sites formed by the gold atoms [181]. These sites are considered as the most stable binding sites on Au (111) with the lowest surface energy compared to the bridges (contacts between Au atoms) and on-top positions [181]. For well-ordered, densely packed saturated n-alkanethiolates on gold, the maximum surface density is 7.5 × 10^{-10} moles × cm^{-2} (4.5 molecules nm^{-2}) corresponding to an average spacing of 5 Å between adjacent S atoms and an area per molecule of 21.6 Å [61]. While the involvement of solvent molecules complicates the kinetics of the monolayer formation, the alkylthiol assembly process can be qualitatively approximated by a Langmuir adsorption model (Section 2.3) which assumes that the rate of deposition is proportional to the available free space [60].

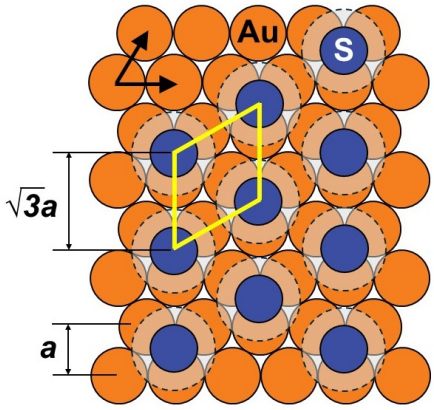

Figure 2.6: A scheme of the superlattice with the $(\sqrt{3}\times\sqrt{3})$R 30° structure of chemisorbed alkanethiols on Au (111) surface (a top view). The basis of sulfur (S) atoms is marked. The sulfur atoms are positioned in the three-fold hollow sites of the Au lattice (a = 2.88 Å [164]). The light gray circles with the dash lines are the approximate projected surface area occupied by each alkane chain. Redrawn from [169].

Later, the scanning tunneling microscopy (STM) was employed by a number or research groups to explore the structural features of the alkanethiol SAM [91, 169, 170, 182]. The literature strongly confirms that along with the ($\sqrt{3}\times\sqrt{3}$)R 30° structure a secondary ordering of the chains (non-equivalent) was found corresponding to a c(4 × 2) superlattice (Figure 2.7). The specific ordering of S atoms determines the free space available to the organic moiety [124]. The details can be found in [170] and the references therein.

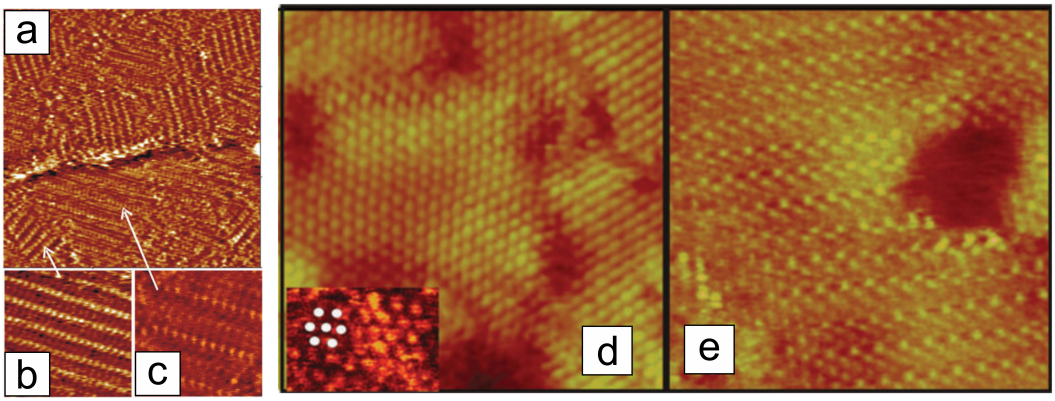

Figure 2.7: STM images of two different striped phases for hexanethiol on Au(111). (a) 28.75 × 28.75 nm^2 image showing domains of the two different lying down phases (b) head-to-head configuration (8.75 × 8.75 nm^2 image); (c) head-to-tail configuration (6.75 × 6.75 nm^2 image). (d) 13.5 × 13.5 nm^2 top view STM images of a ($\sqrt{3}\times\sqrt{3}$)R 30° decanethiol lattice (the inset shows the same lattice on nonanedithiol); (e) a rectangular c(4 × 2) hexanethiol lattice. The bright spots indicate the position of the thiol molecules. The white dots in the inset indicate the hexagonal lattice. Reprinted from [170].

The formation of a SAM has been found to contain a wide variety of defects such as islands, pinholes, collapsed sites, and domains (Figure 2.8). The number of non-idealities of the monolayer depends on substrate surface features like terraces, steps, and crystalline boundaries [183]. Besides, thiolate SAMs cause restructuring of Au electrode surfaces [184].

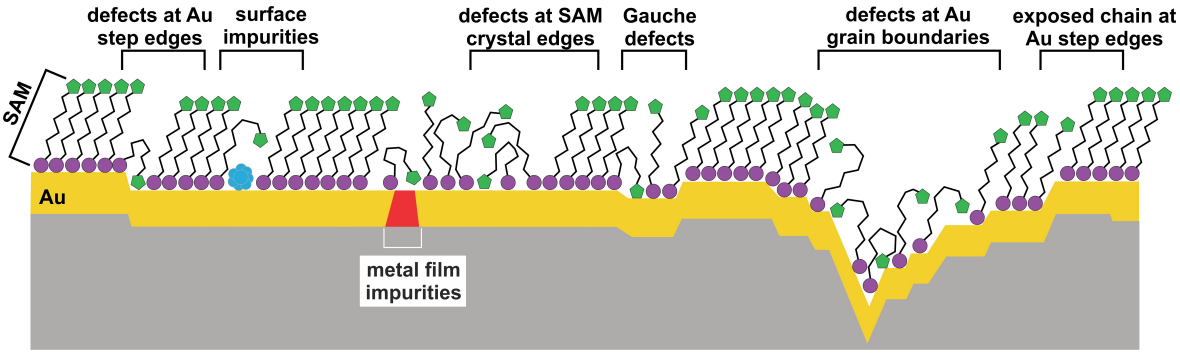

Figure 2.8: A scheme of the intrinsic and extrinsic defects found in SAMs formed on polycrystalline substrates. The Au surface layer is highlighted in yellow that indicates the changing topography of the substrate. Redrawn from [169].

2.3.3.2 Ferrocene-terminated electroactive alkanethiol SAM on gold

In this thesis, the np-Au has been functionalized with ferrocene-terminated electroactive alkanethiol SAM. Ferrocene is an organometallic compound with the formula $Fe(C_5H_5)_2$. It consists of a central iron (Fe) atom sandwiched between two cyclopentadienyl anions $(C_5H_5)^-$ [185]. The complex dimensions are 4.1 Å × 3.3 Å, whereas the ferrocenium ion is slightly bigger 4.1 Å × 3.5 Å. The C-C bond distances are 1.40 Å within the cyclopentadienyl rings, the Fe-C bonds are 2.04 Å [183]. This unique structure is known as a metallocene [186]. In an aqueous electrolyte, ferrocene (Fc) undergoes one-electron oxidation to form ferrocenium (Fc^+) and ion-pairing with anions (X^-) as shown in Figure 2.9.

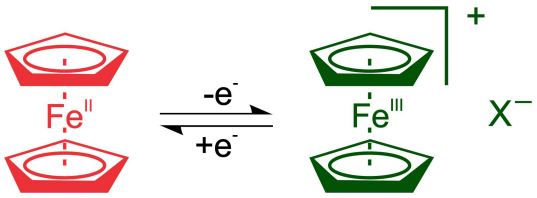

Figure 2.9: The structure of the reversible one-electron redox-reaction of ferrocene with an electrolyte's anion (X^-). Redrawn from [187].

As a functional group of the alkanethiol SAM, the redox-reactions can be representing via the following equation [188]:

$$(Fc)_{SAM} + X^-_{aq} \Leftrightarrow (Fc^+ - X^-)_{SAM} + e^- \quad . \tag{2.19}$$

A stability of the ferrocenyl group in aqueous, aerobic environments, along with the availability of a wide range of derivatives and its advantageous electrochemical characteristics, has led to the popularity of ferrocene and its derivatives mostly in biological applications [187, 189, 190], but also in sensing technologies and nanoactuation [191].

The Fc-SAM on Au were studied by a number of researchers on planar Au [60, 179, 183, 192, 193]. A typical CV of a surface-bound redox species is given in Figure 2.10. In an ideal Fc-SAM, a single peak is observed that correspond to all Fc-moiety in the monolayer are exposed to the electrolyte [183]. However, the experimental results proved the disorder of the Fc-SAM. Among non-idealities are peak broadening, peak splitting, and peak shifting [194, 195].

For an ideally responding surface-confined reactant, an electrochemical caracterization via CV measures the faradaic current, i_p, that is directly proportional to the scan rate, v:

$$i_p = \frac{n^2 F^2}{4RT} v A \Gamma \quad , \tag{2.20}$$

where n - the number of electrons involved in the reaction, F - the Faraday constant, R - the gas constant, T - the absolute temperature, A - the electrode area, and Γ - the surface concentration of the redox moiety. The integration of the area under the anodic or cathodic peak (subtracting the background or charging current, i_{ch}) gives the charge, Q_{Fc}, used to determine the Fc-SAM surface coverage, Θ_{Fc}. In np hybrids, the behavior of the monolayer is non-ideal that might result in a certain mistake in the

determination of the Fc-SAM surface coverage, Θ_{Fc}. The details will be further given in Section 3.4.2.

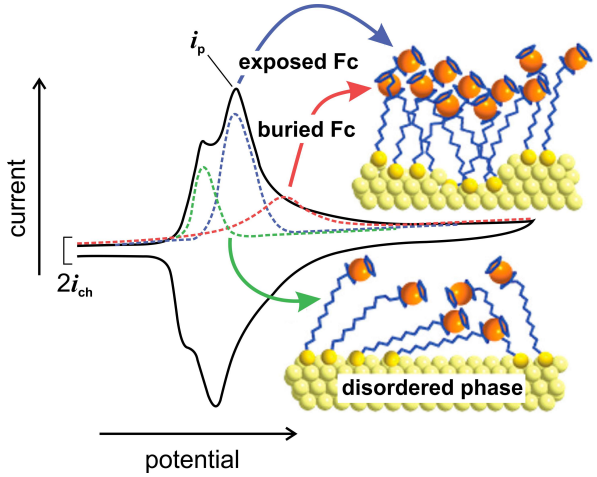

Figure 2.10: A schematic CV of different Fc-SAM states on Au electrode subjected to a potential cycling in 1 M $HClO_4$. The faradaic current, i_p, and the charging current, i_{ch}, are marked. Adapted from [179].

2.2.3.3 Electron transfer in Au/Fc-SAM/electrolyte interfaces

Surface-confined redox molecules such as Fc-terminated alkanethiol SAMs on Au constitute an attractive molecular probe for correlative studies into interfacial electrochemistry and the physicochemical properties of the interface [196–198].

A theory of the interfacial potential distribution of electrodes coated with electroactive SAMs was proposed by Smith and White [199]. The authors derived an analytical expression for the potential variations, which serves as the basis for calculating the driving force for the reversible electron transfer between the electrode and the coated molecules. In that case, it predicts the shape of current-voltage responses observed in CV experiments, highlighting how various factors – such as a film thickness, dielectric properties, an electroactive SAM concentration, electrolyte characteristics, solvent properties, and the potential of zero charge – affect the voltammetric behavior. Additionally, the theory provides an analytical tool for the determination of the capacitance of the coated electrodes. Duffin *et al.* [194] proved that the theory fits well with the experiments (CV) for a number of the methylene groups in the alkyl chains n = 5-11, but the potential drop is noticeably non-linear due to SAM packing effect for n = 12-13, and variations in the nature of the Fc-Au electronic structure which changes as a function of n for $n < 5$. The adapted scheme of the potential variations across the Au/Fc-SAM/electrolyte interfaces is given in Figure 2.11.

The potential drop is given across the metal surface, ϕ_M, and the solution, ϕ_{sol}. The redox center of the molecule is assumed to be located at a finite distance from the electrode surface (depending on the backbone length, n), corresponding to the plane of electron transfer (PET, ϕ_{PET}). If ions are unable to penetrate into the molecular film, the interfacial potential profiles that the authors anticipate to find in these systems are characterized by a linear potential distribution between the electrode surface and

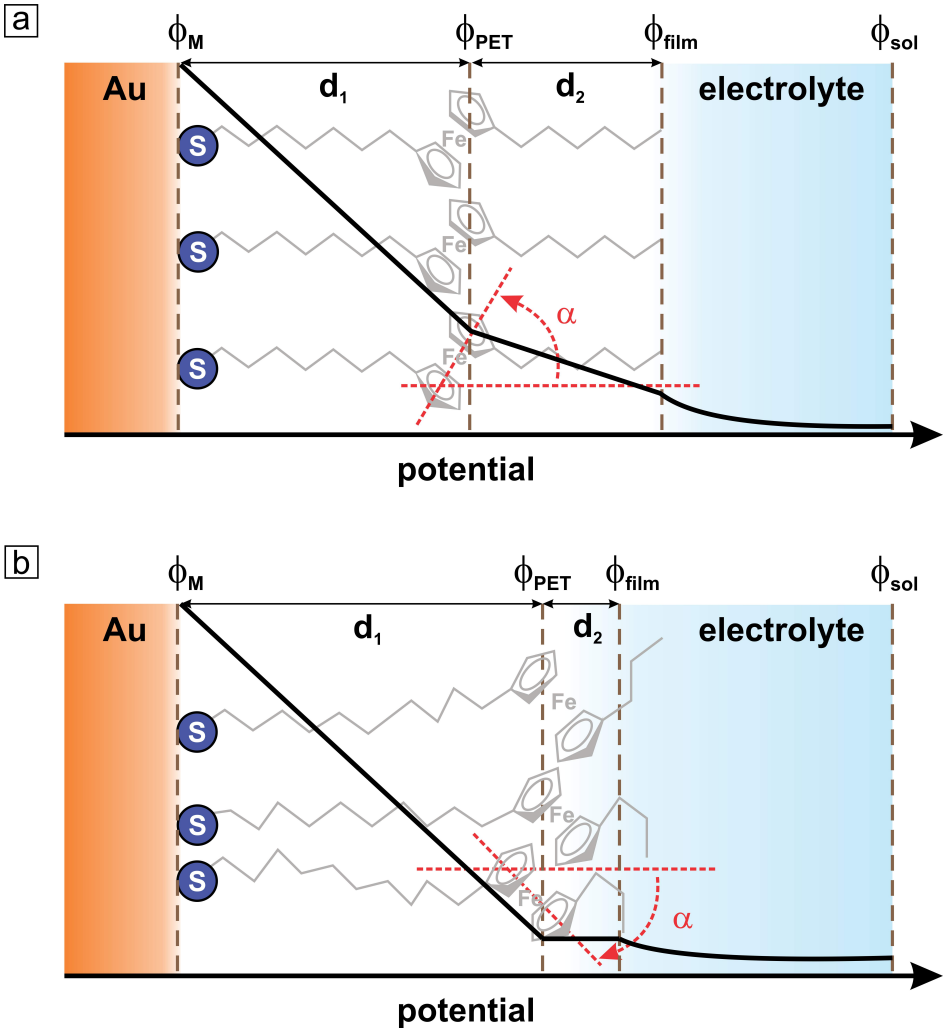

Figure 2.11: A schematic illustration of the potential drop within the Fc-terminated alkanethiol SAM on Au surface. The relative lengths of the alkyl chains below (d_1) and above (d_2) the plane defined by the Fc moieties - the plane of electron transfer (PET) - which determines the position of the Fc units within the SAM. The potential drops linearly across d_1 and d_2, but may do so with different potential decays, following by the non-linear potential drop in solution [199]. The following potentials are marked: ϕ_{PET} - at the Fc moiety, ϕ_{sol} - in the bulk of electrolyte, ϕ_{film} - at the SAM-solution interface, and ϕ_M - of the metal electrode. Here, (a) an ideal model of SC_7FcC_8 SAM on Au; (b) a more realistic view of the SAMs where the flexibility of the alkyl chains may reduce the effective lengths of the alkyl chains of a $SC_{10}FcC_3$ SAM. The odd-even tilt angle, α, change between (a) the odd SAM and (b) the even SAM is marked. Redrawn from [194].

the PET (d_1) and an exponential potential decay in the electrolyte. If a portion of the molecule extends beyond the redox centers, then a second linear potential drop is introduced between the redox center and the solution [199]. This second linear potential drop is illustrated for the odd SAM in (Figure 2.11a) and the even SAM in (Figure 2.11b). Due to the change in the odd-even tilt angle, α, the distance between ϕ_{PET} and ϕ_{film} is varied [194]. This layer is the Stern layer introduced by Fawcett [200], stating that the interfacial model reduces the repulsive effect of neighbouring redox centers and makes the local potential less positive than the average potential in the plane. Increasing the capacitance between ϕ_{PET} and ϕ_{film} (in other words, d_2), the anodic peak shifts to more positive potential along with the broadening of the redox-wave. The phenomenon is governed by the formation of the buried Fc groups within the monolayer significantly influencing the electrochemical response of the SAM. The total double layer capacitance, C_{dl}, (in F m^{-2}) of the monolayer can be estimated via [194]:

$$C_{dl} = \frac{\epsilon_0 \epsilon_r}{d} = \frac{\epsilon_0 \epsilon_r}{d_1 + d_2} \quad , \tag{2.21}$$

where ϵ_0 - the vacuum permittivity (8.85×10^{-14} F cm^{-1}), ϵ_r - the dielectric constant of the SAM, and d - the total thickness of the SAM ($d = d_1 + d_2$).

By employing the CV, the charging current, i_{ch}, can be determined and given as [199]:

$$i_{ch} = C_{dl} A v \quad , \tag{2.22}$$

where v - the scan rate, and A - the surface area of the electrode. Note, the approach of the estimation of the total interfacial capacitance, C_{dl}, is valid for electroactive monolayers, for the electroinactive films the reader is refereed to [199].

The overall relative permittivity of the SAM, ϵ_r, can be derived by merging Eq. 2.21 and Eq. 2.22:

$$\epsilon_r = \frac{i_{ch} d}{A v \epsilon_0} \quad . \tag{2.23}$$

The reversible CV response depends on the distribution of the potential at the interface. The driving force for the electron transfer is influenced by how much of the total potential drop occurs between the electrode and the redox couple. As a result, the concentrations of oxidized and reduced SAMs depend on the electrode potential, which is determined by the electrostatic potential at the redox couple's environment. This potential is affected by the film's molecular structure and other factors in the electrochemical cell, like the solvent's dielectric constant. Furthermore, if the redox species carry different charges, which is common, the potential will also depend on the film's oxidation state. Therefore, the driving force for the electron transfer changes throughout the CV experiment in a complex way [199].

2.3.3.4 Surface stress variations upon SAM adsorption and redox of Fc-SAM

Earlier studies reported microcantilever bending associated with the formation of non-electroactive alkanethiol self-assembled monolayers (SAMs) on its thin gold receptor

layer [113, 201, 202]. The deflection of the microcantilever was attributed to the SAM-induced surface stress change.

The authors in [201] explained the observed surface stress in terms of electrostatic interactions. The apparent dipole moment of the SAM is considered to contain a contribution from (1) the Au^{+}-S^{-} anchoring group and (2) the S^{-}-$alkyl^{+}$ chain. These first findings showed that the surface stress scales linearly with the molecular chain length of the alkanethiols due to the electrostatic dipole repulsion forces. Thus, a densely packed molecules would tend to repel each other resulting in a convex surface curvature, in other words, the compressive surface stress.

According to Haiss [113], another source of the observed surface stress can be the positive charge on the Au surface due to the adsorption of the negatively charged S group. Hence, the surface stress scales linearly with the charge on the surface varying the number of adsorbed S atoms. The increasing surface stress along with the alkyl chain length can be understood if the electron donation from the chain to the S atom increases with the number of the repeated units. The proposed model can explain the linearity of the adsorbate-induced surface stress with the coverage. This suggestion holds also for low coverages where the dipole interaction forces are expected to be negligible.

Later, Godin *et al.* elaborated the idea of Haiss by examining grain size effects on the surface stress [202]. The authors found that the kinetics of the SAM formation and the resulting SAM structure are strongly influenced by the surface morphology of the underlying Au substrate. They confirmed theoretically and experimentally that the adsorption of the alkanethiol SAM on a Au surface causes a shift in the electronic charge density due to slightly polar Au^{+}-S^{-} covalent bond. The redistribution of the charge away from the bulk of the substrate takes place, while Au-Au bonds are elongated due to Coulombic repulsion. It overall results in the large compressive surface stress and the macroscopic strain. In contrast, interactions described by the Lennard-Jones potential (contribute to a molecular tilt of a SAM) and Coulombic repulsion between adsorbed molecules generate relatively smaller (2-4 orders of magnitude) surface stresses [203]. Indeed, a recent investigation by Zhao *et al.* [204] via multiscale modeling based on molecular dynamics simulations confirmed that the primary factor behind the surface stress change is the Au surface reconstruction induced by the thiol adsorption, thus, the SAM interchain repulsions have a minimal contribution. The simulations and experiments showed that the surface stress change increased along with the surface coverage density and larger Au grain size.

In general, a surface stress change can be generated by a physical or chemical event taking place at the functionalized receptor side of a (micro/nano)cantilever causing its deflection.

The impact of the redox-active ferrocene (Fc)-terminated alkanethiol SAM on the surface stress variations of the Au-coated nanocantilevers was studied in [205]. The authors reported the voltage-induced micromechanical motion of a $FcC_{12}SH$-modified Au cantilever substrate in 1 M $HClO_4$ aqueous electrolyte. They explained the cantilever actuation phenomenon via electrostatic forces and structural changes occurring in the stimuli-sensitive SAM due to the electrochemical generation of ferrocenium cations.

Further, Norman and Badia [60] elaborated the idea presented in [205]. They carried out the detailed research on the redox-induced reversible actuation of the Fc-

SAM-modified microcantilevers to quantify the stress changes and probe the dynamics of the system. The authors proved the coverage-dependent surface stress change. It was found that the deflection of the microcantilever scaled quadratically with the fractional coverage of the ferroceniums. The authors observed the delayed bending response of the cantilevers induced by the electric potential comparing with the recorded current (individual molecule's input). Norman and Badia argued that the most likely source of the compressive surface stress changes in the Fc-SAM/cantilever is the collective, not individual, reorientational motions of the molecules caused by the complexation of perchlorate ions to the surface-immobilized ferroceniums (Figure 2.12).

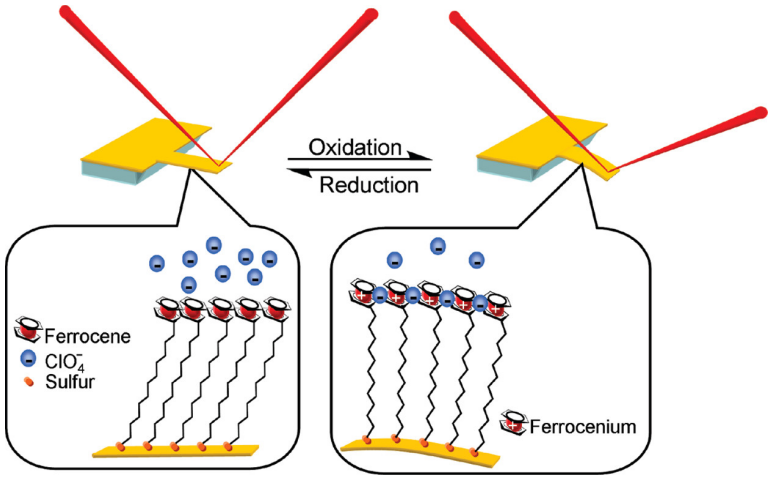

Figure 2.12: A scheme of the redox-induced deflection of a Fc-SAM-functionalized Au-coated Si microcantilever in perchlorate solution. Reprinted from [60].

2.4 Concept of capillarity-induced actuation

The mechanical actuation of a "clean" np-Au has been linked to the electrocapillarity of Au surfaces when the material is impregnated with electrolyte [12]. By polarizing the Au electrode surfaces, the interatomic bond forces between the metal atoms in the outermost interatomic plane are proned to be changed. To preserve the mechanical equilibrium, these changes in the surface stress are compensated by changes of the opposite sign in bulk stresses of the Au ligaments, resulting in overall macroscopic dimensional changes (strain) [12].

The macroscopic strain of a material depends strongly on the geometry of its structural elements [206]. A porous material characterized by an interconnected network of elongated, slender fibers that possess a circular cross-section with a uniform and consistent diameter. They are interconnected at nodes that facilitate the transmission of both force and displacement. The authors of [207] have been assumed a high aspect ratio, where the distance between the nodes significantly exceeds the diameter of the fibers. Consequently, the granular details of stress distribution at the nodes can be disregarded and modeled as points of a rigid contact between the fibers. Np-Au is the material that can be ideally represented as a fiber network. Furthermore, the bulk stress that counteracts the surface stress in each circular fiber is anisotropic, with the radial stress component being only half of the axial stress [207].

The anisotropic strain that results from the stresses can be considered via Hooke's law for a solid with isotropic elasticity [23]:

$$\left(\frac{\delta l}{l}\right)_{\mathrm{A}} = -\frac{2f}{r}\frac{1-v}{Y} \tag{2.24}$$

and

$$\left(\frac{\delta l}{l}\right)_{\mathrm{R}} = -\frac{f}{r}\frac{1-3v}{Y} \quad , \tag{2.25}$$

where $(\delta l/l)_{\mathrm{A}}$ and $(\delta l/l)_{\mathrm{R}}$ are the axial and radial strains, respectively, Y is the Young's modulus, v is the Poisson number, r is the fiber (ligament) radius, and f is the surface stress. For np-Au $v = 0.44$, that leads to an opposite sign of $(\delta l/l)_{\mathrm{A}}$. The qualitative and quantitative evaluation of the surface stress changes will be presented in this thesis for the surface-modified np-Au.

2.5 Origin of tunable elasticity in np-Au

As it was briefly discussed in Chapter 1, capillary forces significantly impact the mechanical performance of the functional nanomaterials. One of the key mechanical properties of the materials is its elasticity. An efficient approach to analyze the origin of free surface effects with respect to the capillarity on the effective elastic moduli of materials with nanoscale microstructures was proposed by Gurtin and Murdoch [67] employing the continuum theoretical framework. The model was later elaborated by Gurtin, Weissmüller, and Larché [208]. It links the elastic response of the surface to various deformation measures, including the projection of bulk strain onto the local tangent plane at the surface. In a simplified model, one can consider a scalar and isotropic surface stress function, $f(e)$, where f represents the strain derivative of the surface tension and e denotes the relative change in the surface area due to the elastic deformation at the surface:

$$f(e) = f_0 + \mathbb{C}e \quad , \tag{2.26}$$

where f_0 - the surface stress in an unstrained state, $\mathbb{C}$ - the surface excess elastic constant.

The variations of the local stiffness at surfaces of a metal can be quantified with respect to the surface stress, f [209]:

$$\mathbb{C} = \left.\frac{\delta f}{\delta \mathrm{e}}\right|_{q} \quad . \tag{2.27}$$

It is more convenient to work with another relevant parameter for the electrode mechanics – the electro-elastic coupling parameter, λ, instead of $\mathbb{C}$ – as λ can be probed in experiments, while determining $\mathbb{C}$ is challenging so far. λ estimates the excess elastic modulus change experimentally with the transferred superficial charge density, q, by [56]:

$$\lambda = \left.\frac{\delta \mathbb{C}}{\delta q}\right|_{e} \quad . \tag{2.28}$$

Up to date, few attempts have been made to estimate theoretically $\mathbb{C}$ [68, 71], along with the experimental attempts on $\mathbb{C}$ [56] and λ [56].

The size-dependent elastic behavior of gold nanowires with a clean, charge neutral surface was investigated by Elsner and colleagues in [71]. They proposed to combine two approaches – density functional theory (DFT) and continuum mechanics – in order to predict the absolute elastic response of nanostructured materials, taking into account the surface excess elasticity. Their results are shown in Figure 2.13. The authors [71] found that upon different deformation modes, the elasticity of Au nanowire is linearly-dependent on its diameter, and exhibit (in bending) up to -1.5 % relative stiffness change when a nanowire diameter is 30 nm similar to experimentally determined sized in this thesis. The value reduces to -0.5 % when the diameter approaches 100 nm. Hence, the surface effect at small sizes is pronounced.

Elsner *et al.* [71] found $\mathbb{C}_{11}$ (Lagrangian coordinates) to be equal -4.33 N m^{-1} for Au (111) and -2.91 N m^{-1} for Au (001) upon axial tension, bending, or torsion.

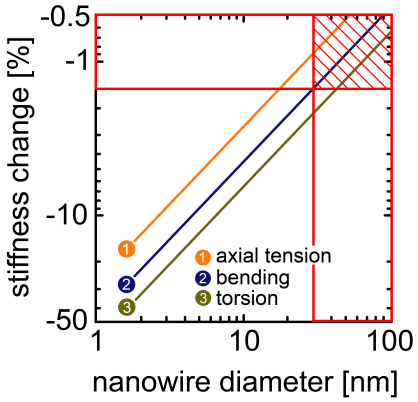

Figure 2.13: The theoretical prediction of the impact of the surface excess elasticity on the effective elastic response of gold nanowires with a clean surface as a function of the nanowire diameter. Reprinted with a permission [71]. The red shaded area corresponds to the ligament size range experimentally studied in this thesis.

The mechanical behavior of np-Au is compared to an idealized open-cell foam (Figure 2.14a) proposed by Gibson [88]. The reference model is based on a regular and periodic 3D arrangement of interconnected cylindrical beams with large aspect ratios (Figure 2.14b) [210]. Such structure mimics the experimentally observed network of Au nanoligaments/beams, which are characterized by a certain superficial layer with distinguished elastic properties (Figure 2.14c) [56].

The experimental findings on np-Au (L = 40 nm) upon the capacitive charging revealed variations of $\delta\mathbb{C}$ = 12 N m^{-1} [56]. The differences in the theoretical and experimental values of $\delta\mathbb{C}$ emphasize the significance of the surface adsorbates or electric polarization for the surface excess elasticity [56].

To evaluate changes in $\mathbb{C}$, the authors in [56] considered an elastically isotropic slab representing a square patch of thin film which is strained by in-plane forces F_1 and F_2 as shown in Figure 2.14c. In the absence of the capillary effects, simple linear elasticity of isotropic media relates the area strain, e, to the sum of the forces F_1 and F_2. Considering the impact of the surface excess elasticity, and measuring e relative to a reference state of the film at the total force, F, equal 0, yields [56]:

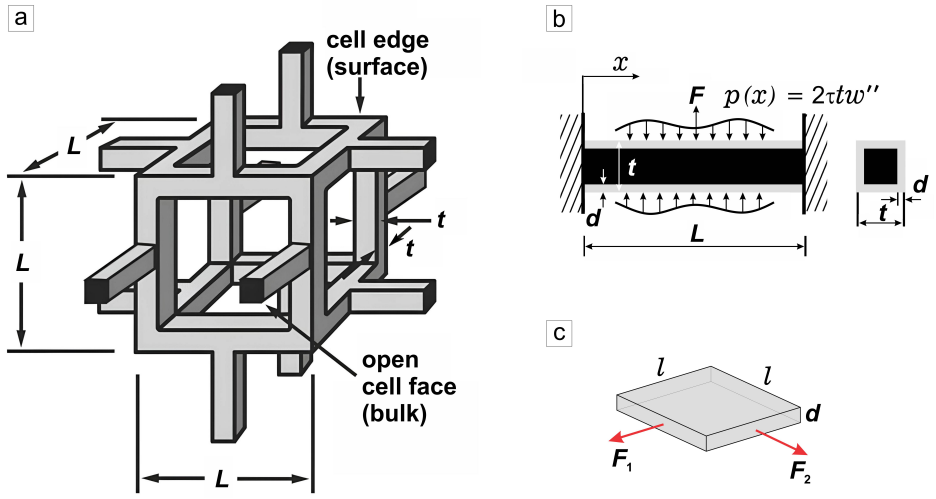

Figure 2.14: Schemes of (a) an idealized unit cell in an open-cell foam, where L is the cell size and t is the thickness of the cell edges [211]; (b) Timoshenko's nanobeam model accounting for surface effects, where $p(x)$ is the surface stress treated as a distributed transverse loading along the longitudinal direction of the nanobeam [210]; (c) a cuboid slab, representing a patch of thin film of area $l \times l$ and thickness d, loaded on two opposite cross-sectional faces by the forces F_1 and F_2 [56]. Reprinted with permissions.

$$F = l(d + 2\tau)Be \quad , \tag{2.29}$$

where l and d - the characteristic sizes of length and thickness of the thin film, respectively, and B - the biaxial modulus of the bulk of the film. The parameter τ is an apparent excess thickness which is calculated as [56]:

$$\tau = \frac{\mathbb{C}}{B} \quad . \tag{2.30}$$

This formal parametrization accounts for the excess stiffness in an intuitive way. The two scenarios are possible. First, when $\mathbb{C} > 0$, it indicates stiffening of a material. Second, when $\mathbb{C} < 0$, it corresponds to softening of the material.

To couple the experimental findings on the stiffness variations with the excess elastic parameters, the Bernoulli beam theory [212] was employed in a form [56]:

$$\frac{\delta I}{I} = \frac{4}{r}\delta\tau \quad , \tag{2.31}$$

where $\delta I/I$ - the relative change in the bending stiffness of a ligament, r - the characteristic ligament radius. In this case, the experimental relative stiffness change, $\delta Y'/Y'_0$, is assumed to be equal to the variation of the bending stiffness of a ligament, $\delta I/I$.

The concept developed for np-Au by Mameka *et al.* [56] is employed in this thesis to determine the sign and magnitude of the surface excess elastic parameters $\mathbb{C}$ and λ for "clean" (capacitively charged) np-Au (Section 4.3.1), OH-covered/np-Au (Section 4.3.2), and Fc-SAM/np-Au (Section 4.3.6) surfaces.

Chapter 3

Materials and methods

This chapter focuses on fundamental principles underlying electrochemical methods and measurements, which provide the essential framework for the synthesis of nanoporous gold and surface-functionalized nanoporous hybrids. It will address the conduction of the electrochemical experiments on these materials under ambient conditions. Furthermore, a comprehensive discussion of the analytical techniques employed to assess the microstructural characteristics of the synthesized materials will be included. Finally, the chapter will explore the experimental methodologies utilized for the characterization of the mechanical properties of these materials.

3.1 Electrochemical equipment

In this thesis, the synthesis of samples and the investigation of material properties were conducted under electrochemical conditions. A potentiostat (Metrohm AUTOLAB, PGSTAT302N) was employed to modulate and regulate the voltage and current. The system's response to variations in these parameters was monitored through NOVA software (version 1.11), which recorded the current and the total charge consumed (potentiostatic mode). The electrode charge was determined by integrating the current over time.

Glass electrochemical cells were used under the study to prevent any unwanted reactions. Additionally, the purity of the cell was carefully maintained to ensure accurate and reliable results. Thus, prior to use the cells were immersed in a piranha solution (96 % H_2SO_4 and 30 % H_2O_2 with a ratio 5 : 1) followed by rinsing in ultrapure water (UPW, resistance of 18.2 MΩ·cm, Sartorius, Arium comfort).

An electrochemical setup typically includes two electrical conductors, known as electrodes, submerged in an electrolyte solution. A potential difference can be established between the working electrode (WE) and reference electrode (RE), allowing for charge transport through either electrons in the electrodes or ions in the electrolyte. While electrons do not change the state of the electrode, ions can influence the electrode surface or the composition of the electrolyte at the interface. The overall electrochemical reactions are the result of the collective processes occurring at each electrode in response to the externally applied potential. The counter electrode (CE) is essential for completing the electrical circuit in an electrochemical cell. It functions as the site for electron transfer, which is critical for maintaining the balance of reactions occurring at

the WE. The CE plays a significant role in preserving electrical neutrality within the cell and facilitates the flow of current during electrochemical measurements. Typically, the CE is constructed from an inert material that does not engage in the electrochemical reactions occurring within the cell.

Under the study, samples were used as WEs. Reference electrodes used in this work are a pseudo silver/silver chloride (Ag/AgCl) and a commercial Ag/AgCl (XR310, Radiometer analytical) reference electrodes. The pseudo (or homemade) silver/silver chloride electrodes were fabricated using an electrolytic deposition of AgCl onto a Ag wire with a diameter of 0.5 mm and purity of 99.999 % (Alfa Aesar). This process occurred in a solution of 1 M HCl at a constant potential of 1 V, with another Ag wire acting as the CE and RE. The deposition took approximately 100 s, after which the coated wire was rinsed with ultrapure water (UPW) and stored in a water bath. Before the deposition, the surface of the Ag wire was cleaned of any oxide layers through mechanical polishing followed by thorough rinsing with UPW. A calibration of the RE was performed versus a standard hydrogen electrode (SHE, HydroFlex, Gaskatel) via a voltmeter in an electrolyte planned to be used in the experiment. Counter electrodes were a silver wire (0.5 mm diameter, Ag 99.999 % Alfa Aesar) for dealloying, a porous carbon cloth (Kynol Europa GmbH) for CV reduction and *in situ* experiments. The CEs were rinsed and stored in UPW.

In this work, the three listed above electrodes were inserted in single- or three-compartment glass cells employed for sample preparation, electrochemical characterization, and *in situ* properties investigation. The cells were resistant to the used aqueous electrolyte of $HClO_4$. A three-electrode cell configuration with a Luggin capillary and a large capacity of 500 mL was used for electrochemical dealloying (Figure 3.1a). A custom-made three-compartment cell with a capacity of 10 mL was used for *in situ* dynamical mechanical analysis (Figure 3.1b). The design of the DMA holder restricts the volume of the cell. Three-compartment cells offer a more precise model of electrochemical reactions, making them the preferred choice for rigorous experimental investigations. Especially, during a dealloying process, when the RE and CE need to be separated from the WE to prevent unwanted reactions or interference. Single-compartment cells were used for *in situ* dilatometry experiments (Section 3.5.2) with a volume of 90 mL, shown in Figure 3.1c.

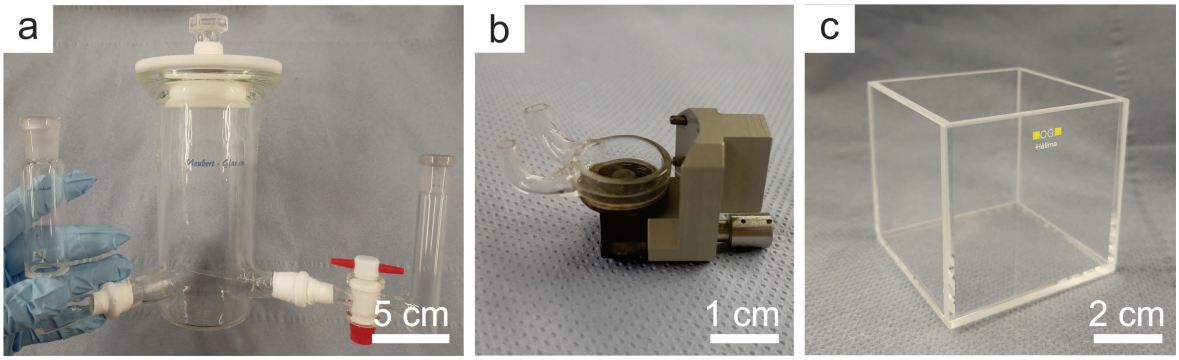

Figure 3.1: Electrochemical cells for (a) dealloying, (b) *in situ* dynamical mechanical analysis, (c) *in situ* dilatometry, and *in situ* mechanical compression.

3.2 Principles of electrochemistry

3.2.1 Chronoamperometry

Chronoamperometry (CA) is an electrochemical method used to study the kinetics and dynamics of electrode reactions. The technique measures a current as a function of time at a constant applied potential and determines the consumed charge. In this thesis, various CA procedures were utilized for fabrication of nanoporous gold at a given potential. Potential jumps of constant potentials were imposed for examination of a response time of a material to the potential switch and *in situ* mechanical experiments.

3.2.1.1 Chronoamperometry for dealloying of nanoporous gold

Np-Au was fabricated via dealloying of $Au_{25}Ag_{75}$ (at. %) in 1 M $HClO_4$ aqueous electrolyte at a constant potential of E_{SHE} = 1.265 V. To ensure the dissolution of Ag in np-Au, subsequent steps of the increased potentials were employed at E_{SHE} = 1.315 V and E_{SHE} = 1.515 V, respectively. At the potential values above the critical dealloying potential, Ag is continuously oxidized into Ag^+ and selectively leached out from the master alloy. The corrosion process takes place till the current drops down below 10 µA.

The fabrication of hierarchical np-Au requires a two-step dealloying procedure combined with a coarsening stage in between. During a *stage I*, the dissolution of Ag from a Au_7Ag_{93} (at. %) master alloy is performed in 0.01 M H_2SO_4 (Figure 3.2). During this process, a nanoporous Ag-Au is obtained via partial dissolution of Ag, and surface diffusion of Au atoms. A relatively low dealloying potential (E_{SHE} = 0.986 V) and the diluted H_2SO_4 electrolyte enable a slow dissolution of Ag. A *stage II* of the dealloying is carried out in 1 M $HClO_4$ at E_{SHE} = 1.315 V and E_{SHE} = 1.515 V till the current decays to zero. The potentiostat records the representative curves of current, potential, and charge. Figure 3.2 schematically shows a typical behavior observed during the electrochemical dealloying process.

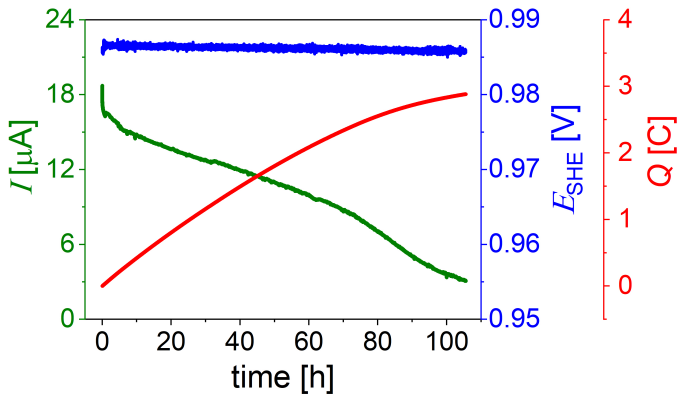

Figure 3.2: Typical behavior of the partial electrochemical dealloying of Au_7Ag_{93} (at. %) in 0.01 M H_2SO_4. Current, I, potential, E_{SHE}, and cumulative charge, Q, are given as a function of time.

3.2.1.2 Chronoamperometry for *in situ* experiments and response time investigation

A potential step technique involves applying a step change in potential to an electrode and measuring the resulting current response. The method provides information about diffusion-controlled processes and electron transfer reactions. The CA allows applying of jumps of certain constant potentials for a defined time interval. Such approach can be used to control the redox state of the Fc-SAM upon the experiments (Figure 3.3). Prior to the *in situ* experiments, the response time of the hybrids were analyzed with respect to the electrochemically active surface state. The redox state of Fc-SAM was controlled by a lower and a higher applied electric potentials. The current-time curves were recorded for all specimens during potential jumps from lower to higher potential, and vice versa with a step of 0.01 s in 0.1 M $HClO_4$ (70 %). An exponential decay fitting was applied to the curves to evaluate the response time of the Fc-SAM-modified np specimens to the potential switch. The response rates were parameterized by the half time needed for a half of a maximum current.

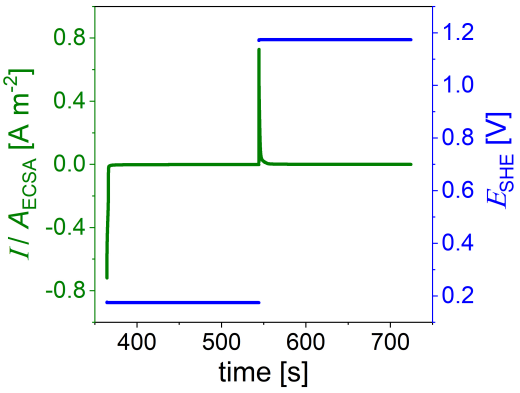

Figure 3.3: The current-potential response of hierarchical np-Au modified with FcC_{11}-SAM in 0.1 M $HClO_4$ upon potential jumps at constant potentials of E_{SHE} = 0.175 V and E_{SHE} = 1.175 V.

3.2.2 Cyclic voltammetry

A cyclic voltammetry is commonly used in various fields such as analytical chemistry, biochemistry, and materials science for applications such as determining a concentration of a species in solution, studying reaction mechanisms, and characterizing electrochemical materials [213]. It is a versatile and powerful tool that can offer insights into the fundamental electrochemical properties of a system providing information about thermodynamics and kinetics of electron transfer processes on the electrode surface [214]. These processes include the electron transport through the interface, ion adsorption, and modifications of the adsorbed layer.

In a cyclic voltammetry experiment, a potential of the WE is scanned by a potentiostat in a fixed potential window, starting from a certain initial potential, E_0, ramping to an upper vertex one (anodic scan), E_1, and then scanning in the reverse direction to

a lower vertex potential (cathodic scan), E_2, at a constant scan rate v (Figure 3.4a). The experiments in this thesis were carried out with a scan rate of 5 mV s^{-1}, unless otherwise stated. The starting potential was chosen with respect to an open circuit potential (OCP). The OCP is a potential difference between the WE and the RE when no current is flowing in the electrochemical cell.

The staircase CV mode was chosen throughout the thesis allowing imposing small potential steps going from E_1 to E_2 and recording the current response at the end of each step. During the entire cycling, the current response to this modulation of the electrode potential is recorded and then plotted as a function of the potential, giving rise to the CV shown in Figure 3.4b.

In this work, the CV was used for an electrochemical reduction of the as-dealloyed samples and the determination of the surface area via the capacitance ratio method (Section 3.3), *in situ* strain (Section 3.5.2), and effective elastic modulus measurements (Section 5.3).

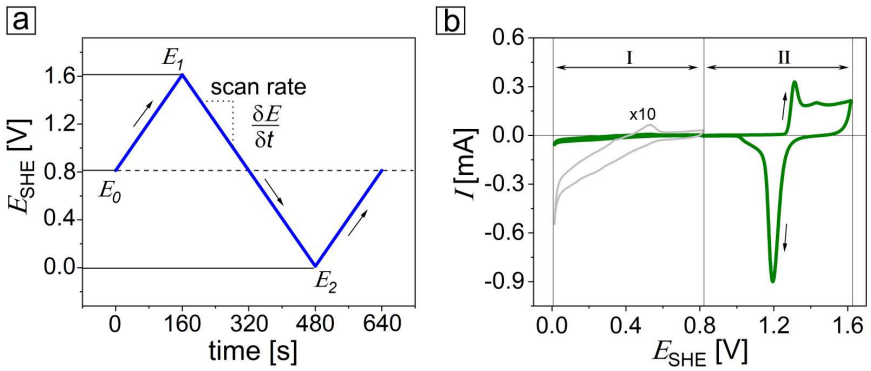

Figure 3.4: Typical cyclic voltammetry experiment on hnp-Au in 1 M $HClO_4$ recorded at a scan rate of 5 mV s^{-1} at ambient conditions: (a) potential-time profile (blue), initial potential (E_0), along with upper (E_1) and lower (E_2) potential limits are indicated; (b) current-potential response (green) divided into two parts related to capacitive charging regime (I) and partially oxidized surface (II). The grey curve shows the 10-times magnified current response in the capacitive regime.

3.3 Materials fabrication

3.3.1 Unimodal nanoporous gold

Macroscopic samples of unimodal nanoporous gold were made of $Au_{25}Ag_{75}$ (at. %) as an alloy precursor for the electrochemically controlled dealloying. The Ag and Au wires (99.99 wt. % metal base purity) were supplied by Alfa Aesar. The arc-melter (MAM-1, Edmund Bühler) was utilized to produce ingots in an argon atmosphere. After each melting step, an ingot was flipped over a minimum of 15 times to ensure a homogeneous distribution of Au and Ag throughout the ingot. The ingot was sealed in a quartz tube under vacuum followed by homogenization in a furnace for 5 days. Silver and gold are completely soluble in each other over the entire range of compositions and temperatures, eliminating the need for an additional heat treatment of the master

alloy [215]. To shape np-Au, the master alloy was drawn to a wire of 1.0 ± 0.1 mm in diameter. A diamond wire saw (Well Diamantdrahtsagen GmbH, Model 3032) was employed to cut the wire with a length of 1.4 ± 0.1 mm. In order to relieve the residual stresses after cutting, an annealing was carried out at 800 °C for 2 h in Ar (infrared furnace behr IRF 10, behr Labor Technik).

The Au-Ag cylinders were fixed within a holder made of a gold foil and subjected to the electrochemical dealloying at a constant potential of E_{SHE} = 1.265 V in 1 M $HClO_4$ (60 %) till the current dropped down below 10 µA. After that, in order to dissolve a residual silver, remove impurities, and adsorbed oxygen species, a subsequent polarization was carried out at the increased potentials E_{SHE} = 1.315 V and E_{SHE} = 1.515 V for 30 min each, followed by 15 full CV cycles (E_0 = 0.800 V, E_1 = 0.0 V, E_2 = 1.600 V as illustrated in Figure 3.4a, scan rate, υ, 5 mV s^{-1}). This corresponds to an adsorbate-free surface state. Afterwards, the samples were rinsed in UPW, dried and stored in a fume hood prior to use. The Au solid fraction of np-Au with L = 40 ± 5 nm, φ_{Au}, was 0.27 ± 0.01. The residual Ag was reduced down to 3 at. %. The sample dimensions (volume, V) before and after dealloying were determined using an optical microscope (Olympus SZX10). The sample mass, m, was measured via a laboratory balance with an accuracy of 0.000001 g (Sartorius, ME36S). The Au solid fraction, φ_{Au}, was calculated with respect to the obtained values via $\varphi_{\mathrm{Au}} = m/V \times 1/\rho_{\mathrm{Au}}^{\mathrm{solid}}$, where $\rho_{\mathrm{Au}}^{\mathrm{solid}}$ = 19.3 g cm^{-3} is a density of a solid Au.

Np-Au is known to undergo a thermally-driven coarsening, manifested as a continuous growth in ligament diameter over time, with rates accelerating at higher temperatures [216]. Hence, the length scale of porosity, thus the ligament size, of np-Au was tuned up to 1 µm while maintaining the characteristic bicontinuous structure either by electrochemical or thermal annealing. L was increased to 100 nm electrochemically via CV cycling. To obtain bigger ligaments, series of annealing in air (infrared furnace behr IRF 10) and under vacuum (MILA-5000 ULVAC) were carried out at temperatures between 200 and 1000 °C with a step of 50 °C and total annealing time of 20-60 min. These samples were used for *in situ* dynamic mechanical analysis (DMA) experiments on np-Au. A part of prepared np-Au specimens with L = 120 nm coarsened at 300 °C during 20 min were used for a comparison with hierarchical (h) np-Au, both subjected to surface modifications (Section 3.4).

In this work, the ligament size, L, was determined over the cross-section of a np sample using scanning electron microscopy, for details the reader is referred to Section 3.5.1.

To eliminate an impact of Ag on np-Au, the CV cycles were applied after the thermal treatment to remove the silver diffused to the surface of the ligaments during coarsening [34]. The cycling was stopped at a clean Au surface state. This treatment resulted in residual Ag less than 3 at. %. The Au solid fractions, φ_{Au}, are 0.27 ± 0.01 (np-Au with L = 40 ± 5 nm) and 0.30 ± 0.01 (np-Au with L = 120 ± 30 nm).

The samples were rinsed in UPW (18.2 MΩ · cm) followed by the immersion in ethanol, dried and stored in a fume hood. The electrochemically active surface area (A_{ECSA}) measurements of np-Au and hnp-Au were carried out using the capacitance ratio method [217] prior to the formation of anodic oxide or SAM deposition. This method does not modify the surface and provide most reliable data. The average values of A_{ECSA} in np-Au with L = 40 nm and np-Au with L = 120 nm were 290 ± 15 cm^2 and

110 ± 10 cm^2, respectively. The corresponding mass-specific surface areas, α_m, were 4.68 m^2 g^{-1} (L = 40 nm) and 3.06 m^2 g^{-1} (L = 120 nm).

3.3.2 Hierarchical nanoporous gold

Hierarchical nanoporous gold samples were prepared out of Au_7Ag_{93} (at. %) master alloy using the same procedures as for the fabrication of np-Au (Section 3.3.1). The ingot was cold-rolled down to 1 mm thickness, and subsequently cut with the diamond wire saw. The final sizes of the cuboid hnp-Au samples were 1 × 0.5 × 0.5 mm^3. After that, the specimens were copiously rinsed with acetone followed by cleaning in ethanol and UPW, dried, and stored in a fume hood prior to dealloying.

The three-stage electrochemical dealloying was performed in the three-electrode cell (Figure 3.1a). The *stage I* was a partial dealloying of Au_7Ag_{93} carried out in 0.01 M H_2SO_4 (97 wt. %) at a constant potential of E_{SHE} = 0.986 V till a pre-defined charge (Cut-Off Charge in Nova 1.11) was reached. This charge corresponds to np Ag-Au with an alloy composition of $Au_{25}Ag_{75}$ (at. %). The cut-off charge was calculated with respect to the initial sample mass and the desired resulting composition via Faraday's law. After the dealloying, the samples were immersed in UPW for at least 10 hours, then water was changed to ethanol in which the samples were stored for 2-4 hours more. The samples were dried and stored in a fume hood prior to the next stage.

The *stage II* was related to coarsening of the partially dealloyed specimens. The nanoporous Ag-Au samples were annealed in an ultra-high vacuum infrared furnace (MILA-5000 ULVAC at pressure of 10^{-6} mbar) at 400 °C for 30 min. The resulting ligament size, L_1, was 120 nm and the solid fraction at the upper hierarchy level, φ_1, was 0.30 ± 0.01.

The *stage III* was dedicated to the second dealloying performed to dissolve a residual Ag and form hnp-Au at potentials of E_{SHE} = 1.315 V and E_{SHE} = 1.515 V for 2 h each in 1 M $HClO_4$ (60 %). After that, the 5 CV cycles between E_{SHE} = 0.855 V and E_{SHE} = 1.515 V were carried out at a scan rate of 5 mV s^{-1} in fresh 1 M $HClO_4$. The cycling was stopped at a potential of E_{SHE} = 0.900 V corresponding to the clean gold surface. The resulting ligament sizes were L_2 = 120 ± 30 nm (upper level) and L_1 = 20 ± 5 nm (lower level). The residual Ag was less than 3 at. %. The total Au solid fraction of hnp-Au after the *stage III*, φ, was 0.12 ± 0.01 calculated via $\varphi_{Au} = m/V \times 1/\rho_{Au}^{solid}$. The solid fraction at the lower hierarchy level was 0.30 ± 0.01. The solid fraction at the upper hierarchy level was estimated as $\varphi_2 = \varphi/\varphi_1 \approx 0.40$ in accordance with [15]. The average of A_{ECSA} in hnp-Au ($L_{1,2}$ = 120/20 nm) was 55 ± 10 cm^2. The mass-specific surface area, α_m, was 9.17 m^2 g^{-1}.

The total number of connections ("struts") in the hnp-Au was calculated with respect to the sample volume (V_{sample}) and the scaled topological genus (g) of the leveled-wave model. By its definition, g represents the number of connections in a representative volume element of the microstructure. The material contains $gV_1/V_{RVE} \approx 3 \times 10^{12}$ of the lower-hierarchy-level struts, where $V_{RVE} = (2L_1)^3$ is a volume at the lower hierarchy level, $g \approx 1$, and $V_1 = \varphi_2 V_{sample}$ is a total volume occupied by the lower-hierarchy-level microstructure [15].

3.3.3 Planar gold

Planar Au films on silicon substrates were used for *in situ* cantilever bending experiments. (100)-oriented silicon wafers of a nominal thickness of 100 µm with a thermally grown 100 nm thick oxide layer were supplied by CrysTec^{TM} GmbH. The Si wafers were cut into a rectangular shape of 8 × 40 mm^2 using a diamond cutter. The multilayered beam structures were fabricated by a DC magnetron sputtering. A 10 ± 1 nm titanium coating was sputtered on top of the electrically insulated Si wafer for adhesion (a wetting layer) followed by the sputtering of the 55 ± 5 nm thin gold film on Ti. In this case, the gold films remain clamped to the silicon substrate, and the stress is calculated via a bending of the cantilever. The bending stiffness of the Si cantilever is negligible. The obtained cantilevers were cleaned with UPW and ethanol followed by drying and storage in a fume hood before the experiments.

3.4 Surface functionalization of np-Au

One of the key challenges facing the application of nanoporous metals in engineering is their tendency to coarsen in certain environments, leading to shortened lifetimes. Surface modification techniques play a vital role in preventing coarsening in electrolytes, where the rate of surface diffusion is influenced by the presence of anion species in the solution. Significant coarsening rates can occur even at room temperature, highlighting the importance of surface functionalization in enhancing the stability and longevity of nanoporous materials in real-world applications. The manipulation of surface properties through adsorption and self-assembly techniques is crucial in the field of materials science. By introducing nanoscale features and chemical gradients on surfaces, it is possible to fine-tune material behavior at the solid-liquid interface. This section will delve into the preparation of electrochemically formed surface oxide (Section 3.4.1) and complex adsorbates on gold, such as the attachment of redox species like alkanethiol self-assembled monolayers with a transition metal complex – ferrocene (Section 3.4.2).

3.4.1 Electrochemical oxide film formation on np-Au

As it was already highlighted in the Introduction, the interaction of water and hydroxyl with surfaces is essential in a wide range of systems, with significant implications for both fundamental research and technological applications such as corrosion, electrolysis, and fuel-cell technology. Among the various adsorption cases, the behavior of water and hydroxyl on metal surfaces, namely, gold has been extensively studied by electrochemical methods in the past [150].

Consider a typical CV on np-Au in 1 M $HClO_4$ (Figure 3.5). The electrolytic oxidation of gold begins at E_{SHE} = 1.20 V and starts with reversible electrosorption of OH. This is followed by the formation of a sub-monolayer of OH and/or O in a two-dimensional arrangement gradually progressing to the growth of a single monolayer with increasing potential and duration till it reaches the Burshtein minimum [218] before the evolution of oxygen. It was shown that the Burshtein minimum is reached around 1.64 V (vs. SHE) and is independent on pH of electrolyte [219]. The formation

of the 2D oxide film is confined to this one monolayer, which can be used to determine the surface area of gold electrodes. Upon reaching higher potentials and longer time, the displacement of Au and O triggers further oxidation of the surface, leading to the generation of a three-dimensional bulk oxide in the configuration of Au_2O_3 or hydrated Au_2O_3 [220].

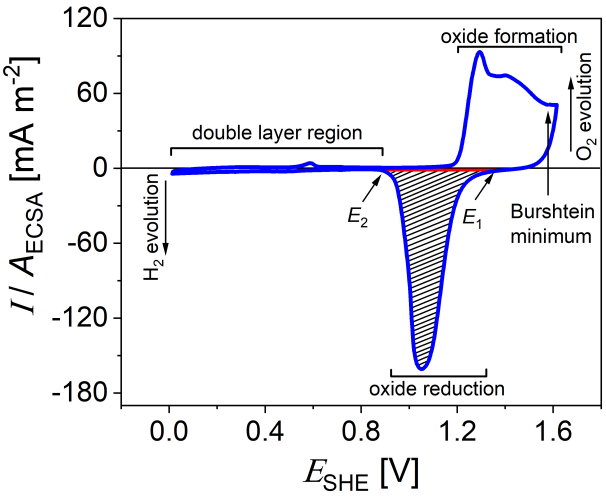

Figure 3.5: Current-voltammetry response of np-Au (L = 40 nm) in 1 M $HClO_4$. The double layer region, oxide formation, and oxide reduction are indicated, along with the region where oxygen and hydrogen evolution begins. The Burshtein minimum marks the current minimum before oxygen evolution and bulk oxide formation. The hatched area can be used for the determination of A_{ECSA}. The red line indicates the background at potentials between E_1 and E_2 which is used for the integration of the peak to determine a charge involved in the reduction process.

In this thesis, the surface state was controlled by the applied electric potential. By using the CV, the evaluation of the OH coverage on a np sample can be done by the integration of the current (I) peak profile over the potential range corresponding to the oxidation between E_{SHE} = 1.20 V and E_{SHE} = 1.60 V or reduction in the potential range of E_{SHE} = 0.85 V and E_{SHE} = 1.30 V, which gives the passed charge, Q, related to the reversible process of the OH adsorption and desorption, respectively [150]:

$$Q = \int_{E_1}^{E_2} I(E)dt = \int_{E_1}^{E_2} \frac{I(E)}{v} dE \quad , \tag{3.1}$$

where v is the potential scan rate.

The OH coverage, Θ_{OH}, increases along with Faradaic surface reaction and is related to the transferred charge for the OH electrosorption, Q, in accordance with:

$$\Theta_{\mathrm{OH}} = \frac{Q}{Q_{\mathrm{OH}} \cdot A_{\mathrm{ECSA}}} \quad , \tag{3.2}$$

where A_{ECSA} is the electrochemically active surface area determined via the capacitance ratio method; Q_{OH} is the charge passed during the formation of one monolayer of oxide

on planar Au electrodes determined as 386 µC cm^{-2} [150]. The error bar of Q_{OH} was estimated as a standard deviation taking into account the variations in A_{ECSA} given in Section 3.3.1 for np-Au and Section 3.3.2 for hnp-Au.

3.4.2 Electroactive self-assembled monolayers

Electroactive ferrocene-terminated alkanethiol self-assembled monolayers are one of the most widely studied self-assembled systems due to their versatility, stability, and functionality. In this work, two types of the molecules were chosen for SAM formation: 6-(Ferrocenyl)hexanethiol ($C_{16}H_{22}FeS$), further will be mentioned as FcC_6, and 11-(Ferrocenyl)undecanethiol ($C_{21}H_{32}FeS$), further will be given as FcC_{11}. All thiols were supplied by Sigma-Aldrich Chemie GmbH. The passive immersion method was employed for the monolayer formation on the samples (Figure 3.6). The specimens were immersed in 1 mM ethanolic solutions (high-grade ethanol, 99.8 %, AppliChem) of each Fc-SAM separately for 20 h in darkness in glass vessels with hermetically closed lids. Upon removal from the incubation solution, the modified specimens were rinsed and stored in absolute ethanol prior to the further tests.

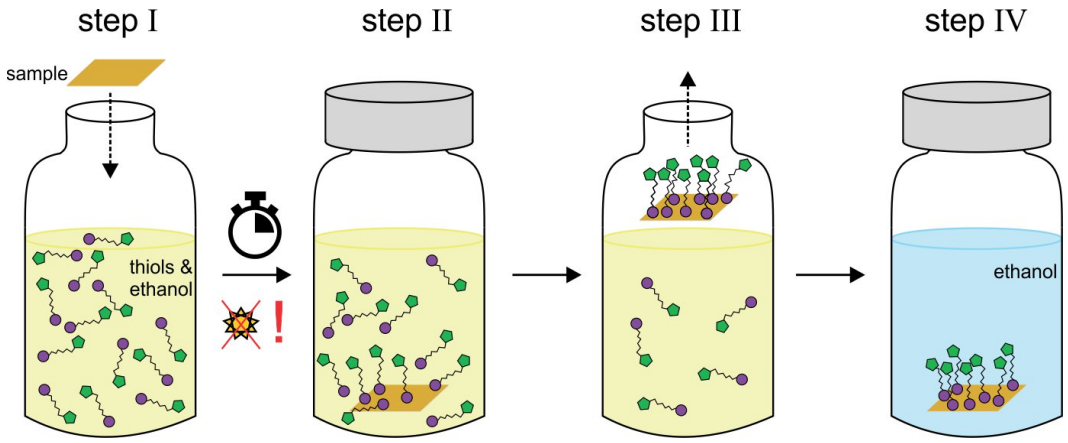

Figure 3.6: A scheme of the passive immersion method in an ethanol-based alkanethiol solution. The ferrocene (Fc)-terminated self-assembled molecule (SAM) is shown as sulfur (purple circle) - alkyl chain (black tail) - Fc (green pentagon). Step I - the sample immersion in a glass vessel filled with a diluted thiol solution. Step II - the vessel storage in a dark place for a given time. Step III - the removal from the incubation solution and rinsing with absolute ethanol of the Fc-SAM-modified sample. Step IV - the sample storage in absolute ethanol prior to the further experiments.

The cyclic voltammetry was employed to characterize the Fc-SAM formation (Figure 3.7). The observed anodic peak potential (E_{pa}) and cathodic peak potential (E_{pc}) correspond respectively to one-step redox-reactions of the terminal group that transform ferrocene (Fc) to ferrocenium (Fc^+). In an ideal Nernstian electron transfer case, the peaks are symmetrical and a peak separation ΔE_{peak} between E_{pa} and E_{pc} is equal to 0. The formal redox potential ($E_{1/2}$) can be calculated as a mid-way between the redox peaks comprising the CV [183]:

$$E_{1/2} = \frac{E_{pa} + E_{pc}}{2} \quad . \tag{3.3}$$

The peak shape is diagnostic of the homogeneity of the monolayer and can be evaluated by the full width at half of the peak maximum height (FWHM). The capacitive current (background or charging current, I_{ch}) can be correlated to the thickness of the SAM. The peak height is proportional to the sweep rate, v, and the surface coverage, Γ_{Fc}.

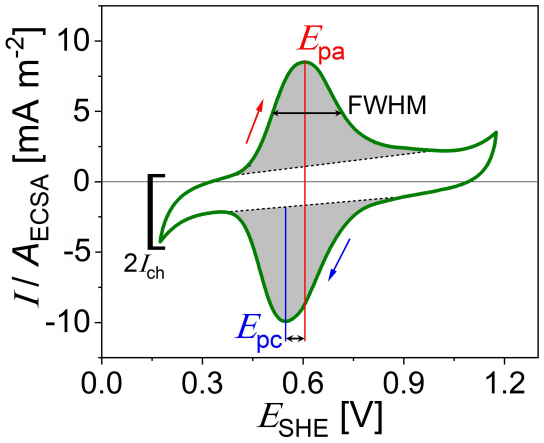

Figure 3.7: Typical current-potential response of the FcC_6-SAM/hnp-Au in 0.1 M $HClO_4$. The red arrow denotes the anodic scan and oxidation peak potential (E_{pa}) of ferrocene. The blue arrow indicates the cathodic scan and reduction peak potential (E_{pc}) of ferrocenium. The background current (I_{ch}) is correlated to the thickness of the SAM. The full width at a half of the peak maximum (FWHM) is indicated. Grey area under the peak equals to the passed charge during redox of Fc-moiety.

To obtain the charge passed during the oxidation reaction of Fc to Fc^+, Q_{Fc^+}, the charging current was corrected by the baseline approximation before the integration of the anodic and cathodic peaks as shown in Figure 3.7. The superficial density of ferrocene-terminated molecules in the oxidized state, Γ_{Fc^+}, can be estimated with respect to Q_{Fc^+} via [60, 183]:

$$\Gamma_{Fc^+} = \frac{Q_{Fc^+}}{n \cdot F \cdot A_{ECSA}} \quad , \tag{3.4}$$

where n is the number of electrons involved in the electron-transfer process (n = 1 for Fc/Fc^+), F is the Faraday's constant, and A_{ECSA} is an active surface area of the exposed substrate electrode prior to the Fc-SAM formation (for nanoporous samples or A for planar ones) that was measured electrochemically. The experimentally determined Γ_{Fc^+} will be discussed in Chapter 4 with respect to the theoretical value of the superficial density of Fc-SAM, Γ_{Fc}^{theor}, of 4.5 × 10^{-10} mol cm^{-2} calculated for the $(\sqrt{3}\times\sqrt{3})$R 30° ideal and well-packed structure of chemisorbed of the Fc-SAM (0.66 nm Fc diameter) on the Au (111) surface [193].

The interactions between the neighboring Fc-SAMs are characterized by the fractional coverage, Φ_{Fc^+} [60]. To estimate Φ_{Fc^+}, the maximum Q_{Fc^+} during each the anodic or cathodic scans was considered as Φ_{Fc^+} = 1.0. This approach characterizes the amount of the electrogenerated ferroceniums with the applied electric potential during the CV cycle.

The Fc-SAM surface coverage, Θ_{Fc}, on np-Au, hnp-Au, and the planar Au can then be estimated using simple calculations:

$$\Theta_{\mathrm{Fc}} = \frac{\Gamma_{\mathrm{Fc^+}} \cdot N_{\mathrm{Avogadro}}}{N_{\mathrm{Au(111)}}} \quad , \tag{3.5}$$

where $N_{\mathrm{Au(111)}}$ is the density of Au atoms in the (111) plane, takes the value of $N_{\mathrm{Au(111)}}$ = 1.381 × 10^{15} atoms cm^{-2}; N_{Avogadro} is the Avogadro's constant, N_{Avogadro} = 6.022 × 10^{23} atoms. The theoretical value of $\Theta_{\mathrm{Fc}}^{\mathrm{theor}}$ is 0.33 ML for a well-packed Fc-SAM on the planar Au [193].

3.5 Materials characterization

In this thesis, the discussed-above materials were characterized by scanning electron microscopy, x-ray energy dispersive spectroscopy, *in situ* dilatometry, *in situ* cantilever bending, *in situ* mechanical tests, and *in situ* dynamic mechanical analysis. The properties of gold were studied in aqueous electrolytes.

3.5.1 Electron microscopy and x-ray energy dispersive spectroscopy

The structural investigations were carried out using scanning electron microscopy (SEM) Helios NanoLab G3 (DualBeam) on fractured surfaces. The images were obtained with a through-the-lens detector in a secondary electron mode at a working distance of 4 mm. The accelerating voltage was 5 kV. The Automatic QUantitative Analysis of Microscopy Images (AQUAMI) software [221] was used to estimate the ligament size, L, of the samples.

The setup is equipped with a detector for an element analysis. The elemental composition of the samples was examined via the energy dispersive X-ray analysis at higher voltage of 10-20 kV.

The transmission electron microscope (TEM) Talos F200X from FEI (Thermo Fisher) was employed to investigate with high resolution the fine structure of the hierarchical nanoporous samples. The sizes of the upper, L_1, and lower level ligaments, L_2, along with the ligament spacing of the upper level, $\tilde{L}^U$, and the lower level ligaments, $\tilde{L}^L$, were determined.

3.5.2 *In situ* dilatometry

To experimentally measure the macroscopic deformation, dilatation experiments on np specimens were carried out in a vertical dilatometer (L75, Linseis) combined with the three-electrode electrochemical cell connected to the potentiostat. The experimental setup is shown in Figure 3.8. The samples were fixed in the sample holder by maintaining a stress of 0.25 MPa throughout the experiments. A clean Au plate of 1 mm thickness coupled with a gold wire of 0.125 mm diameter were placed under the sample (WE) to ensure an electric contact. The reference and counter electrodes were a homemade Ag/AgCl wire and carbon cloth, respectively. The electrochemical environment was an aqueous 0.1 M $HClO_4$ (70 %).

The samples under study were subjected to the CV in potential windows corresponding to, first, the OH electrosorption between E_{SHE} = 0.815 V and E_{SHE} = 1.615 V and, second, redox of the Fc-SAM between E_{SHE} = 0.175 V and E_{SHE} = 1.175 V with a scan rate 5 mV s^{-1}. The obtained results on the transferred current and charge were calculated with respect to the electrochemically active surface area, A_{ECSA} (Section 3.3.1 for np-Au, Section 3.3.2 for hnp-Au), later given as current density, I/A_{ECSA}, in [mA m^{-2}] and charge density, q, in [C m^{-2}], respectively. The macroscopic strain of the sample was calculated as a difference in the sample length change with respect to the initial sample height determined by the optical microscope prior to the test.

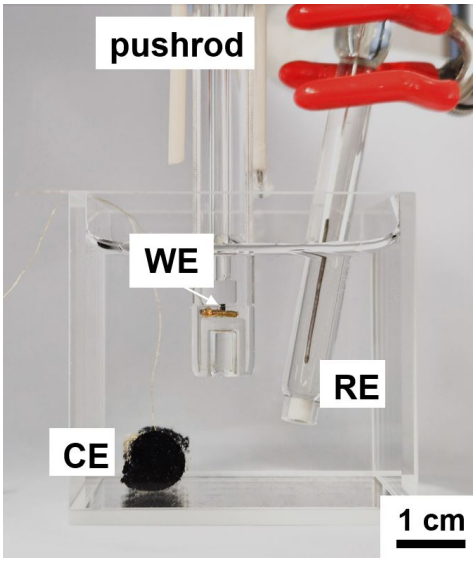

Figure 3.8: *In situ* dilatometer setup combined with an electrochemical cell: WE - the working electrode (sample), RE - the reference electrode (Ag/AgCl), and CE - the counter electrode are immersed in $HClO_4$ aqueous electrolyte.

Variations in macroscopic dimensional change, $\delta l/l$, of porous solid bodies assembled from spheres can be calculated via [206]:

$$\frac{\delta l}{l} = -\frac{2\alpha f}{9K} \quad , \tag{3.6}$$

where $\delta l/l$ is taken as $1/3$ of the macroscopic volume change, f is the surface stress, K is the Au bulk modulus, and $\alpha = 3/r_{\mathrm{s}}$ is the volume-specific surface area for a sphere of radius r_{s}. Here, linear dependencies of $\delta l/l$ versus A/V scale as 1:5.5:7 in simplified geometries, such as spherical particles, bicontinuous structures, and void lattices, respectively.

For a porous solid, it is common to employ the mass-specific surface area, α_{m}, to estimate the variation in the mean surface stress relative to an arbitrary reference state, δf, from the macroscopic strain, $\delta l/l$, via [222]:

$$\delta f = -\frac{9K}{2\alpha_{\mathrm{m}}\rho}\frac{\delta l}{l} \quad , \tag{3.7}$$

where $\alpha_{\mathrm{m}} = A/m$ with m as a sample mass and A as a surface area of sample, ρ is the mass density of the solid phase.

The determination of the surface area, A, might have an uncertainty that can affect the computation of the electrocapillary coupling parameter, ς. Hence, in this work, ς was determined using [222]:

$$\varsigma = -\frac{9Km}{2\rho}\frac{\delta l}{l}\frac{1}{\delta Q} \tag{3.8}$$

where δQ is the transferred charge. When ς takes on positive values, the material experiences contractions ($\delta l/l < 0$), and *vice versa*.

3.5.3 *In situ* cantilever bending

The cantilever bending is the most powerful technique to estimate changes in the surface stress of thin films. It exploits a bending moment of a surface stress acting on thin samples. The idea is that any variation of the surface stress between the front and the back surfaces will result in a bending of the sample. The difference of the surface stress can be obtained in absolute numbers by measuring of the bending. In order to consider the elastic properties and the elastic anisotropy of the substrate, the continuum elasticity theory is employed [223–225]. Then the stress difference can be derived from a radius of sample's curvature, R, where the equilibrium curvature of a compliant substrate is $\Delta k = R^{-1}$, when a surface stress acts tangentially at one of its surfaces. The curvature change induced by the surface stress is related to the spacing of the deflected beams by:

$$\Delta k = \frac{\delta d}{d_0}\frac{\cos\alpha}{2L} \quad , \tag{3.9}$$

where δd is the shift in the beam spacing from the initial spacing, d_0, due to the stress-induced curvature, L is the distance from the specimen to the camera, and α is the angle between the beam array and the sample normal. The resolution of the setup is $\Delta k = 4 \times 10^{-6}$ m^{-1}, meaning that the curvature changes with a radius up to 250 km can be reliably detected [226].

Then the surface stress is proportional to the measured spacing of the deflected beams via the generalized and used in experiment the Stoney's equation [227, 228]:

$$\delta\sigma = \frac{\delta d}{d_0}\frac{M_s h_s^2}{12L}\cos\alpha \quad , \tag{3.10}$$

where M_s is the biaxial modulus of the substrate, h_s is the substrate thickness. Note: $\delta\sigma$ is the generalized stress governed by the processes in the film and not at the surface as δf.

In this thesis, the setup is combined with a custom-made electrochemical cell in electrolyte environment. The electrodes, electrolyte, and potential range were the same as those for the dilatometry experiments on the SAM-modified materials (Section 3.5.2). The cantilever served as a WE and responded to the applied electric potential. The rectangular WE was clamped along its width to a sample manipulator. The setup is connected with a multi-beam optical stress sensor (MOS) system in order to determine with high accuracy any deflection of the cantilever (curvature, Δk) during the measurement optically by monitoring the deflection of parallel beams of light (Figure 3.9).

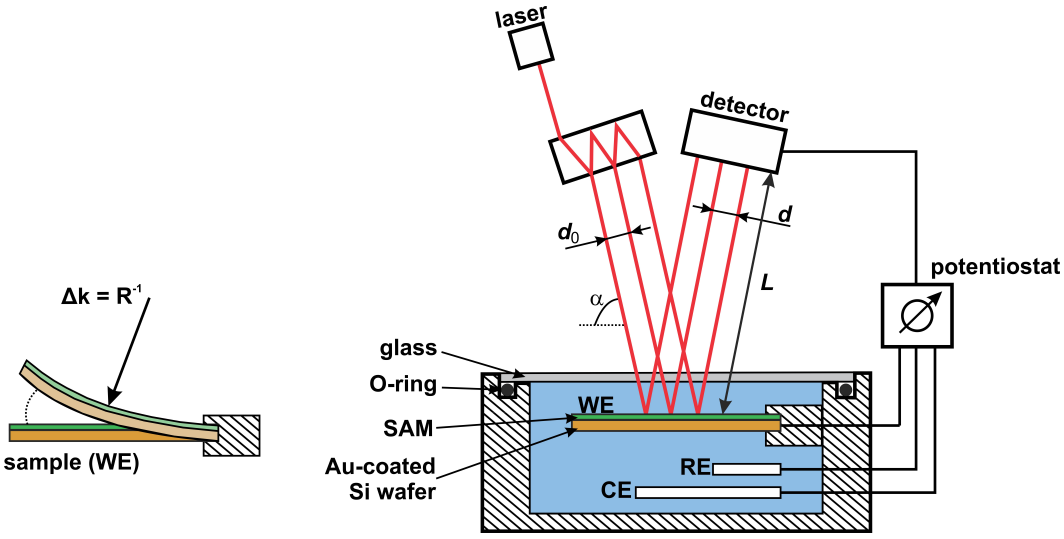

Figure 3.9: *In situ* cantilever bending setup combined with a polytetrafluoroethylene electrochemical cell and sealed with an optical transparent glass slide and a viton O-ring. The cantilever working electrode (WE), made from silicon coated by Au with a Fc-SAM on top, the homemade Ag/AgCl reference electrode (RE) and the carbon cloth counter electrode (CE) are immersed in electrolyte. The electrodes are connected to a potentiostat. A series of laser beams transmits through the glass slide and electrolyte, reflecting off the top side of the wafer before reaching the detector. In this setup, L represents the distance between the wafer and the detector, α denotes the angle between the incident laser beams and the surface normal, and d indicates the distance between the individual laser beams. The schematics is drawn after [226].

In this work, the method was employed to investigate the effect of the redox-reactions of Fc-SAM formed on Au-coated Si cantilevers on surface stress changes.

Taking into account the transferred charge density recorded by the potentiostat, δq, it is possible to evaluate the net experimental stress-charge response (stress-charge coupling coefficient), ς, via:

$$\varsigma = \frac{\delta\sigma}{\delta q} \quad . \tag{3.11}$$

The details on the setup can be found in [228].

3.5.4 Mechanical testing machine

In situ mechanical compression tests were carried out in air and electrolyte on np samples in a testing device Zwick Z010 TN (Figure 3.10). The samples were crack-free that allowed its deformation up to high compression strains. An engineering strain rate was 10^{-4} s^{-1} for all samples under this work. The test device was controlled by a software testXpert II. The laserXtens system was used to record displacements during the compression. The load cells were 0.5 kN (plasticity tests) and 2.5 kN (predeformation for DMA tests).

A plastic deformation was carried out in two modes. The first method is a continuous deformation. The continuous compression mode was applied to prestrain np-Au

sample with L = 40 nm samples in air (Figure 3.10a). The samples were deformed to 10, 20, 30, 40, 50, 60, and 70 % strain. The samples were later measured in the DMA setup to evaluate the effect of prestrain on the effective elastic response of the np-Au in electrolyte (Section 3.5.5).

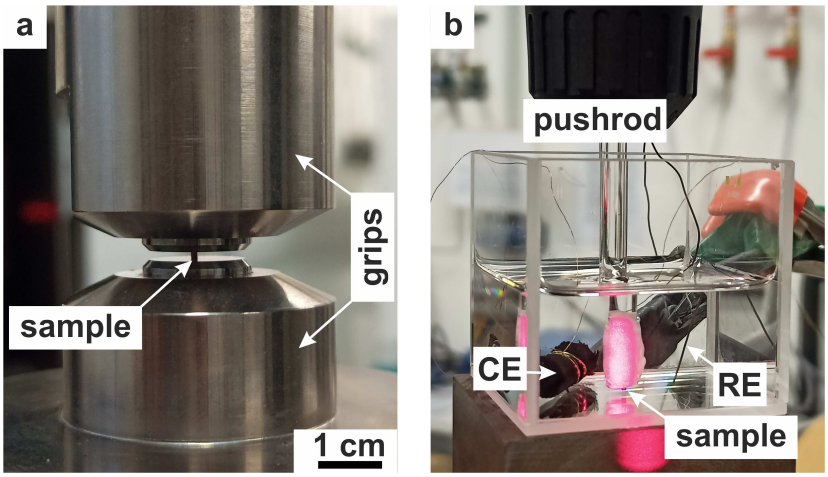

Figure 3.10: *In situ* mechanical compression setup in (a) air and (b) electrolyte in three-electrode cell connected to a potentiostat at the engineering strain rate 10^{-4} s^{-1}. The sample is the working electrode (WE), the carbon cloth is the counter electrode (CE), and the home-made Ag/AgCl is the reference electrode (RE). The gold plate was glued to the quartz pushrod to ensure a good electric contact with the WE. The compression was carried out in an aqueous solution of $HClO_4$.

The second mode is loading/unloading cycles. The latter allows increasing the applied force on the sample and then unloading it till the force reaches the minimum value of 0.5 N, and repeat the cycle with a certain strain step. This approach allows determination of the Young's modulus [229] at different deformation states.

3.5.5 *In situ* dynamic mechanical analysis

A contribution of the surface excess elasticity to the effective elastic behavior of np hybrids were studied *in situ* in a dynamic mechanical analyzer (DMA/SDTA861e, METTLER TOLEDO) in $HClO_4$ aqueous electrolyte under the applied voltage. The potential was controlled via a potentiostat (PGSTAT302N, Metrohm). An electrode charge was calculated by the current integration. The device and the electrochemical cell are displayed in Figure 3.11. The dimensions of the electrodes were smaller than for other experiments under this work due to the configuration of the DMA sample holder.

Before a DMA experiment, the sample was fixed at a constant static force (2.5 ± 0.5 N) while the electric contact was checked. Mechanical oscillations of a predefined frequency (1 Hz) were then applied to the sample with a certain dynamic force (1.0 ± 0.5 N) and displacement amplitude (8.0 ± 1.0 µm). The applied forces were adjusted for np-Au samples tested in the DMA after the predeformation (Section 3.5.4). This was necessary to reach the displacement amplitude of at least 5 µm, in order to maximize the signal-to-noise ratio.

A compliance of the setup was determined using a flat steel sample. The stiffness

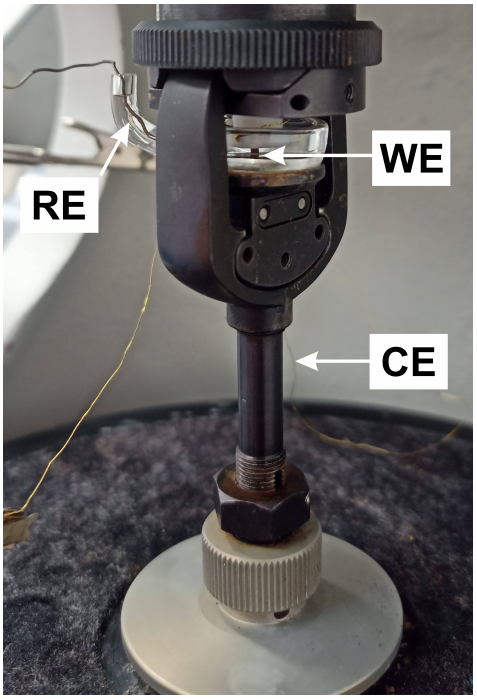

Figure 3.11: *In situ* DMA setup for measurements in electrolyte in three-electrode cell connected to a potentiostat. The sample is the working electrode (WE), the carbon cloth is the counter electrode (CE, not shown), and the homemade Ag/AgCl is the reference electrode (RE). A gold plate was glued to the quartz pushrod to ensure the electric contact with the WE. The compression measurements were carried out in an aqueous electrolyte of $HClO_4$.

of 5.38 MN m^{-1} was taken into account during a signal correction. A typical stiffness of a np sample in this work was at least 5 times lower than the setup's one.

The DMA setup allows recording of such parameters like the storage modulus, Y', the loss modulus, Y'', and strain, ε, upon the measurement.

The dynamic stress (σ) and strain (ε) of a viscoelastic material in DMA can be mathematically presented as functions of time:

$$\sigma(t) = \sigma_0 \sin(\omega t) \tag{3.12}$$

$$\varepsilon(t) = \varepsilon_0 \sin(\omega t + \delta) \tag{3.13}$$

where ω is the applied frequency, ε_0 is the maximum actuation strain, and δ is the phase shift between the stress and strain [230].

Under uniaxial compression, with respect to the Hooke's law, the input stress and output strain can be given as follows:

$$\sigma(t) = Y^*(\omega)\varepsilon(t) \tag{3.14}$$

where Y^* is the complex dynamic Young's modulus of a material defined as:

$$Y^*(\omega) = \frac{\sigma(t)}{\varepsilon(t)} = Y'(\omega) + iY''(\omega) \tag{3.15}$$

where $Y^{'}$ is referred to the storage modulus (real or elastic part) featuring the energy stored per cycle within the sample; and $Y^{''}$ is the loss modulus (imaginary or viscous part) which represents dissipated energy within the sample. Thus, the relationship between the complex (Y^{*}), storage ($Y^{'}$), and loss ($Y^{''}$) moduli can be obtain as:

$$Y^{*}(\omega) = \frac{\sigma_0}{\varepsilon_0}\cos\delta + \mathrm{i}\frac{\sigma_0}{\varepsilon_0}\sin\delta \tag{3.16}$$

The loss factor (or damping factor), $\tan\delta$, indicates the relative degree of energy dissipation or damping of the material and can be calculated via $\tan\delta = Y'/Y''$.

Chapter 4

Results

This Chapter includes three sections. They are devoted to the structural characterization (Section 4.1) and to the mechanical properties of the surface-modified nanoporous gold structures: A mechanical actuation (Section 4.2) and elastic properties (Section 4.3).

4.1 Microstructural investigations

Bicontinuous crack-free mm-sized nanoporous networks were fabricated by electrochemical dealloying. Scanning electron microscopy revealed the microstructural features and the mean ligament size, L, over the cross-sectional areas of as-prepared and post-dealloying processed (coarsened) np-Au (Figure 4.1a), and hnp-Au (Figure 4.2a) samples. The notches in the subfigures originate from the scalpel blade used to cut the samples. By means discussed in Chapter 3 (Section 3.3.1, Section 3.3.2, and Section 3.5.1), geometrical dimensions, sample mass, electrochemically active surface area, A_{ECSA}, relative density, φ_{Au}, and mass-specific surface area, α_{m}, were evaluated.

In this thesis, np-Au will be discussed with a ligament size, L, from 40 nm to 1 µm and relative density, φ_{Au}, varying from 0.27 ± 0.01 to 0.41 ± 0.01 of "sufficiently" self-similar structures [231, 232] as displayed in Figure 4.1b-i. The details on the estimation of L are given in Section 3.5.1. The mass-specific surface area, α_{m}, was from 4.68 $\mathrm{m^2\ g^{-1}}$ (L = 40 nm) to 0.40 $\mathrm{m^2\ g^{-1}}$ (L = 1 µm) in np-Au. Residual Ag content was less than 3 at. % in all np samples under the study as revealed by energy-dispersive x-ray spectroscopy. The details can be found in Section 3.3.1.

The hnp-Au samples will be discussed with the characteristic sizes of L_1 = 120 nm (upper level) and L_2 = 20 nm (lower level) as depicted in Figure 4.2b-d. The ligament spacing of the upper level, $\tilde{L}^U$, was 260 nm (according to the SEM and TEM data) or 324 nm with respect to $\tilde{L} = (2.7 \pm 0.1)L_{\mathrm{SEM}}$ given by Riedel *et al.* in [233]. The ligament spacing of the lower level, $\tilde{L}^L$, was 48 ± 6 nm versus 54 nm predicted. The Au solid fraction, φ, was 0.12 ± 0.01. The solid fraction at the lower hierarchy level was 0.30 ± 0.01. The solid fraction at the upper hierarchy level was $\varphi_2 = \varphi/\varphi_1 \approx 0.40$ [15]. The mass-specific surface area, α_{m}, was 9.17 $\mathrm{m^2\ g^{-1}}$. For details the reader is referred to Section 3.3.2. The samples characteristics are summarized in Table 4.1.

For the sake of conciseness, hnp-Au samples will be compared with np-Au mainly with L = 120 nm and additionally with np-Au L = 40 nm in the course of this work.

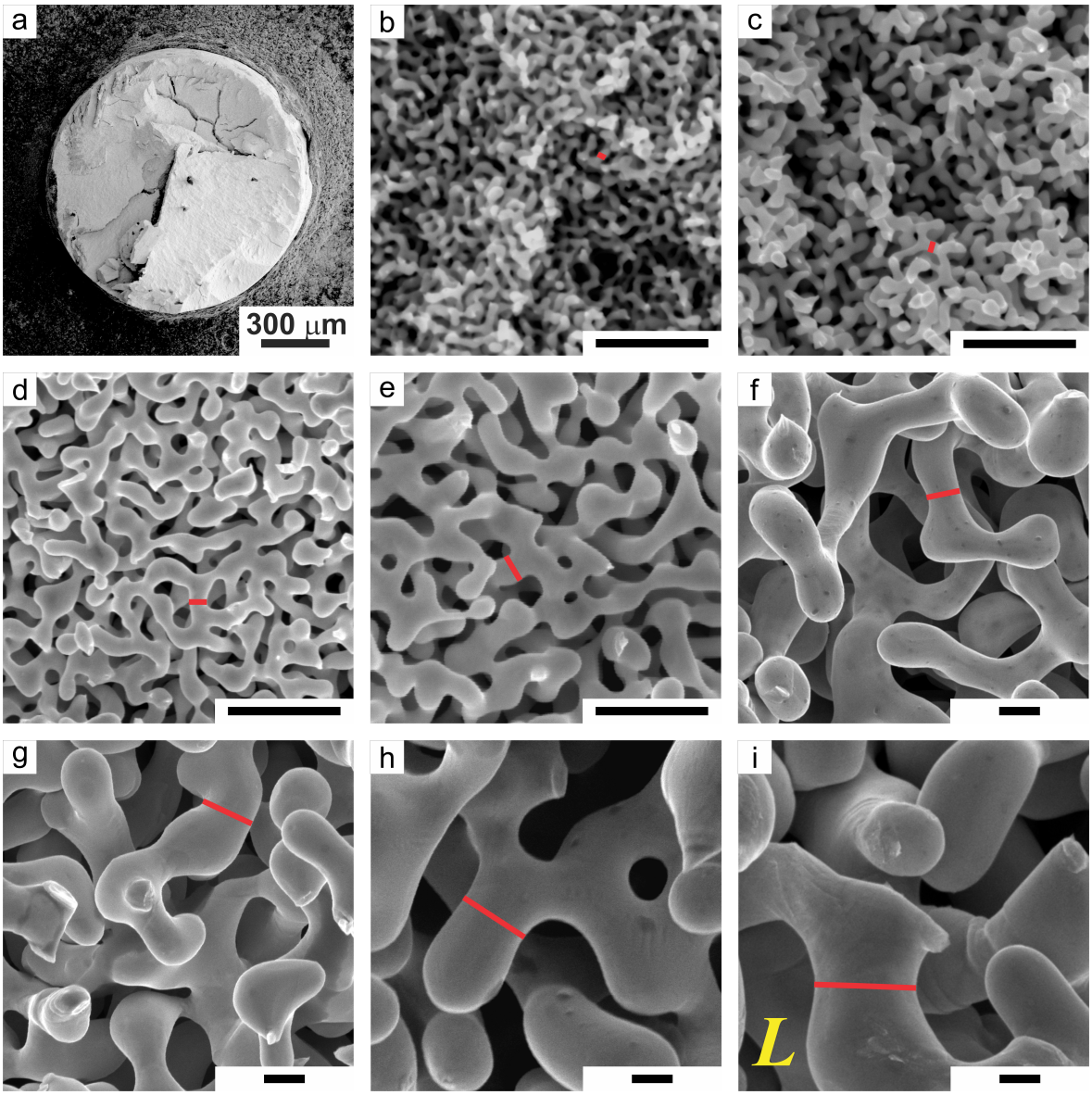

Figure 4.1: Microstructure of nanoporous gold with a ligament size, L: (a) cross-section, (b) as-prepared np-Au with L = 40 nm; (c) coarsened np-Au with L = 80 nm, (d) L = 120 nm, (e) L = 200 nm, (f) L = 400 nm, (g) L = 600 nm, (h) L = 800 nm, (i) L = 1000 nm. The scale bar (black line) in (b)-(i) is 500 nm. The red marks correspond to L.

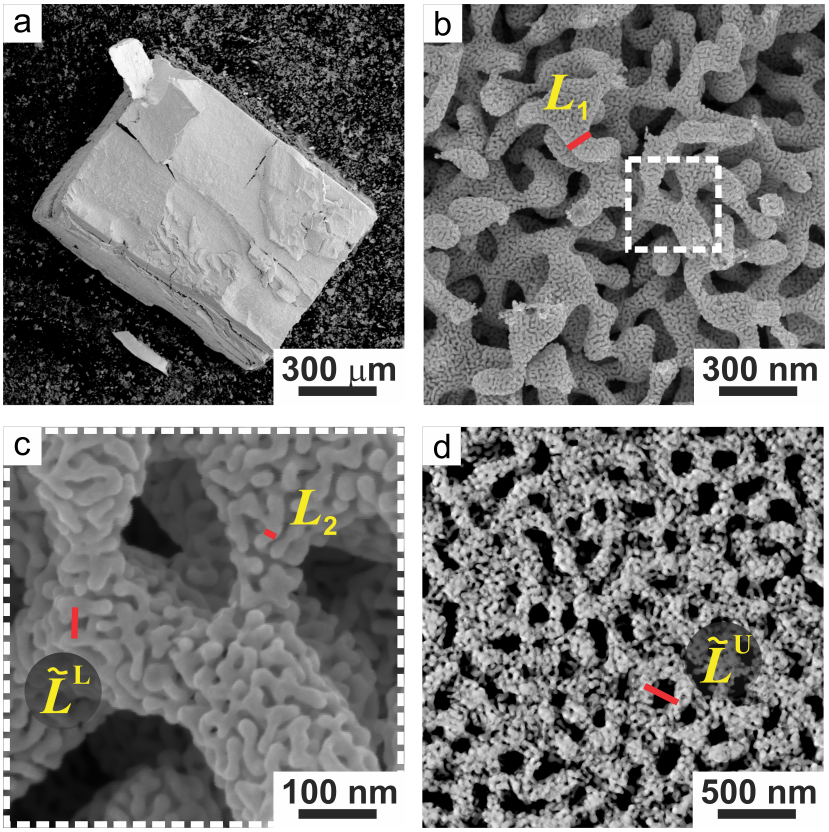

Figure 4.2: Microstructure of hnp-Au with ligaments sizes L_1 = 120 nm (upper level) and L_2 = 20 nm (lower level). The SEM images of (a) the general overview of the fracture surface, (b) the upper level ligament size, L_1, (c) the lower level ligament size, L_2, and the lower level ligament spacing, $\tilde{L}^{\mathrm{L}}$. (d) A TEM image of hnp-Au indicating the upper level ligament spacing, $\tilde{L}^{\mathrm{U}}$.

Table 4.1: A summary of characteristics of np-Au and hnp-Au samples synthesized by electrochemical dealloying and modified by post-dealloying processing. L - the ligament size, A_{ECSA} - the electrochemically active surface area, φ_{Au} - the Au solid fraction, and α_{m} - the mass-specific surface area.

	L, [nm]	A_{ECSA}, [cm^2]	φ_{Au}, [-]	α_{m}, [m^2 g^{-1}]
np-Au	40 ± 5	290 ± 15	0.27 ± 0.01	4.68 ± 0.1
	80 ± 18	150 ± 12	0.26 ± 0.01	4.17 ± 0.1
	120 ± 30	110 ± 10	0.30 ± 0.01	3.06 ± 0.1
	200 ± 32	80 ± 10	0.31 ± 0.01	1.74 ± 0.1
	400 ± 46	62 ± 8	0.33 ± 0.01	1.27 ± 0.1
	600 ± 55	40 ± 5	0.35 ± 0.01	0.70 ± 0.1
	800 ± 82	27 ± 5	0.37 ± 0.01	0.58 ± 0.1
	1000 ± 120	15 ± 4	0.41 ± 0.01	0.40 ± 0.1
hnp-Au	L_1 = 120 ± 30 L_2 = 20 ± 5	55 ± 10	0.12 ± 0.01	9.17 ± 0.1

4.2 Mechanical actuation and electrocapillary coupling in the hybrids

Earlier studies [12, 35, 64] found that the recoverable changes in strain of a non-modified ("bare") np-Au are linked to the electrocapillarity of Au surfaces. The surface state of gold (electrode) can be controlled by the applied electric potential leading to polarization of the electrode surface and the generation of surface stress changes. These changes in the stress must be compensated by a stress of the opposite sign in the subjacent bulk solid skeleton resulting in deformation of the Au nanoscale ligaments in the network. Such deformation of ligaments results in the observable macroscopic actuation strain [12, 206]. The response of the surface stress, f, can be measured with respect to the applied electric potential, E, and thus charge density, q, via the electrocapillary coupling coefficient, ς (Eq. 2.9). So far, several attempts have been made to estimate the underlying ς for capacitive processes in $HClO_4$ aqueous electrolyte for the planar Au (-2.00 ± 0.1 V [228], -1.83 V [234], and -2 ... -2.4 V [235]) and np-Au (-0.60 and -1.70 V [18]). The coupling coefficients ς for adsorption of oxygen on the planar Au (+0.11 ± 0.01 V and +0.14 ± 0.02 V [165], -1.6 V via DFT [236]) and on np-Au (+2.00 V [18]) were estimated as well.

In this thesis, the investigation is devoted to the study of the stress-charge coupling in the adsorbate-covered hnp-Au and np-Au. This section will delve into three parts: the actuation response of the "clean" (capacitively charged) and oxidized np-Au and hnp-Au (Section 4.2.1), the redox-active SAM-induced surface stress in planar Au (Section 4.2.2), and the actuation in the electroactive SAM-modified np hybrids (Section 4.2.3).

4.2.1 Surface oxide effect on actuation response of np-Au and hnp-Au

The dilatation experiments were carried out independently for the capacitive charging and the OH-electrosorption processes for a set of 10 samples under the study.

4.2.1.1 Actuation in np-Au and hnp-Au with clean surface as a reference

In situ dilatometry experiments were carried out on the capacitively charged/discharged np-Au and hnp-Au in 1 M $HClO_4$ while the electric potential was tuned between E_{SHE} = 0.015 V and E_{SHE} = 0.815 V (Section 3.2.2) to determine the electrocapillary coupling parameter, ς, in a reference ("clean") Au surface state.

The CV responses of np-Au and hnp-Au under the study are given in Figure 4.3a. The macroscopic dimensional changes, $\delta l/l$, of np-Au and hnp-Au upon the capacitive charging/discharging are plotted as a function of E_{SHE} in Figure 4.3b. The variations of $\delta l/l$ reached up to 1.3×10^{-4} in hnp-Au, whereas in np-Au (L = 120 nm) were up to 0.8×10^{-4}. The increase in the macroscopic strain response in hnp-Au comparing with np-Au can be attributed to the more curved interface of the hierarchical microstructure as the surface-induced deformation is changed by the geometry of the pores and the Au

solid phase [206]. An enhanced actuation of 2.2×10^{-4} was found in np-Au (L = 40 nm); it will be used below for a comparison with the theory proposed in [206].

Figure 4.3c summarizes the experimental findings of the macroscopic dimensional change, $\delta l/l$, of porous solid bodies with area per volume of a solid, A/V, along with the theoretical prediction reported in [206] and the numerical data presented in [237]. The experimental data (symbols) is in excellent agreement with the trend for the bicontinuous structures (green dashed line) in [237], and in line with [206] confirming that the strain of the bicontinuous np-Au is enhanced relative to the granular porous material (Eq. 3.6), by the factor of 5.5. This factor must be taken into account when calculating the surface stress variations in nanoporous bicontinuous materials using Eq. 3.7.

To further present the dilatometry results of the strain variations with the corresponding charge, the background (irreversible part) of the transferred charge, Q, was subtracted before the calculation of the superficial charge density, δq. The surface stress changes were calculated via Eq. 3.7. The surface stress variations, δf, as a function of the transferred charge density, δq, are plotted in Figure 4.3d. The reversible values of compressive δf up to -0.86 N m^{-1} are consistent with δq of 0.162 C m^{-2} in hnp-Au. Similarly, δf of -0.77 N m^{-1} with δq of 0.360 C m^{-2} was observed in np-Au (L = 120 nm). The electrocapillary coupling, ς, can be determined as $\varsigma = \delta f/\delta q$, giving values of -4.55 V for hnp-Au and -1.71 V in np-Au (L = 120 nm).

The parameter ς can be estimated independently of A_{ECSA} via Eq. 3.8, so that the uncertainty in the surface area does not propagate into the computation of ς. The equation includes the material constants and the variations of the macroscopic length changes, $\delta l/l$, versus the transferred charge, δQ (Figure 4.3e). The positive strain responses observed herein give negative values of coupling ς of -3.12 ± 0.05 V in hnp-Au and -3.11 ± 0.05 V in np-Au (L = 120 nm). These parameters are in the same order as the previously found data for a clean surface state in the planar Au (-2.00 ± 0.1 V [228], -1.83 V [234], and -2 ... -2.4 V [235]) and in np-Au (-0.60 and -1.70 V [18]). The discrepancy in the findings may be caused by the sample fabrication and the test conditions. Besides, the authors of [18] highlighted that Eq. 3.8 may overestimate the magnitude of ς. Thus, we can just qualitatively compare the findings. The presented results are in good agreement with the negative ς reported earlier for the capacitively charged np-Au [18], porous nanocrystalline Pd [222], and the planar Au surfaces [228].

4.2.1.2 OH-electrosorption on Au surface

In this Section, *in situ* dilatometry was employed to determine the strain response of hnp-Au with $L_{1,2}$ = 120/20 nm and compare it to np-Au with L = 120 nm during the OH-electrosorption. The potential was tuned between E_{SHE} = 0.815 V and E_{SHE} = 1.615 V in 1 M $HClO_4$ at a scan rate of 5 mV s^{-1}. The corresponding CVs are presented in Figure 4.4a.

The reproducible length changes, $\delta l/l$, were observed in the np-Au/OH and hnp-Au/OH hybrids with expansion upon the anodic sweeps and contraction under the reverse scans. Figures 4.4b compares the macroscopic dimensional change, $\delta l/l$, in hnp-Au and np-Au with L = 120 nm with respect to the electrode potential, E_{SHE}. The graphs of $\delta l/l$ versus E_{SHE} exhibit positive slopes. The peak-to-peak strain am-

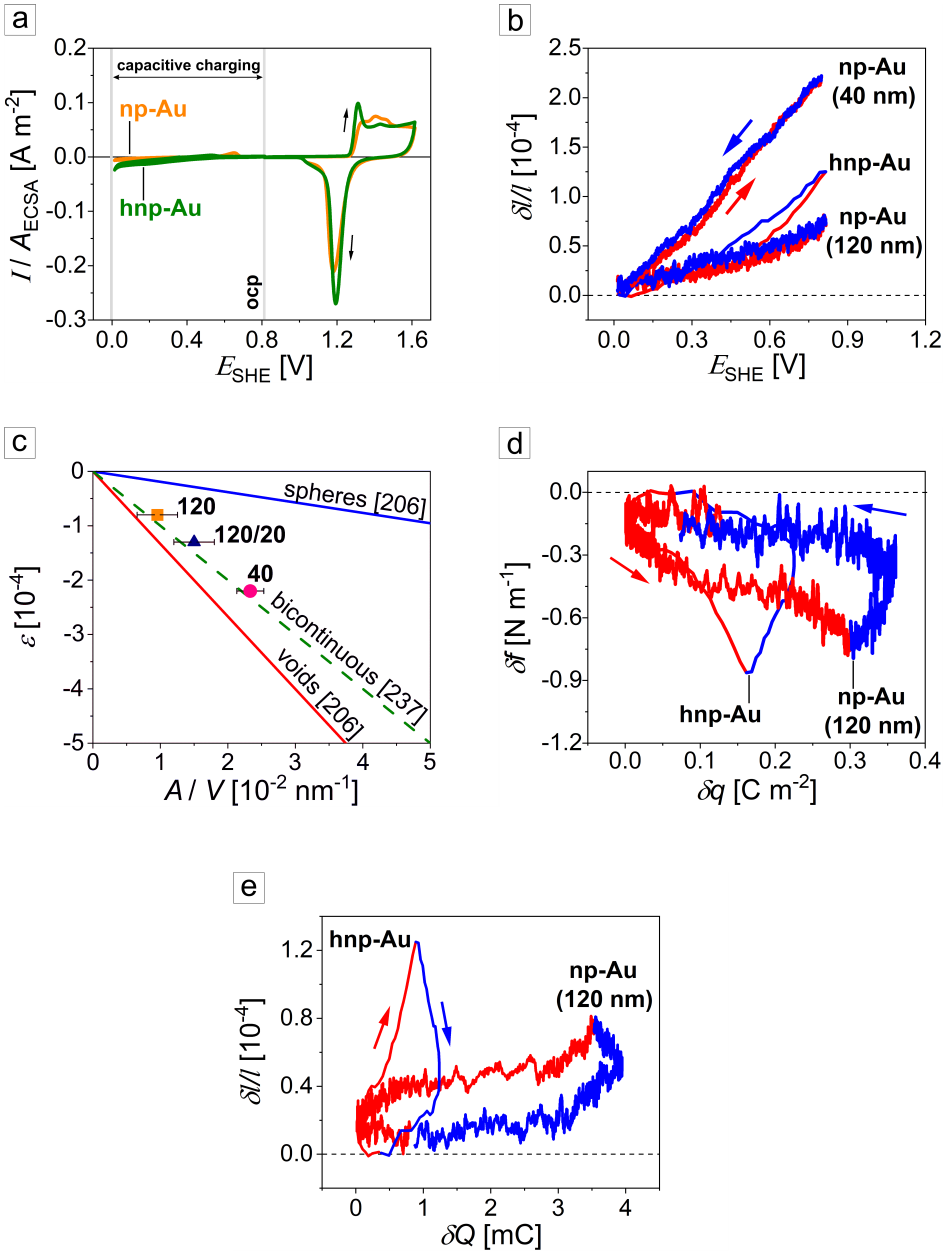

Figure 4.3: (a) Typical CV responses of np-Au with L = 120 nm (orange) and hnp-Au with $L_{1,2}$ = 120/20 nm (green) in 1 M $HClO_4$ at a potential scan rate of 5 mV s^{-1}. The capacitive charging/discharging region is marked by grey solid lines. The open circuit potential (ocp) is at the potential of E_{SHE} = 0.815 V. (b) Variations in the macroscopic dimensional change, $\delta l/l$, as a function of E_{SHE}. (c) Changes in $\delta l/l$ of porous solid bodies with area per volume of a solid, A/V. The experimental findings are given in symbols for the capacitively discharged np-Au with L = 40 nm (pink circle) and L = 120 nm (orange square), and hnp-Au with $L_{1,2}$ = 120/20 nm (navy triangle) with respect to their A_{ECSA}. The deviation bars of A_{ECSA}/V were estimated for 5 samples of each structural type. The solid lines refer to the theory result for granular porous Au assembled from spheres (blue line) and void lattice (red line) [206]. The numerical data for the bicontinuous porous gold reported in [237] is given by the green dashed line as the straight-line best fit. (d) Apparent surface stress, δf, changes as a function of the transferred charge density, δq. δf was calculated based on the experimental $\delta l/l$ via Eq. 3.7. (e) $\delta l/l$ vs. the transferred charge, δQ. The red and blue arrows in (b), (d), and (e) represent anodic and cathodic potential scans, respectively.

plitudes, $(\delta l/l)_{\max}$, were $(\delta l/l)_{\max}$ = 4.7 × 10^{-4} in hnp-Au and $(\delta l/l)_{\max}$ = 1.3 × 10^{-4} np-Au with L = 120 nm. The actuation amplitude of np-Au with L = 40 nm was ($(\delta l/l)_{\max}$ = 10.0 × 10^{-4}) (not shown).

Employing Eq. 3.7, the surface stress changes, δf, of -3.20 ± 0.05 N m^{-1} were found in np-Au and -7.52 ± 0.08 N m^{-1} in hnp-Au during the OH-electrosorption process, respectively (Figure 4.4c). The variations of the transferred charge, δQ, as a function of E_{SHE} are shown in Figure 4.4d. The net charge transferred upon oxidation of the np hybrids reached up to 30 mC in the hnp-Au/OH and 57 mC in the np-Au (120 nm)/OH.

The electrocapillary coupling, ς, via $\varsigma = \delta f/\delta q$, took values of -3.00 V for hnp-Au and -0.27 V in np-Au. To avoid the uncertainty of the specific surface area estimation, the variations of $\delta l/l$ vs. the transferred charge, δQ (Figure 4.4e), were used in Eq. 3.8. The surface stress-charge coupling parameters, ς, were found to be -0.43 ± 0.04 V (hnp-Au) and -0.37 ± 0.03 V (np-Au). The considered approaches in the determination of ς provided the negative values. The results on ς during the OH-electrosorption process have the same sign as the capacitively charged np-Au (Section 4.2.1.1). The given above predictions of ς are qualitative.

According to Eq. 3.2, the OH surface coverage, Θ_{OH}, of np-Au is 1.0 ± 0.1 ML and 1.3 ± 0.1 ML in hnp-Au. The larger Θ_{OH} results in higher adsorbate-induced surface stresses as the interactions between the adsorbed molecules and the adsorbate-substrate (OH-Au) become more pronounced. The phenomenon of the increased macroscopic length changes may be addressed to the differences in the curvature and roughness of the interfaces, affecting the electrosorption of the OH-species on Au surfaces that, in turn, contribute to the surface stress variations.

Additionally, the impact of the potential sweep rate on the actuation response in the hybrids will be presented. Figure 4.4f summarizes the peak-to-peak amplitudes of the macroscopic length variations, $(\delta l/l)_{\max}$, as a function of the scan rate, v, upon the OH electrosorption on np-Au and hnp-Au. The similar trends were observed in both structure types. The variations of $(\delta l/l)_{\max}$ = 5.2 × 10^{-4} (hnp-Au) and $(\delta l/l)_{\max}$ = 1.7 × 10^{-4} (np-Au) were achieved at the slowest scan rate, v, of 2 mV s^{-1} under the study. The actuation amplitude decreases by half when the scan rate is increased to 10 mV s^{-1}. Further increase in the scan rate up to 100 mV s^{-1} had a minimal impact on the strain response. At higher scan rates, mass transport limitations become significant because it's harder for ions to diffuse to the electrode surface quickly enough to maintain the charge balance in the electric double layer. The difference between the steep slope at very small scan rates and the much more shallow slope at larger scan rates may be governed by the superposition of the slow oxygen-species diffusion and the fast quasi diffusion-free Grotthuss proton-conduction for the surface capacitive charging [238].

4.2.2 Redox-active SAM-induced film stress in planar Au

As it was already mentioned in Section 3.5.3, the cantilever bending provides the most widespread and direct experimental approach towards quantitative surface stress measurements. Eq. 3.10 embodies the trend of cantilevers to bend when surface stress, σ, is varied, for instance due to the capacitive charging of an electrode surface or to adsorption. A relevant example of the application of the cantilever bending technique was briefly presented in Section 2.3.3.4. In Refs. [60, 205] the authors measured a

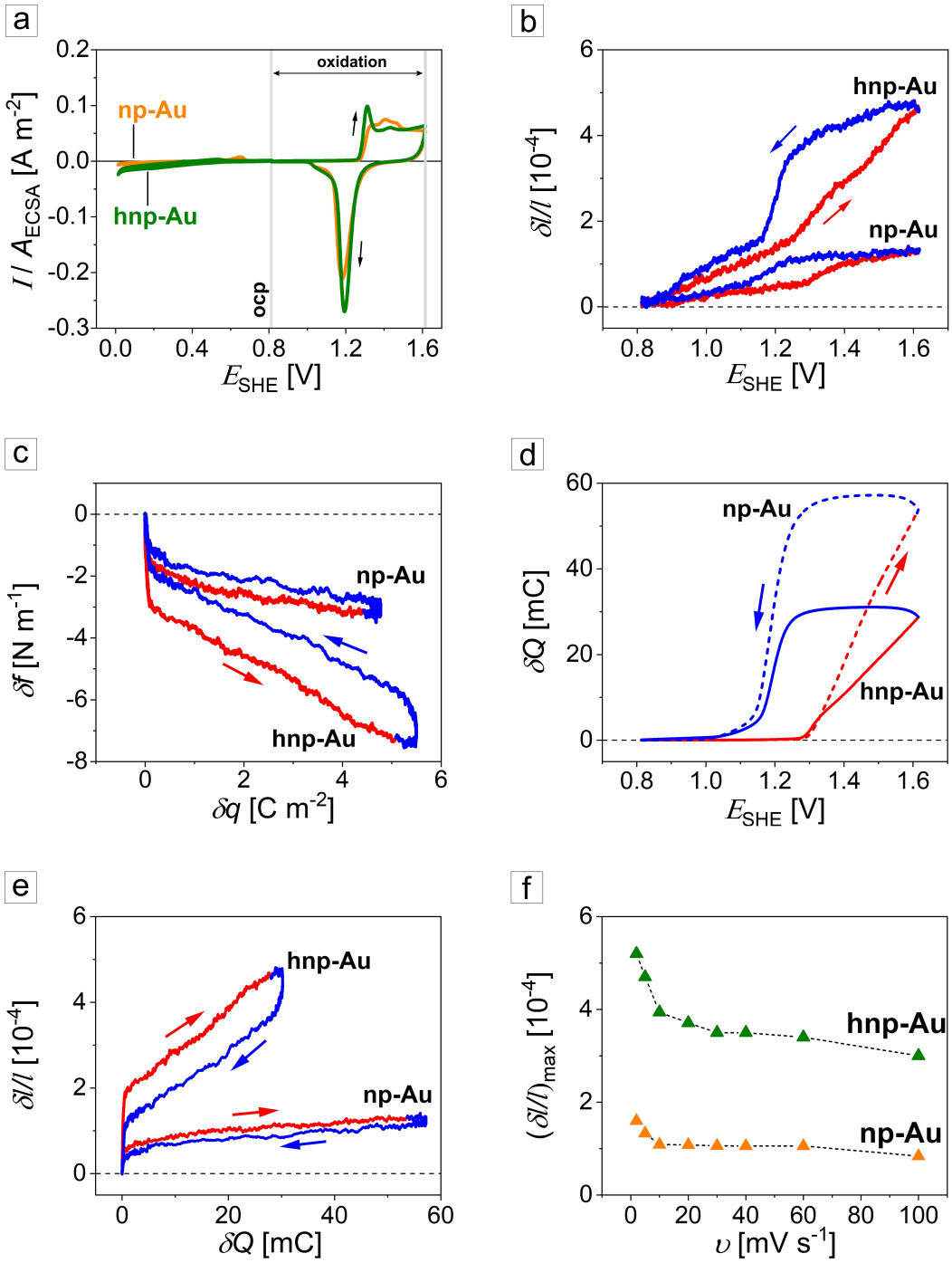

Figure 4.4: The electrochemical characteristics and results of *in situ* dilatometry experiments on np-Au with L = 120 nm and hnp-Au with $L_{1,2}$ = 120/20 nm during the OH-electrosorption in 1 M $HClO_4$ at a potential scan rate of 5 mV s^{-1}.(a) CV responses of np-Au (orange) and hnp-Au (green). (b) Macroscopic dimensional changes, $\delta l/l$, vs. potential, E_{SHE}. (c) Apparent surface stress, δf, variations as a function of the transferred charge density, δq. δf was calculated based on the experimental $\delta l/l$ via Eq. 3.7. (d) The transferred charge, δQ, vs. E_{SHE}. (e) $\delta l/l$ vs. δQ. The red and blue arrows in (b)-(e) represent anodic and cathodic potential scans, respectively. (f) $(\delta l/l)_{max}$ of np-Au (orange symbols) and hnp-Au (green symbols) as a function of a potential scan rate, υ, during the OH-electrosorption in 1 M $HClO_4$ aqueous electrolyte.

deflection of an Au-coated Si microcantilever modified with the electroactive ferrocene-terminated self-assembled monolayer (Fc-SAM) in electrolyte. They reported that the the oxidation of the neutral ferrocene (Fc) to the ferrocenium cation (Fc^+) within the Fc-SAM can generated a surface stress change of a sufficient magnitude to bend the microcantilever.

In this thesis, for a qualitative assessment of the actuation response of the Fc-SAM-modified np-Au (Section 4.2.3.3), we determined the surface stress-charge coupling parameters, ς, of the Fc-SAM on Au-coated µm-thick Si cantilevers as a reference, since ς has not been explicitly determined in the references cited in Section 2.3.3.4. A cyclically varied electrode potential between E_{SHE} = 0.175 V and E_{SHE} = 1.175 V applied to FcC_6- and FcC_{11}-SAM/Au-Si cantilevers allowed observing cantilever's deflections in 0.1 M $HClO_4$ aqueous-based electrolyte. In this case, the surface state of the materials can be electrochemically controlled to precisely measure and evaluate the surface stress change and the stress-charge coupling coefficients.

4.2.2.1 Electrochemical characteristics of electroactive monolayers

The formation of the Fc-SAM on the Au-Si cantilevers was proved by electrochemical means as indicated in the cyclic voltammograms shown in Figure 4.5. The observed CV peaks are related to the standing-up (peaks I and II) and chemisorbed lying-down (peak III) phases of the Fc-SAM. The peak positions are in agreement with the model proposed in [194]. The positions of the peak I during the redox are less shifted in the FcC_{11}-SAM/Au (ΔE_{peak} = 0.015 V) comparing with the FcC_6-SAM/Au (ΔE_{peak} = 0.030 V). The peak shifts and the lying-down phase can be explained by a disorder within the Fc-SAM [195].

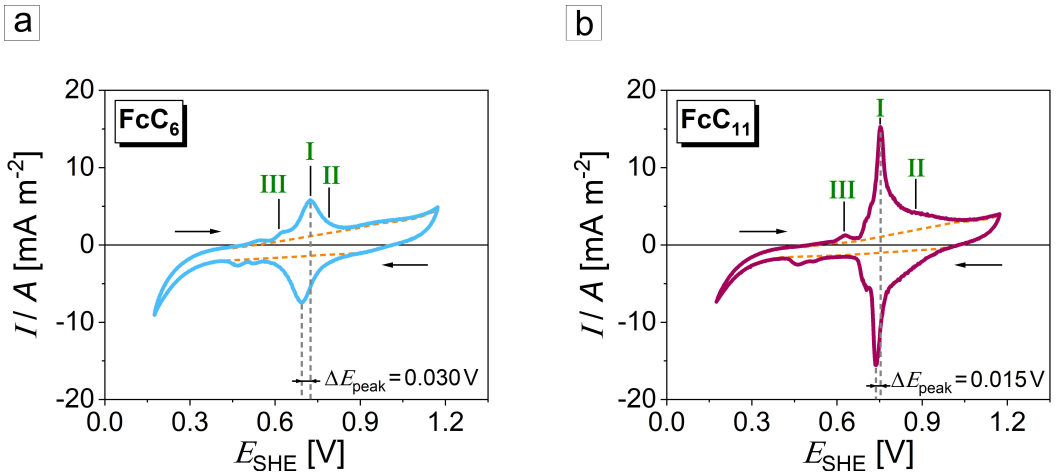

Figure 4.5: The experimental findings of the CV responses (the current density, I/A, vs. the electric potential, E_{SHE}) in (a) the FcC_6- and (b) FcC_{11}-SAM-modified planar Au in 0.1 M $HClO_4$ aqueous electrolyte. The peaks I and II correspond to the standing-up and the peak III denotes the lying-down phases of the Fc-SAM similarly to the model proposed in [194]. The orange dashed lines mark the baselines used to integrate the charge devoted to the oxidation and reduction of the Fc-SAM. The grey dashed lines indicate the peak I shifts during the redox with the corresponding potential difference, ΔE_{peak}.

To determine the charge devoted to the ferrocene-ferrocenium (Fc-Fc^+) transition,

Q_{Fc^+}, it is necessary to subtract the capacitive current. The orange dashed lines in Figure 4.5 indicate the baselines for the integration of the current to evaluate Q_{Fc^+}. In the FcC_6-SAM/Au, Q_{Fc^+} was 33 ± 1 μC, wheres Q_{Fc^+} of 75 ± 1 μC was found in the FcC_{11}-SAM/Au.

The obtained anodic charge, Q_{Fc^+}, was equal to the cathodic charge. Consequently, Q_{Fc^+} was applied in Eq. 3.4 to compute the superficial density of the Fc-terminated molecules, Γ_{Fc^+}, at the Au surface. Γ_{Fc^+} of 2.43 (± 0.10) × 10^{-10} mol cm^{-2} was found in the FcC_{11}-SAM/Au and Γ_{Fc^+} = 1.07 (± 0.10) × 10^{-10} mol cm^{-2} was estimated in the FcC_6-SAM/Au, respectively. With respect to the theoretical value of the superficial density of the Fc-SAM, Γ_{Fc}^{theor}, of 4.5 × 10^{-10} mol cm^{-2} (Section 3.4.2), one can estimate a packing of the monolayer via $\Gamma_{Fc^+}/\Gamma_{Fc}^{theor}$. It yields $\Gamma_{Fc^+}/\Gamma_{Fc}^{theor}$ = 0.24 for the FcC_6-SAM/Au and $\Gamma_{Fc^+}/\Gamma_{Fc}^{theor}$ = 0.54 for the FcC_{11}-SAM/Au, respectively. The values $\Gamma_{Fc^+}/\Gamma_{Fc}^{theor}$ below 1 point to the disorder within the electroactive monolayer [60, 170].

Using Eq. 3.5, the relatively high coverage of the Fc-SAM, Θ_{Fc}, was found in the FcC_{11}-SAM/Au (Θ_{Fc} = 0.11 ± 0.01 ML) comparing with the FcC_6-SAM/Au (Θ_{Fc} = 0.05 ± 0.01 ML). The results of this work on Θ_{Fc} and Γ_{Fc} are lower than the ones presented for the Fc-SAM-modified microcantilevers in [60]. The discrepancy can be explained by the sample fabrication procedure and the experimental conditions.

4.2.2.2 Surface stress evaluation via cantilever bending experiments

Figure 4.6a shows the main results of the *in situ* cantilever bending experiments in electrolyte. The changes of curvatures, Δk, in the Fc-SAM-modified Au cantilevers under the control of the applied electric potential within one CV cycle is highlighted in yellow. The oxidation of the samples resulted in the changes of their curvature of 0.12 km^{-1} in the FcC_6-SAM/Au and 0.19 km^{-1} in the FcC_{11}-SAM/Au, respectively. The variations of the curvatures, Δk (maximum value defined as 100 %), within the single potential cycle are given versus E_{SHE} for the FcC_6-SAM/Au (Figure 4.6b) and FcC_{11}-SAM/Au (Figure 4.6d). To compare the deflections of the cantilevers with the ferroceniums (Fc^+) involved in the oxidation, we employ the fractional coverage, Φ_{Fc^+}. The maximum amount of the electrogenerated Fc^+ is given by Φ_{Fc^+} = 1.0 equivalent to the net Q_{Fc^+}. Figure 4.6c and Figure 4.6e show the plots of Φ_{Fc^+} vs. E_{SHE} in the FcC_6-SAM/Au and the FcC_{11}-SAM/Au, respectively. This approach of the Fc^+ distribution as a function of Φ_{Fc^+} provides an approximate idea of the extent of neighboring Fc^+ interactions with the applied potential and is linked to the electron transfer across the Fc-SAM/electrolyte interface [60].

Let us consider the anodic scan in the FcC_6-SAM/Au. The variations of Δk can be divided into two segments (Figure 4.6b). The first one is between E_{SHE} = 0.175 V and E_{SHE} = 0.700 V, Δk exhibited the linear increase and reached up to 30 %. According to the CV (Figure 4.5a), the Fc-SAM is oxidized up to the appearance of the peak I within the potential window. Interestingly, the cantilever experienced the deflection at these potentials, whereas Φ_{Fc^+} was below 0.05 (Figure 4.6c). The result can be explained by the low coverage of Θ_{Fc} pointing to the disorder within the monolayer and the impact of the capacitive processes allowing the electrolyte to approach the Au surface. In this case, the monolayer can be considered as "porous", where the ability of the Fc-SAM to block counterions is inhibited [183]. Such behavior of the Fc-SAM/cantilevers was not observed in [60], that can be explained by the increased Θ_{Fc} comparing with the

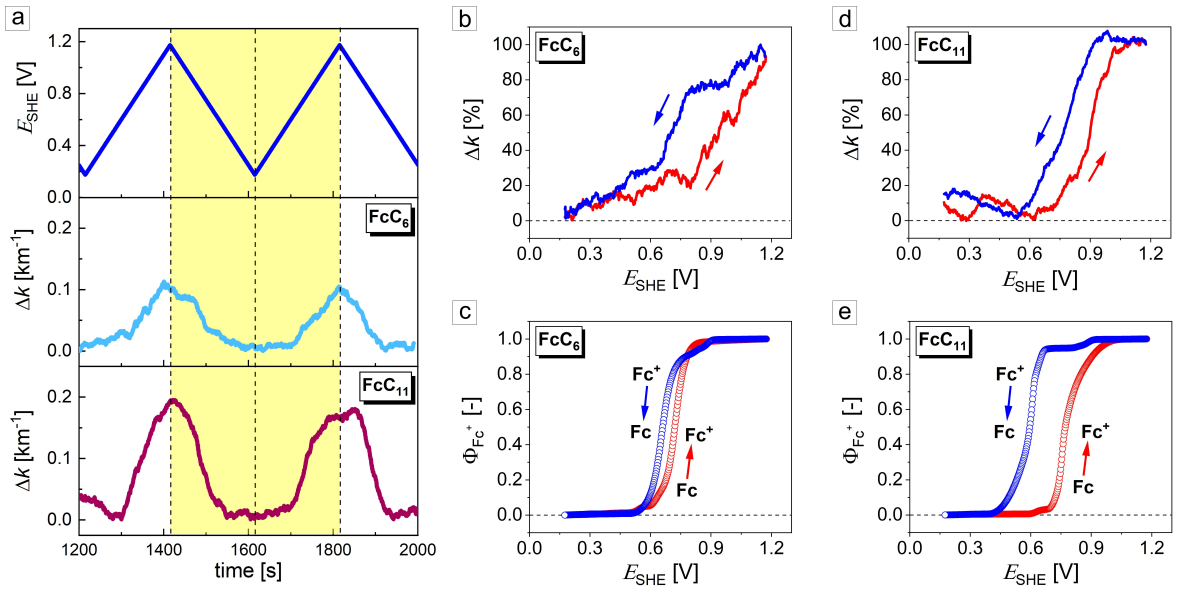

Figure 4.6: (a) Results of the *in situ* cantilever bending measurements in 0.1 M $HClO_4$ aqueous electrolyte. One potential cycle highlighted by yellow color illustrates the changes of curvatures, Δk, in the Fc-SAM-modified planar Au as a function of time and the potential, E_{SHE}. (b) The cantilever deflection, Δk (in %), vs. E_{SHE} in the FcC_6-SAM/planar Au. (c) The fractional coverage of ferrocenium, Φ_{Fc^+}, vs. E_{SHE} in the FcC_6-SAM/planar Au. (d) Δk vs. E_{SHE} in the FcC_{11}-SAM/planar Au. (e) Φ_{Fc^+} vs. E_{SHE} in the FcC_{11}-SAM/planar Au. The arrows mark oxidation (red) and reduction (blue) potential scan directions in (b)-(e).

presented ones in this thesis.

The steeper slope of Δk vs. E_{SHE} was observed at $E_{SHE} > 0.700$ V. Under these potentials, the Fc is oxidized to Fc^+ and the peak II is appeared at the CV. While Φ_{Fc^+} exhibited the rapid increase starting at E_{SHE} = 0.600 V and reached its maximum at E_{SHE} = 0.750 V (Figure 4.6b). Upon the cathodic scan, the similar behavior was found with a shift between the linear segments from E_{SHE} = 0.700 V to E_{SHE} = 0.650 V. The reduction of Fc^+ to Fc started at $\Phi_{Fc^+} > 0.90$ and E_{SHE} = 0.900 V and reached its minimum of $\Phi_{Fc^+} < 0.02$ at E_{SHE} = 0.530 V. There is a narrow hysteresis between the redox of Φ_{Fc^+} vs. E_{SHE} (Figure 4.6c) meaning that the electroactive molecules respond shortly to the applied electric potential, probably due to the low coverage of Θ_{Fc} = 0.05 ± 0.01 ML.

Figure 4.6d presents the impact of the oxidation of the longer alkyl chain FcC_{11}-SAM on the deflection of the Au cantilevers. The FcC_{11}-SAM/Au underwent variations of the curvature, Δk, up to 20 % before the potential reached E_{SHE} = 0.620 V, similarly to the findings in the FcC_6-SAM/Au (Figure 4.6b). Starting at this potential, the formation of the peak III takes place (Figure 4.5b). Here, the fractional coverage of the electrogenerated Fc^+, Φ_{Fc^+}, was below 0.02 (Figure 4.6e). The pronounced deflection of the cantilever was observed within the potential range between $0.620 < E_{SHE} < 1.175$ V with Φ_{Fc^+} reaching its maximum at $E_{SHE} > 1.050$ V. Under the reverse potential scan, the FcC_{11}-SAM/Au experienced the roughly linear contraction of Δk from 100 to 0 % at the applied potential starting from E_{SHE} = 0.960 V to E_{SHE} = 0.536 V followed by the 20 % variations of Δk at lower potentials. The reduction of the Fc^+ started at E_{SHE} = 0.915 V that gradually decreased Φ_{Fc^+} from 1 down to 0.94 at

E_{SHE} = 0.680 V. Under lower potentials, Φ_{Fc^+} exhibited the steep slope down to Φ_{Fc^+} of 0.01 at E_{SHE} = 0.415 V. At the potential below 0.415 V, Φ_{Fc^+} returned to its minimum of 0. The hysteresis in Φ_{Fc^+} vs. E_{SHE} in the FcC_{11}-SAM/Au (Figure 4.6e) is larger than in the FcC_6-SAM/Au (Figure 4.6c). Such finding might be explained by the relatively high surface coverage of Θ_{Fc} and the increased amount of the buried Fc-moieties (peak II) that governed the delayed response of the Fc-SAM layer to the applied potential.

Our finding confirmed the idea proposed in [60] that the observed delayed bending response of the Fc-SAM-modified cantilevers under the applied electric potentials is governed by an ensemble of in-plane molecular interactions; whereas the recorded current, in other words Φ_{Fc^+}, reports individual redox events.

The stress changes, $\delta\sigma$, in the Fc-SAM-modified planar Au were estimated using Eq. 3.10. The variations of $\delta\sigma$ (symbols) are plotted as a function of the applied electric potential, E_{SHE}, along with the corresponding CVs (solid lines) in Figures 4.7a,d. The oxidation of the Fc-SAMs resulted in a compressive stress change. The stress changes for the Fc-SAM-modified Au-coated Si cantilevers took values of $\delta\sigma$ = -0.09 ± 0.05 N m^{-1} for the FcC_6-SAM/Au and $\delta\sigma$ = -0.18 ± 0.05 N m^{-1} for the FcC_{11}-SAM/Au, respectively. The surface stress change is 50 % reduced when the length of the alkyl spacer is diminished from 11 to 6 methylene groups. The observed trend is in good agreement with the findings for the FcC_6-SAM/Au on $\delta\sigma$ = -0.14 ± 0.05 N m^{-1} in [191] and the FcC_{11}-SAM/Au on $\delta\sigma$ = -0.275 N m^{-1} in [239]. The differences in the findings can be explained by the type of the electrolyte used in the experiments and the sample preparation procedure.

Figures 4.7b and 4.7e show the variations of the superficial charge density, δq, as a function of E_{SHE} in the FcC_6-SAM/Au and the FcC_{11}-SAM/Au, respectively. The oxidation scan resulted in δq of 0.469 C m^{-2} in the FcC_6-SAM/Au and 0.531 C m^{-2} in the FcC_{11}-SAM/Au. The increased transferred charge density in the FcC_{11}-SAM/Au upon oxidation can be explained by the ion pairing (ClO^{4-}) with ferrocene moiety (Fc^+-ClO^{4-}) in the Fc-SAM. The hysteresis loops were observed in the both cases. The wider loop in δq vs. E_{SHE} was found in the FcC_6-SAM/Au pointing to the disorder in the monolayer at the very low Θ_{Fc}. In this case, the capacitive current recorded in the CVs in Figure 4.7a had a significant contribution.

The observed chain-length dependence cannot be explained by chain-chain interactions, but by the chemical contribution of Fc moiety (lateral interactions) to the surface stress change [191]. The notion is supported by Figures 4.7c and 4.7f that present an exponentially increasing trend in the changes of the stress, $\delta\sigma$, over the Fc fractional coverage, Φ_{Fc^+}, in the FcC_6-SAM/Au and the FcC_{11}-SAM/Au, respectively. It is remarkable that there is almost no hysteresis in this representation in the FcC_{11}-SAM/Au (Figures 4.7f).

4.2.2.3 Stress-charge coupling in Fc-SAM/planar Au

The hysteresis gets smaller in $\delta\sigma$ vs. δq (Figure 4.8), in contrast to $\delta\sigma$ vs. E_{SHE} (Figures 4.7b,e). The stress-charge coupling coefficients were obtained by a linear fitting of the experimental data on $\delta\sigma$ vs. δq (Eq. 3.11). For the FcC_6-SAM-modified cantilever, the coupling coefficient, ς, was found to be -0.27 ± 0.01 V. For the longer alkyl chain FcC_{11}-SAM, ς increased to -0.51 ± 0.01 V. The findings are in good agreement with the coupling parameter of ς = -0.450 V reported for the Fc-SAM-functionalized micro-

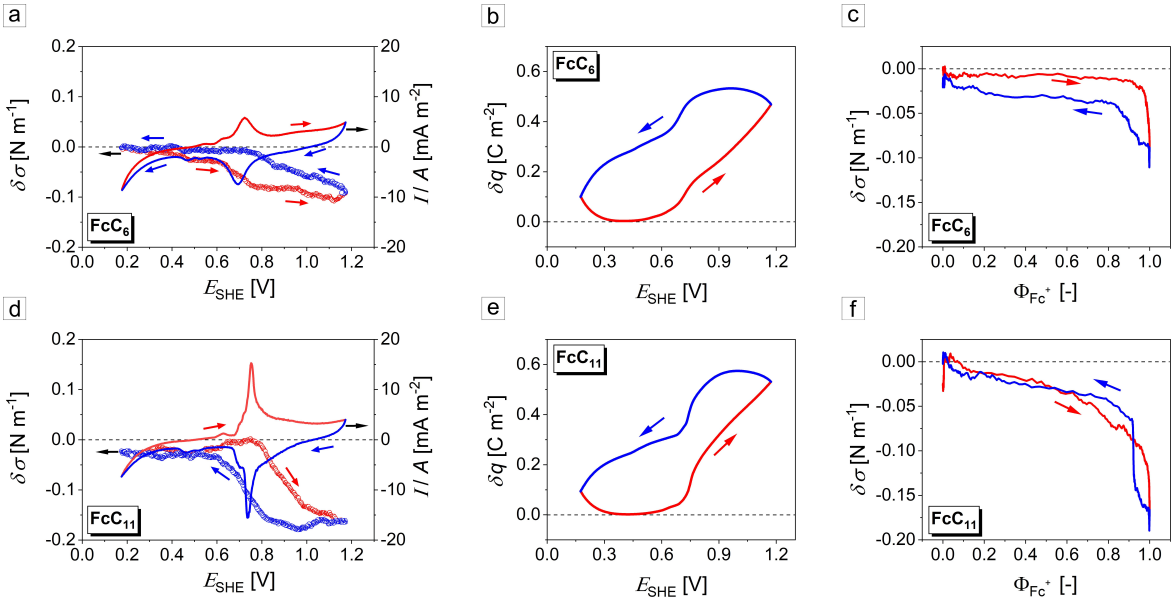

Figure 4.7: Summary on *in situ* cantilever bending experimental results carried out in 0.1 M $HClO_4$ aqueous electrolyte at a scan rate 5 mV s^{-1}. (a) Stress variations, $\delta\sigma$ (symbols), as a function of the applied electric potential, E_{SHE}, in the FcC_6-SAM/planar Au with the CV (solid lines). (b) The corresponding transferred net charge density, δq, vs. E_{SHE} in the FcC_6-SAM/planar Au. (c) $\delta\sigma$ vs. the ferrocene fractional coverage, Φ_{Fc^+}, in the FcC_6-SAM/planar Au. (d) $\delta\sigma$ (symbols) vs. E_{SHE} in the FcC_{11}-SAM/planar Au along with the CV response (solid lines). (e) δq vs. E_{SHE} in the FcC_{11}-SAM/planar Au. (f) $\delta\sigma$ vs. Φ_{Fc^+} in the FcC_{11}-SAM/planar Au. The red and blue colors indicate the anodic and cathodic scans, respectively.

cantilevers in [60]. It is noteworthy that the same order and sign of ς was measured in the polypyrrole-modified (9-106 nm thick) planar Au cantilevers (ς = -0.153 ± 0.011 V) in [226]. According to the literature [228], a clean planar Au surface has the coupling coefficient of -2 V, that about 4-8 times larger than that of the Fc-SAM estimated in this work. The magnitude of the measured cantilever deflection, and, thus, the surface stress changes, are differ in the Au cantilevers coated by the FcC_6- and FcC_{11}-SAMs. A minor signature of the coupling at the Au/electrolyte interface may be observed at low Fc-SAM coverages in the Fc-SAM/planar Au.

4.2.3 Fc-SAM-modified np-Au and hnp-Au

This section begins with the electrochemical characterization of the Fc-SAM-modified np-Au and hnp-Au followed by the estimation of the response rate and investigation on the actuation behavior of these hybrids.

4.2.3.1 Electrochemical characterization of redox-active SAM-modified np-Au and hnp-Au

Electroactive SAMs containing redox-active ferrocene-moieties can undergo reversible transitions between discrete oxidation states upon the application of an electric field. The primary advantages of the electrochemically switchable systems include the ca-

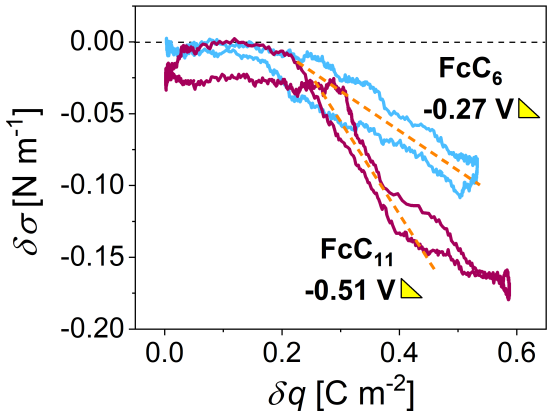

Figure 4.8: The stress-charge coupling in the planar Au modified with Fc-SAMs. The stress, $\delta\sigma$, vs. the net charge density, δq, in the FcC_6- and FcC_{11}-SAM/planar Au in 0.1 M $HClO_4$ at a scan rate of 5 mV s^{-1}. The electrode potential was cycled between E_{SHE} = 0.175 V and E_{SHE} = 1.175 V. The dashed orange lines indicate the best linear fits used for determining the stress-charge coupling parameters, ς, given in V.

pability to uniformly perturb the entire np-Au sample through electrochemical means and the ability to achieve precise control over the redox state of individual molecules by adjusting the magnitude of the applied potential.

Cyclic voltammetry is highly sensitive to the structure and dynamics changes of the Fc-SAM and np-Au. Figure 4.9 shows the CV of the FcC_6-SAM/hnp-Au. Minor changes are observed over 30 successive redox cycles between E_{SHE} = 0.175 V and E_{SHE} = 1.175 V at a potential scan rate 5 mV s^{-1} in 0.1 M $HClO_4$. The CVs obtained in 0.1 M $HClO_4$ for the charging/discharging of a "bare" np-Au and oxidation/reduction of the Fc-SAMs formed on the np networks are summarized in Figure 4.10. The findings on the electrochemical responses of the np hybrids resemble those previously published for the Fc-SAM-modified planar Au surfaces [60, 194, 196] that confirms the successful formation of the stimuli-sensitive monolayers. The measured current densities for the redox of the Fc-SAM-modified np specimens are significantly higher as compared to the capacitively charged/discharged "bare" np-Au. The phenomena may be caused by the features of the electric double layers of the metal/electrolyte ("bare" np-Au) and the metal/Fc-SAM/electrolyte (Fc-SAM/np-Au) discussed in Section 2.2 and Section 2.3.3.3, respectively.

The single redox peaks observed in the FcC_6-SAM-modified np-Au with L = 120 nm (oxidation at E_{pa} = 0.55 V, reduction at E_{pc} = 0.48 V) and hnp-Au (E_{pa} = 0.60 V, E_{pc} = 0.55 V) are related to the oxidation and reduction of the Fc-moiety, indicating the standing-up phase of the Fc-SAM (Figure 4.10a), according to [194]. The peaks are less shifted in hnp-Au (ΔE_{peak} = 0.05 V) compared to np-Au (ΔE_{peak} = 0.07 V).

The redox peak asymmetry in Fc-SAM-modified np-Au (L = 40 nm) is noticeable. Upon the redox of the FcC_6-SAM, E_{pa} was found at 0.72 V and E_{pc} at 0.52 V that gives the largest peak separation of ΔE_{peak} = 0.20 V. In ideal Nernstian absorption, the peak separation at slow scan rates is 0, when a scan rate increases, the peak separation increases in a quasi-reversible process [240]. The asymmetry of the peaks is explained by the non-idealities of the reversible redox behavior of the Fc-SAM [183].

Collapsed site and pinhole defects provide a room for the molecule adsorption giving rise to the faradaic signal corresponding to Fc-moieties surrounded by other Fc-species (the main peaks).

The presence of a broadening of the anodic peak (a right shoulder in Figure 4.9 and Figure 4.10) can be explained as inherent property of a densely packed Fc-terminated SAMs. In other words, strong molecule-molecule interactions, differences in diameters of the Fc units and the alkyl chains which causes steric hindrance and induces local disorder, results in distinct microenvironments of Fc units, also known as "buried" Fc or electronic and supramolecular effects of the SAMs [179, 194].

Figure 4.10b displays the CVs of FcC_{11}-SAM-modified np specimens. The pronounced broadening of the redox peaks indicates that most of the Fc units populate slightly different positions within the Fc-SAM. The Fc-moieties at various distances from the Au surface will not have the same driving force for the electron transfer, that results in the peak shoulders in the CV. The longer alkyl chain Fc-SAM contribute to stronger intermolecular van der Waals attractions between the alkane chains giving better packed monolayers with a higher degree of ordering [194]. Here again, the current density in the hnp-Au is found to be higher than that in np-Au.

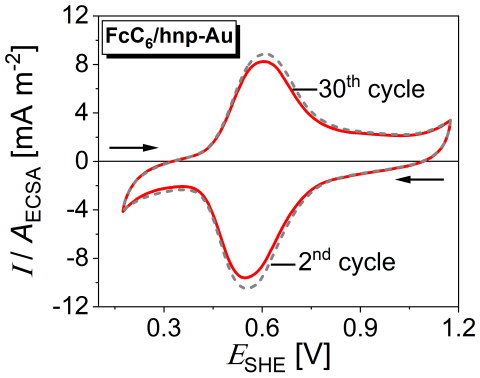

Figure 4.9: The CV of the FcC_6-SAM/hnp-Au upon cycling between E_{SHE} = 0.175 V and E_{SHE} = 1.175 V at a potential scan rate 5 mV s^{-1} in 0.1 M $HClO_4$. The 2^{nd} (grey dashed line) and 30^{th} (red solid line) cycles are presented.

Further the CV data were analyzed to estimate several parameters: the charge involved in the oxidation of the Fc-species, Q_{Fc^+}, the superficial density of the molecules at the Au surfaces, Γ_{Fc}, and the Fc surface coverage, Θ_{Fc}. The capacitive component of the net charge, δQ, transferred during the anodic scan was subtracted before the integration of Q_{Fc^+}. The resulting Q_{Fc^+} was used to estimate Γ_{Fc^+} via Eq. 3.4. To discuss the compactness of the monolayer, we employed a theoretical value of Γ_{Fc}^{theor} = 4.5 × 10^{-10} mol cm^{-2} from [193] calculated for a hexagonal packing of 0.66 nm Fc diameter. It corresponds to Θ_{Fc}^{theor} = 0.33 ML of the $(\sqrt{3}\times\sqrt{3})$R 30° ideal and well-packed structure of the chemisorbed of Fc-SAM on Au (111) surface. In this work, Θ_{Fc} was evaluated using Eq. 3.5. The calculated parameters Q_{Fc^+}, Γ_{Fc^+}, $\Gamma_{Fc^+}/\Gamma_{Fc}^{theor}$, and Θ_{Fc} are summarized in Table 4.2.

The coverage of Θ_{Fc} = 0.14 ± 0.06 ML was found in the FcC_6-SAM/np-Au (L = 120 nm). In this case, $\Gamma_{Fc^+}/\Gamma_{Fc}^{theor}$ = 0.69 pointed to the disorder in the monolayer. The molecular coverage is higher in the FcC_6-SAM/hnp-Au, the value is

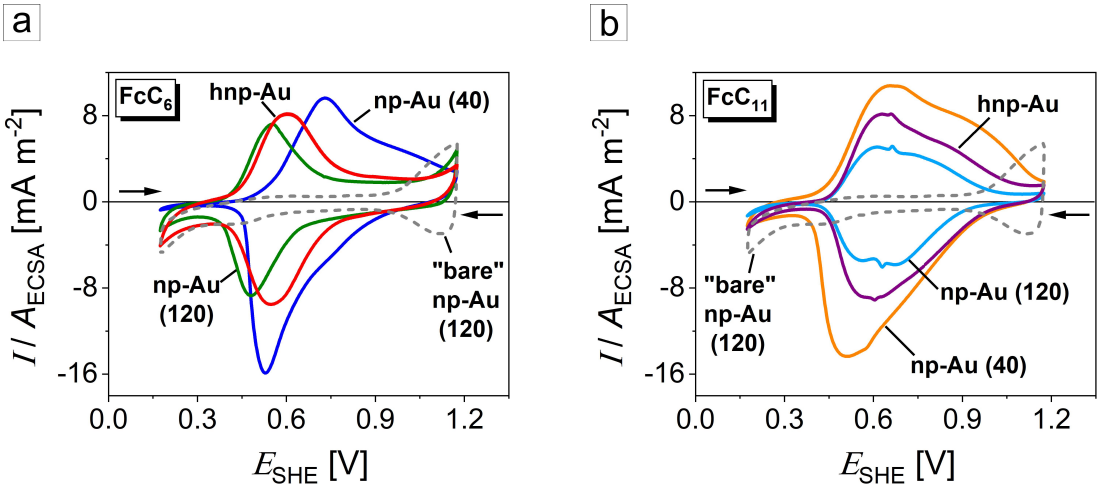

Figure 4.10: The CV responses in the "bare" np-Au (L = 120 nm, dashed grey); (a) FcC_6-SAM-functionalized np-Au (L = 40 nm, blue), np-Au (L = 120 nm, green), and hnp-Au ($L_{1,2}$ = 120/20 nm, red); (b) FcC_{11}-SAM-modified np-Au with L = 120 nm (light blue) and L = 40 nm (orange), and hnp-Au with $L_{1,2}$ = 120/20 nm (purple) hybrids upon potential cycling in 0.1 M $HClO_4$ at a scan rate 5 mV s^{-1}. The arrows indicate a sweep direction.

Θ_{Fc} = 0.24 ± 0.05 ML. The findings prove that Fc-SAM is better packed at highly curved surfaces, despite the fact that the solid Au fraction in hnp-Au (φ_{Au} = 0.12) is twice lower than in np-Au (φ_{Au} = 0.30). The large value of Θ_{Fc} = 0.34 ± 0.05 ML was observed in the FcC_6-SAM/np-Au (L = 40 nm). The discrepancy between the experimental and theoretical values can be explained by a deviation in the surface area measurement and electron transfer processes at the Fc-SAM/electrolyte interface or interactions between Au-S, Fc-Au, Fc-C_n, C_n-C_n or Fc-Fc at the curved surfaces.

The FcC_{11}-SAM coverage of np-Au with L = 120 nm is Θ_{Fc} = 0.17 ± 0.06 ML. Similarly to the findings for the FcC_6-SAM/hnp-Au hybrids, the FcC_{11}-SAM/hnp-Au is characterized by the higher value of Θ_{Fc} = 0.34 ± 0.05 ML, than in np-Au for the same ligament size (upper ligament level, in case of hnp-Au). For the FcC_{11}-SAM/np-Au (L = 40 nm), Θ_{Fc} was 0.42 ± 0.05 ML.

Earlier, $\Theta_{Fc} > 0.33$ ML or $\Gamma_{Fc^+}/\Gamma_{Fc}^{theor}$ in excess of 1 was reported for Fc-SAM-modified microcantilevers studied in perchlorate electrolyte [191]. In addition, the relatively high SAM coverage up to 0.66 ML was found in alkanethiol SAM-modified Au nanoparticles (smaller than 5 nm in size) as discussed in [170] and references therein. The authors suggested that the higher radius of curvature of the cluster the greater SAM coverage. This finding was attributed to the occupancy by the SAM of alternative binding sites (edges and corners) at the Au surface. Moreover, $\Gamma_{Fc^+}/\Gamma_{Fc}^{theor} > 1$ might be attributed to the lateral electron transfer, electrostatic interactions between redox groups, and additional physisorbed molecules [183].

The longer carbon chain in the alkyl groups determines the compactness (Θ_{Fc}) of the SAM layer [241]. Also, the observed higher molecular coverage on the np substrates can be supported by the fact that the degree of freedom of the longer molecules (FcC_{11}-SAM) is higher than that of the FcC_6-SAM, resulting in higher flexibility in binding and packing [242]. In other words, the SAM surface coverages are more ideal for the methylene groups ≥ 8 than for shorter SAMs, which can be attributed to a com-

Table 4.2: The characteristics of the chemisorbed Fc-SAMs on np-Au (L = 120 nm and L = 40 nm) and hnp-Au ($L_{1,2}$ = 120/20 nm) calculated based on the CV data in 0.1 M $HClO_4$ (Figure 4.10). The charge involved in the oxidation of the Fc-species, Q_{Fc^+}, the superficial density of the molecules at the Au surfaces, Γ_{Fc^+}, and the Fc surface coverage, Θ_{Fc}. The theoretical superficial density of Fc-SAM is Γ_{Fc}^{theor} = 4.5 × 10^{-10} mol cm^{-2} [193].

skeleton type	np-Au L = 120 nm		np-Au L = 40 nm		hnp-Au L_1 = 120 nm, L_2 = 20 nm	
Fc-SAM / characteristics	FcC_6	FcC_{11}	FcC_6	FcC_{11}	FcC_6	FcC_{11}
charge, Q_{Fc^+}, [mC]	3.02	4.49	21.80	27.00	2.62	4.03
superficial density of Fc-SAM, Γ_{Fc^+}, × 10^{-10} [mol cm^{-2}]	3.11	4.61	7.79	9.65	4.94	7.60
Γ_{Fc^+} / Γ_{Fc}^{theor}	0.69	1.03	1.73	2.15	1.10	1.69
coverage, Θ_{Fc}, [ML]	0.14	0.17	0.34	0.42	0.24	0.34

petition between Fc and alkyl packing within shorter chains [243].

The growth kinetics of alkanethiol SAMs can be influenced, among a number of factors, by a gold substrate morphology [244]. The statement is supported by the finding of this work on the enhanced molecular surface coverage of the Fc-SAM in hnp-Au and np-Au (L = 40 nm) specimens. The materials have highly curved surfaces providing more available sites for molecules to adsorb onto, increasing the overall coverage. In contrast to np-Au (L = 120 nm), the structure of hnp-Au consists of interconnected pores and channels at multiple length scales (Figure 4.2). This might enhance the transport of molecules within the material, allowing for more efficient adsorption and higher coverage.

4.2.3.2 Response rate of Fc-SAM-modified np-Au and hnp-Au

It is of importance to investigate a responsiveness of an actuator or a sensor. A highly responsive device will be able to adjust quickly and accurately its output or measurements in response to changes, providing the real-time feedback and control. In this thesis, a response of the free-standing mm-sized Fc-SAM-based np actuators was studied under the potential "jumps". The "jumps" during the chronoamperometry (Section 3.2.1.2) between E_{SHE}^{red} = 0.175 V and E_{SHE}^{ox} = 1.175 V were used to change the Fc-SAMs from the reduced to the oxidized state, respectively, in bulk np-Au specimens immersed in a three-electrode electrochemical cell filled with 0.1 M $HClO_4$ aqueous electrolyte.

To study the kinetics of the ferrocene to ferrocenium transition and *vice versa*, the half-time, $t_{1/2}$, was used as an indication of the time required to reach a half of the maximum current during the redox process. Before the potential "jump" was initiated, the samples were kept at E_{SHE}^{red} = 0.175 V for 180 s with a recording step of 0.01 s, followed by the "jumps" corresponding to the redox states of the Fc-SAM.

Figure 4.11 shows a typical potential jump from the reduced, E_{SHE}^{red} = 0.175 V, to

the oxidized, E^{ox}_{SHE} = 1.175 V, Fc-SAM state. The maximum current, I_{max}, marked for the FcC_6-SAM/hnp-Au (red line) is the current reached after the potential switch. An exponential decay fitting was applied to the curves to evaluate the response time, $t_{1/2}$, of the Fc-SAM-modified np specimens to the potential "jumps". The average $t_{1/2}$ over a set of 10 potential "jumps" will be discussed herein.

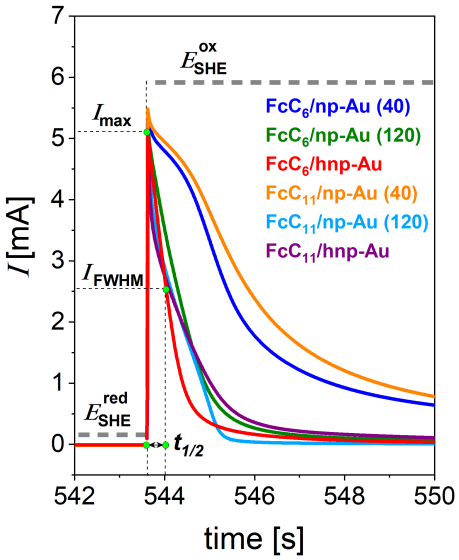

Figure 4.11: The current, I, response of the Fc-SAM/np hybrids determined using the potential "jumps" (chronoamperometry) between the reduced (E^{red}_{SHE} = 0.175 V, grey dashed line) and oxidized (E^{ox}_{SHE} = 1.175 V, grey dashed line) Fc-SAM states in 0.1 M $HClO_4$ aqueous electrolyte. The data is shown for the FcC_6-SAM-modified np-Au (blue, L = 40 nm), np-Au (green, L = 120 nm), and hnp-Au (red, $L_{1,2}$ = 120/20 nm) and FcC_{11}-SAM-functionalized np-Au (orange, L = 40 nm), np-Au (light blue, L = 120 nm), and hnp-Au (purple, $L_{1,2}$ = 120/20 nm). The estimation of the characteristic half-time, $t_{1/2}$, is illustrated for the FcC_6-SAM/hnp-Au ($t_{1/2}$ = 0.39 s). The corresponding maximum current, I_{max}, and a half of the maximum current, I_{FWHM}, determined by an exponential fitting of the experimental data are marked.

It was found that np specimens modified with the FcC_6-SAM can be characterized by the following response rates: $t_{1/2}$ = 0.62 s in np-Au (L = 120 nm), $t_{1/2}$ = 1.68 s in np-Au (L = 40 nm), and $t_{1/2}$ = 0.39 s in hnp-Au. The longer alkyl chain molecules (FcC_{11}-SAM) slow down the response to the potential switch to, respectively, $t_{1/2}$ = 0.70 s in np-Au (L = 120 nm), $t_{1/2}$ = 2.02 s in np-Au (L = 40 nm), and $t_{1/2}$ = 0.53 s in hnp-Au. These findings can be explained by the peak shape and positions, in other words, the Fc-SAM coverage given in Table 4.2. The non-idealities of the monolayers observed in the CVs (Figure 4.10) played a critical role here. The larger peak separation and the peak broadening the slower response was found in the hybrids.

Our measurements revealed that the hnp-Au modified with different types of the Fc-SAM provides the fastest response to the potential switch comparing with np-Au. The findings confirm that the multiscale porosity and relatively low effective density in hnp-Au promotes the mass exchange in the Fc-SAM/hnp-Au hybrids.

4.2.3.3 Actuation in Fc-SAM-modified np-Au and hnp-Au

The *in situ* dilatometry experiments on Fc-SAM-functionalized nanoporous hybrids were carried out under the electric potential cycling between $E_{\mathrm{SHE}}^{\mathrm{red}}$ = 0.175 V and $E_{\mathrm{SHE}}^{\mathrm{ox}}$ = 1.175 V in 0.1 M $HClO_4$ aqueous electrolyte at a scan rate 5 mV s^{-1}. The result of the measurement for the FcC_6-SAM/hnp-Au ($L_{1,2}$ = 120/20 nm) is given in Figure 4.12a. The material underwent expansion during the anodic scan and the contraction under the reverse potential scan. The peak-to-peak amplitude of the macroscopic length changes, $\delta l/l$, upon the 3$^{\mathrm{rd}}$ CV cycle was found to be $(\delta l/l)_{\mathrm{max}} = 8.9 \times 10^{-4}$. The decreased $(\delta l/l)_{\mathrm{max}} = 6.0 \times 10^{-4}$ was observed after 8.5 hours of the dilatometry experiment (30 complete CV cycles). The FcC_6-SAM/hnp-Au experienced the densification of 0.21 % during the measurement. The decrease of $(\delta l/l)_{\mathrm{max}}$ upon the experiment may be explained by the imperfections of the monolayer, that allowed the electrolyte approach the Au surface, destroying the Au-S bonding at the higher potentials, and affecting the reversibility of the Fc-Fc^+ transition. This thesis will not address the long-term stability of the Fc-SAM on np surfaces; however, this aspect must be considered in future research.

To evaluate the reversible $(\delta l/l)_{\mathrm{max}}$ amplitudes, the irreversible densification of the samples was subtracted. The results are presented for the FcC_{11}-SAM/hnp-Au and the "bare" np-Au (L = 120 nm) in Figure 4.12b. The actuation response in the FcC_{11}-SAM/hnp-Au was found to be $(\delta l/l)_{\mathrm{max}} = 11.0 \times 10^{-4}$, while the dimensional changes in the "bare" np-Au (L = 120 nm) were $(\delta l/l)_{\mathrm{max}} = 0.8 \times 10^{-4}$. The enhanced macroscopic strain in the Fc-SAM/hnp-Au underlines the impact of the electroactive molecules and the multiscale porosity in hnp-Au on actuation.

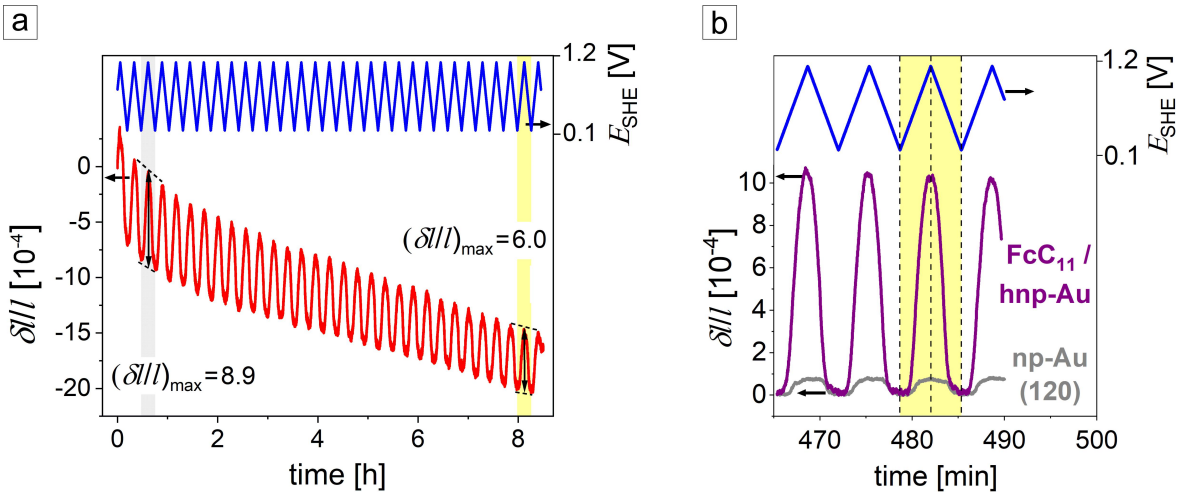

Figure 4.12: (a) Macroscopic length changes, $\delta l/l$ (red data), in the FcC_6-SAM/hnp-Au with respect to the potential, E_{SHE} (blue data), and time during the *in situ* dilatometry experiment in 0.1 M $HClO_4$ aqueous electrolyte at a scan rate of 5 mV s^{-1}. The 3$^{\mathrm{rd}}$ (grey background) and 30$^{\mathrm{th}}$ (yellow background) CV cycles are highlighted with the corresponding the peak-to-peak actuation amplitudes, $(\delta l/l)_{\mathrm{max}}$. (b) Reversible $\delta l/l$ (after subtracting irreversible deformation) shown for the FcC_{11}-SAM/hnp-Au (purple data) and "bare" np-Au (L = 120 nm, grey data) vs. E_{SHE} (blue data) and time. The 30$^{\mathrm{th}}$ CV cycle is marked in yellow. The black dashed lines indicate the upper and lower potential limits.

Figure 4.13a combines the macroscopic length changes, $\delta l/l$, and the corresponding current density, I/A_{ECSA}, vs. the electric potential, E_{SHE}, in the FcC_{11}-SAM/hnp-Au. The steep slope in I/A_{ECSA} vs. E_{SHE} is observed as the potential overcomes 0.45 V, pointing to the transformation of the ferrocene to ferroceniums. However, the actuation strain increases later, at E_{SHE} above 0.55 V. The delay in the actuation response confirms that the phenomenon is governed by the collective in-plane motions of the Fc-SAM rather than the individual oxidized molecule. To illustrate the findings clearly, $\delta l/l$ variations are plotted together with the fractional coverage of the Fc-SAM, $\Phi_{\mathrm{Fc^+}}$, as functions of E_{SHE} in Figure 4.13b. The plot $\Phi_{\mathrm{Fc^+}}$ vs. E_{SHE} had the sigmoidal shape similar to the findings on the Fc-SAM/planar Au (Figures 4.6c,e). The half of $\Phi_{\mathrm{Fc^+}}$ is converted at E_{SHE} = 0.70 V. At this potential, the np hybrid actuates with $(\delta l/l)_{\mathrm{max}} = 2.0 \times 10^{-4}$. The similarities were also found in the variations of $\delta l/l$ versus E_{SHE} in the FcC_{11}-SAM/hnp-Au (Figure 4.13) and in the FcC_{11}-SAM/planar Au (Figure 4.6d). The strain exhibits a continuous increase along with $\Phi_{\mathrm{Fc^+}}$, reaching its maximum value at the upper potential limit. During the reverse scan, the material demonstrates a more rapid response, the complete reduction of the Fc-moieties superimposes with the observed strain data.

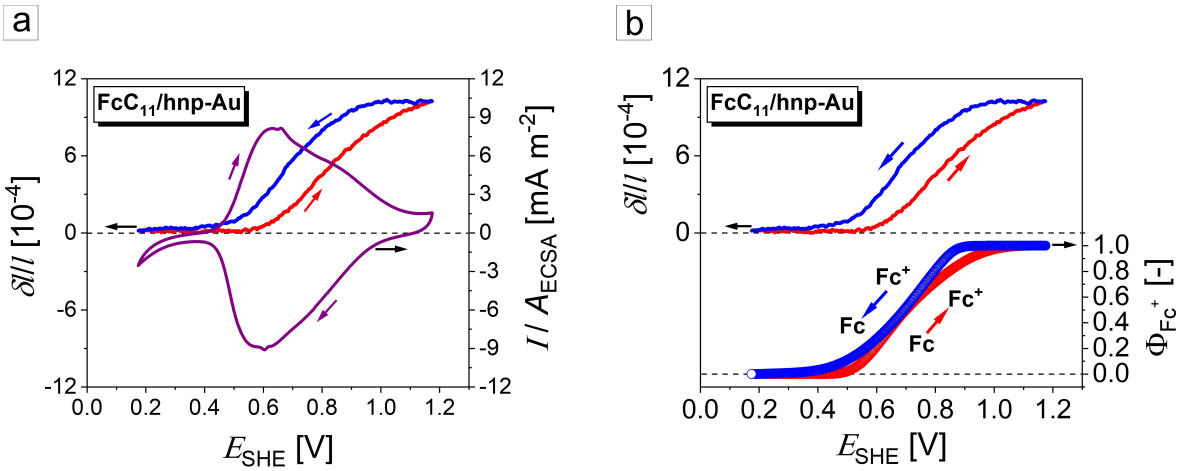

Figure 4.13: Results of the *in situ* dilatometry experiments on the FcC_{11}-SAM/hnp-Au in 0.1 M $HClO_4$ aqueous electrolyte at a scan rate of 5 mV s^{-1}. (a) The macroscopic length changes, $\delta l/l$, vs. the electric potential, E_{SHE} and the corresponding CV. (b) Variations of $\delta l/l$ and the fractional coverage of the Fc-SAM, $\Phi_{\mathrm{Fc^+}}$, vs. E_{SHE}. The red and blue data (and arrows) correspond to the oxidation and reduction scans, respectively.

Figure 4.14 summarizes the macroscopic length changes, $\delta l/l$, plotted as a function of the charge density, δq, transferred to the electrode during the dilatation experiments in 0.1 M $HClO_4$ for every np material and Fc-SAM variant examined. Each of curves represents the 30$^{\mathrm{th}}$ single potential cycle and corresponds to the anodic (solid line) and cathodic (half-transparent line) scans, respectively. It was found that the hybrids undergo expansion upon oxidation with an increase in the transferred net charge density due to the electrolyte's anions uptake (ClO^{4-}), and ion pairing with ferrocenium (Fc^+-ClO^{4-}), while the reverse reduction scan results in the anions release and shrinkage. The plots exhibit curved (non-linear) segments during the redox reactions of the Fc-SAM. The charging-discharging of the "bare" np-Au (L = 120 nm) is shown for the

comparison. The reversible actuation behavior of the hybrids was consistently observed across all samples studied.

The non-modified or "bare" np-Au, when exposed to the applied electric potential, changes its macroscopic length, $\delta l/l$, up to $(\delta l/l)_{max} = 0.8 \times 10^{-4}$, while the transferred charge density is $\delta q = 0.345$ C m^{-2} (Figure 4.14a). In contrast, when the FcC_6 monolayers are formed on np-Au, with a coverage of $\Theta_{Fc} = 0.14 \pm 0.05$ ML, the length variation is nearly doubled $(\delta l/l)_{max} = 1.5 \times 10^{-4}$ with $\delta q = 0.380$ C m^{-2}.

Series of the dilatometry experiments were conducted to compare the actuation performance of np-Au modified with Fc-SAM and an anodic oxide. It was found that the OH adsorption on np-Au with a ligament size of 120 nm induces a length change of $(\delta l/l)_{max} = 1.3 \times 10^{-4}$ at the surface coverage of $\Theta_{OH} = 1.0 \pm 0.1$ ML and $\delta q = 4.750$ C m^{-2} (Section 4.2.1.2). This finding confirms that the Fc-SAMs are more efficient in inducing strain changes (actuation) than the OH adsorption, requiring less superficial charge change and lower applied electric potentials.

The *in situ* dilatometry revealed the increased strain amplitudes ($(\delta l/l)_{max} = 5.8 \times 10^{-4}$) and the charge density ($\delta q = 0.660$ C m^{-2}) in the FcC_6-SAM/hnp-Au as compared to the FcC_6-SAM/np-Au ($L = 120$ nm). The largest amplitude of $(\delta l/l)_{max} = 9.2 \times 10^{-4}$ was found in the FcC_6-SAM/np-Au ($L = 40$ nm) at $\delta q = 0.800$ C m^{-2}. In Figure 4.14a, the plots of np-Au and FcC_6-SAM/np-Au ($L = 120$ nm) show a minimal hysteresis, while the FcC_6-SAM/hnp-Au and the FcC_6-SAM/np-Au ($L = 40$ nm) specimens exhibits a more pronounced "delay" between anodic and cathodic cycles. This may be attributed to the redox-induced changes within the monolayer or even the Au-S bond degradation at the higher potentials [183], that could promote the coadsorption of the electrolyte's species at the Au surface. Smaller pores in np-Au ($L = 40$ nm) and hnp-Au ($L_2 = 20$ nm) may enable the creation of a disordered Fc-SAM, characterized by a higher concentration of clustered and buried Fc groups. This is likely due to the presence of randomly oriented high-index facets with abundant steps and kinks along with residual silver and a lack of well-defined facets in np materials [42].

The dilatometry data for the FcC_{11}-SAM-modified np networks versus the superficial charge density, δq, is given in Figure 4.14b. The hybrids show a similar actuation behavior in response to the redox reaction of the Fc-moieties as the FcC_6-SAM/np materials. The actuation amplitude of the FcC_{11}-SAM/np-Au ($L = 120$ nm) is $(\delta l/l)_{max} = 1.7 \times 10^{-4}$ with $\delta q = 0.480$ C m^{-2} and the molecular coverage of $\Theta_{Fc} = 0.17 \pm 0.05$ ML. The longer alkyl chain Fc-SAMs in hnp-Au provide the enhanced strain amplitude up to $(\delta l/l)_{max} = 11 \times 10^{-4}$ with $\delta q = 0.881$ C m^{-2} and $\Theta_{Fc} = 0.34 \pm 0.05$ ML. The largest $(\delta l/l)_{max}$ was found in the FcC_{11}-SAM/np-Au ($L = 40$ nm) of $(\delta l/l)_{max} = 12 \times 10^{-4}$ with $\delta q = 0.930$ C m^{-2}. A smaller hysteresis in $\delta l/l$ versus δq is observed in the FcC_{11}-SAM/hnp-Au and the FcC_{11}-SAM/np-Au ($L = 40$ nm) compared to the FcC_6-SAM/np hybrids, which can be potentially attributed to the better packing of the FcC_{11}-SAMs (Figure 4.10) [60]. Despite the lower Au solid fraction in hnp-Au as compared to np-Au ($L = 120$ nm), the hierarchically structured hybrids exhibit the superior actuation performance.

The summary on the peak-to-peak amplitudes of the macroscopic length changes, $(\delta l/l)_{max}$, as a function of the transferred charge density, δq, is given in Figure 4.15a. The Fc-SAM coverage (Θ_{Fc})-dependent $(\delta l/l)_{max}$ are presented in Figure 4.15b. A

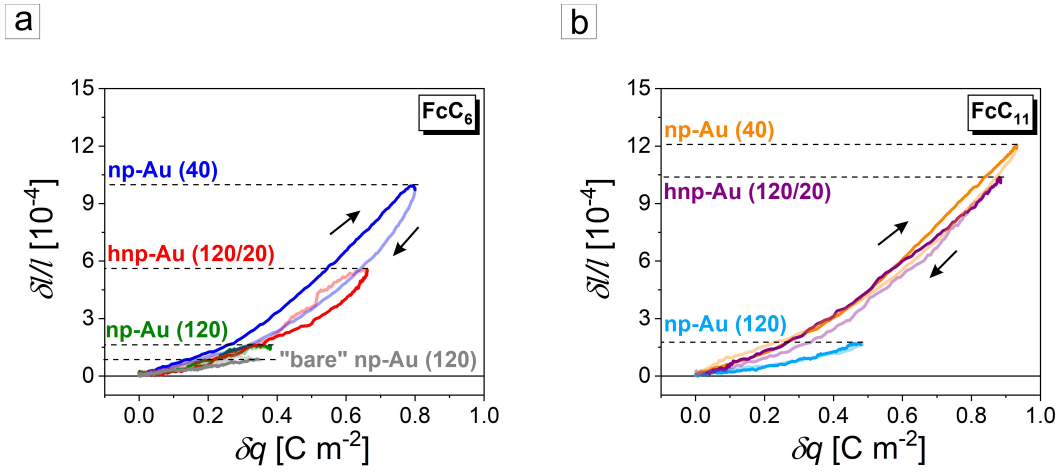

Figure 4.14: A summary on the macroscopic length changes, $\delta l/l$, as a function of the transferred net charge density, δq, in the np hybrids observed during *in situ* dilatation experiments in 0.1 M $HClO_4$ at a scan rate of 5 mV s^{-1}. (a) The "bare" np-Au (L = 120 nm, grey), FcC_6-SAM/np-Au (L = 120 nm, green), FcC_6-SAM/hnp-Au ($L_{1,2}$ = 120/20 nm, red), and FcC_6-SAM/np-Au (L = 40 nm, blue); (b) The FcC_{11}-SAM/np-Au (L = 120 nm, light blue), FcC_{11}-SAM/hnp-Au ($L_{1,2}$ = 120/20 nm, purple), and FcC_{11}-SAM/np-Au (L = 40 nm, orange). The solid and half-transparent lines represent the anodic and cathodic scans, respectively. The arrows show the scan direction. The numbers mark the ligament size, L.

quadratic variation of $(\delta l/l)_{max}$ vs. δq and Θ_{Fc} was found in the Fc-SAM-functionalized nanoporous networks. This is different from the linear surface stress variation, δf, on δq for the np-Au/OH hybrids (Figure 4.4c). The findings of this work are similar to the stimuli-sensitive strain behavior of the polypyrrole-based np actuators discussed in [57].

The electrochemical characteristics of the hybrids along with the corresponding macroscopic length variations are given in Figure 4.16. Figures 4.16a,d show the transferred charge density per the surface coverage of the Fc-SAM via $\delta q/\Theta_{Fc}$ as a function of the potential, E_{SHE}. The graphs exhibited a sigmoidal shape similarly to those presented for the Fc-SAM/planar Au in Figures 4.6c,e. Here, non-linear segments were observed in the potential range of 0.5 - 0.9 V. In this potential window the transition Fc-Fc^+ takes place. The data for the FcC_{11}-SAM-functionalized np samples superimposes well in the Fc-Fc^+ transition range. The shift of the curves of the FcC_6-SAM/np hybrids (Figure 4.16a) can be explained by the anodic/cathodic peak positions in Figure 4.10a. The hysteresis points to the spatial heterogeneity within the monolayers causing a lack of the proper superimposition of the graphs.

The variations of the scaled actuation strain, $(\delta l/l)/(\Theta_{Fc})^2$, over the potential, E_{SHE}, are given in Figures 4.16b,e. The findings confirmed the quadratic dependence of $\delta l/l$ on Θ_{Fc} observed earlier in Figure 4.15. Similarly to Figures 4.16a,d, the non-linear segments are observed at E_{SHE} = 0.5-0.9 V. Here, a slightly incoherent superimposition of the graphs in the FcC_6-SAM/np hybrids takes place as well.

The hysteresis is noticeably diminished when the scaled strain, $(\delta l/l)/(\Theta_{Fc})^2$, is plotted versus the scaled charge density, $\delta q/\Theta_{Fc}$, in Figures 4.16c,f. Non-linear segments are found in the potential range governing the redox of the Fc-SAMs. The deviation from the linearity is even pronounced at $\delta q/\Theta_{Fc} < 0.5$ C m^{-2} and at $\delta q/\Theta_{Fc} > 2.0$ C m^{-2} due

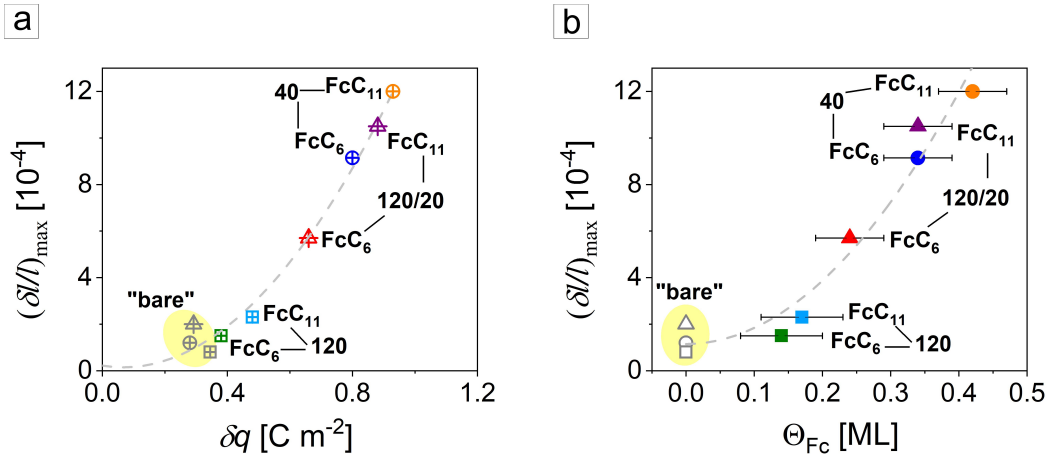

Figure 4.15: Results of the *in situ* dilatometry measurements of the Fc-SAM-modified nanoporous gold hybrids in 0.1 M $HClO_4$ at a scan rate of 5 mV s^{-1}. (a) $(\delta l/l)_{max}$ as a function of the transferred net charge density, δq. (b) The peak-to-peak strain amplitudes, $(\delta l/l)_{max}$, as a function of the Fc-SAM coverage, Θ_{Fc}, in the np hybrids. FcC_6-SAM/np-Au (L = 40 nm, blue), FcC_6-SAM/hnp-Au ($L_{1,2}$ = 120/20 nm, red), and FcC_6-SAM/np-Au (L = 120 nm, green), FcC_{11}-SAM/np-Au (L = 40 nm, orange), FcC_{11}-SAM/hnp-Au ($L_{1,2}$ = 120/20 nm, purple), and FcC_{11}-SAM/np-Au (L = 120 nm, light blue). The data for the non-modified np hybrids are given in grey symbols (40 - triangles, 120 - squares, 120/20 - circles), marked as "bare" and highlighted in yellow. The numbers mark the ligament size, L. The grey dashed lines are the best polynomial fits.

to the impact of the capacitive charging and possible degradation of the electroactive molecules at the higher potentials [183, 245].

To conclude, the pairing of the electrolyte's ions with the Fc-moieties resulted in the non-linear relation between the scaled strain and the charge density in the Fc-SAM/np hybrids. Such phenomenon is aligned with the typical behavior of actuators with organic adsorbates and their strain-charge characteristics, in contrast to linear variations for the actuators [246].

4.2.3.4 Actuation coefficient in Fc-SAM-modified np-Au and hnp-Au

A quantitative evaluation of the material-specific actuation ability is of interest for its potential applications. To quantify the actuation behavior in terms of the charge-response, the actuation coefficient, A^*, is defined as the derivative of the macroscopic, linear strain, $\delta l/l$, with respect to the volumetric charge density, δq, via [57]:

$$A^* = \frac{\delta l}{l}\frac{1}{\delta q} \quad . \tag{4.1}$$

where δq was taken with respect to the sample volume, in contrast to the charge density discussed above ($\delta q = \delta Q / A_{ECSA}$).

Figure 4.17 summarizes the experimental findings on A^* as a function of Θ_{Fc}. The slope derived from the linear regression is:

$$A^* = (0.12 \pm 0.02)\Theta_{Fc}\ \frac{mm^3}{C} \tag{4.2}$$

with the standard deviation as uncertainty.

The findings of this work on the mean actuation coefficient, A^*, are in good agreement with the reported A^* for the electrochemical oxidation of the polypyrrole-functionalized np-Au hybrids in [57]. However, the thickness of the Fc-SAM is about 1-2 nm, that is much lower than the reported ones for the conductive polymer (10-40 nm [57]).

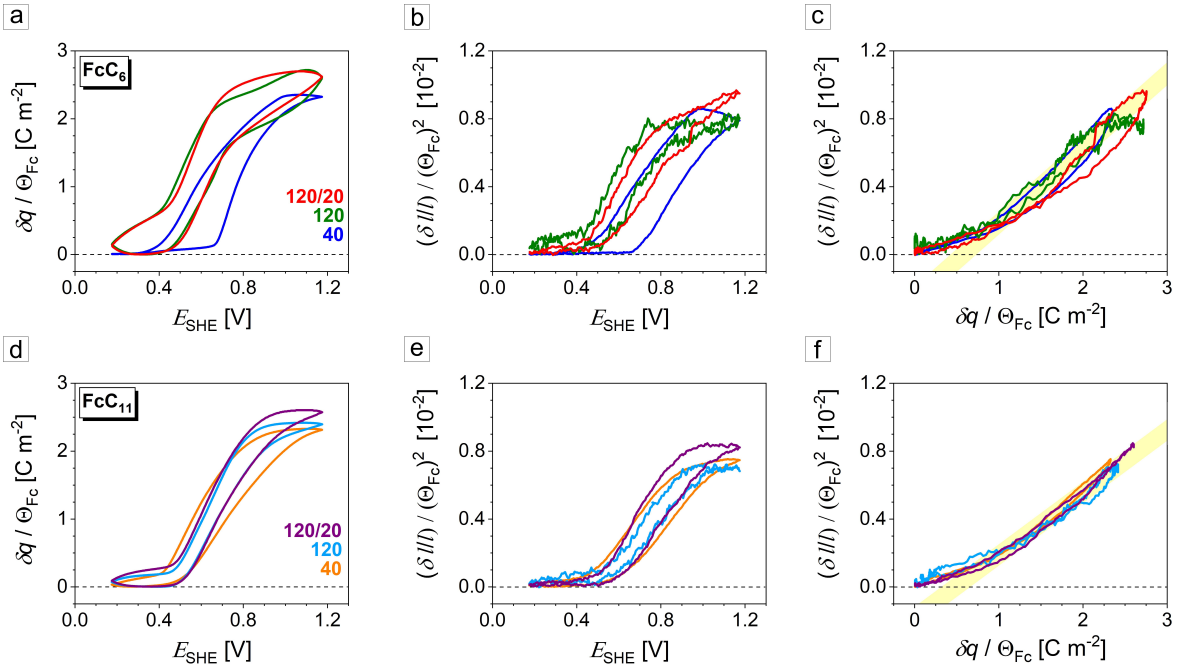

Figure 4.16: Electrochemical characteristics of the Fc-SAM/np actuators in 0.1 M $HClO_4$ aqueous electrolyte at a scan rate 5 mV s^{-1}. (a), (d) The scaled transferred net charge density, $\delta q/\Theta_{Fc}$, vs. potential, E_{SHE}. (b), (e) The scaled strain, $(\delta l/l)/(\Theta_{Fc})^2$, vs. E_{SHE}. (c), (f) Variations of $(\delta l/l)/(\Theta_{Fc})^2$ vs. $\delta q/\Theta_{Fc}$. The linear segments are highlighted by yellow. The data in (a)-(c) is shown for the FcC_6-SAM-modified np-Au (blue and green) and hnp-Au (red). The curves in (d)-(f) are given for the FcC_{11}-SAM-modified np-Au (orange and light blue) and hnp-Au (purple). The numbers mark the ligament sizes.

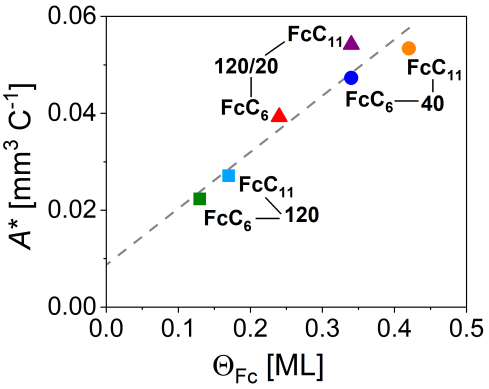

Figure 4.17: The mean strain-charge coupling coefficient, A^*, versus the Fc-SAM surface coverage, Θ_{Fc}, in the Fc-SAM/np hybrids. The data obtained using the *in situ* dilatometry in 0.1 M $HClO_4$ at a scan rate 5 mV s^{-1}. The numbers correspond to ligament sizes in the hybrids. The dashed grey line represents the best-fit straight line of the experimental data.

4.3 Effective elastic response of np hybrids

It has been found that the most important parameters in controlling the mechanical properties of np metals made by dealloying are the relative density or porosity, morphology, and connectivity [97, 99, 109]. In this thesis, the mechanical properties with an emphasis on a wide range of np-Au porosities and ligaments sizes were evaluated in electrochemical environment and will be addressed in relation to the parameters.

4.3.1 Experimental findings on elasticity of adsorbate-free (capacitively charged) np-Au in electrolyte

This study was motivated by the findings of Mameka *et al.* [56], which demonstrated the effective elastic response of bulk np-Au in an electrolyte medium, as well as by the theoretical predictions regarding the elastic properties of clean (charge neutral surface) Au nanowires by Elsner *et al.* [71]. Nevertheless, fundamental scientific challenges persist in the understanding how the elasticity and the electro-elastic coupling in nanomaterials vary with the size.

In this thesis, the influence of the electrode polarization on the effective elastic response of np-Au was investigated for a set of the samples with a wide range of the ligament sizes (L = 40-1000 nm) in 1 M $HClO_4$ aqueous electrolyte. To mitigate the influence of a residual Ag and associated oxides present on np-Au surfaces on the elastic response of np-Au, the samples underwent CVs before and after a thermal annealing process, as detailed in Section 3.3.1. The samples were tested in an as-prepared state via *in situ* dynamic mechanical analysis (DMA) combined with an electrochemical cell (Section 3.5.5).

The DMA experiments were carried out upon the potential cycling in the range between E_{SHE} = 0.0 V and E_{SHE} = 0.7 V with scan rate of 5 mV s^{-1} (Figure 4.18b). The chosen potential limits correspond to the double layer charging region. The Au surface can be characterized by the clean state at E_{SHE} = 0.7 V, while involving the

hydrogen evolution reaction (HER) at E_{SHE} = 0.0 V [150]. The HER contribution to the effective relative change was found to be less than 0.2 %.

Figure 4.18a shows a typical elastic response of np-Au during the potential cycling in the capacitive regime. The variations of strain, $\delta l/l$ (black), storage modulus, Y' (red), loss modulus, Y'' (green), and potential, E_{SHE} (blue), are plotted versus time.

The hybrid exhibited the reversible expansion, as $\delta l/l$ increased upon the charging and contracted while being discharged. The strain amplitude, $(\delta l/l)_{\max}$, reached up to 2.3 (± 0.1) × 10^{-4} in a single potential cycle. The negative net strain value of $\delta l/l$ reflects densification of the sample by 1.1 × 10^{-2}. The loss modulus, Y'', exhibited an increase up to 0.20 ± 0.03 % when the surface was charged, and decreased upon the discharging. To analyze the cyclic variations of the storage modulus, Y', with respect to E_{SHE}, we subtracted a background (grey line) which appeared due to the sample densification under the static and dynamic loads of the DMA setup. Hence, the baseline represented the absolute values of the storage modulus, Y'_0. The variation of Y' during the capacitive charging/discharging was calculated as $\delta Y'$ = Y'-Y'_0. The relative stiffness changes, $\delta Y'/Y'_0$, were determined for each potential cycle during the measurement. The average value of $\delta Y'/Y'_0$ was evaluated for each ligament size, L, in this Section.

Let us consider the variations of $\delta Y'/Y'_0$ in np-Au with L = 40 nm upon one potential cycle. A corresponding CV response is shown in Figure 4.18b. At this ligament size, we observed the highest relative stiffness change of -1.4 % in np-Au (Figure 4.18c). The variations of $\delta Y'/Y'_0$ with the transferred charge density, δq, are given in Figure 4.18d. The material softens upon positive potential scan, and stiffens under a reversible scan. The results are in good agreement with [56]. The stiffness variations display a linear dependence on the applied potential. The transferred charge density of 0.53 C m^{-2} was recorded upon the charging of the np hybrid. The findings on the stiffness change in "clean" np-Au were attributed to the charging/discharging of the electric double layer of np-Au in a weakly adsorbing aqueous electrolyte [56].

Figure 4.19a shows a comparison of the experimental (red linear fit) *in situ* DMA data on the relative elastic modulus variations, $\delta Y'/Y'_0$, along with the theoretical (green line) values proposed in [56], if an apparent excess thickness change, $\delta\tau$, of a beam (ligament) is $\delta\tau$ = 88 pm. Assuming $\delta\tau$ is independent of a ligament size, L, the bending stiffness of a ligament can be determined via Eq. 2.31.

As it has been already mentioned, the highest compliance of -1.4 % was observed in np-Au with L = 40 ± 10 nm (Figure 4.18c). The lowest relative stiffness change of -0.1 % was measured at L = 1000 ± 200 nm. The linear dependence of the relative stiffness change on L was found in np-Au under the double layer charging in electrolyte. The scatter in $\delta Y'/Y'_0$ might have been caused by the loss of connectivity along with the reduced specific surface area in np-Au which is induced by the coarsening. The trends for the measured data and the predicted values are qualitatively comparable. The presented experimental data confirms a contribution of the surface to the electrochemically-modulated elasticity change of nanoporous networks with various specific surface areas.

To determine the electro-elastic coupling parameter, λ, we assume that the experimental relative stiffness change, $\delta Y'/Y'_0$, is equal to the variation of the bending stiffness of a ligament, $\delta I/I$. In this case, an apparent excess thickness, $\delta\tau$, of a nanoligament

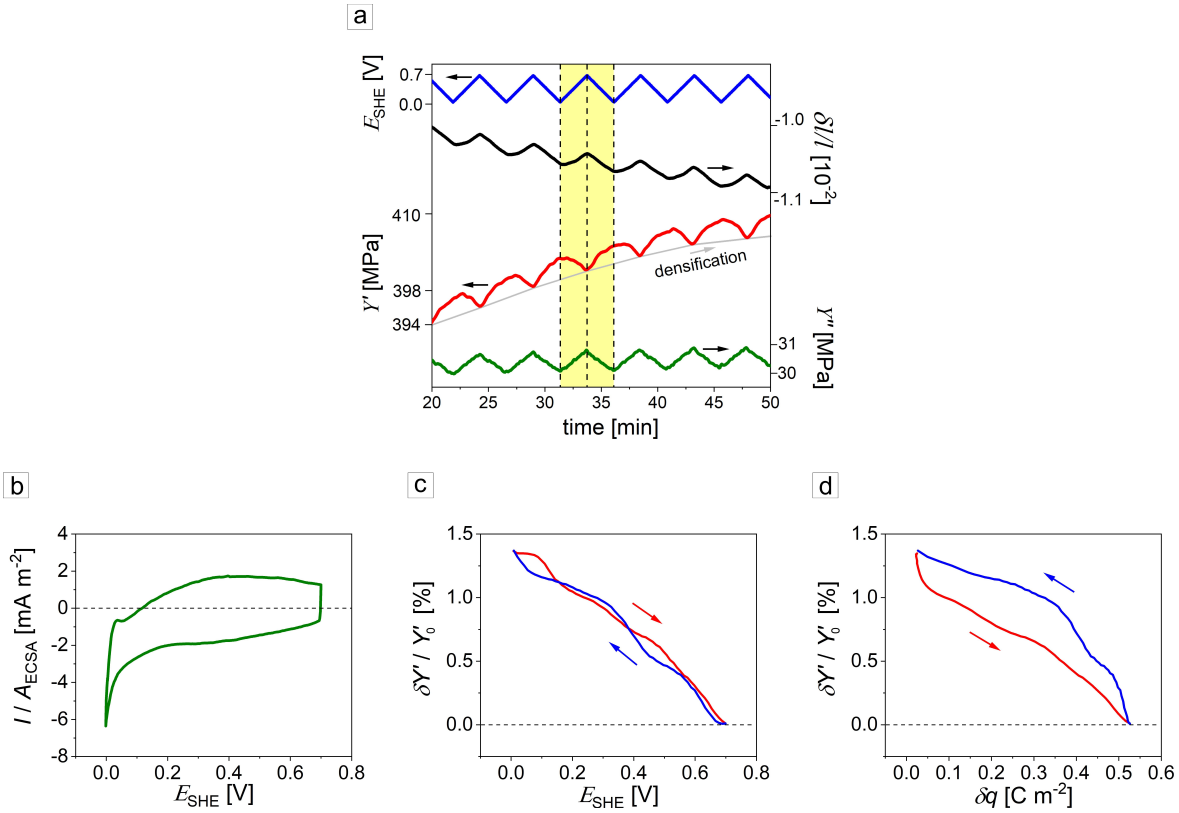

Figure 4.18: (a) The results of the *in situ* DMA experiment of np-Au (L = 40 nm) during the capacitive charging/discharging in 1 M $HClO_4$ aqueous electrolyte at a scan rate 5 mV s^{-1}. Variations of the storage modulus, Y' (red), the loss modulus, Y'' (green), and strain, $\delta l/l$ (black), are plotted with respect to the applied electric potential, E_{SHE} (blue), and time. A single potential cycle is highlighted in yellow. The dashed lines indicate the change in the potential sweep direction. The grey line marks the baseline for Y', used to subtract a background due to the sample densification. (b) The typical current density, I/A_{ECSA}, and (c) relative stiffness change, $\delta Y'/Y'_0$, are plotted as functions of E_{SHE}. (d) The variations of $\delta Y'/Y'_0$ with the transferred charge density, δq. The red and blue arrows indicate the capacitive charging and discharging, respectively, in (c) and (d).

due to the charging can be evaluated via Eq. 2.31. By introducing $\delta\tau$ in Eq. 2.30, we estimated the excess elastic modulus change, $\delta\mathbb{C}$. Then, the electro-elastic coupling parameter, λ, was calculated using $\delta\mathbb{C}$ with the transferred superficial charge density, δq, via Eq. 2.28. The main finding of this thesis is the linearly-dependent parameter λ on L in np-Au with clean surfaces (Figure 4.19b). It takes on the negative values upon the charging of the Au surface. The results on the negative slope of the straight-line best fit in Figure 4.19b can be addressed to the stronger variations of $\delta\mathbb{C}$ at smaller ligament sizes. The surface-to-volume aspect ratio increases with smaller L, pointing to the greater contribution of the surface [210].

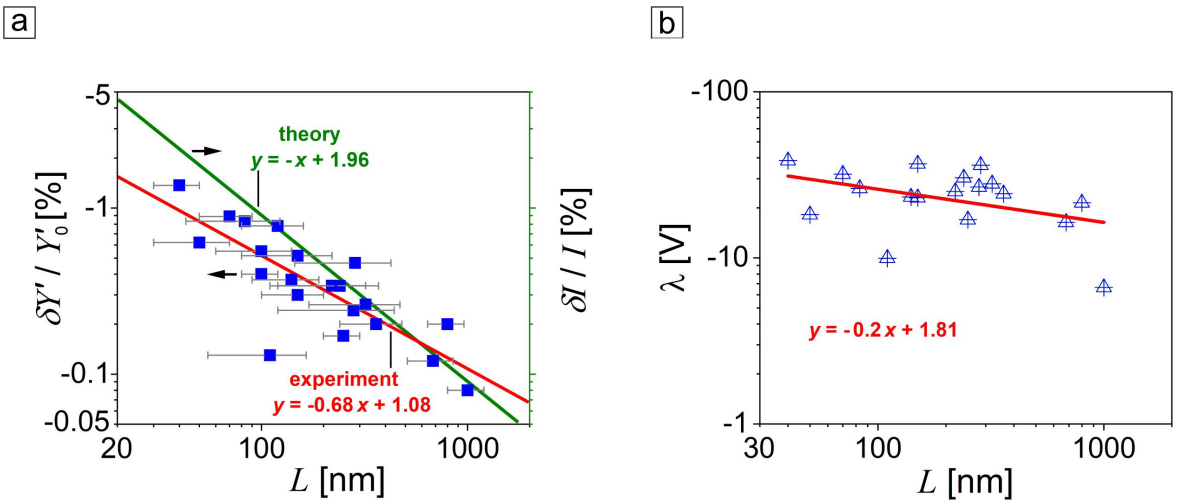

Figure 4.19: The results of the *in situ* DMA measurements during the capacitive charging/discharging of np-Au in 1 M $HClO_4$ at a scan rate 5 mV s^{-1} and a comparison to the theory predictions using Eq. 2.31. (a) The ligament size-dependent, L, relative stiffness change, $\delta Y'/Y'_0$ (blue closed squares, the linear fit is the red line), and the bending stiffness of a ligament (green line), $\delta I/I$. A ligament size is given with a standard deviation bar. The red line represents the linear fit of the data. The coefficient of determination, R^2, is 0.66 (experiment). (b) The electro-elastic coupling parameter, λ, as a function of L. The red line is the best straight-line fit of the data. Here, R^2 = 0.16.

4.3.2 Elasticity of np-Au covered with surface oxide in electrolyte

The effect of the surface (anodic) oxide on the effective elastic response of np-Au was studied upon the *in situ* DMA measurement in 1 M $HClO_4$ for a set of samples with L = 40-1000 nm. The DMA setup parameters were as presented in Section 3.5.5.

The OH-electrosorption/desorption was controlled by tuning the electric potential between E_{SHE} = 0.715 V and E_{SHE} = 1.615 V at scan rate of 5 mV s^{-1}. A typical response of the np-Au/OH hybrids with L = 40 nm is shown in Figure 4.20. Variations of the storage modulus, Y' (red), the loss modulus, Y'' (green), and strain, $\delta l/l$ (black), are plotted with respect to the applied electric potential, E_{SHE} (blue), and time in Figure 4.20a. The CV response of the sample during the experiment is given in Figure 4.20b. The observed redox peaks correspond to the oxidation and reduction of the Au surface, respectively.

The strain of the hybrids increased during the anodic scan and decreased on the reverse scan. The largest peak-to-peak strain amplitude, $(\delta l/l)_{max}$, was found 9.0×10^{-4} in the np-Au/OH hybrids with L = 40 nm. The similar amplitude was obtained by *in situ* dilatometry in this thesis (Section 4.2.1.2). The variations of $(\delta l/l)_{max}$ diminished with L in the surface-oxide-functionalized np-Au.

The grey line in Figure 4.20a, similarly to Figure 4.18a, marks the baseline for Y'_0, used to subtract a background due to the sample densification and was used to determine the reversible variations of Y^{eff}. Figures 4.20c and 4.20d present the relative stiffness changes, $\delta Y'/Y'_0$, as functions of E_{SHE} and the transferred charge density, δq, respectively, for one potential cycle during the measurement.

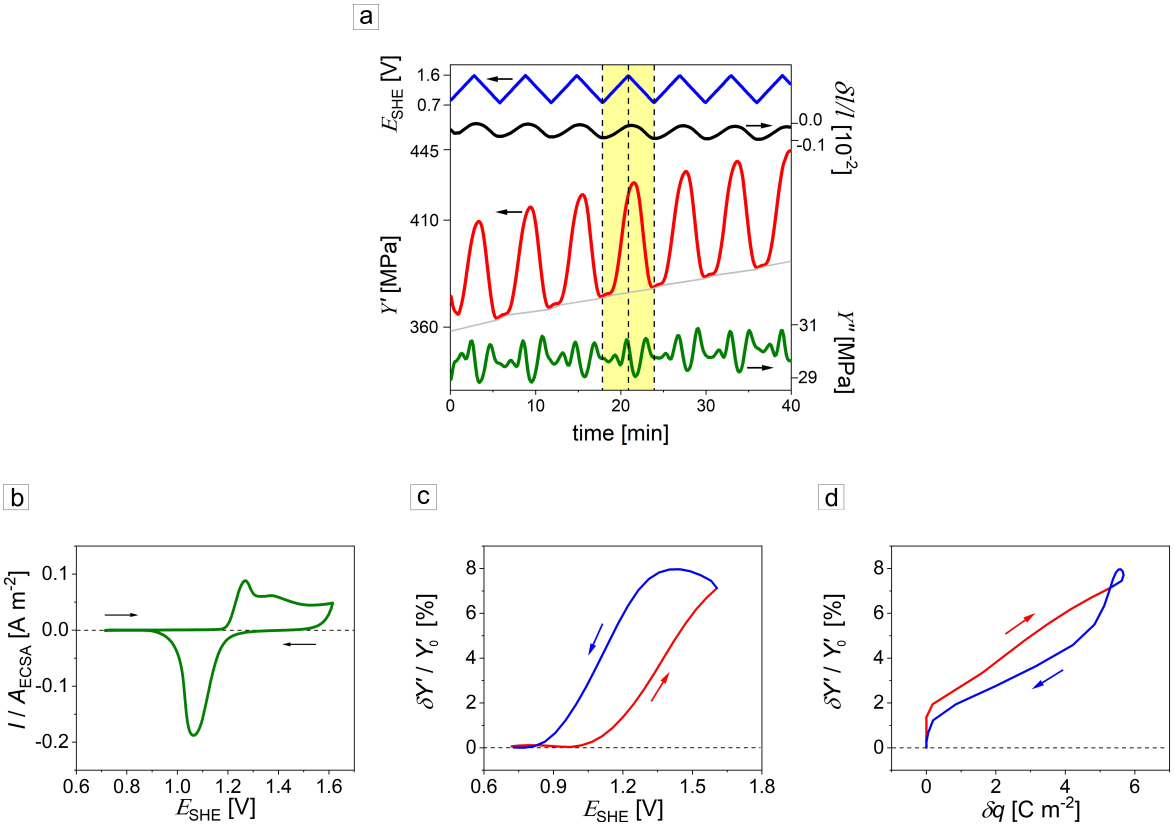

Figure 4.20: (a) The results of the *in situ* DMA experiment of np-Au/water hybrid (L = 40 nm) during the OH-electrosorption process in 1 M $HClO_4$ aqueous electrolyte at a scan rate of 5 mV s^{-1}. Variations of the storage modulus, Y' (red), the loss modulus, Y'' (green), and strain, $\delta l/l$ (black), are plotted with respect to the applied electric potential, E_{SHE} (blue), and time. A single potential cycle is highlighted in yellow. The dashed lines indicate the change in the potential sweep direction. The grey line marks the baseline for Y', used to subtract a background due to the sample densification. (b) The typical CV response via the current density, I/A_{ECSA}, and E_{SHE}. (c) The relative stiffness change, $\delta Y'/Y'_0$, is given vs. E_{SHE}. (d) $\delta Y'/Y'_0$ vs. the transferred charge density, δq. The red and blue arrows indicate oxidation and reduction, respectively, in (c) and (d).

The effective elastic modulus change, $\delta Y'/Y'_0$, of 8 % was found in np-Au/OH hybrid with L = 40 nm (Figure 4.20c). The material stiffens during the OH-electrosorption, and becomes more compliant upon the reversible potential scan. The maximum transferred charge density, δq, for the cycle reached 5.65 C m^{-2}. The observed tunable stiffness behavior is in excellent agreement with [56].

The summary on the relative effective stiffness change, $\delta Y'/Y'_0$, the absolute stiffness variation, $\delta Y'$, and the OH-adsorbate coverage, Θ_{OH}, versus ligament size, L, is presented in Figure 4.21. The coverage Θ_{OH} was determined with respect to Eq. 3.2 using the transferred charge (δQ) and electrochemically active surface area (A_{ECSA}) of a np sample. The analysis of these results will be divided into three distinct sections to facilitate a comprehensive discussion. Each section will emphasize how the variations in the ligament size impact the mechanical properties of the np-Au.

1. As the characteristic length scale, L, increases from a lower value of 40 nm, the stiffness changes exhibit a clear monotonic decrease, dropping from $\delta Y'/Y'_0$ = 8.0 %

($\delta Y'$ = 51 MPa) to approximately $\delta Y'/Y_0'$ = 4.5 % ($\delta Y'$ = 17 MPa) when L reaches 100 nm. This behavior suggests an inverse relationship between the stiffness and the ligament size in this regime, possibly due to the "smaller is stiffer" scenario. The observed findings can be attributed to the variation in the amount of adsorbates, Θ_{OH}, on the np surface. The data indicate that the coverage of the hydroxyl groups ranges between 1.38 ML and 0.83 ML for L between 40 nm and 100 nm, respectively. It becomes clear that the size dependence arises due to the increasing importance of the surface area at $L < 100$ nm, and, as a consequence, the higher OH coverage.

2. Upon further increase of L within the range of 100 to 260 nm, the relative stiffness change enters a phase characterized by a variability, fluctuating between values of approximately 4.3 % ($\delta Y'$ = 25 MPa) and 5.6 % ($\delta Y'$ = 28 MPa). The scatter might be explained by the variations of Θ_{OH} between 0.83 ML and 1.29 ML.

3. When L approaches 1000 nm, $\delta Y'/Y_0'$ significantly diminishes, decreasing to around 1.0 % ($\delta Y'$ = 27 MPa). This further decline in the stiffness may be attributed to the dominance of bulk effects and the low surface-to-volume ratio that overshadow the reinforcement mechanisms present at smaller dimensions. The adsorbate coverage, Θ_{OH}, reaches its lowest value of 0.43 ML when the ligaments are as large as 1000 nm. Obviously, the adsorption of species is strongly dependent on the surface features.

In summary, the stiffness change initially decreases monotonically with decreasing the ligament size followed by an apparent plateau, and ultimately reaches a lower threshold as the size increases further. This testifies to the complex interdependencies between the microstructure and stiffness of np-Au.

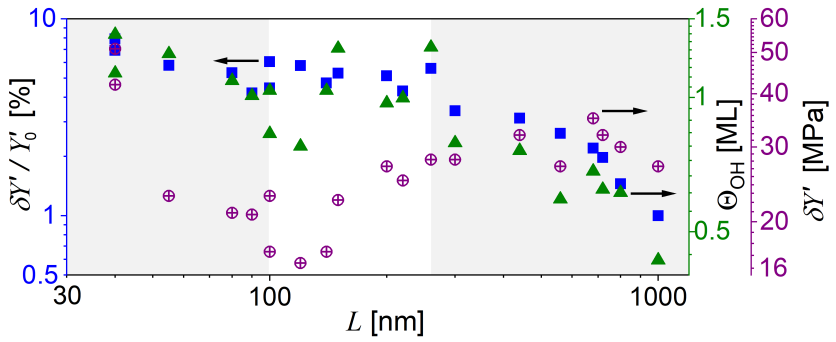

Figure 4.21: A summary of the *in situ* DMA results on np-Au with different ligament sizes in 1 M $HClO_4$ aqueous electrolyte. The relative stiffness change, $\delta Y'/Y_0'$ (blue squares), the absolute stiffness change, $\delta Y'$ (purple circles), and the OH coverage, Θ_{OH} (green triangles), as functions of the ligament size, L.

4.3.3 (Pre)strain effect on elastic response of np-Au

In this Section, the effect of (pre)strain (or deformation) on the effective elastic response of np-Au with L = 40 nm during the OH-electrosorption will be presented. The experiments were carried out in the same setup and the potential range as given in Section 4.3.2. Before the DMA measurement, the np-Au samples were plastically deformed up to strain of 70 % using the mechanical testing machine (Section 3.5.4).

The absolute values of the effective elastic modulus, Y^{eff}, as a function of strain, ε, obtained via the compression tests and the DMA measurements are summarized in Figure 4.22. The DMA findings demonstrate strong concordance with the *in situ* mechanical compression tests.

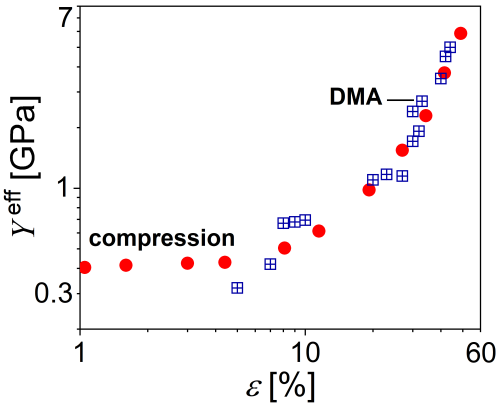

Figure 4.22: A comparison on the effective elastic moduli, Y^{eff}, of np-Au with L = 40 nm vs. (pre)strain, ε, obtained via compression tests (in air) and the DMA measurements (in electrolyte).

Upon the DMA tests, significant variability on $\delta Y'/Y'_0$ was observed in np-Au subjected to prestrain levels ranging from 50 % to 70 %. At deformation strains exceeding 40 %, the material experiences substantial structural modifications, thereby deviating from the self-similarity when compared to as-prepared np-Au. Furthermore, as the material undergoes strengthening due to plastic deformation, it requires an increased applied force during the DMA tests, which may contribute to the variability in $\delta Y'/Y'_0$. Hence, the data on the prestrained np-Au to 50-70 % will not be discussed here.

The consistent data set was obtained for np-Au prestrained to 10-40 %. The results are given in Figure 4.23a. The relative effective elastic modulus, $\delta Y'/Y'_0$, increases linearly with the strain, ε, ranging from 7.2 ± 0.8 % (non-deformed state) to 13.6 ± 0.6 % (ε = 40 %) during the OH-electrosorption process which appeared at the potential cycling between E_{SHE} = 0.715 V and E_{SHE} = 1.615 V with a scan rate of 5 mV s^{-1}.

To explain the phenomenon, the CV responses of the predeformed np-Au are shown in Figure 4.23b. Prior to the DMA tests, the electrochemically active surface area, A_{ECSA}, of the samples was determined via the capacitance ratio method [217]. The obtained current and integrated charge will be discussed with respect to A_{ECSA}. The analysis of the reduction peaks indicated that the transferred charge density (δq) rises linearly as the prestrain increases. Additionally, a notable broadening of the reduction peaks was observed after a deformation threshold of 10 %. Hence, the OH coverage was calculated using Eq. 3.2. Figure 4.23c summarizes the OH coverage, Θ_{OH}, as a function of the prestrain, ε. The Θ_{OH} of np-Au rises linearly from 1.32 ± 0.1 ML to 1.73 ± 0.1 ML with the strain applied to the material. These findings may be explained by the deformation-induced defects at the surface of the np samples which promoted the OH adsorption [134]. To inspect the effect of the adsorbate coverage on the stiffness response, the relative stiffness change, $\delta Y'/Y'_0$, was plotted versus Θ_{OH} in Figure 4.23d. The data indicates a clear trend – $\delta Y'/Y'_0$ exhibits an increase as the

Θ_{OH} rises. Indeed, the deformation of np-Au involves the formation and propagation of so-called "densification" bands leading to a number of defects within the material [80]. The latter may promote adsorption of OH-species. To conclude, the surface effect on the elastic properties of np-Au is pronounced.

4.3.4 Impact of structural hierarchy on effective elastic response of np-Au

The dynamic mechanical analyzer (DMA/SDTA861e, METTLER TOLEDO) does not have a pre-load control adjustment option. The hnp-Au/water hybrids experienced high plastic deformation during the tests. To minimize the effect of the strain and/or non-linearity impact on the elastic response, another setup was used to investigate hnp-Au specimens. It is important to mention, despite the fact that the hnp-Au samples underwent the significant plastic deformation (up to 70 %) upon the DMA measurements using the DMA/SDTA861e, METTLER TOLEDO, the obtained results had the similar trends in $\delta Y'/Y'_0$ and $\delta l/l$ variations as it will be presented in this Section.

The measurements of the effective elastic response of hnp-Au ($L_{1,2}$ = 120/20 nm) were carried out in the Netzsch DMA 242 E (Institute of Metal Research, Chinese Academy of Sciences, Shenyang, China) combined with an electrochemical cell of 10 mL. This setup provides a precise control of the applied force during the pre-load stage, high signal-to-noise ratio, and allows measurements at as low displacement amplitude as 1 µm.

The following parameters were set during the measurement: the static load, F_{static}, 0.62-0.70 N (2.70-3.05 MPa), dynamic force, F_{dynamic}, 0.13-0.20 N, displacement amplitude, X_{dynamic}, 1 µm, and frequency of 1 Hz.

A typical elastic behavior of the hnp-Au/OH hybrids under the DMA conditions is shown in Figure 4.24a. The response of the hybrid had a similar trend as presented for the np-Au/OH in Figure 4.20. The reproducible data set was obtained for 5 hnp-Au samples. The variations of the storage modulus, Y', loss modulus, Y'', and strain, $\delta l/l$, within a single (5^{th}) potential cycle is highlighted in yellow. The CV of the hnp-Au/OH hybrid upon the indicated cycle is given in Figure 4.24b. The electrosorption/desorption of oxygen-species on the Au surface was controlled by tuning the electric potential between E_{SHE} = 0.815 V and E_{SHE} = 1.615 V at scan rate of 5 mV s^{-1}. Further the variations of Y' will be presented for the 5^{th} potential cycle.

The hierarchical np sample densified under the applied loads that caused the stiffness increase (Y'). To evaluate the relative stiffness changes, we employed the approach discussed earlier for np-Au. The relative stiffness changes, $\delta Y'/Y'_0$, versus the potential, E_{SHE}, are shown in Figure 4.24c. The reversible relative stiffness change, $\delta Y'/Y'_0$, of hnp-Au upon the OH-electrosorption was found to be 17.8 % ± 0.8 % during the experiment. The elastic behavior of hnp-Au resembles the ones found in np-Au in this work (Section 4.3.2) and in the literature [56] – the hybrid undergoes stiffening while subjected to oxidation and softens upon the reversible scan (Figure 4.24c).

The transferred charge density, δq, upon the redox-reactions of hnp-Au was about 8 C m^{-2} (Figure 4.24d). The remarkably large hysteresis in $\delta Y'/Y'_0$ vs. δq was observed throughout the measurement (Figure 4.24d). The findings can be addressed

to the relatively high OH coverage of hnp-Au (1.3 ± 0.1 ML), as it was presented in Section 4.2.1.2. Note, the determination of a real surface area, A, or an electroactive surface area, A_{ECSA}, of the sample was not carried out during the DMA experiment. The presented charge density is associated with the initial A_{ECSA}, consequently, it may include inherent uncertainties in the computed δq.

The sample was densified by $\delta l/l$ of 19.4 × 10^{-2} during the test as shown in Figure 4.25a. The major part of the deformation (up to 15.3 × 10^{-2}) took place during the first half of the measurement. Figure 4.25b shows the strain, $\delta l/l$, as a function of time, when the sample densification was subtracted. The amplitude of $(\delta l/l)_{\max}$ = 264 × 10^{-4} was recorded for the 1$^{\mathrm{st}}$ CV cycle. The value is noticeably larger than found using *in situ* dilatometry in Section 4.2.1.2. The loads set in the DMA setup was an order higher than ones in the dilatometer. In this case, the rapid growth of $(\delta l/l)_{\max}$ may be explained by the plastic deformation or creep of the sample that enhanced the OH-electrosorption, similarly to the increased strength in [55] or the results in Figure 4.23a. The peak-to-peak strain amplitude, $(\delta l/l)_{\max}$, was exponentially decreasing from 264.0 × 10^{-4} (1$^{\mathrm{st}}$ CV cycle) to 19.0 × 10^{-4} (14$^{\mathrm{th}}$-19$^{\mathrm{th}}$ CV cycles) during the experiment (Figure 4.25b). The variations of $(\delta l/l)_{\max}$ versus the electric potential, E_{SHE}, are given for the 5$^{\mathrm{th}}$ and 18$^{\mathrm{th}}$ CV cycles in Figure 4.25c. During the test, the lower-level structure (L_2) remained in its original state that is in agreement with previously reported results on the microstructure of the hnp-Au experienced the uniaxial compression [15, 247]. It is remarkable that the maximum of $(\delta l/l)_{\max}$ was observed during the reduction scans at E_{SHE} = 1.4 V. Such actuation behavior might be explained by the densification of the upper-level (L_1) structure. The further investigation of the fine structure of hnp-Au samples is required.

4.3.5 Implication of surface excess elasticity theory to np-Au

In this Section, the prediction of the surface excess elasticity theory for Au nanowires will be presented and compared to the experimental data on the np-Au/OH (Section 4.3.2) along with the hnp-Au/OH (Section 4.3.4) hybrids.

Similarly to the analysis of the elasticity in the "clean" np-Au discussed in Section 4.3.1, the assumption was made that OH adsorption results in a constant surface excess elasticity change for any ligament size, L. Earlier in [56], the enhanced elasticity in the np-Au/OH hybrids was understood as a result of the electrosorption of the oxygen-species quantitatively evaluated as the 430 pm apparent excess thickening, τ, of ligaments (L = 45 nm). The corresponding surface excess elastic constant variation was found as $\delta\mathbb{C}$ = 60 N m^{-1} [56]. Figure 4.26a proves an excellent agreement of the theoretical trend as embodied in Eq. 2.31 with the experiment found for $L < 100$ nm. A deviation of the experimental results on np-Au from the theory is observed at $L > 100$ nm. This findings confirm that the surface excess elasticity contributes to the size-dependent elastic behavior at only relatively small ligament sizes for the case of the OH adsorption.

In the case of the np-Au/OH hybrids in Figure 4.26a, the bending stiffness change, $\delta I/I$, of a nanoligament with a diameter of 20 nm upon the OH-electrosorption was estimated to be 17.2 %, according to the theoretical prediction employed above [56]. The experimental findings of this thesis on the effective elastic response, $\delta Y'/Y_0'$, of

hnp-Au revealed 17.8 % ± 0.8 %. The result is in good agreement with the theoretical prediction for a Au nanowire.

The electro-elastic coupling parameter, λ, takes on the positive values, the average λ = 10.7 ± 0.6 V for $L < 100$ nm (Figure 4.26b). The results will be discussed in Section 5.3.2.

4.3.6 Elastic behavior of Fc-SAM-modified np-Au

The orientation and order of alkanethiol molecules have been well studied as summarized in Chapter 2 (Section 2.3.3). So far, the impact of the inelectroactive alkanethiol self-assembled molecules on the mechanical performance of Au was addressed, but it has still been a matter of debate [41, 203, 248]. In this Section, the effect of the redox-active self-assembled monolayers (SAMs) on the elastic behavior of np-Au macroscopic samples will be reported.

Stiffness variations of np-Au (L = 40-1000 nm) functionalized with electroactive ferrocene (Fc)-bearing alkanethiol SAMs were investigated using *in situ* DMA in 1 M $HClO_4$ aqueous electrolyte. To control the electrochemical processes occurring at the electrolyte-monolayer interface, the applied electric potential was cycled between E_{SHE} = 0.175 V and E_{SHE} = 1.175 V with a scan rate of 5 mV s^{-1}. The DMA parameters were as follows: the static force of 2.5 ± 0.5 N, the dynamic force of 1.5 ± 0.5 N, the frequency of the mechanical oscillations of 1 Hz, and the displacement amplitude of 8.0 ± 1.0 μm.

The Fc-SAM coverage, Θ_{Fc}, on np-Au and the response time of the hybrids were presented in Section 4.2.3.1 and in Section 4.2.3.2, respectively.

Figure 4.27a displays the characteristic response of the FcC_6-SAM-modified np-Au (L = 40 nm) during the DMA measurement, where parameters such as the storage modulus, Y', loss modulus, Y'', static length change (strain), $\delta l/l$, were determined. The overall increase of the Y' (or Y^{eff}) can be explained by the densification observed in the DMA experiments on np-Au as presented in this thesis and in [56]. The loss modulus, Y'', exhibited an increase during the oxidation of the Fc-SAM/np-Au hybrid meaning that the energy dissipation ability of the material was enhanced, followed by the decrease of Y'' on the reverse potential scan. The same approach to the data analysis as discussed in Section 4.3.2 was employed to obtain the absolute and relative changes of the stiffness. The corresponding CV of the hybrid is given in Figure 4.27b.

It was found that upon anodic scan, the Fc-SAM/np-Au exhibited, first, softening (-0.2 %) before the transition of ferrocenes to ferroceniums (the capacitive regime) followed by the continuous stiffening up to 3.0 %. While a softening response was recorded during the subsequent cathodic scan till the current reached the capacitive value and the material experienced a stiffer trend. The observed findings are given for one CV cycle in Figure 4.27c.

Figure 4.27d shows the typical behavior of the "bare" np-Au (L = 40 nm) under the same test conditions. The material's behavior was found to be similar to the findings on the capacitively charged np-Au in Section 4.3.1. In this Section, the potential window for the CV was shifted to more negative potentials (Figure 4.27e). However, the hybrid exhibited the same trend – softens under the anodic scan and stiffens on the reverse scan – as given in Figure 4.27f along with the electrochemical characteristic (current

density). The impact of the electroactive SAMs is obvious, as the non-modified np-Au responded differently.

A comparison of the effective elastic responses of the "bare" and FcC_6-SAM- and FcC_{11}-SAM-modified np-Au hybrids with a ligament size of 40 nm and 120 nm within a single potential cycle is presented in Figure 4.28.

Figure 4.28a presents the compliance of the hybrids during the capacitive discharging at 0.175 V $< E_{\mathrm{SHE}} <$ 1.175 V that is in line with Mameka *et al.* [56]. The relative stiffness changes, $\delta Y'/Y_0'$, were found to be 1.34 % that was equal to $\delta Y'$ of 5.2 MPa (np-Au with L = 40 nm) and 0.87 % that was $\delta Y'$ = 3.9 MPa (np-Au with L = 120 nm). The variations of $\delta Y'/Y_0'$ were plotted as a function of the transferred charge density, δq, in Figure 4.28b. Upon oxidation of the np-Au specimens with sizes of 40 nm and 120 nm, the measured values of δq were found to be 0.363 C m^{-2} and 0.289 C m^{-2}, respectively. The variations of δq versus E_{SHE} are given in Figure 4.28c. The charge linearly decreased with the potential. The hysteresis loops in Figure 4.28b and Figure 4.28c were found to be wider in np-Au with L = 120 nm as compared to L = 40 nm. The finding can be caused by the coarsen ligaments and/or residual Ag effect interfering the surface response during the electric double layer charging/discharging.

Figure 4.28d represents the strain, $\delta l/l$, of a "bare" np-Au as a function of δq. The hybrids expanded upon the anodic scan, and contracted during the cathodic one. The peak-to-peak strain amplitudes, $(\delta l/l)_{\mathrm{max}}$, of 3.7 × 10^{-4} and 0.8 × 10^{-4} were recorded in np-Au with ligament sizes of 40 nm and 120 nm, respectively, during the DMA experiments under the potential cycling between E_{SHE} = 0.175 V and E_{SHE} = 1.175 V. The findings are in good agreement with the *in situ* dilatometry data presented in Section 4.2.3.

The surface-modification by FcC_6- and FcC_{11}-SAMs led to the enhancement of the viscoelastic properties of np-Au as given in Figure 4.28e-l.

First, consider the impact of the FcC_6-SAM on the mechanical properties of np-Au (Figure 4.28e-h). The changes of the stiffness, $\delta Y'$, up to 13.7 MPa (L = 40 nm) and 3.3 MPa (L = 120 nm) were measured upon the redox reactions of FcC_6. This resulted in $\delta Y'/Y_0'$ of 2.85 % (L = 40 nm) and 1.45 % (L = 120 nm) (Figure 4.28e). The stiffness variations versus the potential can be correlated with the CV responses given in Figure 4.10 (120 nm) and Figure 4.27b (40 nm). During the redox reactions of the FcC_6-SAM, the large hysteresis in $\delta Y'/Y_0'$ as a function of E_{SHE} was observed. The hysteresis diminishes when $\delta Y'/Y_0'$ plotted versus δq in Figure 4.28f. This can be a consequence of the buried Fc-units within the monolayer that respond to the potential changes differently. However, the hysteresis in $\delta Y'/Y_0'$ vs. δq was more pronounced in np-Au with 120 nm (δq = 0.460 C m^{-2}) than in np-Au with 40 nm (0.871 C m^{-2}). The phenomenon can be caused by the disorder within the SAM (the coverage is higher when L is smaller) and, as a consequence, a weak response of the hybrid [179].

The variations of the scaled charge density, $\delta q/\Theta_{\mathrm{Fc}}$, versus E_{SHE} are presented in Figure 4.28g. Depending on the initiation of the Fc-Fc$^+$ transition, $\delta q/\Theta_{\mathrm{Fc}}$ scales linearly in the Fc oxidation window.

Upon oxidation, the Fc-SAM-modified hybrids underwent expansion, and were shrinked under the negative potential scan. The strain, $\delta l/l$, varied up to 9.3 × 10^{-4} (δq = 0.874 C m^{-2}) and 1.2 × 10^{-4} (δq = 0.430 C m^{-2}) in the np-Au specimens with sizes of 40 nm and 120 nm, respectively. The findings on $\delta l/l$ resemble the previ-

ously presented strain data estimated via *in situ* dilatometry – $(\delta l/l)_{\max}$ = 9.2 × 10^{-4} (δq = 0.800 C m^{-2}) and $(\delta l/l)_{\max}$ = 1.5 × 10^{-4} (δq = 0.380 C m^{-2}) in the FcC_6-SAM-modified np-Au with 40 and 120 nm ligament sizes, respectively.

The investigation of the FcC_{11}-SAM impact on the effective elastic response of np-Au revealed a reproducible enhanced $\delta Y'/Y_0'$ as compared to the FcC_6-SAM/np-Au. As the alkyl chain length increases, the degree of the freedom of the FcC_{11}-molecule becomes higher and results in the enhanced mechanical response as it was found in Sections 4.2.2 and 4.2.3. It agrees well with the findings on $\delta Y'$ and $\delta Y'/Y_0'$ in the FcC_{11}-SAM/np-Au. The variations of 17.65 MPa (3.35 %) and 4.75 MPa (1.86 %) were observed upon the potential cycling in the np hybrids with a ligament size of 40 nm and 120 nm, respectively (Figure 4.28i-j). The relatively high coverage of the FcC_{11} molecules led to the pronounced hysteresis in Figure 4.28j. This can be caused by the surface structure resulting in the change of Fc-SAM properties [192]. The variations of the scaled charge density, $\delta q/\Theta_{Fc}$, versus E_{SHE} are presented in Figure 4.28k. The graph superimposed well. The linear segments were found at the potentials 0.45 - 0.90 V.

The FcC_{11}-SAM/np-Au experienced reversible length changes up to $(\delta l/l)_{\max}$ = 16.0 × 10^{-4} with δq = 0.960 C m^{-2} at the smallest ligament size of L = 40 nm. According to the dilatometry results presented in Section 4.2.3, variations of $(\delta l/l)_{\max}$ = 12.0 × 10^{-4} at δq = 0.972 C m^{-2} were found for L = 40 nm and up to $(\delta l/l)_{\max}$ = 1.7 × 10^{-4} with δq = 0.480 C m^{-2} when L = 120 nm (Figure 4.28l). The DMA results agree well with the dilatation experiments.

It is of interest to examine results on the FcC_6-SAM/np-Au with relatively large ligaments of L = 800 ± 82 nm. The material was subjected to seventeen CV scans in the same potential range as given in this Section. The selected data on 5^{th} and 17^{th} scans is shown in Figure 4.29a. The monolayer experienced certain changes and/or reorganizations during cycling in 1 M $HClO_4$ aqueous electrolyte. These changes can be attributed to the hydrogen or oxygen evolution, at the lower (E_{SHE} = 0.175 V) and upper (E_{SHE} = 1.175 V) potential limits, respectively. According to Eq. 3.5, the FcC_6-SAM coverage of np-Au (L = 800 nm) was 0.09 ± 0.02 ML. The FcC_6-SAM/np-Au (L = 800 nm) exhibited the same trend as shown in Figure 4.28e-h – the hybrids stiffened during the anodic scan and softened on the reverse scan. The relative stiffness changes, $\delta Y'/Y_0'$, were found to vary from 0.4 % to 0.5 % during the measurement (Figure 4.29b). It is remarkable that the organic molecules lie flat on Au at low coverages interacting weakly with neighboring molecules, and stand up at higher coverages [194], but in both cases the observed elastic response of the Fc-SAM-functionalized np networks differs from the non-modified np hybrids.

The variations of the scaled charge density, $\delta q/\Theta_{Fc}$, are given as a function of E_{SHE} for the 5^{th} and 17^{th} CV scans in Figure 4.29c. In this case, $\delta q/\Theta_{Fc}$ is significantly larger as well as the wider hysteresis loop is found than in the hybrids with smaller L (Figure 4.28g). Thus, the phenomenon can be explained by the impact of the capacitive processes in the monolayer/Au interface on the overall elastic response of the Fc-SAM/np-Au.

4.3.6.1 Elasticity of Fc-SAM/hnp-Au hybrids

The results on the impact of the FcC_6-SAM on the effective elastic modulus variations of hnp-Au are shown in Figure 4.30. The corresponding CV is given in Figure 4.30a. The Fc-SAM-coverage of hnp-Au under the DMA tests was 0.23 ± 0.03 ML. During the oxidation of the FcC_6-SAM/hnp-Au, the hybrid stiffens by $\delta Y'/Y_0'$ = 2.5 % when the potential reaches E_{SHE} = 1.175 V (Figure 4.30b). At the begging of the anodic scan, it is difficult to distinguish the softening stage observed in the FcC_6-SAM/np-Au (L = 40 nm) as shown in Figure 4.27c. While the reverse potential scan leads to the material's softening up to the full ferroceniums to ferrocene transition at E_{SHE} = 0.470 V, following by the stiffening to 0.2-0.3 %, similarly to the findings in Figure 4.27c. The hysteresis in $\delta Y'/Y_0'$ vs. E_{SHE} may be explained by the presence of the left shoulder in the CV (Figure 4.30a), thus pointing to some irreversible processes in the monolayer. The variations of the scaled superficial density, $\delta q/\Theta_{Fc}$, versus E_{SHE} are given in Figure 4.30c. The similar values of $\delta q/\Theta_{Fc}$ were observed earlier in this thesis for the actuation (Figures 4.16b,e) and the elastic responses of the Fc-SAM/np-Au hybrids (Figures 4.28g,k). The hysteresis in $\delta q/\Theta_{Fc}$ plotted as a function of E_{SHE} points to the disorder within the monolayer. This, in turn, allows the electrolyte's ions approach the Au surface, and impacts on the electro-elastic coupling in the hybrids.

4.3.6.2 Size-dependent elastic behavior of Fc-SAM-modified np-Au

Figure 4.31a combines the size-dependent Fc-SAM-coverage and effective elastic response of the FcC_6-SAM-functionalized np-Au in a log-log scale. The relative stiffness change, $\delta Y'/Y_0'$ (blue closed symbols), exhibited a roughly linear decrease as the ligament size, L, increased. The largest response $\delta Y'/Y_0'$ of 3.0 % was found in the hybrids with L = 40 nm. The linear segment was observed on the decrease of $\delta Y'/Y_0'$ vs. L at $40 < L < 120$ nm, following by the non-linear dependence of $\delta Y'/Y_0'$ vs. L at $120 < L < 1000$ nm. The lowest $\delta Y'/Y_0'$ of 0.2 % was measured in the specimens with L = 1000 ± 120 nm.

The Fc-SAM surface coverage, Θ_{Fc} (open orange symbols), was found to decrease monotonically from 0.34 ± 0.04 ML (L = 40 nm) to 0.14 ± 0.04 ML (L = 120 nm) in Figure 4.31a. Θ_{Fc} exhibited a less pronounced slope (0.13 - 0.08 ML) in its variations versus L in a range of 180-1000 nm. These results can be explained by the increased amount of adsorption sites when $L < 100$ nm as the surface-to-volume ratio is enhanced. Here, hnp-Au is presented in Figure via the upper ligament level L = 120 nm ($\delta Y'/Y_0'$ - the red closed symbol and Θ_{Fc} - the red open symbol in Figure 4.31). The lower level ligaments promoted the higher Fc-SAM coverage that led to the enhanced effective Young's modulus changes compared to np-Au with a ligament size of 120 nm.

By plotting $\delta Y'/Y_0'$ as a function of Θ_{Fc} for L ranging from 40 to 120 nm in Figure 4.31b, a parabolic trend is observed in the FcC_6-SAM/np-Au. An enhanced $\delta Y'/Y_0'$ was found in the FcC_6-SAM/hnp-Au when comparing with the response of np-Au with the similar Fc-coverage.

Using Eq. 2.31, one can estimate an apparent ligament thickening, $\delta\tau$, in the Fc-SAM/np hybrids. Consequently, the surface excess elastic constant change, $\delta\mathbb{C}$, can be determined via Eq. 2.30. For the case of L = 40 nm, it gives values of $\delta\tau$ = 150 pm for the FcC_6-SAM/np-Au and $\delta\tau$ = 168 pm for the FcC_{11}-SAM/np-Au that results in $\delta\mathbb{C}$

of 20.9 N m^{-1} and 23.4 N m^{-1}, respectively.

The electro-elastic coupling parameter, λ, can be derived from the slope of the absolute effective stiffness variations, $\delta Y'$, versus the transferred charge, δQ, as shown in Figure 4.32. The best linear fit of the data in the capacitively charged non-modified np-Au yields the slope -522.49 ± 9.00 MPa C^{-1} (Figure 4.32a). The oxidation of the electroactive SAM in np hybrids results in the non-linear positive values of λ (Figures 4.32b,c).

To conclude, the overall effect of the electroactive alkanethiol Fc-SAM on the elastic properties of np-Au is pronounced. The stiffness of the Fc-SAM-modified np-Au undergoes the reversible elastic changes up to 3.5 % upon the redox-reactions in the Fc-based monolayer during the *in situ* DMA measurement in aqueous electrolyte of 1 M $HClO_4$. The impact of the surface excess elasticity on the elastic response of the Fc-SAM-modified np hybrids will be discussed in Chapter 5 (Section 5.3.3).

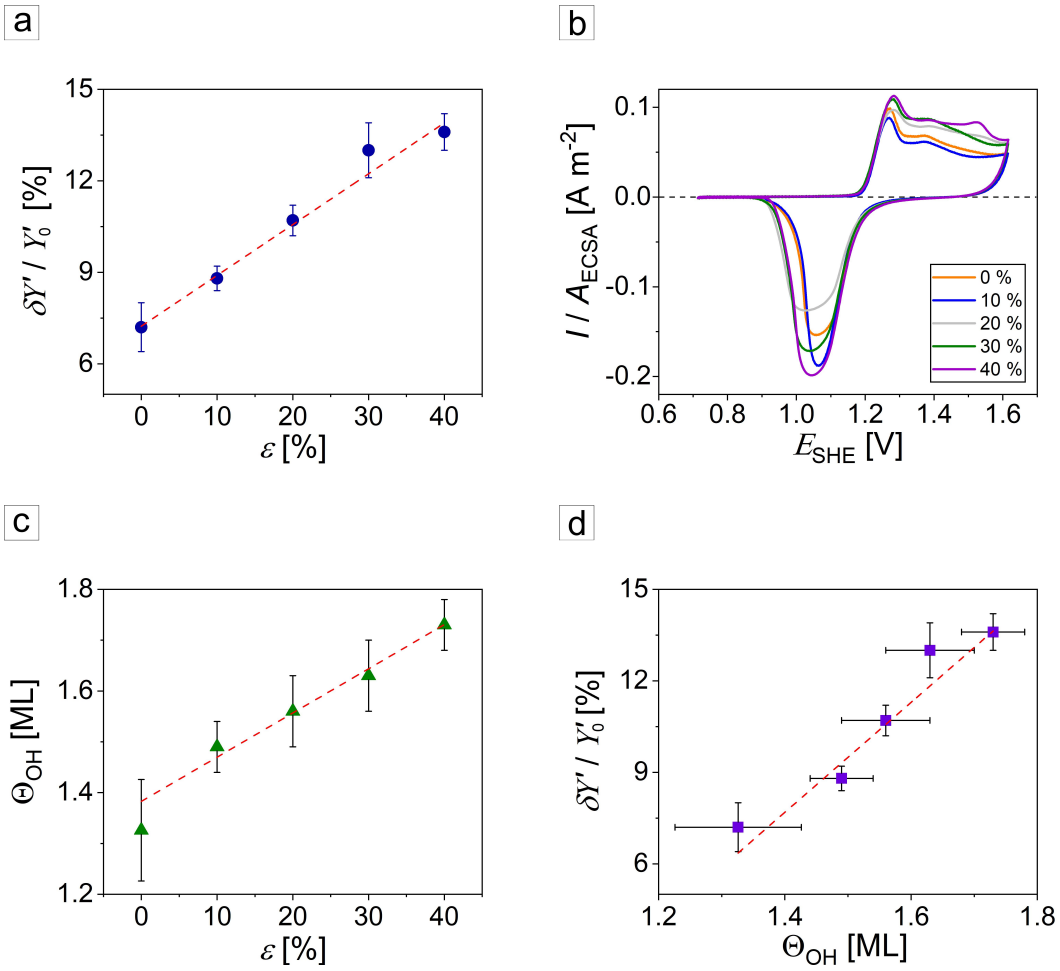

Figure 4.23: The prestrain effect on the elastic response of np-Au with a ligament size of 40 nm upon *in situ* DMA experiments at the potential cycling between E_{SHE} = 0.715 V and E_{SHE} = 1.615 V in 1 M $HClO_4$ at a scan rate of 5 mV s^{-1}. (a) The relative stiffness change, $\delta Y'/Y'_0$, plotted as a function of prestrain, ε. (b) The CVs of np-Au samples in non-deformed (0 %) and prestrained states (10-40 %). The current density, I/A_{ECSA}, is shown as a function of E_{SHE}. (c) The OH coverage, Θ_{OH}, as a function of ε. (d) $\delta Y'/Y'_0$ vs. Θ_{OH}. The error bars were calculated based on the data from 4 samples for each prestrain value. The red dash lines represent the linear fits.

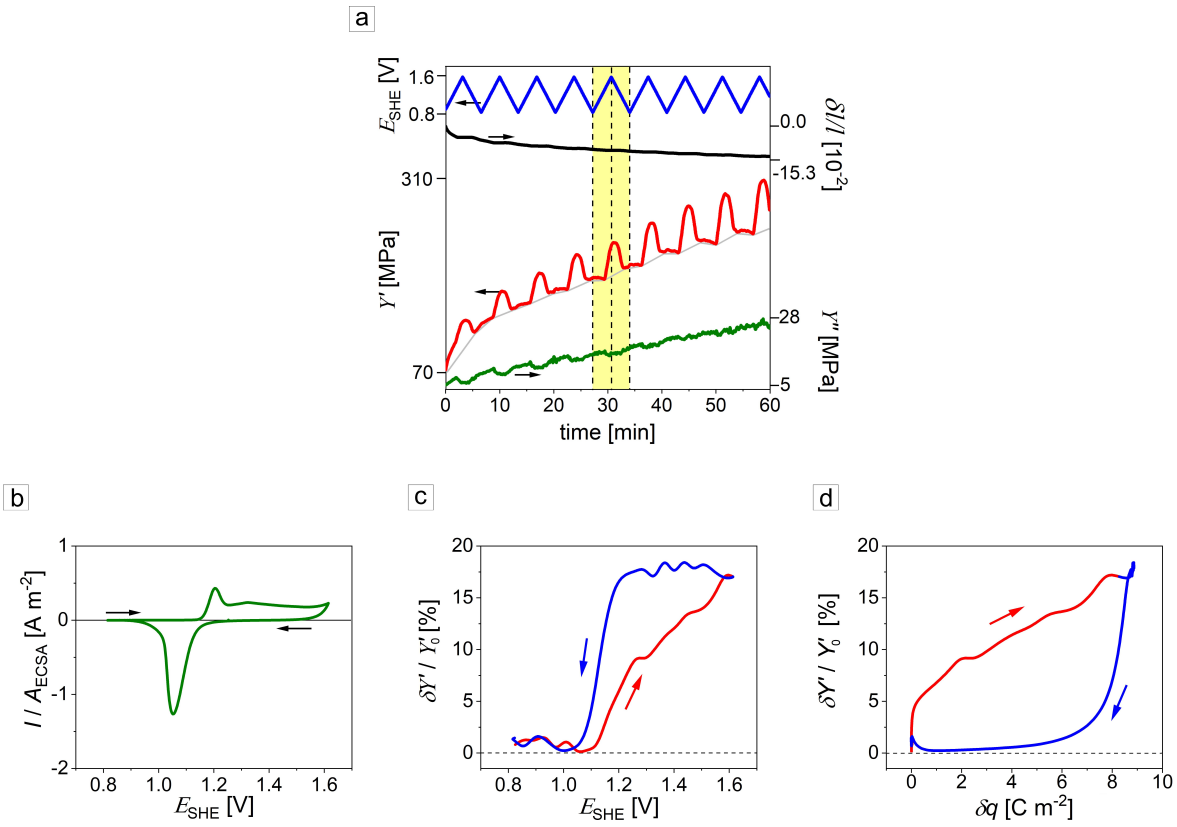

Figure 4.24: (a) The results of the *in situ* DMA experiment of hnp-Au/OH hybrid during the OH-electrosorption process in 1 M $HClO_4$ aqueous electrolyte at a scan rate of 5 mV s^{-1}. Variations of the storage modulus, Y' (red), the loss modulus, Y'' (green), and strain, $\delta l/l$ (black), are plotted vs. the potential, E_{SHE} (blue), and time. A single potential cycle is highlighted in yellow. The dashed lines indicate the change in the potential sweep direction. The grey line marks the baseline for Y', used to subtract a background due to the sample densification. (b) A typical CV response of the hybrid via the current density, I/A_{ECSA}, and E_{SHE}. (c) The relative stiffness change, $\delta Y'/Y'_0$, is given vs. E_{SHE}. (d) $\delta Y'/Y'_0$ vs. the transferred charge density, δq. The red and blue arrows in (c) and (d) indicate oxidation and reduction, respectively.

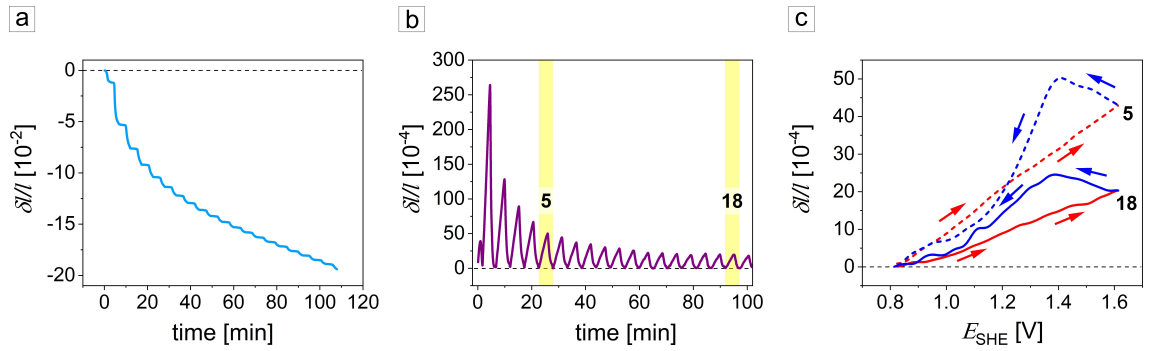

Figure 4.25: The strain, $\delta l/l$, variations in the hnp-Au/OH hybrids during the *in situ* DMA experiment in 1 M $HClO_4$ aqueous electrolyte at a scan rate of 5 mV s^{-1}. (a) $\delta l/l$ vs. time. (b) $\delta l/l$ vs. time after subtraction of the irreversible strain signal. The 5^{th} and 18^{th} CV cycles are highlighted in yellow. (c) $\delta l/l$ vs. the potential, E_{SHE}. The red and blue lines correspond to the oxidation and reduction, respectively. The numbers mark the 5^{th} (dashed lines) and 18^{th} (solid lines) CV cycles.

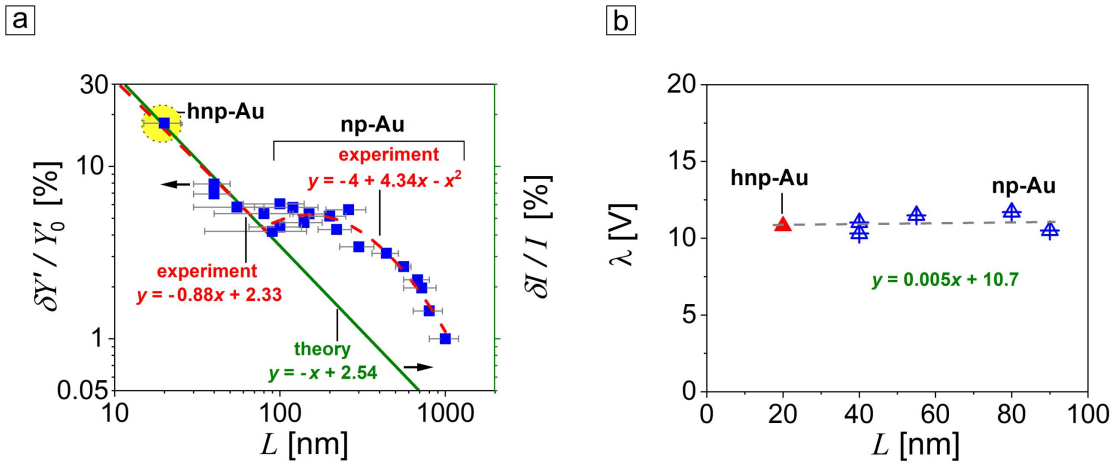

Figure 4.26: The results of the *in situ* DMA measurements upon the OH-electrosorption on np-Au and hnp-Au in 1 M $HClO_4$ at a scan rate of 5 mV s^{-1} and a comparison to the theory prediction using Eq. 2.31. (a) Relative stiffness changes, $\delta Y'/Y'_0$, and the bending stiffness of a ligament, $\delta I/I$, as functions of a ligament size, L. The comparison of experimental data (blue squares) with the theoretical prediction (green line). A ligament size is given with a standard deviation bar. The red dashed lines are linear and polynomial fits to the experimental data. The coefficients of determination, R^2, are 0.93 (linear fit) and 0.95 (polynomial fit) in the experiment. (b) The electro-elastic coupling parameter, λ, vs. L in np-Au (blue crossed triangles) and hnp-Au (red closed triangle). The grey dashed line is the linear regression of λ at $L < 100$ nm. $R^2 = 0.06$.

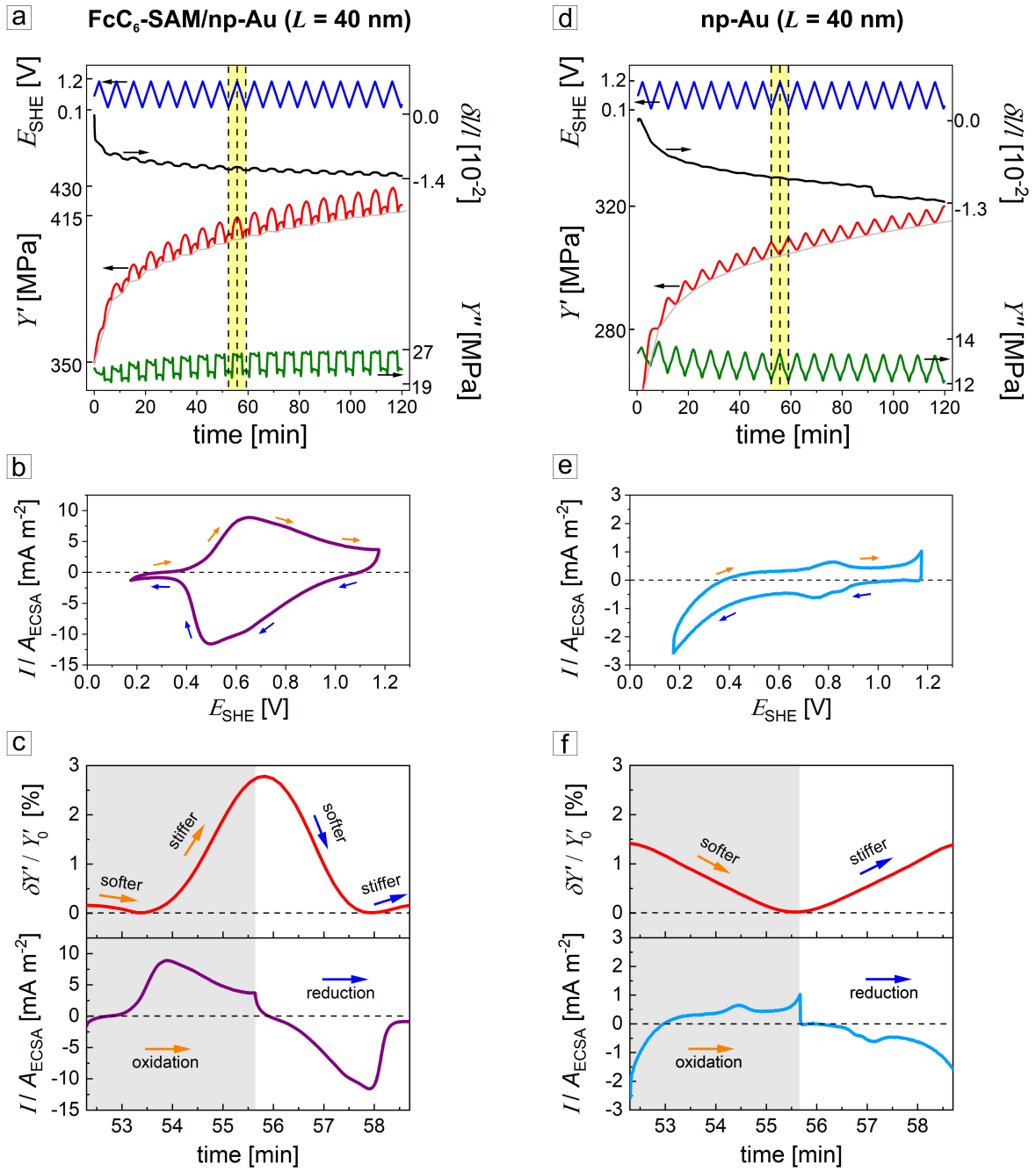

Figure 4.27: The results of the *in situ* DMA experiment on (a) FcC_6-SAM-modified and (d) non-modified np-Au with a ligament size L = 40 nm. Where Y' - the storage modulus, Y'' - the loss modulus, $\delta l/l$ - the strain, and E_{SHE} - the applied electric potential. A single potential cycle is highlighted in yellow. The grey lines indicate the baseline for the determination of the relative stiffness changes. The CV responses of (b) the FcC_6-SAM-modified (purple) and (e) the "bare" np-Au (light blue). Relative stiffness variations, $\delta Y'/Y'_0$, and the current density, I/A_{ECSA}, vs. time in (c) the FcC_6-SAM-modified and (f) the "bare" np-Au. The data is given for one potential cycle. The orange and blue arrows in (b)-(f) mark the oxidation and reduction scans, respectively. The electrolyte was 1 M $HClO_4$, a scan rate was 5 mV s^{-1}.

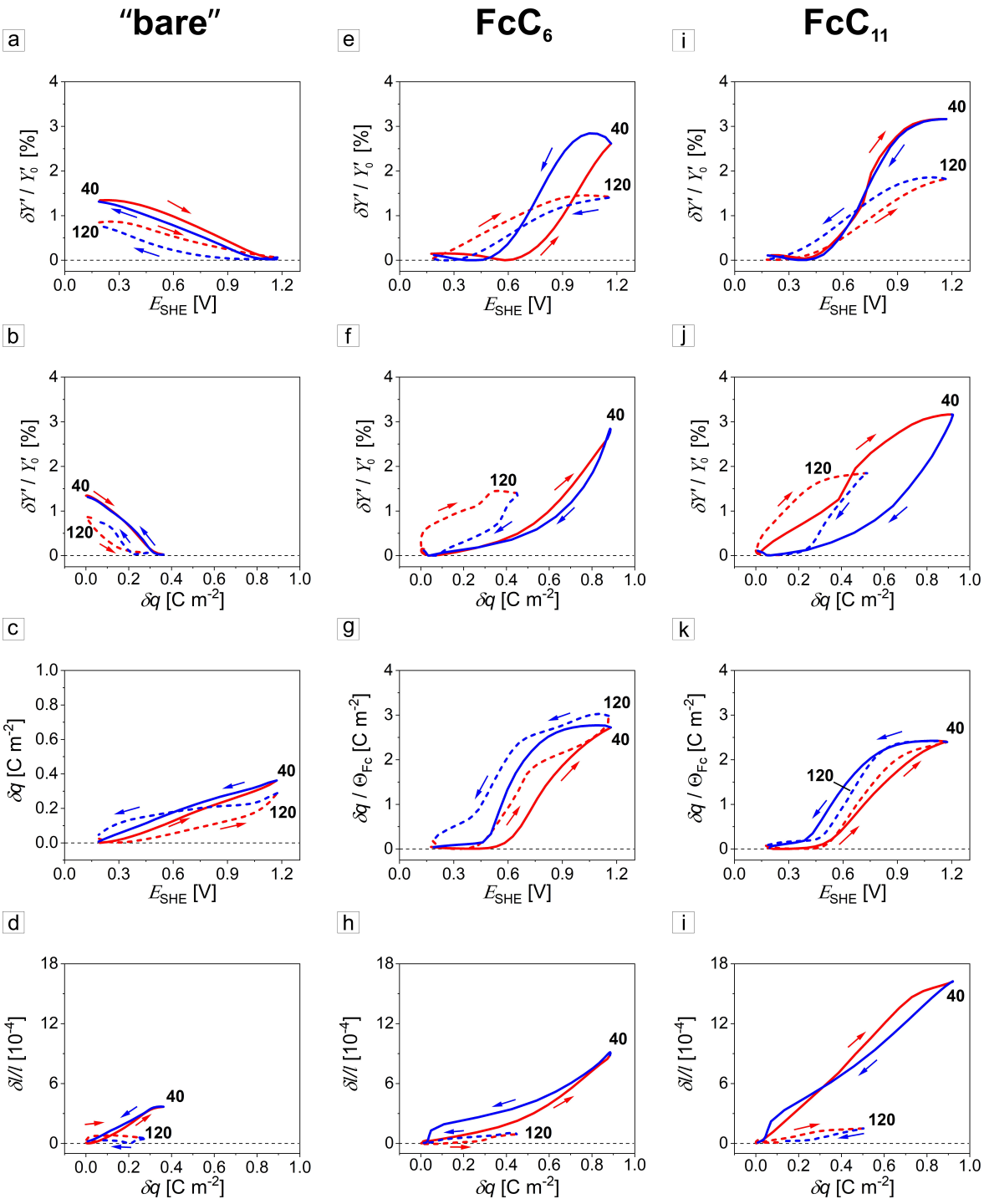

Figure 4.28: The summary of the *in situ* DMA findings on Fc-SAM-functionalized np-Au in 1 M $HClO_4$ electrolyte at a scan rate 5 mV s^{-1} (L in [nm] marked on plots as 40 and 120): "bare" (non-modified)(a)-(d), FcC_6-SAM-(e)-(h), FcC_{11}-SAM-modified (i)-(l) hybrids. The data presented via the relative stiffness variations, $\delta Y'/Y'_0$, strain, $\delta l/l$, potential, E_{SHE}, charge density, δq, and scaled charge density, $\delta q/\Theta_{\mathrm{Fc}}$. The red and blue arrows (lines) indicate oxidation and reduction scans, respectively.

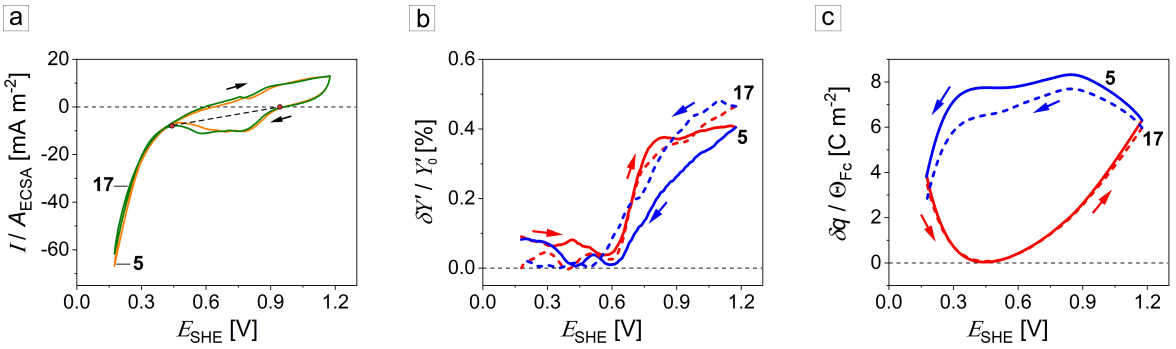

Figure 4.29: *In situ* DMA measurements on FcC_6-SAM/np-Au (L = 800 ± 82 nm) in 1 M $HClO_4$ at a scan rate 5 mV s^{-1}. (a) CV responses in the 5th (orange) and 17th (green) cycles. The dashed line indicates the background of the peak, the area under the line was used to determined the Fc-surface coverage. (b) Relative stiffness change, $\delta Y'/Y_0'$, vs. potential, E_{SHE}. (c) The scaled charge density, $\delta q/\Theta_{Fc}$, vs. E_{SHE}. The red and blue lines/arrows in (b) and (c) indicate the oxidation and reduction scans, respectively.

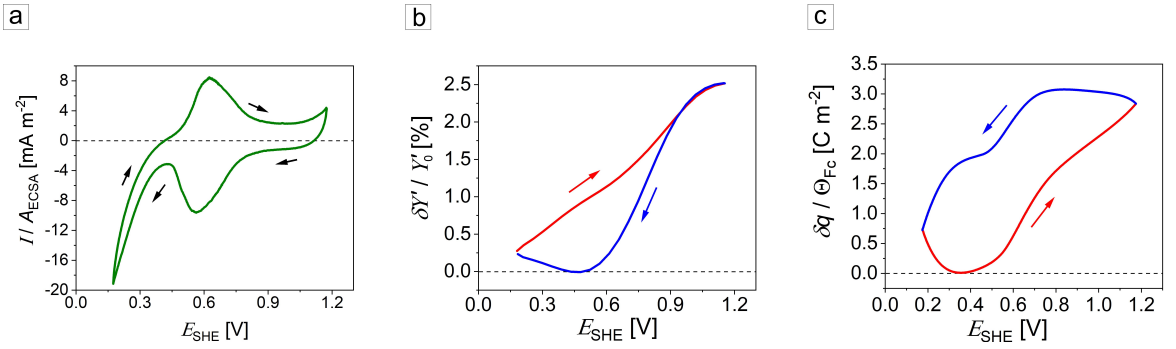

Figure 4.30: Results of the *in situ* DMA measurement on the FcC_6-SAM-functionalized hnp-Au ($L_{1,2}$ = 120/20 nm) in 1 M $HClO_4$ at a scan rate 5 mV s^{-1}. (a) The CV response of FcC_6-SAM/hnp-Au. (b) Relative stiffness change, $\delta Y'/Y_0'$, as a function of the potential, E_{SHE}. (c) The scaled transferred charge density, $\delta q/\Theta_{Fc}$ vs. E_{SHE}. The red and blue lines (arrows) in (b) and (c) indicate oxidation and reduction scans, respectively.

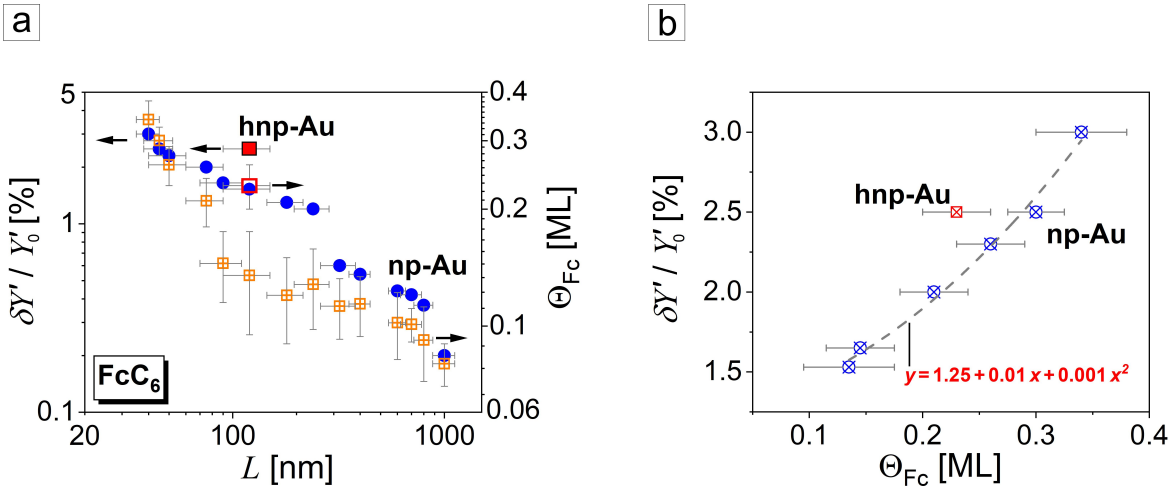

Figure 4.31: A summary of the experimental results on the tunable elasticity in the FcC_6-SAM/np hybrids obtained using *in situ* DMA setup. The electrolyte was in 1 M $HClO_4$, a potential scan rate was 5 mV s^{-1}. (a) Relative stiffness, $\delta Y'/Y'_0$, and FcC_6-SAM coverage, Θ_{Fc}, variations as functions of a ligament size, L, of np-Au (blue circles and orange squares) and hnp-Au (red squares). The closed symbols show $\delta Y'/Y'_0$ data and open ones correspond to Θ_{Fc}. The standard deviation bars are given in grey. (b) $\delta Y'/Y'_0$ vs. Θ_{Fc} for L ranging from 40 to 120 nm in np-Au (blue symbols) and hnp-Au (red symbol). The grey dashed line is a polynomial fit of the data with the coefficient of determination, R^2, of 0.99.

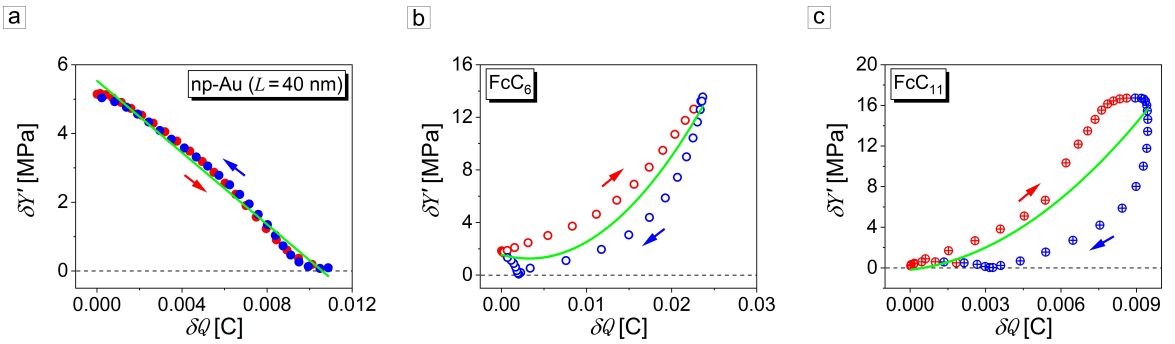

Figure 4.32: Absolute variations of the storage modulus, $\delta Y'$, as a function of the transferred net charge, δQ, in np-Au with the ligament size, L, of 40 nm. (a) The capacitive double-layer regime in the non-modified np-Au. The redox of (b) the FcC_6-SAM/np-Au and (c) the FcC_{11}-SAM/np-Au hybrids. The red and blue symbols (arrows) correspond to the oxidation and reduction scans, respectively. The green lines indicate the best (a) linear and (b), (c) polynomial fits of the experimental data. The potential, E_{SHE}, was tuned between 0.175 V and 1.175 V at a scan rate of 5 mV s^{-1} in 0.1 M $HClO_4$ aqueous electrolyte.

Chapter 5

Discussion

Electrochemistry provides a particularly convenient way of manipulating the chemistry at surfaces, especially when adsorption or electric charging phenomena take place. This manipulation is critical for understanding of an impact of these processes on the mechanics, which leads us to the discussion of the electro-chemo-mechanical coupling. One of the ways to characterize and evaluate the coupling is to focus on the local stresses of the solid surfaces [148]. These stresses can be quantified by the surface stress. The surface state can be tuned during adsorption or electric charging upon the mechanical testing of the macroscopic samples that opens up new functionalities.

The discussion begins with the actuation phenomenon in the surface-modified np-Au followed by the reversible changes of its effective Young's modulus revealed in electrochemical environment.

5.1 Enhanced actuation in hnp-Au via electrosorbed oxygen-species

Nanoporous metals actuate under imposed electrode potential change. Thus, they are ideal candidates that contribute to a concept of making metallic muscles which could convert the (electro)chemical energy directly into mechanical work, mimicking the behavior of biologic systems. The presence of a surface oxide may be advantageous for the actuation performance due to lower surface atom mobility (that stabilizes the np structure) [23].

Clean metal surfaces as well np metals as a whole tend to expand during adsorption of oxygen species such as OH^- with the stress-charge parameter $\varsigma < 0$ [35, 249]. When a negatively charged oxygen-species bind to a positively charged Au surface, the metal surface tend to expand laterally.

In this thesis, we employed *in situ* dilatometry as an indirect way to estimate the surface stress change, δf, and the electrocapillary coupling coefficient, ς. This technique has been previously utilized for np metals [10, 18, 63, 222]. The impact of the anodic oxide formation on the actuation response of np-Au (L = 120 nm) and hnp-Au ($L_{1,2}$ = 120/20 nm) was studied upon the potential cycling between E_{SHE} = 0.815 V and E_{SHE} = 1.615 V. Remarkably, hnp-Au exhibited the macroscopic length change amplitude (peak-to-peak) of $(\delta l/l)_{\mathrm{max}} = 4.7 \times 10^{-4}$, which is 3.6 times greater than the

strain observed in np-Au with L = 120 nm ($(\delta l/l)_{\max}$ = 1.3 × 10^{-4}) under the same test conditions (Figure 4.4d).

The enhanced strain amplitude in hnp-Au at the Au solid fraction, φ_{Au}, as low as 0.12 highlights the significance of the pore size and the structural hierarchy. The introduction of the second level of the porosity in np-Au increases the number of defects in the structure promoting additional adsorption sites. Consequently, the OH surface coverage, Θ_{OH}, rises up to 1.3 ± 0.1 ML in hnp-Au (vs. 1.0 ± 0.1 ML in np-Au). The OH coverage in excess of 1.0 was earlier reported for the as-prepared np-Au (1.2 ML) [18]. Later, Haensch *et al.* in [220] proved the surface oxide coverage up to 2.25 ML on np-Au under specific conditions (potential and exposure time). Additionally, Θ_{OH} up to 2 ML was observed on polycrystalline Au electrodes electrochemically oxidized in 0.1 M $HClO_4$ [161].

Earlier, Weissmüller *et al.* [10] showed that the observed strains in a np metal are consistent with the change of the surface stress due to the electrosorption where the localized charge up to a few tenths of an electron near each atom is strong enough to affect electron density and perturb the bonds between the atoms in plane. It is intuitive to expect that an increased Θ_{OH} would correlate with higher adsorbate-induced stresses. Due to the enhanced interactions between the adsorbed molecules and oxygen-species/Au (bond forces) in a 3D-like oxide-layer, the Au-O replacement turnover process becomes complicated, wherein Au atoms may migrate from terrace- or step-sites to adatoms sites and coordinate with oxygen (Section 2.3.2).

Our dilatometry experiments revealed that the OH-electrosorption process induced the surface stress changes, δf, of -3.20 ± 0.05 N m^{-1} in np-Au (L = 120 nm) at the transferred charge density, δq, of 4.75 C m^{-2}. Whereas the reversible oxidation of the hnp-Au resulted in δf of -7.52 ± 0.08 N m^{-1} at δq = 5.53 C m^{-2}. The larger δq leads to greater changes in the interatomic bonding forces between surface atoms causing the appearance of the hysteresis loop in δf vs. δq (Figure 4.4c). The stresses induced by the OH-electrosorption are noticeably larger than the stresses due to the capacitive charging/discharging of the same materials (Figure 4.3d). The phenomenon can be explained in a way that the capacitive charging/discharging involves the accumulation (redistribution) of a charge at the surface of the metal. This charge creates an electric field but does not significantly alter the volume or structure of the material itself comparing with the electrosorbed oxygen-species (Section 2.3.2), that overall results in the lower surface-induced stresses. This is supported by several studies [113, 139] that reported the dependence of the adsorbate, like oxygen or sulfur, induced stress changes on the coverage – as the neighboring adsorbate species may interact at high surface coverages.

In this work, the expansion of the hybrids upon oxidation resulted in the coupling parameters, ς, of -0.43 ± 0.04 V (hnp-Au) and -0.37 ± 0.03 V (np-Au, L = 120 nm) in a weakly adsorbing aqueous electrolyte of 1 M $HClO_4$. In the case of perchlorate electrolyte, a smaller fraction of the net charge is transferred away from the electrode's surface and towards bonds with adsorbed ions, which contributes to more negative values of ς [250]. The obtained negative coupling parameters are different from the coupling in clean transition metal surfaces [10, 113, 228] and oxidized Au surfaces [249, 250]. The discrepancy most likely arises from the different approaches employed to determine surface stress variations. Moreover, it is noteworthy that oxidized metal surfaces

exhibit $\varsigma > 0$ under specific experimental conditions (frequency/time variations [165] or a surface state of a test sample [18]). The conflicting results might point out to the differences in the OH-electrosorption processes, leading to changes in the (electro)-chemo-mechanical coupling at the surface.

Our findings confirmed the impact of the large specific surface area to the variations of f and q, in other words, the surface stress-charge response. In conclusion, *in situ* dilatometry experiments hold significant relevance as the obtained strain and surface stress are essential for evaluating the performance of porous materials in actuator applications.

5.1.1 Characteristics of hnp-Au actuators

Another important characteristics of an actuator is its mechanical stability parameterized by the "matched load", σ_{M}, at which the actuator does maximum work without mechanical failure. In the case of a linear elastic actuator, σ_{M} can be estimated via the maximum strain amplitude, $(\delta l/l)_{\mathrm{V}}$, and the effective macroscopic Young's modulus, Y^{eff}, using [23]:

$$\sigma_{\mathrm{M}} = \frac{1}{2} Y^{\mathrm{eff}} \left(\frac{\delta l}{l}\right)_{\mathrm{V}} \quad , \tag{5.1}$$

where $(\delta l/l)_{\mathrm{V}}$ - the maximum relative volume change. For hnp-Au with $\varphi_{\mathrm{Au}} = 0.119$, $(\delta l/l)_{\mathrm{V}} = 3(\delta l/l)_{\mathrm{max}} = 0.00141$ and $Y^{\mathrm{eff}} = 60$ MPa [15]. Thus, for the good actuation performance of hnp-Au, the yield strength should exceed $\sigma_{\mathrm{M}} > 0.0423$ MPa. This finding on the maximum pressure limits the practical applications of hnp-Au-based hybrids. The porous sample will yield and undergo further densification under higher loads, that will affect the overall functional and mechanical performance of the material [10].

Other measures for an actuator are the volumetric work (W_{V}) and mass-specific strain energy densities (W_{M}) at the matched load [10]:

$$W_{\mathrm{V}} = \frac{1}{2} Y^{\mathrm{eff}} \left(\frac{\delta l}{l}\right)_{\mathrm{V}}^{2} \tag{5.2}$$

and

$$W_{\mathrm{M}} = \frac{W_{\mathrm{V}}}{\rho} \quad , \tag{5.3}$$

where ρ denotes the density of the np material (2 g cm^{-3}). The energy density parameters W_{V} and W_{M} were estimated to be 59.70 J m^{-3} and 0.03 J kg^{-1}, respectively. The values are much lower than that of the skeleton muscle (40 kJ m^{-3}) [63] or previously published data for np metals: $W_{\mathrm{V}} = 0.016$-1.0 J cm^{-3} and $W_{\mathrm{M}} = 4.3$-160 J kg^{-1} for np-Pt synthesized by consolidating commercial Pt black with a nanocrystal size of 6 nm [10]; $W_{\mathrm{V}} = 6.0$ MJ m^{-3} and $W_{\mathrm{M}} = 1200$ J kg^{-1} for np-$Au_{0.8}Pt_{0.2}$ [63]; $W_{\mathrm{V}} = 1.64$ MJ m^{-3} and $W_{\mathrm{M}} = 191$ J kg^{-1} for ultrafine np-Pt [251]. The comparison of the actuator's measures in different materials can be found in [63].

The findings of this thesis indicate the need for further enhancement of the mechanical performance of hnp-Au and the development of its surface functionalization methods to better support applications in the field of actuator materials.

5.2 Electrochemistry and origin of actuation in np-Au/electroactive Fc-SAM

The first up to date consistent set of the experimental data on the Fc-SAM-induced actuation in np-Au was obtained in this thesis. The 6-(Ferrocenyl)hexanethiol (FcC_6-) and 11-(Ferrocenyl)undecanethiol (FcC_{11}-) SAMs were used to functionalize the planar Au and highly curved np-Au surfaces. To understand the findings, let us first consider the electrochemical characteristics of the hybrid materials.

5.2.1 Electrochemical response of Fc-SAM/np-Au

According to the CV responses obtained in 0.1 M $HClO_4$ (Figure 4.10) and physicochemical parameters (Table 4.2), the ferrocene surface coverage, Θ_{Fc}, was found to be strongly dependent on the structural features of Au substrates (Table 4.2), in agreement with [42, 252, 253]. Hierarchy in np-Au ($L_{1,2}$ = 120/20 nm) promoted the higher Θ_{Fc} adsorbate coverage up to 0.24 ± 0.05 ML (FcC_6-SAM) and 0.34 ± 0.05 ML (FcC_{11}-SAM) as compared to np-Au with L = 120 nm (Θ_{Fc} = 0.14 ± 0.05 ML for FcC_6-SAM, Θ_{Fc} = 0.17 ± 0.05 ML for FcC_{11}-SAM). A noticeable finding is Θ_{Fc} of 0.34 ± 0.05 ML (FcC_6-SAM) and 0.42 ± 0.05 ML (FcC_{11}-SAM) in np-Au (L = 40 nm) that is higher than in np-Au (L = 120 nm) and hnpg-Au ($L_{1,2}$ = 120/20 nm). The obtained values are larger than the theoretically proposed ones of Θ_{Fc} = 0.33 ML for the $(\sqrt{3}\times\sqrt{3})$R 30° structure of chemisorbed alkanethiols on the Au (111) surface [170]. In that case, the Fc-units will exhibit significant layering, also known as "buried" functional groups [194]. As a remarkable finding, only the standing-up phases of the Fc-SAMs were found in np hybrids, whereas the lying-down phase (striped phase [169]) was detected in the Fc-SAM/planar Au (Figure 4.5).

The stability studies by the first-principles calculations indicate that thiols form more stable attachments to the highly curved np-Au [252]. The stronger S-Au interactions govern the additional stability of the monolayer [253], as the reduction peaks in np-Au and hnp-Au (Figure 4.10) are shifted to more negative electrode potentials than in the planar Au (Figure 4.5). The improved stability was attributed to the increased binding energy explained by (1) defect sites on the np-Au surface and (2) the presence of the residual Ag [253]. The Au or Ag substrate determines the tilt angle of the alkyl backbone of the SAM (the details on the differences of the SAM packing mechanisms on Au and Ag can be found in [254, 255]).

Here, we observed the relatively low Fc-SAM coverage, Θ_{Fc}, of the hnp-Au's surface ($\Theta_{Fc} < 0.4$ ML) in contrast to the electrosorbed oxygen-species ($\Theta_{OH} > 1.0$ ML) as characterized by the electrochemical means in Section 5.1. We assume that the nanopores (20 nm or smaller) within hnp-Au may be inaccessible to the Fc-bearing SAM.

The shape of the CV peaks in hnp-Au are more symmetrical than in the CV of np-Au (L = 40 nm). This enables the fastest response times among the multiscale porous materials measuring 0.39 s for the FcC_6-SAM/hnp-Au and 0.53 s for the FcC_{11}-SAM/hnp-Au (Section 4.2.3.2). It agrees qualitatively with the expectation that the ion transport will be accelerated by the significant porosity in the low-density hnp-Au. For a comparison, the response rates of the polypyrrole-functionalized np-Au (L = 120 nm) under the potential "jumps" vary from 1.5 s to 3.3 s (depending on

the polymer fraction) [57]. The longer times point to the differences in the diffusion mechanisms of ClO_4^- between the Fc-SAM and PPy.

The significant peak shifts, broadening, and asymmetry in np-Au (L = 40 nm) are attributed to the heterogeneous binding sites, e.g., "buried" Fc-moieties within the monolayer in line with [179], which overall complicates the electron transfer process [256]. The electrostatic modeling of the interfacial potential distribution (Section 2.3.3.3) usually assumes that the redox centers are all located in one plane, at a certain distance from the electrode surface. But, Fc-groups are likely to be distributed within a range of distances from the electrode surface because of the surface defects. Besides, the "buried" Fc-moieties experience a more hydrophobic environment than those which are in contact with an electrolyte. In this case, the double-layer effects are expected to have a pronounced impact on the CVs, due to the variations of the local potential at each electron transfer plane [256]. Thus, the increased amount of the Fc-species, along with the relatively small pores, results in a delayed (4 times slower than in hnp-Au) response of the Fc-SAM/np-Au (L = 40 nm) hybrids to the potential switches between the oxidized and reduced states of the Fc-terminal groups of the SAM.

5.2.2 Origin of the redox-induced surface stress variation in Fc-SAM/planar Au

In this thesis, the deflection of the Fc-SAM-functionalized Au-coated Si cantilever under the applied voltage was found using the *in situ* cantilever bending technique. The observed surface stress changes, $\delta\sigma$, were -0.09 ± 0.05 N m^{-1} for the FcC_6-SAM/planar Au and -0.18 ± 0.05 N m^{-1} for the FcC_{11}-SAM/planar Au in 0.1 M $HClO_4$ aqueous electrolyte. These results reflect the electrochemical modulation of the monolayer and its influence on the overall mechanical response of the cantilever.

Understanding the factors contributing to the nature (compressive or tensile) and magnitude of surface stress changes in these systems can be challenging, particularly due to involved complex molecular interactions. Various mechanisms, including steric and electrostatic repulsions, configurational entropy, hydration forces, conformational changes, and variations in osmotic pressure, have been proposed to influence the resulting surface stress variations during the redox of the Fc-moiety [60, 205, 239]. These phenomena stem from the interplay of multiple interactions at the electrode/monolayer interface.

The electrochemical oxidation of the SAM-bound Fc to Fc^+ proceeds via the one-electron transfer and ion-pairing reactions [193]. Previous studies have highlighted the role of anions, such as ClO_4^-, in stabilizing Fc^+ through strong complex formation, resulting in 1:1 ion pairs at the monolayer/solution interface [196]. This stabilization diminishes Coulombic repulsion between adjacent Fc^+ groups as well as the positively charged gold surface and Fc^+. Consequently, Coulombic interactions are unlikely to be the primary driver of the observed mechanical deformation [60].

Instead, physical crowding of the Fc groups within the monolayer induces lateral in-plane repulsive forces (e.g., 132 pN per FcC_{11}-molecule). Moreover, the Fc to Fc^+ transformation leads up to 12° change in the static perchlorate solution contact angle, the monolayer volumetric expansion by 10-20 cm^3 mol^{-1} [60, 191, 192]. The latter

might produce an internal film pressure up to 0.2 GPa. As a result, the monolayer experiences lateral tension that tends to bend the Fc-SAM-functionalized cantilever. The magnitude of this deflection correlates with the distribution of the Fc-moieties within the electroactive layer, with a distinction between "isolated" (peak I in Figure 4.5) and "buried" (peak II in Figure 4.5) Fc-moieties. It indicates that the spatial arrangement and density of Fc units influence the surface stress response. On top of that, a disordering in the Fc-SAM may contribute to less cohesive intermolecular interactions and a more random distribution of Fc orientations. This reflects the differences in the tensile contributions of the chain-chain interactions to the overall surface stress of the Fc-SAM [60].

Disordering within the Fc-SAM can further diminish cohesive intermolecular interactions, resulting in a more random orientation of Fc groups. This disordering affects the collective interactions and the net surface stress, highlighting the importance of monolayer organization [60]. The quadratic dependence of the surface stress change on ferrocene fractional coverage observed in this (Figures 4.7c,f) and previous studies [60, 191] suggests that collective in-plane Fc^+-Fc^+ interactions, rather than isolated electron transfer events, are likely the main source of the surface stress changes.

The coupling parameters, ς, determined in this work for the FcC_6-SAM/planar Au (-0.27 ± 0.01 V) and FcC_{11}-SAM/planar Au (-0.51 ± 0.01 V) resemble the reported values for the Fc-SAM-functionalized microcantilevers of ς = -0.45 V in [60]. These parameters are qualitatively consistent with ς = -0.153 ± 0.011 V in the conductive polypyrrole/planar Au electrodes [226] but markedly different from ς in the "clean" Au surface of -2.00 ± 0.1 V [228]. The negative sign of ς points a net compressive surface stress associated with the redox process of the Fc-SAM.

This study confirms that electrochemical redox reactions within Fc-SAM monolayers induce measurable changes in surface stress, resulting in mechanical deflections of the cantilever. The interplay of molecular interactions governs the magnitude and nature of these stress responses. The findings enhance our understanding of the coupling between electrochemical stimuli and mechanical deformation at the nanoscale, providing insights relevant for the design of stimuli-responsive nanosystems, sensors, and actuators. Future work should further elucidate the detailed molecular mechanisms and explore the influence of monolayer organization and environmental conditions on the functional behavior of nanoporous materials.

5.2.3 Actuation mechanism in Fc-SAM/nanoporous gold hybrids

In this thesis, the reversible expansion-contraction (actuation) of the non-modified ("bare") and Fc-SAM-functionalized np-Au and hnp-Au was examined using *in situ* dilatometry under the potential cycling in 0.1 M $HClO_4$ aqueous electrolyte. The largest redox-induced macroscopic length changes (peak-to-peak), $(\delta l/l)_{max}$, were found in the samples with the highest Θ_{Fc} – $(\delta l/l)_{max}$ = 11.0 × 10^{-4} at Θ_{Fc} = 0.34 ± 0.05 ML in hnp-Au (L = 120/20 nm) and $(\delta l/l)_{max}$ = 12.0 × 10^{-4} at Θ_{Fc} = 0.42 ± 0.05 ML in np-Au (L = 40 nm) modified with the FcC_{11}-SAM.

The strain responses of the fabricated hybrids are in the same order as has been found in the np-Au/OH (Section 5.1) or in the np-Au/polypyrrole (PPy) when the

fraction of PPy in the pores below 20 % (up to 25 nm thick) [57]. Indeed, the actuation response of the Fc-SAM-functionalized np hybrids as characterized by the actuation coefficient (Section 4.2.3.4) proved the enhanced strain amplitudes at lower fraction of the stimuli-sensitive organic matter on the surface.

Understanding of the actuation phenomena induced by the complex organic adsorbates, such as the electroactive alkanethiol Fc-SAM, begins with the impact of the Fc-SAM on the silicon (micro)cantilevers coated by a nm-thick Au layer as presented in [60, 205] and discussed in Section 5.2.2. In summary, the monolayer experienced lateral tension during the oxidation, that caused the compressive surface stress changes in the cantilever, that was transformed into mechanical work (deflection).

Hence, the actuation of the np hybrid modified with the electroactive SAM can be attributed to the surface stress changes at the Au nanoligaments induced by the redox-processes within the monolayer. These stresses must be compensated by the stresses of the opposite sign in the subjacent Au bulk, leading to the reversible macroscopic length changes (strain) of the Fc-SAM/np hybrid during the potential cycling.

The quadratic variations of the strain with the charge density are in conflict with the electron transfer model presented for the electrolyte/Fc-SAM/Au interface in Figure 2.11 [194]. The authors of [194] found that the potential drop is linear for the alkyl chain length, n, of 5-11. Our findings on the non-linearity (for n = 6 and 11) point to the electronic changes in the nature of the Fc-electrode interaction and supramolecular changes within the monolayers at the highly curved surfaces of nanoporous materials. In the dense Fc-SAM, Fc-groups can be partially located in the different planes due to steric hindrance as the Fc units have larger diameters than the alkyl chain [256]. The observed non-idealities of the monolayers observed in the CV responses of the Fc-SAM/np hybrids (Section 4.2.3.1), among which peak splitting, peak broadening, and peak shifts, governed the difficulties in the oxidation of the "buried" Fc-moieties rather than the Fc units atop.

In this work, the exchange of the electrolyte's ions with the Fc-moieties resulted in the non-linear relation between the scaled strain, $(\delta l/l)/(\Theta_{Fc})^2$, and the scaled charge density, δq / Θ_{Fc}, in nanoporous hybrids (Figure 4.16c). Such results are in agreement with the findings for the np-Au/PPy actuators [57]. The non-linear variations of the actuation coefficient with the charge density highlights the electrochemical origin of the observed strain response, that is also typical notion for the strain-charge characteristics of actuators containing organic matter.

Speaking of the actuator characteristics, the energy density parameters – the volumetric work density, W_V (Eq. 5.2), and the mass-specific strain energy density, W_M (Eq. 5.3), – were estimated to be W_V = 327 J m^{-3} and W_M = 0.164 J kg^{-1}, respectively, for the FcC_{11}-SAM/hnp-Au hybrids. As it has been discussed in Section 5.2.1, the hierarchy-based np actuator does maximum work at the matched load of σ_M = 0.099 MPa.

The better mechanical performance was found in np-Au with L = 40 nm (φ_{Au} = 0.270) with Y^{eff} = 360 MPa. In the case of the FcC_{11}-SAM/np-Au (L = 40 nm), $\sigma_M > 0.648$ MPa is essential for practical applications. Here, ρ = 4.5 g cm^{-3} with the following characteristics of W_V = 2340 J m^{-3} and W_M = 0.520 J kg^{-1}. The relatively low values as compared to the previously reported W_V and W_M for nanoporous metals [10, 63, 251] point to the limitations for the potential applications of the hierar-

chical material. The findings of this work confirmed the need in further modifications of mechanical properties of the hierarchical networks.

To conclude, we demonstrate that the Fc-SAM-modified np hybrids exhibit the redox-activated macroscopic mechanical actuation. Upon oxidation in a perchlorate electrolyte, the hybrids respond to the surface stress induced by the lateral pressure via the collective re-orientational motions of the Fc-SAM. These motions are governed by the ion pairing between the electrolyte's anions and the redox-active ferrocene-moieties. Comparing with the anodic oxide, the actuation amplitudes of the Fc-SAM-functionalized np hybrids are of the same order, but required lower applied electric potentials and the superficial charge density that makes them ideal alternative for actuator and sensor technologies.

5.3 Electrochemically modulated elastic modulus variations and surface excess elasticity in np gold materials

The experimental findings on the cyclic changes in the effective elastic modulus of np-Au under various surface state modification approaches were presented in Chapter 4. Here, the discussion is devoted to how the theory of the surface excess elasticity — which has been earlier proposed to govern the tunable effective elastic response [56] — can explain the observations in this work.

5.3.1 Surface excess elasticity at clean Au surfaces

Using *in situ* dynamic mechanical analysis, a ligament size-dependent effective stiffness change was observed in np-Au upon the capacitive charging/discharging in 1 M $HClO_4$. The linear trend of the relative stiffness variations, $\delta Y'/Y_0'$, with a ligament size, L, is confirmed in this thesis (Figure 4.19).

By employing the theory of the surface excess elasticity, the authors of [56] explained the variations of the stiffness during the capacitive charging/discharging of np-Au (L = 45 nm) via an apparent excess ligament thickening, $\delta\tau$, of 88 pm. We assume that a change on the theoretical $\delta\tau$ via bending deformation, $\delta I'/I_0'$ (clean, charge neutral surface), and $\delta\tau$ calculated via the experimental data on $\delta Y'/Y_0'$ can be explained by the charge-induced changes during the capacitive charging/discharging of the Au surface (Figure 4.19a). The observed scatter in the experimental findings may be attributed to the coarsening-induced structural features (e.g., roughness and curvature), the loss of connectivity [97], other dominating deformation modes [257], residual Ag [34, 258–260], and/or predeformation (Section 4.3.3).

The employed in this thesis theory takes into account only bending stiffness of a nanobeam, while in the experiment, an impact of the torsion and tension is expected. Also, when a np material is subjected to compressive loading, elastic buckling may occur in its ligaments, leading to microstructural collapse [210]. In addition, higher-order elasticity effects such as shear softening or even shear instability of the bulk [71] along with nonlinear bulk elasticity are not readily separated from surface excess elasticity in the experiment.

The electro-elastic coupling parameter, λ, takes on negative values for the capacitive surface charging regime. This points to the weakening of the hybrids due to the electron deficiency in the bonding regions reducing both the surface stress and the surface excess elasticity [56]. In this thesis, the parameter λ varied from -31 V to -16 V with L from 40 to 1000 nm. The fluctuations of λ may be governed by the reasons discussed above for $\delta Y'/Y_0'$.

Our observations create a link between λ and Y^{eff} for solid networks with the bicontinuous nanostructure. In summary, the findings communicate a linear power-law relation between the elasticity variation amplitude and the ligament size on a log-log scale.

5.3.2 Impact of OH-electrosorption on elastic behavior of np-Au and surface excess elasticity: Comparison with theory

Mameka *et al.* [56] via the DMA experiments revealed a stiffening of np-Au (L = 45 nm) upon the electrosorption of oxygen-species in 1 M $HClO_4$ aqueous electrolyte. The phenomenon was explained by interpreting the stiffening of the hybrid as the equivalent of the apparent excess ligament thickening, $\delta\tau$, of 430 pm. The change of the surface elastic modulus, $\delta\mathbb{C}$, was found to be 60 N m^{-1}.

The findings of this thesis further elaborated the challenging task on the size-dependence of the electrochemically modulated elastic response of np-Au hybrids subjected to the oxidation in perchlorate electrolyte. We observed an excellent agreement of the surface excess elasticity theory via the bending deformation of the Au nanowires with the experiment for np-Au with relatively small structural sizes of 20 - 90 nm. The result can be understood by the domination of the surface over the bulk at this scale.

A remarkable result of the relative stiffness change, $\delta Y'/Y_0'$, of 17.8 % ± 0.8 % was measured in the hnp-Au/OH hybrids ($L_{1,2}$ = 120/20 nm). In the literature, preliminary findings showed that the uniaxial compression of hnp-Au resulted in a collapse of the large rings consisting of the upper-level ligaments, L_1, while the small connectivity rings formed of the lower-level ligaments, L_2, preserved their original structure [15, 247]. It is therefore expected that the effective elastic response of hnp-Au is governed by the lower-level ligaments.

A deviation of the experimental results on np-Au from the theory employed in [56] is observed at a ligament size larger than 100 nm. Such findings might be caused by a thermal coarsening-induced anisotropy that affects surface functionalities of np-Au [261]. Comparing the findings for the capacitively charged np-Au and the oxidized np-Au, it is clearly that the scatter from the linear trends and non-linear elastic behavior is mainly governed by the presence of the electrosorption of oxygen-species, along with the factors discussed in Section 5.3.1.

The variations of the relative effective elastic modulus, $\delta Y'/Y_0'$, of np-Au with L = 100-260 nm resemble the changes of the effective Young's modulus, Y^{eff}, in np-Au reported previously in [97].

The variations of λ at $L < 100$ nm take the average value of 10.7 V (Figure 4.26b). In contrast to the coupling λ for the clean Au surface (Section 5.3.1), the formation of the anodic oxide on np-Au is characterized by the positive values of λ. To conclude, these findings allow to assume a strong link between the adsorbate-induced bonding

rearrangement at the gold surface and the elastic response of the hybrids.

5.3.3 Elastic modulus modulation by electroactive SAM & surface excess elasticity

In this thesis, we present a significant advancement in the understanding of the elastic behavior of nanomaterials, specifically the reversible changes in Young's modulus associated with the redox reactions of electroactive ferrocene-terminated self-assembled monolayers (Fc-SAMs) on np-Au. This phenomenon, presented in Section 4.3.6, is explored for the first time in the literature, underlying the impact of the electrochemical state of the Fc-SAM on the mechanical properties of np-Au.

Our findings reveal that non-modified (clean) np-Au exhibits a decrease in stiffness during a positive electrode potential scan between E_{SHE} = 0.175 V and E_{SHE} = 1.175 V in a perchlorate electrolyte. This reduction in stiffness is attributed to the electron deficiency that weakens interatomic bonds between surface atoms [56]. In contrast, np-Au functionalized with the Fc-SAMs demonstrated an increase in stiffness in the same potential range (Figures 4.27, 4.28).

The oxidation of the Fc-SAM leads to the thickening of the film. Literature reports indeed indicate that the redox-active Fc-SAM increases its thickness from 110 pm to 145 pm for the FcC_6-SAM during oxidation in perchlorate electrolyte [191, 262]. Corresponding variations in the surface excess elastic constant, $\delta\mathbb{C}$, were estimated to be of 20.9 N m^{-1} (FcC_6-SAM/np-Au with L of 40 nm) and 23.4 N m^{-1} (FcC_{11}-SAM/np-Au with L of 40 nm), smaller than $\delta\mathbb{C}$ of 60 N m^{-1} determined for the np-Au/OH hybrids [56].

The electro-elastic coupling parameter, λ, in the capacitively charged non-modified np-Au took on negative values -522.49 ± 9.00 MPa C^{-1} (Figure 4.32a). The similar trend was observed in [56]. The oxidation of the electroactive SAM in np hybrids results in the non-linear positive values of λ (Figures 4.32b,c).

We further investigated the dependence of the relative stiffness change, $\delta Y'/Y_0'$, on the ligament size in the FcC_6-SAM-modified np hybrids. Our experimental results revealed the linear variations of the effective elastic modulus with a ligament size of 40 - 100 nm. Beyond this size, the non-linear response was observed.

The coarsening of np-Au led to a reduction in Θ_{Fc} and consequently in reduced $\delta Y'/Y_0'$. This observation can be attributed to the non-ideal characteristics of the monolayers, as discussed in Chapter 4 and in recent studies [195]. Notably, it is remarkable that organic molecules can maintain a flat orientation at coverages as low as 0.09 ML (this work) and adopt an upright configuration at higher coverages [124], with both orientations contributing to the observed elastic response and allowing the tuning the elastic modulus response of np-Au from more compliant to stiffer upon oxidation within the same potential window.

The reorientational motions within the monolayer during its oxidation discussed in Section 5.2.3 likely contribute to the change in the elastic response of the hybrids. Previous studies using electrochemical quartz crystal microbalance (EQCM) have shown that compact Fc-SAMs do not absorb water upon ferrocene oxidation and perchlorate ion pairing [263] (in line with [192]), in contrast to the plasticization (softening due to water uptake) occurring in the PPy-based materials [58]. For well-packed SAMs, the

strong two-dimensional lattice of Fc^{+}-ClO_4^{-} ion pairing at the monolayer/electrolyte interface behaves as a rigid layer [263]. This rigidity facilitates oscillation with the quartz crystal, enabling EQCM detection of mass changes, whereas weaker ion adsorption would yield less sensitivity in the EQCM response. A similar concept of a rigid two-dimensional ionic layer was discussed in [264], supported by findings from Fourier Transform Surface-Enhanced Raman Spectroscopy.

The tunable stiffness in the Fc-SAM/np-Au resembles the findings in the np hybrids with the electroactive PPy [58]. The monolayer undergoes the volume changes upon the oxidation similarly to the swelling of PPy. The authors of [58] reported that the oxidation of the PPy/np-Au (L = 160 ± 40 nm) in perchlorate electrolyte increases its relative stiffness changes up to 3 %, when the fraction of PPy increased to 30 % (40 nm thick). They attributed the phenomena to the enhanced interchain bonding in the PPy layer, during the cycling in a potential window between E_{SHE} = 0.4 V and E_{SHE} = 0.8 V. However, the surface stress change per charge density observed in Fc-SAM-based materials is larger than in the polymer-modified materials, in line with [60].

In our study, we confirmed that the oxidized Fc-SAM rigid layer enhances the stiffness in the Fc-SAM/np-Au hybrid, significantly influencing the electro-elastic coupling parameter, λ. The coupling in the Fc-SAM/np hybrids points to the more efficient response of the materials comparing with the anodic oxide formation in np networks.

In conclusion, the observed stiffening of soft-hard hybrid structures upon the oxidation of electroactive SAMs can be attributed to the collective re-orientational motions within the Fc-SAMs. This study marks the first measurement of relative stiffness changes up to 3.5 % in these novel hybrid materials. The results underscore a critical role of stimuli-sensitive layers in modulating the mechanical properties of nanoporous materials, offering promising avenues for future research and applications of responsive material systems.

Chapter 6

Summary and outlook

6.1 Summary

The surface plays a crucial role in the deformation behavior of nanoporous metals. This thesis investigates the mechanical properties of surface-modified nanoporous gold (np-Au), with structural sizes ranging from L = 40-1000 nm, and hierarchical nanoporous gold (hnp-Au), characterized by $L_{1,2}$ = 120/20 nm. The surface functionalization was achieved using anodic oxide and ferrocene-terminated alkanethiol self-assembled monolayers (Fc-SAM). A variety of experimental techniques was employed to explore the electro-chemo-mechanical coupling of these hybrid materials.

***In situ* dilatometry** in perchlorate electrolyte was employed to measure the actuation strain. The electrocapillary coupling of the bulk mm-sized np hybrid materials has been assessed. Notably, hnp-Au exhibited greater strain responses during the capacitive charging and the oxygen-species electrosorption compared to np-Au with a 120 nm ligament size. The smaller structural size in hnp-Au promoted the adsorption of the OH-species. All hybrids experienced expansion during the charging, characterized by a negative surface stress-charge coupling parameter, which reflects compressive surface stress.

The thesis introduces novel soft-hard hybrid actuators based on electrochemically dealloyed np-Au/hnp-Au with the ferrocene-bearing self-assembled monolayers (Fc-SAM), which demonstrate maximum macroscopic length changes of 12×10^{-4} and 11×10^{-4} for np-Au (40 nm) and hnp-Au, respectively — an order of magnitude higher than in non-modified np-Au. The findings confirm that introducing the multiscale porosity in np-Au enhances its functionalities. The actuation behavior strongly correlates with the transferred charge density, δq, upon the ferrocene redox reaction along with the coverage of the Fc-SAM, Θ_{Fc}. This testifies to the significant contribution of the redox-induced molecular interactions, in particular, the ion-pairing formation between Fc^+ and ClO_4^-, on the chemomechanical macroscopic strain of np-Au. The mean actuation coefficient of the Fc-SAM/np hybrids was found to be similar to the one in the np materials functionalized with the conductive polymers, yet, at the significantly lower fraction of the organic adsorbate.

Wetting the nanopore surfaces with electrolyte and transferring charge by applying an external voltage leads to surface stress changes and, hence, macroscopic strain of the porous body. The observations in this thesis emphasize the relevance of processes

occurring within the molecular layers for the surface stress-charge coupling and the effective functional behavior of the hybrid materials. By varying the molecules type and the applied potential, it is possible to modulate the extent of the actuation response of the smart stimuli-sensitive hybrids.

The second part of the thesis has been devoted to the investigation of the elastic properties of np-Au. ***In situ* dynamic mechanical analysis (DMA)** combined with an electrochemical cell enabled investigations of the reversible modulation of the capillary forces at gold surfaces on the effective stiffness response of np-Au. The impact of the surface on the elastic properties was qualitatively characterized via the surface excess elasticity theory. The variations of surface excess elastic modulus, $\delta\mathbb{C}$, and the electro-elastic coupling parameters, λ, were evaluated throughout of this thesis for "clean", OH-covered, and Fc-SAM-modified Au surfaces.

The linearly dependent $\delta\mathbb{C}$ and λ on L were estimated for the "clean" Au surface state. The variations of $\delta\mathbb{C}$ become more pronounced as the ligament size, L, decreases, whereas λ remains consistently negative and exhibits only minor changes across the entire range of L. The results indicate that np-Au turns more compliant at smaller L when its surface is capacitively (positively) charged.

Whereas the oxidation of the hybrids in perchlorate electrolyte resulted in a different trend. The L-independent λ at $L < 100$ nm was found. Here, λ takes on the positive average value of 10.7 V for the oxygen species electrosorption, implying the enhanced stiffness of the material in the oxidized state. The stiffening can be understood as an elastic behavior of apparently thicker gold nanoligament. The impact of the surface excess elasticity obviously becomes more pronounced when $L < 100$ nm. This line of reasoning is also applicable to hnp-Au as the functional response is presumed to be predominantly governed by the lower-level ligaments (20 nm).

Factors that may contribute to the discrepancies with the theory at larger L were discussed in the thesis, among which coarsening-induced structural features, loss of connectivity, possible different deformation modes, etc.

This thesis represents the first experimental study on the impact of the electroactive Fc-SAM on the elasticity of np metals. The most pronounced changes in the effective stiffness have been observed upon the Fc redox transformation similarly to the actuation behavior of the Fc-SAM/np-Au hybrids. The ligament-size-dependent effective elastic response of Fc-SAM/np-Au was found. To explain the phenomenon, the theory of the surface excess elasticity was employed in this case for the smallest L under study. The oxidation of the Fc-SAM/np-Au hybrids with with L of 40 nm resulted in up to 3.5 % stiffness change. While the corresponding apparent excess elastic constant variations, $\delta\mathbb{C}$, were 20.9 N m^{-1} for the FcC_6-SAM/np-Au and 23.4 N m^{-1} for the FcC_{11}-SAM/np-Au, respectively. These findings can be understood as elastic behavior of apparently thicker (up to 150 and 168 pm depending on the alkyl chain length) gold nanoligaments. The coupling parameters λ in the Fc-SAM-modified and the OH-electrosorbed np hybrids are qualitatively comparable. The eprocesses taking place in the monolayer upon its oxidation that caused variations of the surface stress of the metallic substrate resulted in the enhanced stiffness of np-Au.

In conclusion, this thesis provides experimental insights into the mechanics of the soft-hard hybrids under electrolyte environment. Roles of surface excess elastic modulus and surface stress were studied in the double layer region of nanoporous gold

(clean surface), OH^- adsorption/desorption on np-Au, and upon the redox reactions of the electroactive organic monolayers/np-Au. The experimental findings confirmed the impact of the capillary forces on the functional behavior of np-Au. Experimentally it was shown that the hierarchy in a np metal opens up new horizons for the research providing the enhanced functionalities and the fastest response rates.

6.2 Outlook

6.2.1 Surface chemistry effect on stiffness of np-Au

In this thesis, the effective elastic properties of np-Au have been studied in air and $HClO_4$ electrolyte. To probe the surface chemistry effect on the mechanics of the hybrids, the *in situ* DMA setup (METTLER TOLEDO) was used to study the relationship between the residual Ag and the stiffness of np-Au.

Figure 6.1 shows the effective elastic response of np-Au with the excess residual Ag (later given as np-Au-Ag) in 1 M H_2SO_4. According to the EDX, the sample composition of the electrochemically dealloyed sample was np-$Au_{86}Ag_{14}$ (at. %) prior to the DMA test. A typical current-voltammetry (CV) response of np-Au-Ag is given in Figure 6.1a for the 1^{st} and 50^{th} potential cycles. It is clear that the amount of the Ag decreases upon cycling. The Ag dissolution peak is shifted to more positive potentials (1^{st} cycle) as compared to the same peak ($E_{SHE} \approx 0.55$ V) in 1 M $HClO_4$ (Figure 3.5). The peak further shifts to the 0.55 V with the subsequent dissolution of Ag.

The absolute values of the storage, Y', and the loss moduli, Y'', remain almost invariant throughout the experiment. The strain, ε, variations are in line with the previous findings – the hybrid experiences expansion upon oxidation and contracts during the reverse scan (Figure 6.1b). The relative effective stiffness change, $\delta Y'/Y'_0$, up to 230 % was observed in np-Au-Ag under the potential cycling in 1 M H_2SO_4. The $\delta Y'/Y'_0$ value decreases with the number of the cycles down to 14.95 % after 10 hours of the DMA measurement. The reproducible result was obtained for the data set of 5 samples.

The oxidation of np-Au-Ag in 1 M H_2SO_4 might hinder the OH^- electrosorption process at the surface as the peak corresponding to the 100 terraces [265], which is typically observed on np-Au at E_{SHE} = 1.3 V, is diminished. Thus, the excess residual Ag provokes the formation of the complex interface between the electrolyte and the metal surface. Previous studies [266] indicate a resistive porous layer Ag_2SO_4 formation on the working electrode upon the positive potential scan with a sweep rate 5 mV s^{-1}. The layer gradually dissolves and fresh Ag is exposed to the electrolyte, which is able to be oxidized to Ag_2SO_4 under further CV cycles. The events taking place upon the reduction (between E_{SHE} = 1.4 V and E_{SHE} = 0.9 V) of np-Au-Ag add on to the $\delta Y'/Y'_0$ change (blue lines in Figures 6.1c,d). To understand the phenomenon, the further research is needed.

To conclude, other electrolytes and the master alloy composition can be employed to tune microstructure [258] of np metals and to continuously modulate its elastic behavior. This approach is a promising tool to open up new functionalities of these materials. Understanding of the surface chemistry-mechanics coupling in np metals requires further research.

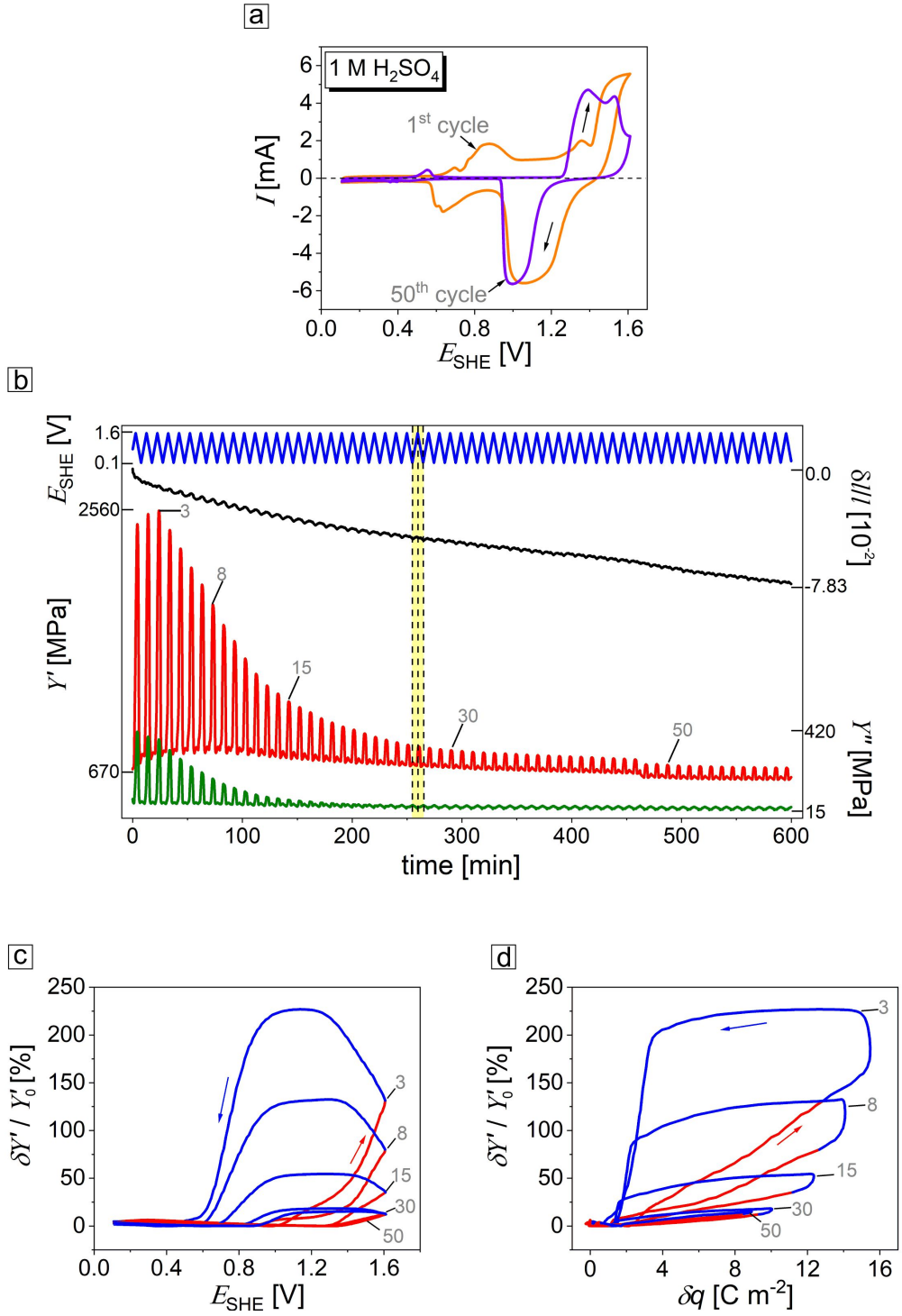

Figure 6.1: The results of the *in situ* DMA experiment on np-Au with residual Ag in 1 M H_2SO_4 aqueous electrolyte at a scan rate of 5 mV s^{-1}. (a) CV responses of the sample during the 1st (orange) and 50th (violet) potential cycles. (b) 10 hours experimental findings on the storage modulus, Y', loss modulus, Y'', and strain, $\delta l/l$, variations upon the tunable electric potential, E_{SHE}. The numbers 3, 8, 15, 30, and 50 correspond to the potential cycles. The single potential cycle is highlighted by yellow, the dash lines signalize the change in the potential sweep direction. The relative effective stiffness changes, $\delta Y'/Y'_0$, as a function of E_{SHE} (c), and the transferred charge density, δq (d), are given for the marked cycles. The red and blue arrows refer to the oxidation and reduction, respectively.

6.2.2 Plastic behavior of Fc-SAM-modified np-Au in electrolyte

Preliminary studies on the plastic properties of np-Au in electrolyte environment revealed a pronounced contribution of various surface effects (Section 1.2). For example, the effect of the OH-electrosorption on the plasticity of bulk np-Au was studied by Jin and Weissmüller in [55]. By polarizing the internal interface via an applied electric potential, the authors reversibly tuned such properties as yield strength, flow stress, and ductility of the np material. A role of the surface tension on the plastic properties was highlighted along with surface stress and surface excess elasticity. However, there are still some open scientific questions. How do more complex adsorbates affect the mechanics of high surface area materials? Is surface tension dominant factor in the plasticity of a np metal at any adsorbates [104]?

In this work, the plastic properties of the FcC_6-SAM-modified np-Au were studied *in situ* in 0.1 M $HClO_4$ under uniaxial compression. To investigate the impact of the adsorbate state on the plasticity of np-Au, the experiments were carried out at the potential jumps corresponding to the oxidized (E_{SHE} = 0.8 V) and reduced (E_{SHE} = 0.2 V) states of the Fc-SAM. The potential jumps were applied after engineering strain reached 10 % (plastic regime). The potential was switched every 10 min.

The reference samples were "bare" np-Au with L of 40 and 120 nm. Figure 6.2a illustrates typical voltammograms of the non-modified materials in 0.1 M $HClO_4$ at a scan rate 5 mV s^{-1} recorded before the mechanical testing. The potential window chosen for the plasticity experiments corresponds to the capacitive double layer region (Figure 3.5).

Typical CV responses of the FcC_6-SAM-modified np-Au with L = 40 and 120 nm are given in Figure 6.2b. The Fc surface coverages, Θ_{Fc}, were 0.39 ± 0.02 ML (L = 40 nm) and 0.14 ± 0.02 ML (L = 120 nm) throughout the experimental series.

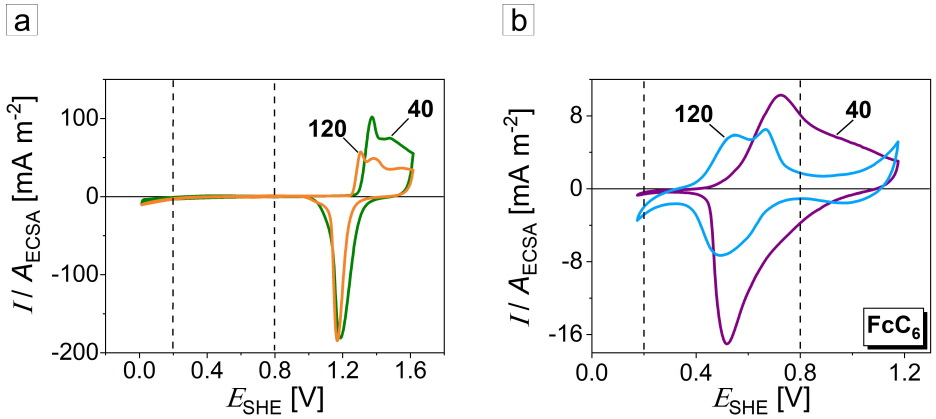

Figure 6.2: The CV responses of (a) "bare" and (b) FcC_6-SAM-modified np-Au with ligament sizes of 40 and 120 nm. The black dashed lines indicate the potentials jumps at E_{SHE} = 0.2 V and E_{SHE} = 0.8 V, respectively, as a means to control the charging/discharging in the "non-modified" np-Au and the redox state of the monolayer in the Fc-SAM/np-Au.

Figure 6.3a displays the stress-strain, σ - ε_{eng}, curves of the materials under study obtained and strain rate 10^{-4} s^{-1} at potential jumps between E_{SHE} = 0.2 V and E_{SHE} = 0.8 V. The reproducible data was obtained for at least 5 samples of each hybrid type in the body of this work. Remarkably, a surface-sensitive plastic behavior was observed

for all tested hybrids. The compression tests under potential jumps revealed that the strengthening of the "bare" np-Au occurred when the lower potential of 0.2 V was applied (Figure 6.3b). The surface effect is clear when comparing the plastic behavior of np-Au with ligaments of 40 and 120 nm, as the variations on σ decrease at larger ligament size. Moreover, the flow stress variations get larger with increasing ε_{eng} in all "bare" np samples in Figure 6.3a.

A striking observation on the flow stress variations is due to the impact of the FcC_6-SAM on the plastic properties of np-Au as shown in Figure 6.3a and zoomed in Figure 6.3c. The hybrid experienced weakening at the lower potential. The flow stress drops when the potential was switched from 0.8 V to 0.2 V. At the higher potential of 0.8 V, the oxidation of the Fc-moiety caused strengthening of the hybrids.

Figure 6.4 combines the variations of the flow stress via the flow stress at the upper potential, $\sigma_{0.8}^{\text{flow}}$, versus the flow stress at the lower potential, $\sigma_{0.2}^{\text{flow}}$. For the case of the Fc-SAM-modified np-Au, the changes are presented via $\sigma_{0.8}^{\text{flow}}/\sigma_{0.2}^{\text{flow}}$. A reverse way via $\sigma_{0.2}^{\text{flow}}/\sigma_{0.8}^{\text{flow}}$ is used for the "bare" np-Au.

In the non-modified np-Au $\sigma_{0.2}^{\text{flow}}/\sigma_{0.8}^{\text{flow}}$ increased with strain, ε_{eng}. The changes of $\sigma_{0.2}^{\text{flow}}/\sigma_{0.8}^{\text{flow}}$ varied from 1.03 to 1.10 for the samples with L = 40 nm and from 1.02 to 1.08 for the samples with L = 120 nm throughout the measurement. In contrast to the trend found in the "bare" np-Au, $\sigma_{0.8}^{\text{flow}}/\sigma_{0.2}^{\text{flow}}$ decreased upon deformation of the FcC_6-modified np-Au from 1.05 to 1.03 for the samples with L = 40 nm and from 1.03 to 1.01 for the samples with L = 120 nm.

In contrast to the OH-electrosorption, the Fc-SAM remains clamped at the surface upon the redox-reaction during the compression. In that case, a mechanism of the plastic deformation might differ and should be further investigated.

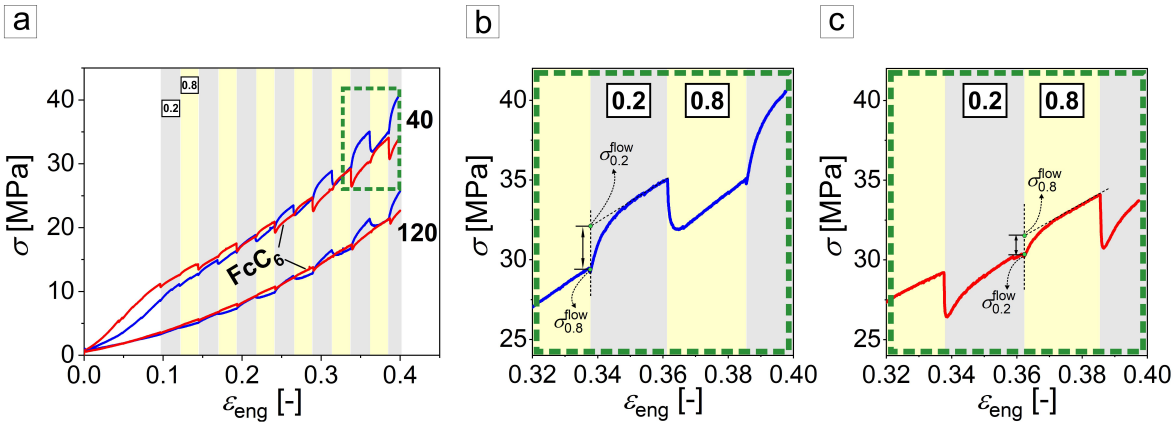

Figure 6.3: (a) The stress-strain, σ-ε_{eng}, behavior of the FcC_6-SAM-modified (red curves) and "bare" (blue curves) np-Au during *in situ* compression in 0.1 M $HClO_4$ at strain rate 10^{-4} s^{-1}. The potential jumps between E_{SHE} = 0.2 V and E_{SHE} = 0.8 V are shown in grey and yellow, respectively. The potentials were applied after ε_{eng} reached 0.1. Ligament sizes of np-Au specimen are marked as 40 and 120 (in nm). Green dashed area shows zoomed-in plots of (b) "bare" and (c) FcC_6-SAM-modified np-Au (40 nm). The flow stress jump values were determined as shown by black dashed lines (marked as $\sigma_{0.8}^{\text{flow}}$ and $\sigma_{0.2}^{\text{flow}}$ at E_{SHE} = 0.8 V and E_{SHE} = 0.2 V, respectively).

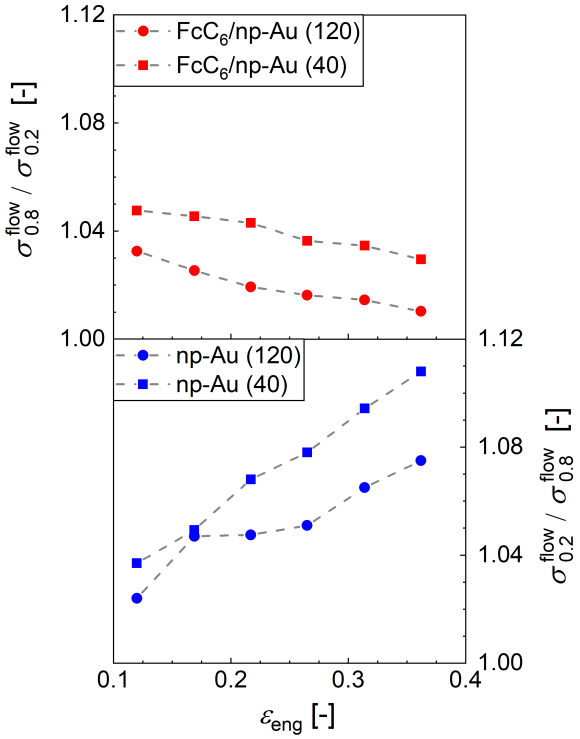

Figure 6.4: The results of the *in situ* compression under the potential jumps between E_{SHE} = 0.2 V and E_{SHE} = 0.8 V in 0.1 M $HClO_4$ at strain rate 10^{-4} s^{-1}. The corresponding maximum flow stresses in the "bare" np-Au are given via $\sigma_{0.2}^{\mathrm{flow}}/\sigma_{0.8}^{\mathrm{flow}}$ (blue symbols) and via (b) $\sigma_{0.8}^{\mathrm{flow}}/\sigma_{0.2}^{\mathrm{flow}}$ (red symbols) in the FcC_6-SAM/np-Au hybrids. The structural sizes are given as 40 and 120 (in nm).

Bibliography

[1] Pickering, H. W. Characteristic features of alloy polarization curves. *Corrosion Science* **1983**, *23*, 1107–1120.

[2] Newman, R. C.; Corcoran, S. G.; Erlebacher, J.; Aziz, M. J.; Sieradzki, K. Alloy corrosion. *MRS Bulletin* **1999**, *24*, 24–28.

[3] Lai, L.; Gaskey, B.; Chuang, A.; Erlebacher, J.; Karma, A. Topological control of liquid-metal-dealloyed structures. *Nature Communications* **2022**, *13*, 2918.

[4] Erlebacher, J.; Aziz, M. J.; Karma, A.; Dimitrov, N.; Sieradzki, K. Evolution of nanoporosity in dealloying. *Nature* **2001**, *410*, 450–453.

[5] McCue, I.; Karma, A.; Erlebacher, J. Pattern formation during electrochemical and liquid metal dealloying. *MRS Bulletin* **2018**, *43*, 27–34.

[6] Wei, S.; Wei, Y.; Chen, T.; Liu, C.; Tang, Y. Porous lithium ion sieves nanofibers: General synthesis strategy and highly selective recovery of lithium from brine water. *Chemical Engineering Journal* **2020**, *379*, 122407.

[7] Qian, L. H.; Chen, M. W. Ultrafine nanoporous gold by low-temperature dealloying and kinetics of nanopore formation. *Applied Physics Letters* **2007**, *91*.

[8] Braun, M. M.; Pilon, L. Effective optical properties of non-absorbing nanoporous thin films. *Thin Solid Films* **2006**, *496*, 505–514.

[9] Sun, Y.; Ye, J.; Shan, Z.; Minor, A. M.; Balk, T. J. The mechanical behavior of nanoporous gold thin films. *JOM* **2007**, *59*, 54–58.

[10] Weissmuller, J.; Viswanath, R. N.; Kramer, D.; Zimmer, P.; Wurschum, R.; Gleiter, H. Charge-induced reversible strain in a metal. *Science* **2003**, *300*, 312–315.

[11] Li, J.; Jiang, H.; Yu, N.; Xu, C.; Geng, H. Fabrication and characterization of bulk nanoporous copper by dealloying Al-Cu alloy slices. *Corrosion Science* **2015**, *90*, 216–222.

[12] Kramer, D.; Viswanath, R. N.; Weissmüller, J. Surface-stress induced macroscopic bending of nanoporous gold cantilevers. *Nano Letters* **2004**, *4*, 793–796.

[13] Sun, L.; Chien, C.-L.; Searson, P. C. Fabrication of nanoporous nickel by electrochemical dealloying. *Chemistry of Materials* **2004**, *16*, 3125–3129.

[14] Li, R.; Liu, X. J.; Wang, H.; Wu, Y.; Chu, X. M.; Lu, Z. P. Nanoporous silver with tunable pore characteristics and superior surface enhanced Raman scattering. *Corrosion Science* **2014**, *84*, 159–164.

[15] Shi, S.; Li, Y.; Ngo-Dinh, B.-N.; Markmann, J.; Weissmüller, J. Scaling behavior of stiffness and strength of hierarchical network nanomaterials. *Science* **2021**, *371*, 1026–1033.

[16] Fujita, T. Hierarchical nanoporous metals as a path toward the ultimate three-dimensional functionality. *Science and Technology of Advanced Materials* **2017**, *18*, 724–740.

[17] Shi, H.; Zhou, Y.-T.; Yao, R.-Q.; Wan, W.-B.; Ge, X.; Zhang, W.; Wen, Z.; Lang, X.-Y.; Zheng, W.-T.; Jiang, Q. Spontaneously separated intermetallic Co_3Mo from nanoporous copper as versatile electrocatalysts for highly efficient water splitting. *Nature Communications* **2020**, *11*, 2940.

[18] Jin, H.-J.; Parida, S.; Kramer, D.; Weissmüller, J. Sign-inverted surface stress-charge response in nanoporous gold. *Surface Science* **2008**, *602*, 3588–3594.

[19] Haensch, M.; Balboa, L.; Graf, M.; Olaya, A. R. S.; Weissmüller, J.; Wittstock, G. Mass Transport in Porous Electrodes Studied by Scanning Electrochemical Microscopy: Example of Nanoporous Gold. *Chem.Electro.Chem.* **2019**, *6*, 3160–3166.

[20] Gleiter, H.; Weissmüller, J.; Wollersheim, O.; Würschum, R. Nanocrystalline materials: A way to solids with tunable electronic structures and properties? *Acta Materialia* **2001**, *49*, 737–745.

[21] Snyder, J.; Fujita, T.; Chen, M. W.; Erlebacher, J. Oxygen reduction in nanoporous metal-ionic liquid composite electrocatalysts. *Nature Materials* **2010**, *9*, 904–907.

[22] Ding, Y.; Chen, M. Nanoporous metals for catalytic and optical applications. *MRS Bulletin* **2009**, *34*, 569–576.

[23] Jin, H.-J.; Weissmüller, J. Bulk nanoporous metal for actuation. *Advanced Engineering Materials* **2010**, *12*, 714–723.

[24] Cheng, C.; Lührs, L.; Krekeler, T. Simultaneous enhancement of actuation strain and mechanical strength of nanoporous Ni-Mn actuators. *Advanced Electronic Materials* **2021**, *7*, 2100381.

[25] Zhang, J.; Li, C. M. Nanoporous metals: fabrication strategies and advanced electrochemical applications in catalysis, sensing and energy systems. *Chemical Society Reviews* **2012**, *41*, 7016–7031.

[26] Jalas, D.; Shao, L.-H.; Canchi, R.; Okuma, T.; Lang, S.; Petrov, A.; Weissmüller, J.; Eich, M. Electrochemical tuning of the optical properties of nanoporous gold. *Scientific Reports* **2017**, *7*, 44139.

[27] Wang, Z.; Du, J.; Zhang, Y.; Han, J.; Huang, S.; Hirata, A.; Chen, M. Free-standing nanoporous gold for direct plasmon enhanced electro-oxidation of alcohol molecules. *Nano Energy* **2019**, *56*, 286–293.

[28] Koya, A. N.; Zhu, X.; Ohannesian, N.; Yanik, A. A.; Alabastri, A.; Zaccaria, R. P.; Krahne, R.; Shih, W.-C.; Garoli, D. Nanoporous metals: From plasmonic properties to applications in enhanced spectroscopy and photocatalysis. *ACS Nano* **2021**, *15*, 6038–6060.

[29] Zhao, H.; Lei, D.; He, Y.-B.; Yuan, Y.; Yun, Q.; Ni, B.; Lv, W.; Li, B.; Yang, Q.-H.; Kang, F. Compact 3D copper with uniform porous structure derived by electrochemical dealloying as dendrite-free lithium metal anode current collector. *Advanced Energy Materials* **2018**, *8*, 1800266.

[30] Li, Q.; Zhu, S.; Lu, Y. 3D porous Cu current collector/Li-metal composite anode for stable lithium-metal batteries. *Advanced Functional Materials* **2017**, *27*, 1606422.

[31] Wittstock, G.; Bäumer, M.; Dononelli, W.; Klüner, T.; Lührs, L.; Mahr, C.; Moskaleva, L. V.; Oezaslan, M.; Risse, T.; Rosenauer, A. Nanoporous gold: From structure evolution to functional properties in catalysis and electrochemistry. *Chemical Reviews* **2023**, *123*, 6716–6792.

[32] Sun, Y.; Burger, S. A.; Balk, T. J. Controlled ligament coarsening in nanoporous gold by annealing in vacuum versus nitrogen. *Philosophical Magazine* **2014**, *94*, 1001–1011.

[33] Qi, Z.; Weissmuller, J. Hierarchical nested-network nanostructure by dealloying. *ACS Nano* **2013**, *7*, 5948–5954.

[34] Krekeler, T.; Straßer, A.; Graf, M.; Wang, K.; Hartig, C.; Ritter, M.; Weissmüller, J. Silver-rich clusters in nanoporous gold. *Materials Research Letters* **2017**, *5*, 314–321.

[35] Weissmüller, J. Electrocapillarity of solids and its impact on heterogeneous catalysis. *Electrocatalysis* **2013**, *14*, 163–220.

[36] Shreiber, D.; Jesser, W. A. Size dependence of lattice parameter for $Si_xGe_1 - x$ nanoparticles. *Surface Science* **2006**, *600*, 4584–4590.

[37] Lemier, C.; Weissmüller, J. Grain boundary segregation, stress and stretch: Effects on hydrogen absorption in nanocrystalline palladium. *Acta Materialia* **2007**, *55*, 1241–1254.

[38] H.-J. Butt, K. G.; Kappl, M. *Physics and chemistry of interfaces*; John Wiley and Sons, 2003.

[39] Yang, M.; Zhang, L.; Chen, B.; Wang, Z.; Chen, C.; Zeng, H. Silver nanoparticles decorated nanoporous gold for surface-enhanced Raman scattering. *Nanotechnology* **2016**, *28*, 055301.

[40] Singh, B. K.; Shaikh, A.; Badrayyana, S.; Mohapatra, D.; Dusane, R. O.; Parida, S. Nanoporous gold–copper oxide based all-solid-state micro-supercapacitors. *RSC Advances* **2016**, *6*, 100467–100475.

[41] Mameka, N.; Lührs, L.; Heissler, S.; Gliemann, H.; Wöll, C. Tailoring the strength of nanoporous gold by self-assembled monolayers of alkanethiols. *ACS Applied Nano Materials* **2018**, *1*, 6613–6621.

[42] Patel, D. A.; Weller, A. M.; Chevalier, R. B.; Karos, C. A.; Landis, E. C. Ordering and defects in self-assembled monolayers on nanoporous gold. *Applied Surface Science* **2016**, *387*, 503–512.

[43] Hengge, E.; Hirber, M.; Brunner, P.; Steyskal, E.-M.; Nidetzky, B.; Würschum, R. Nanoporous gold electrodes modified with self-assembled monolayers for electrochemical control of the surface charge. *Physical Chemistry Chemical Physics* **2021**, *23*, 14457–14464.

[44] Miyazawa, N.; Ishimoto, J.; Hakamada, M.; Mabuchi, M. Mechanical characterization of nanoporous Au modified with self-assembled monolayers. *Applied Physics Letters* **2016**, *109*.

[45] Zeis, R.; Mathur, A.; Fritz, G.; Lee, J.; Erlebacher, J. Platinum-plated nanoporous gold: An efficient, low Pt loading electrocatalyst for PEM fuel cells. *Journal of Power Sources* **2007**, *165*, 65–72.

[46] Xue, Y.; Scaglione, F.; Rizzi, P.; Battezzati, L.; Denis, P.; Fecht, H.-J. Electrodeposited platinum on de-alloyed nanoporous gold with enhanced electro-catalytic performance. *Applied Surface Science* **2019**, *476*, 412–417.

[47] Jia, C.; Yin, H.; Ma, H.; Wang, R.; Ge, X.; Zhou, A.; Xu, X.; Ding, Y. Enhanced photoelectrocatalytic activity of methanol oxidation on TiO_2-decorated nanoporous gold. *The Journal of Physical Chemistry C* **2009**, *113*, 16138–16143.

[48] Chen, A. Y.; Shi, S. S.; Wang, J. W.; Liu, F.; Wang, F.; Wang, Y.; Ruan, H. H.; Xie, X. F. Microstructure and electrocatalytic performance of nanoporous gold foils decorated by TiO_2 coatings. *Surface and Coatings Technology* **2016**, *286*, 113–118.

[49] Biener, M. M.; Biener, J.; Wichmann, A.; Wittstock, A.; Baumann, T. F.; Bäumer, M.; Hamza, A. V. ALD functionalized nanoporous gold: Thermal stability, mechanical properties, and catalytic activity. *Nano Letters* **2011**, *11*, 3085–3090.

[50] Lang, X.; Hirata, A.; Fujita, T.; Chen, M. Nanoporous metal/oxide hybrid electrodes for electrochemical supercapacitors. *Nature Nanotechnology* **2011**, *6*, 232–236.

[51] Kang, N.-R.; Kim, Y.-C.; Jeon, H.; Kim, S. K.; Jang, J.-I.; Han, H. N.; Kim, J.-Y. Wall-thickness-dependent strength of nanotubular ZnO. *Scientific Reports* **2017**, *7*, 4327.

[52] Yu, Y.; Gu, L.; Lang, X.; Zhu, C.; Fujita, T.; Chen, M.; Maier, J. Li Storage in 3D nanoporous Au-supported nanocrystalline tin. *Advanced Materials* **2011**, *21*, 2443–2447.

[53] Chen, L. Y.; Hou, Y.; Kang, J. L.; Hirata, A.; Fujita, T.; Chen, M. W. Toward the theoretical capacitance of RuO_2 reinforced by highly conductive nanoporous gold. *Advanced Energy Materials* **2013**, *3*, 851–856.

[54] Tan, Y.; Liu, P.; Chen, L.; Cong, W.; Ito, Y.; Han, J.; Guo, X.; Tang, Z.; Fujita, T.; Hirata, A. Monolayer MoS_2 films supported by 3D nanoporous metals for high-efficiency electrocatalytic hydrogen production. *Advanced Materials (Deerfield Beach, Fla.)* **2014**, *26*, 8023–8028.

[55] Jin, H.-J.; Weissmüller, J. A material with electrically tunable strength and flow stress. *Science* **2011**, *332*, 1179–1182.

[56] Mameka, N.; Markmann, J.; Jin, H.-J.; Weissmüller, J. Electrical stiffness modulation - confirming the impact of surface excess elasticity on the mechanics of nanomaterials. *Acta Materialia* **2014**, *76*, 272–280.

[57] Roschning, B.; Weissmüller, J. Nanoporous-gold-polypyrrole hybrid materials for millimeter-sized free standing actuators. *Advanced Materials Interfaces* **2020**, *7*, 2001415.

[58] Li, J.; Markmann, J.; Weissmüller, J.; Mameka, N. Nanoporous gold-polypyrrole hybrid electrochemical actuators with tunable elasticity. *Acta Materialia* **2021**, *212*, 116852.

[59] Meng, F.; Ding, Y. Sub-micrometer-thick all-solid-state supercapacitors with high power and energy densities. *Advanced Materials* **2011**, *35*, 4098–4102.

[60] Norman, L. L.; Badia, A. Redox actuation of a microcantilever driven by a self-assembled ferrocenylundecanethiolate monolayer: An investigation of the origin of the micromechanical motion and surface stress. *Journal of the American Chemical Society* **2009**, *131*, 2328–2337.

[61] Ulman, A. Formation and structure of self-assembled monolayers. *Chemical Reviews* **1996**, *96*, 1533–1554.

[62] Gokhshtein, A. Y. *Surface tension and electrical charging of interface*; Akademia Nauk SSSR, 1971; p 63.

[63] Jin, H.-J.; Wang, X.-L.; Parida, S.; Wang, K.; Seo, M.; Weissmüller, J. Nanoporous Au- Pt alloys as large strain electrochemical actuators. *Nano Letters* **2010**, *10*, 187–194.

[64] Biener, J.; Wittstock, A.; Zepeda-Ruiz, L. A.; Biener, M. M.; Zielasek, V.; Kramer, D.; Viswanath, R. N.; Weissmüller, J.; Bäumer, M.; Hamza, A. V. Surface-chemistry-driven actuation in nanoporous gold. *Nature Materials* **2009**, *8*, 47–51.

[65] Liu, L.-Z.; Mameka, N.; Markmann, J.; Jin, H.-J.; Weissmüller, J. Surface-driven actuation: Sign reversal under load and surface load-memory effect. *Physical Review Materials* **2019**, *3*, 066001.

[66] Detsi, E.; Onck, P.; Hosson, J. T. M. D. Metallic muscles at work: High rate actuation in nanoporous gold/polyaniline composites. *ACS Nano* **2013**, *7*, 4299–4306.

[67] Gurtin, M. E.; Murdoch, A. I. A continuum theory of elastic material surfaces. *Archive for rational mechanics and analysis* **1975**, *57*, 291–323.

[68] Shenoy, V. B. Atomistic calculations of elastic properties of metallic fcc crystal surfaces. *Physical Review B — Condensed Matter and Materials Physics* **2005**, *71*, 094104.

[69] Wu, B.; Heidelberg, A.; Boland, J. J. Mechanical properties of ultrahigh-strength gold nanowires. *Nature Materials* **2005**, *4*, 525–529.

[70] Olsson, P. A. T.; Park, H. S. Atomistic study of the buckling of gold nanowires. *Acta Materialia* **2011**, *59*, 3883–3894.

[71] Elsner, B. A. M.; Müller, S.; Bargmann, S.; Weissmüller, J. Surface excess elasticity of gold: Ab initio coefficients and impact on the effective elastic response of nanowires. *Acta Materialia* **2017**, *124*, 468–477.

[72] Petrova, H.; Perez-Juste, J.; Zhang, Z.; Zhang, J.; Kosel, T.; Hartland, G. V. Crystal structure dependence of the elastic constants of gold nanorods. *Journal of Materials Chemistry* **2006**, *16*, 3957–3963.

[73] Röhlig, C.-C.; Niebelschütz, M.; Brueckner, K.; Tonisch, K.; Ambacher, O.; Cimalla, V. Elastic properties of nanowires. *Physica Status Solidi (b)* **2010**, *247*, 2557–2570.

[74] Dou, R.; Derby, B. Deformation mechanisms in gold nanowires and nanoporous gold. *Philosophical Magazine* **2011**, *91*, 1070–1083.

[75] ParK, H. S.; Cai, W.; Espinosa, H. D.; Huang, H. Mechanics of crystalline nanowires. *MRS Bulletin* **2009**, *34*, 178–183.

[76] Zhou, L. G.; Huang, H. Are surfaces elastically softer or stiffer? *Applied Physics Letters* **2004**, *84*, 1940–1942.

[77] Esfahani, M. N.; Alaca, B. E. A review on size-dependent mechanical properties of nanowires. *Advanced Engineering Materials* **2019**, *21*, 1900192.

[78] Greer, J. R.; Oliver, W. C.; Nix, W. D. Size dependence of mechanical properties of gold at the micron scale in the absence of strain gradients. *Acta Materialia* **2005**, *53*, 1821–1830.

[79] Deshpande, V. S.; Needleman, A.; der Giessen, E. V. Plasticity size effects in tension and compression of single crystals. *Journal of the Mechanics and Physics of Solids* **2005**, *53*, 2661–2691.

[80] Jin, H.-J.; Kurmanaeva, L.; Schmauch, J.; Rösner, H.; Ivanisenko, Y.; Weissmüller, J. Deforming nanoporous metal: Role of lattice coherency. *Acta Materialia* **2009**, *57*, 2665–2672.

[81] Ngô-Dinh, B.-N.; Stukowski, A.; Mameka, N.; Markmann, J.; Albe, K.; Weissmüller, J. Anomalous compliance and early yielding of nanoporous gold. *Acta Materialia* **2015**, *93*, 144–155.

[82] Liu, M.; Weissmüller, J. Imaging the deformation-induced accumulation of defects in nanoporous gold. *Materials Research Letters* **2021**, *9*, 359–365.

[83] Afanasyev, K. A.; Sansoz, F. Strengthening in gold nanopillars with nanoscale twins. *Nano Letters* **2007**, *7*, 2056–2062.

[84] Parthasarathy, T. A.; Rao, S. I.; Dimiduk, D. M.; Uchic, M. D.; Trinkle, D. R. Contribution to size effect of yield strength from the stochastics of dislocation source lengths in finite samples. *Scripta Materialia* **2007**, *56*, 313–316.

[85] Greer, J. R.; Hosson, J. T. M. D. Plasticity in small-sized metallic systems: Intrinsic versus extrinsic size effect. *Progress in Materials Science* **2011**, *56*, 654–724.

[86] King, A. H. Triple lines in materials science and engineering. *Scripta Materialia* **2010**, *62*, 889–893.

[87] Yao, Y.; Huang, Q.; Wang, S. Effects of porosity and pore microstructure on the mechanical behavior of nanoporous silver. *Materials Today Communications* **2020**, *24*, 101236.

[88] Gibson, L. J. Cellular materials: Structure, properties, and applications. Frontiers of Engineering: Reports on Leading Edge Engineering from the 1996 NAE Symposium on Frontiers of Engineering. 1997; p 75.

[89] Li, Y.; Ngô, B.-N. D.; Markmann, J.; Weissmüller, J. Topology evolution during coarsening of nanoscale metal network structures. *Physical Review Materials* **2019**, *3*, 076001.

[90] Lilleodden, E. T.; Voorhees, P. W. On the topological, morphological, and microstructural characterization of nanoporous metals. *MRS Bulletin* **2018**, *43*, 20–26.

[91] Biener, M. M.; Biener, J.; Friend, C. M. Revisiting the S-Au (111) interaction: Static or dynamic? *Langmuir* **2005**, *21*, 1668–1671.

[92] Hodge, A. M.; Biener, J.; Hayes, J. R.; Bythrow, P. M.; Volkert, C. A.; Hamza, A. V. Scaling equation for yield strength of nanoporous open-cell foams. *Acta Materialia* **2007**, *55*, 1343–1349.

[93] Lee, D.; Wei, X.; Chen, X.; Zhao, M.; Jun, S. C.; Hone, J.; Herbert, E. G.; Oliver, W. C.; Kysar, J. W. Microfabrication and mechanical properties of nanoporous gold at the nanoscale. *Scripta Materialia* **2007**, *56*, 437–440.

[94] Balk, T. J.; Eberl, C.; Sun, Y.; Hemker, K. J.; Gianola, D. S. Tensile and compressive microspecimen testing of bulk nanoporous gold. *JOM* **2009**, *61*, 26–31.

[95] Bürckert, M.; Briot, N. J.; Balk, T. J. Uniaxial compression testing of bulk nanoporous gold. *Philosophical Magazine* **2017**, *97*, 1157–1178.

[96] Briot, N. J.; Kennerknecht, T.; Eberl, C.; Balk, T. J. Mechanical properties of bulk single crystalline nanoporous gold investigated by millimetre-scale tension and compression testing. *Philosophical Magazine* **2014**, *94*, 847–866.

[97] Liu, L.-Z.; Ye, X.-L.; Jin, H.-J. Interpreting anomalous low-strength and low-stiffness of nanoporous gold: Quantification of network connectivity. *Acta Materialia* **2016**, *118*, 77–87.

[98] Mameka, N.; Wang, K.; Markmann, J.; Lilleodden, E. T.; Weissmüller, J. Nanoporous gold – testing macro-scale samples to probe small-scale mechanical behavior. *Materials Research Letters* **2016**, *4*, 27–36.

[99] Zandersons, B.; Lührs, L.; Li, Y.; Weissmüller, J. On factors defining the mechanical behavior of nanoporous gold. *Acta Materialia* **2021**, *215*, 116979.

[100] Sun, X.-Y.; Xu, G.-K.; Li, X.; Feng, X.-Q.; Gao, H. Mechanical properties and scaling laws of nanoporous gold. *Journal of Applied Physics* **2013**, *113*.

[101] Liu, L.-Z.; Zhang, Y.-Y.; Xie, H.; Jin, H.-J. Transition from homogeneous to localized deformation in nanoporous gold. *Physical Review Letters* **2021**, *127*, 095501.

[102] Zhang, Y.-Y.; Xie, H.; Liu, L.-Z.; Jin, H.-J. Surface triple junctions govern the strength of a nanoscale solid. *Physical Review Letters* **2021**, *126*, 235501.

[103] Lührs, L.; Zandersons, B.; Huber, N.; Weissmüller, J. Plastic Poisson's ratio of nanoporous metals: A macroscopic signature of tension–compression asymmetry at the nanoscale. *Nano Letters* **2017**, *17*, 6258–6266.

[104] Mameka, N.; Markmann, J.; Weissmüller, J. On the impact of capillarity for strength at the nanoscale. *Nature Communications* **2017**, *8*, 1976.

[105] Wu, P.; Ye, X.-L.; Liu, L.-Z.; Jin, H.-J. Monolayer oxide enhanced flow stress in nanoporous gold: The size dependence. *Materials Research Letters* **2018**, *6*, 508–514.

[106] Soyarslan, C.; Bargmann, S.; Pradas, M.; Weissmüller, J. 3D stochastic bicontinuous microstructures: Generation, topology and elasticity. *Acta Materialia* **2018**, *149*, 326–340.

[107] Liu, L.-Z.; Jin, H.-J. Scaling equation for the elastic modulus of nanoporous gold with "fixed" network connectivity. *Applied Physics Letters* **2017**, *110*.

[108] Roberts, A. P.; Garboczi, E. J. Computation of the linear elastic properties of random porous materials with a wide variety of microstructure. *Proceedings of the Royal Society of London. Series A: Mathematical, Physical and Engineering Sciences* **2002**, *458*, 1033–1054.

[109] Sohn, S.; Richert, C.; Shi, S.; Weissmüller, J.; Huber, N. Scaling between elasticity and topological genus for random network nanomaterials. *Extreme Mechanics Letters* **2024**, *68*, 102147.

[110] Gibbs, J. W. *Scientific papers of J. Willard Gibbs, in two volumes*; Longmans, Green, 1906; Vol. 1; p 315.

[111] Shuttleworth, R. The surface tension of solids. *Proceedings of the Physical Society. Section A* **1950**, *63*, 444.

[112] Cahn, J. W. Surface stress and the chemical equilibrium of small crystals – I. the case of the isotropic surface. *Acta Metallurgica* **1980**, *28*, 1333–1338.

[113] Haiss, W. Surface stress of clean and adsorbate-covered solids. *Reports on Progress in Physics* **2001**, *64*, 591.

[114] Bagotsky, V. S. *Fundamentals of electrochemistry*; John Wiley and Sons, 2005.

[115] Bard, A. J.; Faulkner, L. R.; White, H. S. *Electrochemical methods: Fundamentals and applications*; John Wiley and Sons, 2022.

[116] Helmholtz, H. Studien über electrische Grenzschichten. *Annalen der Physik* **1879**, *243*, 337–382.

[117] Gouy, G. J. Constitution of the Electric Charge at the Surface of an Electrolyte. *Phys.* **1910**, *9 (4)*.

[118] Chapman, D. L. LI. A contribution to the theory of electrocapillarity. *The London, Edinburgh, and Dublin Philosophical Magazine and Journal of Science* **1913**, *25*, 475–481.

[119] Debye, P.; Huckel, E. The theory of electrolytes I. The lowering of the freezing point and related occurrences. *Physik. Z.* **1923**, *24*.

[120] Bolt, G. H. Analysis of the validity of the Gouy-Chapman theory of the electric double layer. *Journal of Colloid Science* **1955**, *10*, 206–218.

[121] Stern, O. On the theory of the electrolytic double layer (in German). *Zeitschrift für Elektrochemie und Angewandte Physikalische Chemie* **1924**, *30*, 508–516.

[122] Grahame, D. C. The electrical double layer and the theory of electrocapillarity. *Chemical Reviews* **1947**, *41*, 441–501.

[123] Frumkin, A. N.; Damaskin, B. B. *Adsorbtion and electric double layer in electrochemistry (in Russian)*; Nauka, 1972.

[124] Schmickler, W.; Santos, E. *Interfacial electrochemistry*; Springer Science and Business Media, 2010.

[125] Duleba, D.; Dutta, P.; Denuga, S.; Johnson, R. P. Effect of electrolyte concentration and pore size on ion current rectification inversion. *ACS Measurement Science Au* **2022**, *2*, 271–277.

[126] Lippmann, G. Relations entre les phénomènes électriques et capillaires. *Ann. Chim. Phys* **1875**, *5*, 494–549.

[127] Couchman, P. R.; Davidson, C. R. The Lippmann relation and surface thermodynamics. *Journal of Electroanalytical Chemistry and Interfacial Electrochemistry* **1977**, *85*, 407–409.

[128] Ibach, H.; Bach, C. E.; Giesen, M.; Grossmann, A. Potential-induced stress in the solid-liquid interface: Au (111) and Au (100) in an HClO4 electrolyte. *Surface Science* **1997**, *375*, 107–119.

[129] Vasiljevic, N.; Trimble, T.; Dimitrov, N.; Sieradzki, K. Electrocapillarity behavior of Au (111) in SO_4^{2-} and F. *Langmuir* **2004**, *20*, 6639–6643.

[130] Deng, Q.; Gosslar, D.-H.; Smetanin, M.; Weissmüller, J. Electrocapillary coupling at rough surfaces. *Physical Chemistry Chemical Physics* **2015**, *17*, 11725–11731.

[131] Lipkowski, J.; Schmickler, W.; Kolb, D. M.; Parsons, R. Comments on the thermodynamics of solid electrodes. *Journal of Electroanalytical Chemistry* **1998**, *452*, 193–197.

[132] Guidelli, R. Superficial work and surface stress at solid electrodes: a thermodynamic assessment. *Journal of Electroanalytical Chemistry* **1998**, *453*, 69–77.

[133] Kramer, D.; Weissmüller, J. A note on surface stress and surface tension and their interrelation via Shuttleworth's equation and the Lippmann equation. *Surface Science* **2007**, *601*, 3042–3051.

[134] Lüth, H. *Solid surfaces, interfaces and thin films*; Springer, 2001; Vol. 4.

[135] Weissmüller, J.; Viswanath, R. N.; Kibler, L. A.; Kolb, D. M. Impact of surface mechanics on the reactivity of electrodes. *Physical Chemistry Chemical Physics* **2011**, *13*, 2114–2117.

[136] Tilley, R. J. *Crystals and crystal structures*; John Wiley and Sons, 2020.

[137] Silva, F.; Martins, A. Surface reconstruction of gold single crystals: electrochemical evidence of the effect of adsorbed anions and influence of steps and terraces. *Electrochimica Acta* **1998**, *44*, 919–929.

[138] Needs, R. J.; Godfrey, M. J.; Mansfield, M. Theory of surface stress and surface reconstruction. *Surface Science* **1991**, *242*, 215–221.

[139] Ibach, H. The role of surface stress in reconstruction, epitaxial growth and stabilization of mesoscopic structures. *Surface Science Reports* **1997**, *29*, 195–263.

[140] Heine, V.; Marks, L. D. *Studies in Surface Science and Catalysis*; Elsevier, 1986; Vol. 26; pp 229–232.

[141] Hamelin, A.; Vitanov, T.; Sevastyanov, E.; Popov, A. The electrochemical double layer on sp metal single crystals: The current status of data. *Journal of Electroanalytical Chemistry and Interfacial Electrochemistry* **1983**, *145*, 225–264.

[142] Kolb, D. M. Reconstruction phenomena at metal-electrolyte interfaces. *Progress in Surface Science* **1996**, *51*, 109–173.

[143] Gründer, Y.; Lucas, C. A. Potential-induced structural deformation at electrode surfaces. *Current Opinion in Electrochemistry* **2020**, *19*, 168–174.

[144] Gong, J. Structure and surface chemistry of gold-based model catalysts. *Chemical Reviews* **2012**, *112*, 2987–3054.

[145] Gileadi, E. *Electrosorption*; Springer Science and Business Media, 2012.

[146] Feibelman, P. J. First-principles calculations of stress induced by gas adsorption on Pt (111). *Physical Review B* **1997**, *56*, 2175.

[147] Sethuraman, V. A.; Vairavapandian, D.; Lafouresse, M. C.; Maark, T. A.; Karan, N.; Sun, S.; Bertocci, U.; Peterson, A. A.; Stafford, G. R.; Guduru, P. R. Role of elastic strain on electrocatalysis of oxygen reduction reaction on Pt. *The Journal of Physical Chemistry C* **2015**, *119*, 19042–19052.

[148] Weissmüller, J. Adsorption–strain coupling at solid surfaces. *Current Opinion in Chemical Engineering* **2019**, *24*, 45–53.

[149] Bruckenstein, S.; Shay, M. An in situ weighing study of the mechanism for the formation of the adsorbed oxygen monolayer at a gold electrode. *Journal of electroanalytical chemistry and interfacial electrochemistry* **1985**, *188*, 131–136.

[150] Conway, B. Electrochemical oxide film formation at noble metals as a surface-chemical process. *Progress in Surface Science* **1995**, *49*, 331–452.

[151] Thiel, P. A.; Madey, T. E. The interaction of water with solid surfaces: fundamental aspects. *Surface Science Reports* **1987**, *7*, 211–385.

[152] Henderson, M. A. The interaction of water with solid surfaces: fundamental aspects revisited. *Surface Science Reports* **2002**, *46*, 1–308.

[153] Stojanovski, K.; Briega-Martos, V.; Zlatar, M.; Göllner, C.; Cherevko, S. pH dependence of noble metals dissolution: Gold. *Chem.Electro.Chem.* **2024**, e202400373.

[154] Koper, M. T. M.; van Santen, R. A. Interaction of H, O and OH with metal surfaces. *Journal of Electroanalytical Chemistry* **1999**, *472*, 126–136.

[155] Ikeda, S.; Nakajima, T.; Hirao, K. A theoretical study of transition metal hydroxides: CuOH, AgOH and AuOH. *Molecular Physics* **2003**, *101*, 105–110.

[156] Goldsmith, Z. K.; Andrade, M. F. C.; Selloni, A. Effects of applied voltage on water at a gold electrode interface from ab initio molecular dynamics. *Chemical Science* **2021**, *12*, 5865–5873.

[157] Li, Y.; Chen, Y.-X.; Liu, Z.-F. OH-Au hydrogen bond and its effect on the oxygen reduction reaction on Au (100) in alkaline media. *The Journal of Physical Chemistry Letters* **2022**, *13*, 9035–9043.

[158] Angerstein-Kozlowska, H.; Conway, B. E.; Barnett, B.; Mozota, J. The role of ion adsorption in surface oxide formation and reduction at noble metals: general features of the surface process. *Journal of Electroanalytical Chemistry and Interfacial Electrochemistry* **1979**, *100*, 417–446.

[159] Tremiliosi-Filho, G.; Dall'Antonia, L. H.; Jerkiewicz, G. Limit to extent of formation of the quasi-two-dimensional oxide state on Au electrodes. *Journal of Electroanalytical Chemistry* **1997**, *422*, 149–159.

[160] Cherevko, S.; Zeradjanin, A. R.; Keeley, G. P.; Mayrhofer, K. J. J. A comparative study on gold and platinum dissolution in acidic and alkaline media. *Journal of The Electrochemical Society* **2014**, *161*, H822.

[161] Angerstein-Kozlowska, H.; Conway, B.; Tellefsen, K.; Barnett, B. Stochastically-gated surface processes involving anions in oxidation of Au: Time-resolution of processes down to 0.25 % coverages and 50 μs time-scales. *Electrochimica Acta* **1989**, *34*, 1045–1056.

[162] Baker, T. A.; Friend, C. M.; Kaxiras, E. Effects of chlorine and oxygen coverage on the structure of the Au (111) surface. *The Journal of Chemical Physics* **2009**, *130*.

[163] Yoon, B.; Häkkinen, H.; Landman, U. Interaction of O_2 with gold clusters: Molecular and dissociative adsorption. *The Journal of Physical Chemistry A* **2003**, *107*, 4066–4071.

[164] Iro, E.; Ariga-Miwa, H.; Sasaki, T.; Asakura, K.; Olea, M. Elimination of indoor volatile organic compounds on Au/SBA-15 catalysts: Insights into the nature, size, and dispersion of the active sites and reaction mechanism. *Catalysts* **2022**, *12*, 1365.

[165] Deng, Q.; Gopal, V.; Weissmüller, J. Less noble or more noble: How strain affects the binding of oxygen on gold. *Angewandte Chemie International Edition* **2015**, *54*, 12981–12985.

[166] Bigelow, W. C.; Pickett, D. L.; Zisman, W. A. Oleophobic monolayers: I. Films adsorbed from solution in non-polar liquids. *Journal of Colloid Science* **1946**, *1*, 513–538.

[167] Nuzzo, R. G.; Allara, D. L. Adsorption of bifunctional organic disulfides on gold surfaces. *Journal of the American Chemical Society* **1983**, *105*, 4481–4483.

[168] Strong, L.; Whitesides, G. M. Structures of self-assembled monolayer films of organosulfur compounds adsorbed on gold single crystals: electron diffraction studies. *Langmuir* **1988**, *4*, 546–558.

[169] Love, J. C.; Estroff, L. A.; Kriebel, J. K.; Nuzzo, R. G.; Whitesides, G. M. Self-assembled monolayers of thiolates on metals as a form of nanotechnology. *Chemical Reviews* **2005**, *105*, 1103–1170.

[170] Vericat, C.; Vela, M. E.; Benitez, G.; Carro, P.; Salvarezza, R. C. Self-assembled monolayers of thiols and dithiols on gold: New challenges for a well-known system. *Chemical Society Reviews* **2010**, *39*, 1805–1834.

[171] Amdursky, N.; Ferber, D.; Pecht, I.; Sheves, M.; Cahen, D. Redox activity distinguishes solid-state electron transport from solution-based electron transfer in a natural and artificial protein: Cytochrome C and hemin-doped human serum albumin. *Physical Chemistry Chemical Physics* **2013**, *15*, 17142–17149.

[172] Casalini, S.; Bortolotti, C. A.; Leonardi, F.; Biscarini, F. Self-assembled monolayers in organic electronics. *Chemical Society Reviews* **2017**, *46*, 40–71.

[173] Quek, S. Y.; Choi, H. J.; Louie, S. G.; Neaton, J. B. Thermopower of amine-gold-linked aromatic molecular junctions from first principles. *ACS Nano* **2011**, *5*, 551–557.

[174] Akkerman, H. B.; Blom, P. W. M.; Leeuw, D. M. D.; Boer, B. D. Towards molecular electronics with large-area molecular junctions. *Nature* **2006**, *441*, 69–72.

[175] DiBenedetto, S. A.; Facchetti, A.; Ratner, M. A.; Marks, T. J. Molecular self-assembled monolayers and multilayers for organic and unconventional inorganic thin-film transistor applications. *Advanced Materials* **2009**, *21*, 1407–1433.

[176] Paulsson, M.; Datta, S. Thermoelectric effect in molecular electronics. *Physical Review B* **2003**, *67*, 241403.

[177] Simão, C.; Mas-Torrent, M.; Crivillers, N.; Lloveras, V.; Artés, J. M.; Gorostiza, P.; Veciana, J.; Rovira, C. A robust molecular platform for non-volatile memory devices with optical and magnetic responses. *Nature Chemistry* **2011**, *3*, 359–364.

[178] Tao, F.; Bernasek, S. L. Understanding odd- even effects in organic self-assembled monolayers. *Chemical Reviews* **2007**, *107*, 1408–1453.

[179] Nerngchamnong, N.; Thompson, D.; Cao, L.; Yuan, L.; Jiang, L.; Roemer, M.; Nijhuis, C. A. Nonideal electrochemical behavior of ferrocenyl–alkanethiolate SAMs maps the microenvironment of the redox unit. *The Journal of Physical Chemistry C* **2015**, *119*, 21978–21991.

[180] Lavrich, D. J.; Wetterer, S. M.; Bernasek, S. L.; Scoles, G. Physisorption and chemisorption of alkanethiols and alkyl sulfides on Au (111). *The Journal of Physical Chemistry B* **1998**, *102*, 3456–3465.

[181] Sellers, H.; Ulman, A.; Shnidman, Y.; Eilers, J. E. Structure and binding of alkanethiolates on gold and silver surfaces: implications for self-assembled monolayers. *Journal of the American Chemical Society* **1993**, *115*, 9389–9401.

[182] Guo, Q.; Li, F. Self-assembled alkanethiol monolayers on gold surfaces: resolving the complex structure at the interface by STM. *Physical Chemistry Chemical Physics* **2014**, *16*, 19074–19090.

[183] Eckermann, A. L.; Feld, D. J.; Shaw, J. A.; Meade, T. J. Electrochemistry of redox-active self-assembled monolayers. *Coordination Chemistry Reviews* **2010**, *254*, 1769–1802.

[184] Lucas, F. W. S.; Ramos, N. C.; Schwartz, D. K.; Medlin, J. W.; Holewinski, A. Understanding reactivity of self-assembled monolayer-coated electrodes: SAM-induced surface reconstruction. *Electrochimica Acta* **2023**, *459*, 142586.

[185] Wilkinson, G.; Rosenblum, M.; Whiting, M. C.; Woodward, R. B. The structure of iron bis-cyclopentadienyl. *Journal of the American Chemical Society* **1952**, *74*, 2125–2126.

[186] Woodward, R. B.; Rosenblum, M.; Whiting, M. C. A new aromatic system. *Journal of the American Chemical Society* **1952**, *74*, 3458–3459.

[187] Ornelas, C.; Astruc, D. Ferrocene-based drugs, delivery nanomaterials and fenton mechanism: state of the art, recent developments and prospects. *Pharmaceutics* **2023**, *15*, 2044.

[188] Uosaki, K.; Sato, Y.; Kita, H. Electrochemical characteristics of a gold electrode modified with a self-assembled monolayer of ferrocenylalkanethiols. *Langmuir* **1991**, *7*, 1510–1514.

[189] Staveren, D. R. V.; Metzler-Nolte, N. Bioorganometallic chemistry of ferrocene. *Chemical Reviews* **2004**, *104*, 5931–5986.

[190] Herbert, D. E.; Mayer, U. F. J.; Manners, I. Strained metallocenophanes and related organometallic rings containing π-hydrocarbon ligands and transition-metal centers. *Angewandte Chemie International Edition* **2007**, *46*, 5060–5081.

[191] Norman, L. L.; Badia, A. Microcantilevers modified with ferrocene-terminated self-assembled monolayers: Effect of molecular structure and electrolyte anion on the redox-induced surface stress. *The Journal of Physical Chemistry C* **2011**, *115*, 1985–1995.

[192] Rudnev, A. V.; Zhumaev, U.; Utsunomiya, T.; Fan, C.; Yokota, Y.; Fukui, K.-I.; Wandlowski, T. Ferrocene-terminated alkanethiol self-assembled monolayers: An electrochemical and in situ surface-enhanced infra-red absorption spectroscopy study. *Electrochimica Acta* **2013**, *107*, 33–44.

[193] Chidsey, C. E.; Bertozzi, C. R.; Putvinski, T. M.; Mujsce, A. M. Coadsorption of ferrocene-terminated and unsubstituted alkanethiols on gold: Electroactive self-assembled monolayers. *Journal of the American Chemical Society* **1990**, *112*, 4301–4306.

[194] Duffin, T. J.; Nerngchamnong, N.; Thompson, D.; Nijhuis, C. A. Direct measurement of the local field within alkyl-ferrocenyl-alkanethiolate monolayers: Importance of the supramolecular and electronic structure on the voltammetric response and potential profile. *Electrochimica Acta* **2019**, *311*, 92–102.

[195] Huffman, B. L.; Bredar, A. R. C.; Dempsey, J. L. Origins of non-ideal behaviour in voltammetric analysis of redox-active monolayers. *Nature Reviews Chemistry* **2024**, 1–16.

[196] Wong, R. A.; Yokota, Y.; Wakisaka, M.; Inukai, J.; Kim, Y. Probing consequences of anion-dictated electrochemistry on the electrode/monolayer/electrolyte interfacial properties. *Nature Communications* **2020**, *11*, 4194.

[197] Sumner, J. J.; Weber, K. S.; Hockett, L. A.; Creager, S. E. Long-range heterogeneous electron transfer between ferrocene and gold mediated by n-alkane and n-alkyl-carboxamide bridges. *The Journal of Physical Chemistry B* **2000**, *104*, 7449–7454.

[198] Pajkossy, T.; Ceblin, M. U.; Meszaros, G. Dynamic electrochemical impedance spectroscopy for the charge transfer rate measurement of the ferro/ferricyanide redox couple on gold. *Journal of Electroanalytical Chemistry* **2021**, *899*, 115655.

[199] Smith, C. P.; White, H. S. Theory of the interfacial potential distribution and reversible voltammetric response of electrodes coated with electroactive molecular films. *Analytical Chemistry* **1992**, *64*, 2398–2405.

[200] Fawcett, W. R. Discreteness-of-charge effects at an electrode covered with a self-assembled monolayer containing a simple redox couple. *Journal of Electroanalytical Chemistry* **1994**, *378*, 117–124.

[201] Berger, R.; Delamarche, E.; Lang, H. P.; Gerber, C.; Gimzewski, J. K.; Meyer, E.; Guntherodt, H.-J. Surface stress in the self-assembly of alkanethiols on gold. *Science* **1997**, *276*, 2021–2024.

[202] Godin, M.; Williams, P. J.; Tabard-Cossa, V.; Laroche, O.; Beaulieu, L. Y.; Lennox, R. B.; Grütter, P. Surface stress, kinetics, and structure of alkanethiol self-assembled monolayers. *Langmuir* **2004**, *20*, 7090–7096.

[203] Godin, M.; Tabard-Cossa, V.; Miyahara, Y.; Monga, T.; Williams, P. J.; Beaulieu, L. Y.; Lennox, R. B.; Grutter, P. Cantilever-based sensing: The origin of surface stress and optimization strategies. *Nanotechnology* **2010**, *21*, 075501.

[204] Zhao, Y.; Gosai, A.; Kang, K.; Shrotriya, P. Multiscale modeling reveals the cause of surface stress change on microcantilevers due to alkanethiol SAM adsorption. *Journal of Chemical Information and Modeling* **2020**, *60*, 2998–3008.

[205] Quist, F.; Tabard-Cossa, V.; Badia, A. Nanomechanical cantilever motion generated by a surface-confined redox reaction. *The Journal of Physical Chemistry B* **2003**, *107*, 10691–10695.

[206] Weissmüller, J.; Duan, H.-L.; Farkas, D. Deformation of solids with nanoscale pores by the action of capillary forces. *Acta Materialia* **2010**, *58*, 1–13.

[207] Shao, L.-H.; Jin, H.-J.; Viswanath, R. N.; Weissmüller, J. Different measures for the capillarity-driven deformation of a nanoporous metal. *Europhysics Letters* **2010**, *89*, 66001.

[208] Gurtin, M. E.; Weissmüller, J.; Larche, F. A general theory of curved deformable interfaces in solids at equilibrium. *Philosophical Magazine A* **1998**, *78*, 1093–1109.

[209] Weissmüller, J.; Kramer, D. Balance of force at curved solid metal-liquid electrolyte interfaces. *Langmuir* **2005**, *21*, 4592–4603.

[210] Xia, R.; Li, X.; Qin, Q.; Liu, J.; Feng, X.-Q. Surface effects on the mechanical properties of nanoporous materials. *Nanotechnology* **2011**, *22*, 265714.

[211] Ashby, M. F. The properties of foams and lattices. *Philosophical Transactions of the Royal Society A: Mathematical, Physical and Engineering Sciences* **2006**, *364*, 15–30.

[212] Timoshenko, S. P.; Goodier, J. N. *Theory of elasticity*; McGraw-hill New York, 1982; Vol. 3.

[213] Rusling, J. F.; Suib, S. L. Characterizing materials with cyclic voltammetry. *Advanced Materials* **1994**, *6*, 922–930.

[214] Kissinger, P. T.; Heineman, W. R. Cyclic voltammetry. *Journal of Chemical Education* **1983**, *60*, 702.

[215] Okamoto, H.; Massalski, T. The Ag-Au (Silver-Gold) system. *Bulletin of Alloy Phase Diagrams* **1983**, *4*, 30–38.

[216] Li, R.; Sieradzki, K. Ductile-brittle transition in random porous Au. *Physical Review Letters* **1992**, *68*, 1168.

[217] Bapari, S.; Lührs, L.; Weissmüller, J. Metrics for the characteristic length scale in the random bicontinuous microstructure of nanoporous gold. *Acta Materialia* **2023**, *260*, 119333.

[218] Michri, A. A.; Pshenichnikov, A. G.; Burshtein, R. K. Determination of the true surface of smooth au electrodes. *Elektrokhimiya* **1972**, *8*, 364–366.

[219] Hamelin, A. Cyclic voltammetry at gold single-crystal surfaces. Part 1. Behaviour at low-index faces. *Journal of Electroanalytical Chemistry* **1996**, *407*, 1–11.

[220] Haensch, M.; Behnken, J.; Balboa, L.; Dyck, A.; Wittstock, G. Redox titration of gold and platinum surface oxides at porous microelectrodes. *Physical Chemistry Chemical Physics* **2017**, *19*, 22915–22925.

[221] Stuckner, J.; Frei, K.; McCue, I.; Demkowicz, M. J.; Murayama, M. AQUAMI: An open source Python package and GUI for the automatic quantitative analysis of morphologically complex multiphase materials. *Computational Materials Science* **2017**, *139*, 320–329.

[222] Viswanath, R.; Weissmüller, J. Electrocapillary coupling coefficients for hydrogen electrosorption on palladium. *Acta Materialia* **2013**, *61*, 6301–6309.

[223] Marcus, P. M. Epitaxial strain and epitaxial bending. *Surface Science* **1996**, *366*, 219–227.

[224] Sander, D.; Enders, A.; Kirschner, J. Stress and magnetic properties of surfaces and ultrathin films. *Journal of Magnetism and Magnetic Materials* **1999**, *200*, 439–455.

[225] Overmeere, Q. V.; Vanhumbeeck, J.-F.; Proost, J. On the use of a multiple beam optical sensor for in situ curvature monitoring in liquids. *Review of Scientific Instruments* **2010**, *81*.

[226] Roschning, B.; Weissmüller, J. Stress-charge coupling coefficient for thin-film polypyrrole actuators – Investigation of capacitive ion exchange in the oxidized state. *Electrochimica Acta* **2019**, *318*, 504–512.

[227] Stoney, G. G. The tension of metallic films deposited by electrolysis. *Proceedings of the Royal Society of London. Series A, Containing Papers of a Mathematical and Physical Character* **1909**, *82*, 172–175.

[228] Smetanin, M.; Viswanath, R. N.; Kramer, D.; Beckmann, D.; Koch, T.; Kibler, L.; Kolb, A.; Dieter, M.; Weissmüller, J. Surface stress-charge response of a (111)-textured gold electrode under conditions of weak ion adsorption. *Langmuir* **2008**, *24*, 8561–8567.

[229] Standard test method for Young's modulus, tangent modulus, and chord modulus. **2004**,

[230] Ferry, J. D. *Viscoelastic properties of polymers*; John Wiley and Sons, 1980.

[231] Ziehmer, M.; Hu, K.; Wang, K.; Lilleodden, E. T. A principle curvatures analysis of the isothermal evolution of nanoporous gold: Quantifying the characteristic length-scales. *Acta Materialia* **2016**, *120*, 24–31.

[232] Kwon, Y.; Thornton, K.; Voorhees, P. W. The topology and morphology of bicontinuous interfaces during coarsening. *Europhysics Letters* **2009**, *86*, 46005.

[233] Riedel, L.; Markmann, J.; Weissmüller, J.; Shi, S. Tailoring hierarchical nanoporous gold on dual length scales. *Physical Review Materials* **2023**, *7*, 116001.

[234] Smetanin, M.; Kramer, D.; Mohanan, S.; Herr, U.; Weissmüller, J. Response of the potential of a gold electrode to elastic strain. *Physical Chemistry Chemical Physics* **2009**, *11*, 9008–9012.

[235] Lafouresse, M. C.; Bertocci, U.; Beauchamp, C. R.; Stafford, G. R. Simultaneous electrochemical and mechanical impedance spectroscopy using cantilever curvature. *Journal of the Electrochemical Society* **2012**, *159*, H816.

[236] Mavrikakis, M.; Stoltze, P.; Nørskov, J. K. Making gold less noble. *Catalysis Letters* **2000**, *64*, 101–106.

[237] Crowson, D. A.; Farkas, D.; Corcoran, S. G. Geometric relaxation of nanoporous metals: The role of surface relaxation. *Scripta Materialia* **2007**, *56*, 919–922.

[238] Xu, K. Diffusionless charge transfer. *Nature Energy* **2019**, *4*, 93–94.

[239] Dionne, E. R.; Dip, C.; Toader, V.; Badia, A. Micromechanical Redox Actuation by Self-Assembled Monolayers of Ferrocenylalkanethiolates: Evens Push More Than Odds. *Journal of the American Chemical Society* **2018**, *140*, 10063–10066.

[240] Roy, G.; Gupta, R.; Sahoo, S. R.; Saha, S.; Asthana, D.; Mondal, P. C. Ferrocene as an iconic redox marker: From solution chemistry to molecular electronic devices. *Coordination Chemistry Reviews* **2022**, *473*, 214816.

[241] Telegdi, J. Formation of self-assembled anticorrosion films on different metals. *Materials* **2020**, *13*, 5089.

[242] Ye, S.; Haba, T.; Sato, Y.; Shimazu, K.; Uosaki, K. Coverage dependent behavior of redox reaction induced structure change and mass transport at an 11-ferrocenyl-1-undecanethiol self-assembled monolayer on a gold electrode studied by an in situ IRRAS–EQCM combined system. *Physical Chemistry Chemical Physics* **1999**, *1*, 3653–3659.

[243] Cao, L.; Yuan, L.; Yang, M.; Nerngchamnong, N.; Thompson, D.; Yu, X.; Qi, D.-C.; Nijhuis, C. A. The supramolecular structure and van der Waals interactions affect the electronic structure of ferrocenyl-alkanethiolate SAMs on gold and silver electrodes. *Nanoscale Advances* **2019**, *1*, 1991–2002.

[244] Schwartz, D. K. Mechanisms and kinetics of self-assembled monolayer formation. *Annual Review of Physical Chemistry* **2001**, *52*, 107–137.

[245] Green, J.-B. D.; McDermott, M. T.; Porter, M. D. Real time monitoring of the electrochemical transformation of a ferrocene-terminated alkanethiolate monolayer at gold via an adhesion-based atomic force microscopic characterization. *The Journal of Physical Chemistry* **1996**, *100*, 13342–13345.

[246] Otero, T.; Martínez, J.; Zaifoglu, B. Using reactive artificial muscles to determine water exchange during reactions. *Smart Materials and Structures* **2013**, *22*, 104019.

[247] Jeon, H.; Markmann, J.; Shi, S. Effects of structural hierarchy and size on mechanical behavior of nanoporous gold. *Acta Materialia* **2024**, *273*, 119954.

[248] Aponte-Roman, M.; Mohanty, B.; Mann, A. B. Chemomechanical effects of self-assembled monolayers on gold films. *Acta Materialia* **2014**, *68*, 52–60.

[249] Deng, Q.; Weissmüller, J. Electrocapillary coupling during electrosorption. *Langmuir* **2014**, *30*, 10522–10530.

[250] Umeno, Y.; Elsässer, C.; Meyer, B.; Gumbsch, P.; Nothacker, M.; Weissmüller, J.; Evers, F. Ab initio study of surface stress response to charging. *Europhysics Letters* **2007**, *78*, 13001.

[251] Sun, H.; Huang, Y.; Shi, S. Bulk nanoporous platinum for electrochemical actuation. *Energy Materials and Devices* **2023**,

[252] Hakamada, M.; Takahashi, M.; Furukawa, T.; Tajima, K.; Yoshimura, K.; Chino, Y.; Mabuchi, M. Electrochemical stability of self-assembled monolayers on nanoporous Au. *Physical Chemistry Chemical Physics* **2011**, *13*, 12277–12284.

[253] Chu, Y.; Seo, B.-R.; Kim, J.-W. Electrochemical properties of alkanethiol monolayers adsorbed on nanoporous Au surfaces. *Bulletin of the Korean Chemical Society* **2010**, *31*, 3407–3410.

[254] Chang, S.-C.; Chao, I.; Tao, Y.-T. Structure of self-assembled monolayers of aromatic-derivatized thiols on evaporated gold and silver surfaces: Implication on packing mechanism. *Journal of the American Chemical Society* **1994**, *116*, 6792–6805.

[255] Fenter, P.; Eisenberger, P.; Li, J.; III, N. C.; Bernasek, S.; Scoles, G.; Ramanarayanan, T. A.; Liang, K. S. Structure of octadecyl thiol self-assembled on the silver (111) surface: An incommensurate monolayer. *Langmuir* **1991**, *7*, 2013–2016.

[256] Chidsey, C. E. D. Free energy and temperature dependence of electron transfer at the metal-electrolyte interface. *Science* **1991**, *251*, 919–922.

[257] Jiao, J.; Huber, N. Deformation mechanisms in nanoporous metals: Effect of ligament shape and disorder. *Computational Materials Science* **2017**, *127*, 194–203.

[258] Olaya, A. R. S.; Zandersons, B.; Wittstock, G. Effect of the residual silver and adsorbed lead anions towards the electrocatalytic methanol oxidation on nanoporous gold in alkaline media. *Electrochimica Acta* **2021**, *383*, 138348.

[259] Moskaleva, L. V.; Röhe, S.; Wittstock, A.; Zielasek, V.; Klüner, T.; Neyman, K. M.; Bäumer, M. Silver residues as a possible key to a remarkable oxidative catalytic activity of nanoporous gold. *Physical Chemistry Chemical Physics* **2011**, *13*, 4529–4539.

[260] Hodge, A. M.; Doucette, R. T.; Biener, M. M.; Biener, J.; Cervantes, O.; Hamza, A. V. Ag effects on the elastic modulus values of nanoporous Au foams. *Journal of Materials Research* **2009**, *24*, 1600–1606.

[261] Chen-Wiegart, Y.-C. K.; Wang, S.; Chu, Y. S.; Liu, W.; McNulty, I.; Voorhees, P. W.; Dunand, D. C. Structural evolution of nanoporous gold during thermal coarsening. *Acta Materialia* **2012**, *60*, 4972–4981.

[262] Norman, L. L.; Badia, A. Electrochemical surface plasmon resonance investigation of dodecyl sulfate adsorption to electroactive self-assembled monolayers via ion-pairing interactions. *Langmuir* **2007**, *23*, 10198–10208.

[263] Shimazu, K.; Yagi, I.; Sato, Y.; Uosaki, K. Electrochemical quartz crystal microbalance studies of self-assembled monolayers of 11-ferrocenyl-1-undecanethiol: structure-dependent ion-pairing and solvent uptake. *Journal of Electroanalytical Chemistry* **1994**, *372*, 117–124.

[264] Valincius, G.; Niaura, G.; Kazakeviciene, B.; Talaikyte, Z.; Kažemėkaite, M.; Butkus, E.; Razumas, V. Anion effect on mediated electron transfer through ferrocene-terminated self-assembled monolayers. *Langmuir* **2004**, *20*, 6631–6638.

[265] Silva Olaya, A. R.; Zandersons, B.; Wittstock, G. Restructuring of nanoporous gold surfaces during electrochemical cycling in acidic and alkaline media. *ChemElectroChem* **2020**, *7*, 3670–3678.

[266] McGinnity, J. J.; Nicol, M. J. The role of silver in enhancing the electrochemical activity of lead and lead–silver alloy anodes. *Hydrometallurgy* **2014**, *144*, 133–139.